STRUCTURE AND PHYSICAL PROPERTY CORRELATION STUDIES OF $DyMnO_3$ AND SUBSTITUTED OXIDES

By

Yadagiri Karampuri

(PHYS 02 2012 04 002)

X-ray Scattering and Crystal Growth Section
Condensed Matter Physics Division
Materials Science Group
Indira Gandhi Centre for Atomic Research, Kalpakkam, India

A thesis submitted to the
Board of Studies in Physical Sciences
In partial fulfillment of requirements
for the Degree of

DOCTOR OF PHILOSOPHY

of

HOMI BHABHA NATIONAL INSTITUTE

November, 2017

Homi Bhabha National Institute

Recommendations of the Viva Voce Committee

As members of the Viva Voce Committee, we certify that we have read the dissertation prepared by **Yadagiri Karampuri** entitled **"Structure and physical property correlation studies of $DyMnO_3$ and substituted oxides"** and recommend that it may be accepted as fulfilling the thesis requirement for the award of Degree of Doctor of Philosophy.

Chairman - Prof. G. Amarendra G. Amarendra Date: July 19, 2018

Guide / Convener - Dr. R. Nithya Nithya Date: 19/7/2018

Examiner - Dr. P. N. Santhosh Date: 19/7/18

Member 1- Dr. Sharat Chandra Date: 19/7/18

Member 2- Dr N. Subramanian fc N.V. Chandra Sh (Dean (A1)) Date: 19/7/18

Final approval and acceptance of this thesis is contingent upon the candidate's submission of the final copies of the thesis to HBNI.

I/We hereby certify that I/we have read this thesis prepared under my/our direction and recommend that it may be accepted as fulfilling the thesis requirement.

Date: 19/7/2018

Place: IGCAR, Kalpakkam

Nithya
Guide

STATEMENT BY AUTHOR

This dissertation has been submitted in partial fulfillment of requirements for an advanced degree at Homi Bhabha National Institute (HBNI) and is deposited in the Library of IGCAR to be made available to borrowers under rules of the HBNI.

Brief quotations from this dissertation are allowable without special permission, provided that accurate acknowledgement of source is made. Requests for permission for extended quotation from or reproduction of this manuscript in whole or in part may be granted by the Competent Authority of HBNI when in his or her judgment the proposed use of the material is in the interests of scholarship. In all other instances, however, permission must be obtained from the author.

Date: 19/7/18

Place: Kalpakkam

K. Yadagiri

DECLARATION

I, hereby declare that the investigations presented in the thesis have been carried out by me. The work is original and has not been submitted earlier as a whole or in part for a degree / diploma at this or any other Institution / University.

K. Yadagiri

List of Publications

Journals

1. “Modification of low temperature magnetic interactions in $Dy_{1-x}Eu_xMnO_3$”by **K. Yadagiri**, R. Nithya, Shilpam Sharma and A.T.Satya, RSC Adv., **8**, (2018), 13537-13545.
2. “Hole doping effect on structure, transport and magnetic properties of $Dy_{1-x}Ba_xMnO_3$ $(0<x<1)$” by **K. Yadagiri**, R. Nithya, A.T. Satya, and K. Sethupathi, J. Alloy .Compd. **744** (2018), 82-89.
3. “Effects of Dy sub lattice dilution on transport and magnetic properties in $Dy_{1-x}K_xMnO_3$”, by **K. Yadagiri,** R. Nithya, Neeraj Shukla and A.T. Satya, AIP Advances **7**, (2017), 035003 (1-10).
4. “Role of trivalent bismuth ion substitution at Dy site on the physical properties of $DyMnO_3$”, by **K. Yadagiri,** R. Nithya, Neeraj Shukla and A.T. Satya, J. Alloys. Compd. **695**, (2017), 2959-2964.
5. “Structural and micro-Raman studies of $DyMnO_3$ with potassium substitution at Dy site”, by **K. Yadagiri** and R. Nithya, RSC Adv., **6**, (2016), 95417-95424.
6. “Synthesis and crystal structure refinement of new perovskite oxides, $Dy_{0.55}Sr_{0.45}Mn_{1-x}Fe_xO_3$ (x=0.0 and 0.2) from X-ray powder diffraction data”, by **K. Yadagiri** and R. Nithya, Powder Diffr., **31**, (2016), 285-287.

Conference Proceedings

1. “Synthesis and characterization of $Dy_{0.55}Sr_{0.45}Mn_{1-x}Fe_xO_3$”, by **K. Yadagiri**, R. Nithya and T.R. Ravindran”, AIP Conf. Proc., **1665**, (2015), 140015 (1-3).

Communicated/ prepared manuscripts

1. “Dielectric and Impedance relaxations of $Dy_{0.55}Sr_{0.45}Mn_{1-x}Fe_xO_3$”, by **K. Yadagiri** and R. Nithya (Manuscript Under Preparation).
2. “Structure, transport and magnetic properties of $Dy_{0.55}Sr_{0.45}Mn_{1-x}Fe_xO_3$ (x=0.0-1.0:0.2)”, by **K. Yadagiri,** R. Nithya, A.T. Satya, K. Sethupathi and V.R. Reddy (Manuscript Under Preparation).
3. “Impedance relaxation of potassium substituted $DyMnO_3$”, by **K. Yadagiri** and R. Nithya (Manuscript Under Preparation).

Conferences

1. “Effect of monovalent ion substitution at Dy site on the magnetic properties of $DyMnO_3$” (Poster presentation), K. Yadagiri, R. Nithya, T.R. Ravindran, K. Sethupathi, A.T. Satya and Nanda Gopal Krishna. International Conference on Magnetism and Magnetic Materials (ICMAGMA-2015), at VIT Vellore, December 2-4, 2015.
2. “Dielectric and impedance properties of semi insulating perovskite material $Dy_{1-x}K_xMnO_3$ (x = 0.1, 0.2)” (Poster presentation), **K. Yadagiri,** R. Nithya and T.R. Ravindran, Emerging Trends in Advance Functional Materials (ETAFM-2016) at Institute of Physics, Bhubaneswar, January 18-22, 2016.
3. “Transport and magnetic properties of $DyMnO_3$ with isovalent (Bi^{3+}) ion substitution at Dy site” (Oral presentation), **K. Yadagiri,** R. Nithya, Neeraj Shukla, A.T. Satya and R. Rajaraman, International Conference on Materials Science and Technology (ICMTech-2016) at University of Delhi, March 1-4, 2016.

4. “Investigations of multifunctional properties of $Dy_{1-x}Eu_xMnO_3$ ($0\leq x\leq 0.5$)” (Oral presentation), **K. Yadagiri,** R. Nithya, A.T. Satya and Shilpam Sharma, International Conference on Materials for Advanced Technologies (ICMAT-2017), Suntec, Singapore, June 18-23, 2017.

Workshops

1. International Workshop on Electronic Materials and Technology at Anna University, Chennai, India, 13-15 March 2014.
2. Neutrons as Probes of Condensed Matter at Bhabha Atomic Research Center Mumbai, India, 27-31 January 2015.
3. Bringing the Nano World Together (Oxford Instrumentations) at IIT Chennai, India, 3-4 November 2015.
4. Winter School -2016 (Frontier of Materials Science) at Jawaharlal Nehru Center for Advanced Scientific Research, Bangalore, India, 5-9 December 2016.

DEDICATED

To my beloved father and mother

ACKNOWLEDGEMENTS

First of all, I would like to thank you whoever helped me directly or indirectly to complete my Ph.D. programme at IGCAR. I am happy to express my deep sincere and gratitude to Dr. R. Nithya, X-ray Scattering and Crystal Growth Section, Condensed Matter Physics Division, Materials Science Group, IGCAR for her constant support, encouragement and significant discussion during my research work.

I would like to thank the Director IGCAR, Dr. A. K. Bhaduri and Dr. P. Vasudeva Rao, Former Director of IGCAR and the Director MSG, Dr. G. Amarendra for permitting me to pursue my Ph. D.

I thank Dr. M. Saibaba for a pleasant hospitality at JRF enclave & Department of Atomic Energy for financial support.

My sincere thanks to doctoral committee chairman Dr. G. Amarendra and members Dr. N. Subramanian, Dr. Sharat Chandra for their valuable suggestions and encouragement.

I would like to thank my collaborators Dr. A.T. Satya, Dr. T. Geetha Kumary and Dr. T.R. Devidas for electrical resistivity measurement at Low Temperature Studies Section, Materials Science Group and Dr. Neeraj Shukla, Dr. Shilpam Sharma for magnetic measurement at UGC-DAE CSR Kalpakkam Node, Kokilamedu. I sincerely thank Dr. R. Rajaraman for Raman spectroscopy measurements at UGC-DAE CSR, Kalpakkam Node, and Kokilamedu. I would like to thank Dr. T.R. Ravindran for significant and fruitful discussions. I thank Mr. Nanda Gopal Krishna, MMG, IGCAR for recording XPS spectra. I would like to thank Ms. Srividya, MMG for SEM and EDX studies.

I am thankful to collaborators outside IGCAR, Prof. K. Sethupathi and Mr. Srinivasan, Department of Physics, IIT Madras for magnetic measurements, Prof. G. Govindaraj for Dielectric measurements at Central Instrumentation Facility, Pondicherry University and useful discussions and Dr. V. Raghavendra Reddy, UGC-DAE CSR, at Indore for Mossbauer spectroscopy measurements.

I thank Dr. B. Venkatraman, Director, Health, Safety and Environment Group, for allowing carrying out research at Materials Science Group.

I deeply express my heartfelt thanks to all Scientific Officers at X-ray Scattering and Crystal Growth Section, Dr. N. Subramanian, Dr. V. Sridharan, Dr. Ganesh Moorthy, Dr. Sonadurai and Dr. Sarguna for sharing of scientific thoughts.

I would like to thank Dr. M.T. Jose, Dr. U. Madhusoodanan and Dr, Dr. O. Anna Lakshmi, Radiological Safety Division, IGCAR, for initial guiding me.

I sincerely thank Dr. N.V. Chandra Sekhar, Dean, Physical Sciences, HBNI, IGCAR, Dr. B.V.R. Tata, Former Dean, Physical Sciences, HBNI, IGCAR, Dr. S. Kalavathi and Smt. O.K. Sheela for their constant support and encouragement during Ph.D.

I would like to thank Dr. G. Jaiganesh, for thesis formatting and Dr. G. Murugesan for helping samples preparation.

I thank all my batch mates (JRF-2012), and my roommate (Mr. Prashant Panigrahi) at JRF enclave and all my friends at Kalpakkam.

I owe a deep gratitude to my parents Mr. Kistaiah and Mrs. Pushpa Kistaiah, my brothers Mr. Venu and Mr. Prashanth, my friend Ms. Uma and all my friends for their adoration, affinity and inspiration which force me throughout my journey of life.

K. Yadagiri

CONTENTS

CHAPTER - 1

INTRODUCTION

CHAPTER – 2

EXPERIMENTAL DETAILS

CHAPTER - 3

STRUCTURE AND OTHER PHYSICAL PROPERTIES OF MONOVALENT POTASSIUM ION SUBSTITUTION AT Dy SITE IN $DyMnO_3$ – $Dy_{1-x}K_xMnO_3$

CHAPTER - 4

STRUCTURAL PHASE TRANSITION AND OTHER PHYSICAL PROPERTIES OF DIVALENT ION (Ba^{2+}) SUBSTITUTION AT Dy SITE IN $DyMnO_3$ – $Dy_{1-x}Ba_xMnO_3$

CHAPTER - 5

MULTIFUNCTIONAL PROPERTIES OF ISOVALENT IONS (Bi & Eu) SUBSTITUTION AT Dy SITE IN $DyMnO_3$ - $Dy_{1-x}Bi_xMnO_3$ AND $Dy_{1-x}Eu_xMnO_3$

CHAPTER - 6

INVESTIGATION of MULTIFUNCTIONAL PROPERTIES OF CO - SUBSTITUTION AT Dy AND Mn SITE OF $DyMnO_3$ - $Dy_{0.55}Sr_{0.45}Mn_{1-x}Fe_xO_3$

CHAPTER- 7

CONCLUSIONS AND FUTURE WORK

SYNOPSIS

Multifunctional materials exhibit two or more physical properties, one of which is normally structural and the other can be functional properties such as optical, electrical, magnetic, thermal etc. The systems (multifunctional materials) include aspects of smart materials or systems and biologically-inspired materials (biomimetics). These multifunctional materials cover all types of materials (like polymers, ceramics, metals, composites) and other forms like bulk, coatings, fibers, fabrics etc.

The multiferroic materials are one of the categories of multifunctional materials. The term multiferroic has been coined to describe materials in which two or all three of the properties ferroelectricity, ferromagnetism, and ferroelasticity occur in a single phase. This means that they have a spontaneous magnetization that can be reoriented by an applied magnetic field, a spontaneous polarization that can be reoriented by an applied electric field and a spontaneous deformation that can be reoriented by an applied stress. Specific device applications that have been suggested for these multiferroic materials include multiple state memory elements, electric-field-controlled ferromagnetic resonance devices and transducers with magnetically modulated piezoelectricity. In addition to these, the ability to couple with either the magnetic or the electric polarization offers an extra degree of freedom in the design of conventional actuators, transducers and storage devices. Therefore, these multiferroic materials can be classified into two categories according to their methods of exhibiting multiferroic property and they are Type I & Type II multiferroics.

Features of Type I multiferroics

Type I multiferroics undergo a structural, nonpolar-to-polar phase transition (typically involving breaking of inversion symmetry) leading to ferroelectricity at high temperatures, whereas the commencement of magnetic order occurs below a phase transition at lower temperatures. In many such materials, both ferroelectric transitions and magnetic transitions take place above room temperature, fulfilling an essential requirement for technological application. The common example of a room-temperature, Type-I multiferroic is $BiFeO_3$ which is presently the most-studied multiferroic owing to the room - temperature functionality. Ferroelectric transition temperature for $BiFeO_3$ is $T_{FE} \sim 1103$ K and magnetic transition temperature is $T_N \sim$

633 K. However, in Type I multiferroics, the coexisting magnetic and ferroelectric order parameters are naturally weakly coupled. $BiMnO_3$ is also another example for Type I multiferroic material in which ferroelectric transition occurs at $T_{FE} \sim 800$ K and magnetic transition at $T_{FM} \sim 110$ K, below which the two orders coexist.

Features of Type II multiferroics

Presence of a magnetic ordering in materials plays a key role in Type II multiferroics. The magnetic ordering below a given temperature lowers the symmetry group from a nonpolar parent phase to a polar magnetic phase and an electrically polar state with inclusion of improper ferroelectricity that is obtained from magneto structural coupling to the crystal structure. In this case, magnetic and ferroelectric order parameters are closely coupled; on the other hand, polar non - centrosymmetric magnetic structures tend to result from the complex magnetic ordering of geometrically frustrated states or from competing interactions. The frustration suppresses (or) removes the ordering temperature. Type II multiferroicity is typically found below room temperature. Moreover, the ferroelectricity in this type of materials is secondary to the magnetic ordering and so are usually several orders of magnitude weaker than that of proper ferroelectrics. Therefore, these systems are not yet suitable for any technological applications. However, the evidence for ordering temperatures and saturated polarizations of Type II multiferroics have been increasing following the continual discovery of new and more interesting materials. $TbMnO_3$ and $DyMnO_3$ are good examples of Type II multiferroic materials.

$DyMnO_3$ (DMO) exhibits either orthorhombic or hexagonal crystal structure depending upon synthesis conditions. In the literature it is reported that DMO adopts orthorhombic structure when synthesized at low temperatures and is found to be electrically insulating in nature. The insulating orthorhombic DMO shows antiferromagnetic ground state. The investigation suggested that in DMO, Mn^{3+} and Dy^{3+} spins are ordered at ~39 and ~6 K respectively. In case of hexagonal $DyMnO_3$, these ordering temperatures are seen at ~70 K and ~7 K respectively. These ordering temperatures are quite large due to geometrical frustrations at low temperatures in comparison to orthorhombic structure.

Since the last few decades, considerable amount of research is going on these multi ferroic materials because of couple of major reasons. The first reason is the fascinating physics involved in these coupling phenomena of the magnetic and ferroelectric orders. The second reason is from the point of view of promising potential applications like spintronics and data storages. The intimate coupling between the two orders gives rise to giant Magneto Electric (ME) effect, for instance Polarization (P) switching in multiferroics leading to a Spiral Spin Order (SSO). In general, these type-II multiferroics with magnetic origin for ferroelectricity can be further classified in two groups according to the details of microscopic mechanism. The first group includes those having a non collinear spiral spin order, making broken space inversion symmetry and thus a spontaneous ferroelectric (FE) polarization via the well-known inverse Dzyaloshinski-Moriya Interaction (DMI). The polarization is formulated as $\mathbf{P \sim e_{ij} (S_i \times S_j)}$ where e_{ij} is the vector connecting two neighboring spins S_i and S_j. The second group has a specific collinear spin configuration and consequently an improper ferroelectricity which may be driven by the so called exchange striction mechanism. The polarization can be expressed as $\mathbf{P \sim S_i . S_j}$. This is explained in case of $Ca_3Co_{1-x}Mn_xO_6$ and orthorhombic $HoMnO_3$.

The present thesis is focused on the study of rare earth manganites with an aim to understand the effect of Dy site substitution by heterovalent ions on the physical properties of $DyMnO_3$. The thesis is organized into 7 Chapters. Chapters 1 and 2 are devoted to introduction and experimental methods. Chapters 3 to 6 describe the experimental results of individual systems. A brief description of each Chapter is given below:

Chapter 1: Introduction

Chapter 1 discusses various aspects of multifunctional materials and applications. One of the characteristics of multifunctional materials is the multiferroic property. Since the present research work is on manganites, multiferroic properties of $RMnO_3$ and $R_{1-x}A_xMnO_3$ (A=substituted element) are reviewed. In addition to these properties, transport and vibrational properties of orthorhombic and hexagonal $RMnO_3$ are also included in this chapter.

Chapter 2: Experimental Techniques

Chapter 2 contains synthesis methods and characterization techniques used to characterize the materials in this thesis. Polycrystalline materials for the present study are synthesized by high temperature solid state reaction. Mechanism and process of solid state method with advantages over other methods are explained in this chapter. The synthesized compounds are characterized by X-ray diffraction (XRD) technique at room temperature to know the structure and composition. Raman spectroscopy is employed to identify the Raman modes arising from the atomic vibrations. To probe transport properties, temperature dependence of electrical resistivity was measured by employing four probe method, and to explore magnetic properties of these materials, SQUID Vibrating Sample Magnetometer (VSM) has been used. In addition to these measurements, SEM, EDX, XPS, Mossbauer spectroscopy and dielectric spectroscopy were carried out for elemental analysis, oxidation state determination and dielectric and impedance properties of these materials. Details of the respective experimental techniques are covered in this chapter.

Chapter 3: Structure and other physical properties of monovalent ion (K^{+1}) substitution at Dy site of $DyMnO_3$ – $Dy_{1-x}K_xMnO_3$

Chapter 3 deals with the synthesis process of parent compound $DyMnO_3$ (DMO) and monovalent potassium (K^{+1}) substituted $DyMnO_3$ ($Dy_{1-x}K_xMnO_3$, x=0.0 to 0.3). Phase integrity and composition were checked by XRD, SEM-EDAX, XPS and Raman spectroscopy techniques. Electrical and magnetic properties of these compounds were undertaken. All these compounds under investigation showed orthorhombic structure. The compounds showed semiconducting nature with hopping type of conduction. Room temperature Raman spectra of orthorhombic compounds exhibited four high intensity modes among 24 theoretical calculated modes which are identified as symmetric stretching, anti symmetric stretching (Jahn –Teller mode), bending, and tilting modes for x=0.0 to 0.3. For higher concentration of potassium (x=0.3), new Raman modes (A_{1g} and B_{2g}) were observed in addition to the Raman modes that were observed for low values of x. Temperature dependent magnetization of DMO showed a series of three magnetic transitions corresponding to Mn and Dy spins. Although a large irreversibility between Zero Field Cooled (ZFC) and Field Cooled (FC) magnetization data was observed with a peak for x=0.3, the peak temperatures did not alter with frequency ruling out the possibility of spin glass behavior. All the compounds show hysteresis loops for temperatures below 10 K. However, magnetization does not saturate even at 7 Tesla fields. Thus the presence of hysteresis loops and lack of saturation magnetization may be ascribed to a parasitic ferromagnetism due to canting of Mn ions besides Dy and Mn exchange interactions.

Dielectric measurements were performed on the first two substituted compounds (x=0.1 and 0.2) in the temperature range 125 K to 300 K in the frequency range 0.1 Hz to 10^7 Hz. $Dy_{0.8}K_{0.2}MnO_3$ possessed high dielectric constant as compared to $Dy_{0.9}K_{0.1}MnO_3$. DC conductivity data extracted from AC conductivity followed hopping conduction thus complimenting DC resistivity results. Grain and grain boundary resistances were determined by fitting Cole-Cole plots of impedance to a circuit model.

Chapter 4: Structural phase transition and other physical properties of divalent ion (Ba^{2+}) substitution at Dy site in $DyMnO_3$ – $Dy_{1-x}Ba_xMnO_3$

Chapter 4 discusses effects of divalent ion (Ba^{2+}) substitution at Dy site on the structure and other physical properties of $Dy_{1-x}Ba_xMnO_3$; x=0.0, 0.1, 0.3, 0.5, 0.8 and 1.0. All the compounds were synthesized by following the same procedure used for analogous compounds studied here. With lower valent Ba ion substitution for trivalent Dy ion, tetravalent manganese ions are generated whose concentration increases with increase in the Ba content. The presence of tri and tetra valent manganese ions was evidenced by X-ray photoelectron spectroscopy (XPS) technique. XRD technique was used to verify the phase formation. A structural phase transition was found from orthorhombic to hexagonal. While DMO has orthorhombic structure, $BaMnO_3$ (x=1.0) adopted hexagonal structure. While compounds with x = 0.1 & 0 .3 crystallized in the orthorhombic structure, compounds corresponding to 0.5 and 0.8 contained mixed phases. Structural phase transition was probed by Raman spectra that showed structural variations. Temperature dependence of electrical resistivity showed semiconducting nature with hopping conduction. Hopping energy and polaron binding energies are calculated. Temperature variation of magnetization measured in the ZFC and FC modes bifurcate at low temperatures suggesting the onset of superexchange correlations among the magnetic ions, Dy^{3+}, Mn^{3+} and Mn^{4+}. $BaMnO_3$ showed a high and a low temperature magnetic transitions around 230K around 43K respectively. The temperature dependence of molar susceptibility does not follow CW law in the whole temperature range measured indicating magnetic anisotropy. Details of the nature of these transitions are discussed in the thesis. Isothermal magnetization data of all the compounds recorded at 5 K showed hysteresis loops whose magnetization at the highest applied field reduced with increase in temperature. High coercive field values (~kOe) obtained from MH curves may be attributed to magnetic anisotropy as mentioned earlier.

Chapter 5: Multifunctional properties of isovalent ions (Eu^{3+}, Bi^{+3}) substitution at Dy site in $DyMnO_3 – Dy_{1-x} (Eu, Bi)_x MnO_3$

Investigations on the effects of isovalent magnetic (Eu) and non-magnetic (Bi) ion substitution at Dy site in DMO are discussed in this Chapter 5. Phase formation was tracked by room temperature powder X-ray diffraction technique. All the compounds under study crystallized in distorted perovskite structure with Pnma space group. From the analysis of Raman spectra data collected at room temperature, Raman bands corresponding to movements of octahedral units have been identified. Wave numbers corresponding to tilting and bending bands shifted to low wave numbers (softening) with the increasing of Eu^{3+} concentration. Transport properties of these materials displayed insulating behavior with activated (Arrhenius) type of conduction in contrast to hopping conduction observed in the end compounds, (Dy, Eu)MnO_3. Temperature dependence of magnetization revealed a single magnetic transition whose magnitude decreased with increase in the europium content. Molar susceptibility data of all the compounds above the respective magnetic transition temperatures were fitted to Curie-Weiss (CW) law to extract Curie-Weiss temperature and effective paramagnetic moment. By assuming individual atomic moments for the magnetic ions, (Dy, Eu and Mn) effective magnetic moments were calculated and the magnetic moment was found to reduce with increase in the europium content. Effective magnetic moments determined from CW fit parameters were also found to decrease with europium content. Field dependence of magnetization (M-H) curves recorded at different temperatures for substituted compounds exhibited S-type hysteresis curves for temperatures below 10K suggesting the presence of a weak ferromagnetism. However, end members of this series, showed hysteresis loops with high coercive fields indicating strong ferromagnetic correlations.

Among a series of $Dy_{1-x}Bi_xMnO_3$ compounds, only $Dy_{0.9}Bi_{0.1}MnO_3$ was synthesized in a single phase using the conventional solid state reaction. Single phase compounds for higher x values of Bi could not be prepared using the same synthesis conditions due to evaporation of Bi. We investigated effects of Bi substitution for this compound alone. Both compounds showed orthorhombic structure, nevertheless, bond angles and bond distances alter for Bi^{3+}substitution compound with comparing of $DyMnO_3$. Raman bands for the substituted compound were found to increase with respect to the parent compound. Transport properties of these compounds indicated that these both materials show semiconducting behavior with small polaron hopping conduction. Magnetization as a function of temperature revealed that the Dy spin ordering is reduced in the Bi substituted compound while transition corresponding to Mn spins is retained. Both compounds displayed hysteresis loops with high coercive fields without saturation magnetization. Unlike in $LaMnO_3$ where A-type antiferromagnetism due to orbital ordering was found, these compounds show ferromagnetism that may be ascribed to super exchange interactions between nearest neighbor Dy and Mn spins.

Chapter 6: Investigations on multifunctional properties of Sr and Fe co-substituted at Dy and Mn site of $DyMnO_3$ - $Dy_{0.55}Sr_{0.45}Mn_{1-x}Fe_xO_3$

Chapter 6 describes structural, electrical, vibrational, dielectric and magnetic properties of Fe ion substitution at Mn site in $Dy_{0.55}Sr_{0.45}Mn_{1-x}Fe_xO_3$ (x=0.0 - 1.0: 0.2). The results of XRD studies on these materials indicated that all the compounds exhibited orthorhombic structure. Low concentrations of iron yielded single phase while the higher iron concentrations contained small impurity peaks. Room temperature Raman spectra for all the compounds were recorded using micro-Raman spectrometer with an excitation wavelength of 514.5 nm Ar ion laser. Temperature variation of electrical resistivity of these materials revealed the semiconducting nature with hopping conduction. Studies of temperature and field dependence of DC magnetization and room temperature Mossbauer spectra revealed the valence state of iron as well as the magnetic nature of the compounds. At lower fields and lower temperature these materials showed the deviation in Zero field cooled curve (ZFC) and field cooled curve (FC) of temperature dependence of magnetization. The ratio of effective magnetic moment determined from CW fits to experimental susceptibility data and theoretical magnetic moment calculated suggest that weak ferromagnetic clusters are present in the compounds even at high temperatures. It is interesting to note that compounds with iron substitution exceeding 60at.% at Mn site showed hysteresis loops even at 300K revealing ferromagnetic correlations at high temperatures. Dielectric properties of $Dy_{0.55}Sr_{0.45}Mn_{1-x}Fe_xO_3$ (x=0.0, 0.2, 0.4 and 1.0) are studied in the frequency range from 0.1 to 10 MHz and in the temperature range of 125 K - 300 K. The results revealed that x=0.4 shows dielectric relaxation peak among all other compounds in this series. AC conductivity, impedance and modulus spectra were analyzed to get the activation energy for dielectric relaxation. Nyquist plots were analyzed to get resistances between the grain and grain boundaries.

Chapter 7: Brief summary of the thesis and scope of future work

In Chapter 7, major findings of the thesis are summarized and the directions for future work on these materials to make them useful for modern applications are suggested.

LIST OF FIGURES

LIST OF TABLES

CHAPTER – 1

INTRODUCTION

1.1. INTRODUCTION

Multifunctional materials exhibit two or more physical properties, one of which is normally structural and the other can be functional properties such as optical, electrical, magnetic, thermal etc. The multifunctional materials display properties that include aspects of smart materials or systems and biologically-inspired materials (biomimetics). These cover all types of materials like polymers, ceramics, metals, composites and forms examples bulk, coatings, fibers, fabrics etc. Based on the multi-functional materials, additional new research and development areas have emerged and they are:

- Composite materials
- Hybrids
- Interpenetrating networks
- Coatings
- Interfacial and surface properties
- Biomimetics
- Materials with nanostructures
- Structural integration
- Materials modeling

On the whole, the essential feature of most multifunctional materials will be some form of composite structure, with interfacial properties playing a major role in determining their properties.

Multifunctional materials represent the next big step in product development by efficiently combining structural properties with an additional functionality. Many such next generation products may draw inspiration from nature, where size and weight is often critical and multifunctionality is a necessity rather than a luxury. For example, desert beetles, butterflies and electric eels integrate useful thermal, optical and electromagnetic features within their body structures. Multifunctional materials technologically take part in a crucial role in the future-generation of intelligent devices and sensors, smart homes, autonomous devices and robotics. This multifunctionality is applicable to nano level in the form of nano materials (powders and thin films) and nano composites. An understanding of multifunctionality of materials is not only stimulating scientific interest but also technologically important. The study of these materials with strong electric and magnetic fields will be a highlight for modern electronics and will open the gate for fascinating applications. Particularly for very high density memory storage using both magnetic and electric orders are being considered, with moreover the possibility of electrical read or write operations on magnetic memory devices and vice versa. Multiferroics and composites permit harnessing of electrical energy from stray magnetic fields from minute but ever-present variations in the Earth's field [1, 2].

1.2. MULTIFERROIC MATERIALS

Multiferroic materials are one of the categories of multifunctional materials. The term multiferroic has been coined to describe materials in which two or all three of the properties: ferroelectricity, ferromagnetism, and ferroelasticity occur in a single phase [3-6]. This means that they have a spontaneous magnetization that can be reoriented by an applied magnetic field, a spontaneous polarization that can be reoriented by an applied electric field and a spontaneous deformation that can be reoriented by an applied stress. Specific device applications that have been suggested for these multiferroic materials include multiple state memory elements, electric-field-controlled ferromagnetic resonance devices and transducers with magnetically modulated piezoelectricity. In addition to these, the ability to couple with either the magnetic or the electric polarization offers an extra degree of freedom in the design of conventional actuators, transducers and storage devices [7-11]. Therefore, according to their methods of exhibiting multiferroic property, these multiferroic materials are broadly divided into two types and they are: Type 1 & Type 2 multiferroics

1.2.1. Features of Type 1 multiferroics

Type 1 multiferroics undergo a structural, nonpolar-to-polar phase transition (typically involving the breaking of inversion symmetry) leading to ferroelectricity at high temperatures, whereas the commencement of magnetic order occurs below a phase transition at lower temperatures. In many such materials, both ferroelectric transitions and magnetic transitions take place above room temperature, fulfilling an essential requirement for technological applications. The common example of a room-temperature, Type 1 multiferroic is $BiFeO_3$ which is presently the most-studied multiferroic owing to the room-temperature functionality [12-15]. Ferroelectric transition temperature (T_{FE}) for $BiFeO_3$ is 1103 K and magnetic transition temperature (T_N) is 633 K. However, in Type 1 multiferroics, the coexisting magnetic and ferroelectric order parameters are naturally weakly coupled. $BiMnO_3$ is another example for Type

1 multiferroics in which ferroelectric transition occurs at $T_{FE} \sim 800$ K and magnetic transition at $T_{FM} \sim 110$ K, below which the two orders coexist [16, 17].

1.2.2. Features of Type 2 multiferroics

Presence of antiferromagnetic magnetization plays a key role in Type 2 multiferroic materials. Magnetic ordering below a given temperature lowers the symmetry group from a nonpolar parent phase to a polar magnetic phase and an electrically polar state with inclusion of improper ferroelectricity that is obtained from magneto-structural coupling to the crystal structure [18]. In this case, magnetic and ferroelectric order parameters are closely coupled; on the other hand, polar noncentrosymmetric magnetic structures tend to result from the complex magnetic ordering of geometrically frustrated states or from competing interactions. The frustration either suppresses or removes the ordering temperature. Type 2 multiferroicity is typically found below room temperature. Moreover, the ferroelectricity in this type of materials is secondary to the magnetic ordering and so are usually several orders of magnitude weaker than that of proper ferroelectrics. Therefore, these systems are not yet suitable for any technological applications. However, the evidence for ordering temperatures and saturated polarizations of Type 2 multiferroics have been increasing following the continual discovery of new and more interesting materials. Rare earth (R) manganites, $TbMnO_3$ and $DyMnO_3$ are good examples of Type 2 multiferroic materials [19, 20]. In view of the multifunctional properties of rare earth manganites, $RMnO_3$ we have chosen a member of these manganites, $DyMnO_3$ and substituted compounds for the present study and we briefly discuss the properties of rare earth compounds in the following sections.

1.3. MULTIFERROIC PROPERTIES OF RARE EARTH MANGANITES ($RMnO_3$) AND RELATED COMPOUNDS

Rare-earth perovskites, $RMnO_3$ have been extensively studied due to their wide variety of physical phenomena: for instance superconductivity, ferroelectricity and colossal magneto resistance. All the phenomena exhibited by the perovskite oxides are closely related to the lattice. Many of the interesting phenomena involve a complex interplay between the spin, charge and orbital degrees of freedom, accompanied with small displacements in the crystal lattice. While it is frequently accepted that spin and charge determine the electronic properties in perovskites, it has become a topic of new interest to study the consequences of orbital degeneracy on physical properties.

1.3.1. Crystal structure of perovskite oxides

Perovskites belong to a large family of crystalline ceramics (metallic elements combining with non metals, usually oxygen or halide), which derive their name from a specific mineral known as perovskite, $CaTiO_3$. It was first described in the 1830s by the geologist Gustav Rose who named it after the famous Russian mineralogist Count Lev Aleksevich Von Perovski. The general formula of perovskites is ABX_3 where A-site is generally occupied by large cations such as rare earth ions or alkaline earth metal ions, B-site is occupied by smaller cations such as transition metal ions and X is an anion, usually oxide or halide. The basic structural unit of a perovskite is a cube and can be arranged by a polyhedral one in which the six X anions surround each B cation. In such a model, the basic structural unit becomes a group of eight corner-shared octahedrons around the A-cation. Figure 1.1 shows the cubic perovskite structure (both A-type and B-type). The perovskite oxides structure, ABO_3 can be viewed as a cubic close packed array of O^{2-} anions (with radius r_O), and A^{2+} or A^{3+} cations (with radius r_A), with small B^{4+} or B^{3+} cations (with radius r_B) in octahedral interstitial sites where, r_A must be same as the radii of the oxide ions, $r_O = r_A = 0.14$ nm and r_B is $= 0.058$ nm.

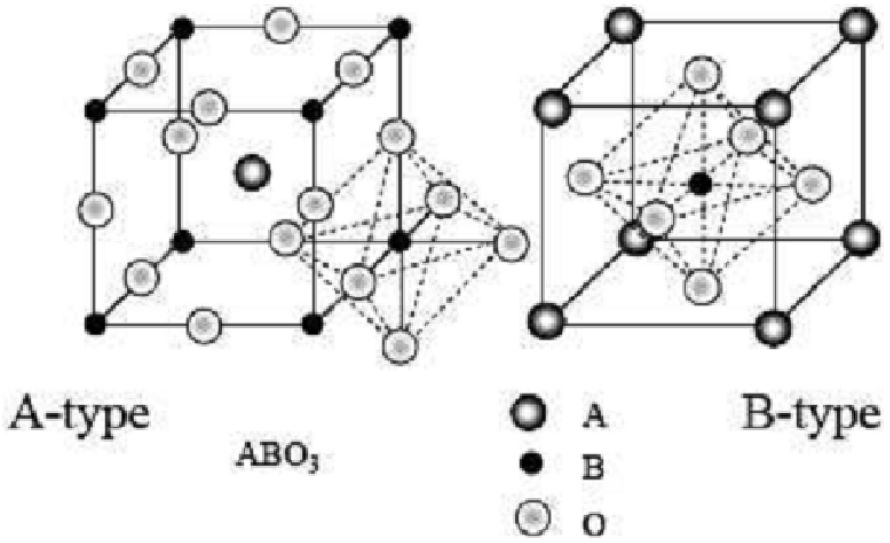

Figure 1.1. Schematic diagrams of the ideal cubic perovskite structures with A-type (B cation at origin) and B-type (A cation at origin) arrangements.

Goldschmidt defined a tolerance factor [21-23],

$$t = \frac{r_A + r_O}{\sqrt{2}(r_B + r_O)}$$

For t = 1, perovskite structure is cubic with space group Pm3m and number of formula units per unit cell (Z) is 1. Generally, most of the perovskite oxides show a structural distortion due to mismatch of the ionic size of cations and other factors, so that the crystal symmetry is reduced to hexagonal/trigonal, rhombohedral, orthorhombic etc. There are two possible characteristic distortions, which influence the perovskite structure; one arises from the A-site cation size mismatch and the other due to the Jahn-Teller effect of B-site ions (such as Mn^{3+}). The B-O-B bond angle is also sensitive to the size of the A-site ion and is reduced from 180°. Thus, if the tolerance factor is in the range $0.75 < t < 0.9$, a cooperative buckling of the corner sharing octahedra occurs to optimize the A-O bond lengths which enlarges the unit cell resulting in orthorhombic distortion of the ideal cubic perovskite structure. When the tolerance factor lies in range of $0.9 < t < 1$, then rhombohedral symmetry with small distortions is stabilized. If tolerance factor, $t > 1$, i.e., the A-site ion is too large and perovskite structure will be transferred to a hexagonal close packing structure.

1.3.2. Jahn-Teller (JT) distortions in $RMnO_3$

In stiochiometric $RMnO_3$ (RMO) compounds, manganese ions exist in the trivalent state (Mn III) with 4 electrons in the 3d orbital. Due to the smaller ionic size of rare earth ion, polyhedra of cations in RMO get distorted whose bond lengths and bond angles differ from the ideal cubic perovskite structure and the local symmetry of the 3d orbital reduces from the cubic symmetry. As a consequence of this, the crystalline electric field lifts the degeneracy of the d orbital. The five fold degenerate 3d-orbitals split into three t_{2g} orbitals and two e_g orbitals in a crystal field of octahedral symmetry which is lower than the cubic symmetry. The degeneracy of the e_g orbital of Mn^{3+} ion is further lifted by a cooperative Jahn-Teller (JT) distortion due to the presence of a single electron in the e_g orbital. In general, in RMO, the crystal field splitting (Δ), energy between the lowest t_{2g} level and the highest e_g level is $\Delta \sim 1.5$ eV while the corresponding exchange energy according to Hund's rule is about 2.5 eV which is higher than Δ.

Figure 1.2 shows distortions in the case of JT ion, Mn^{3+} for an axial elongation of the oxygen octahedron. Due to this distortion, the energy of Mn^{3+} is lowered whereas energy of Mn^{4+} is not changed. Thus, Mn^{3+} has an obvious tendency to distort its octahedral environment in contrast to Mn^{4+}. This Jahn-Teller distortion is quite effective for the lightly doped manganites because of a large concentration of Mn^{3+} ions. The Jahn-Teller distortions are interconnected from one Mn^{3+} site to another (cooperative Jahn-Teller effect). While increasing of the Mn^{4+} content, the Jahn-Teller distortions are reduced and the stabilization of the $3z^2$-r^2 e_g orbital becomes less effective. Even so, in case of large number of manganites, the e_g orbitals of two types $3z^2$-r^2, x^2-y^2 are not occupied by the e_g electrons of Mn^{3+} at random and an orbital order is achieved [24, 25].

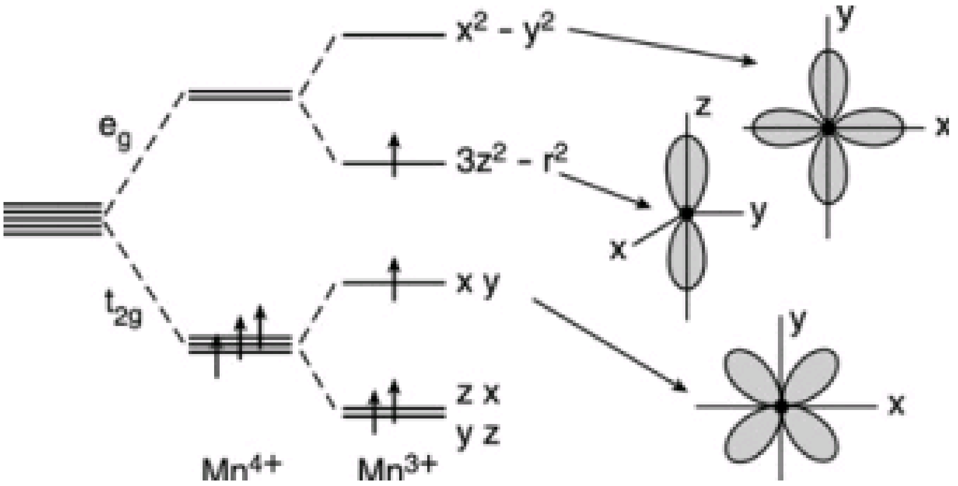

Figure 1.2. Typical energy level diagram for Mn^{4+} and Mn^{3+} ions present in a crystalline electric field of octahedral symmetry.

The first member of RMO series compounds is $LaMnO_3$ which crystallizes in a distorted orthorhombic structure with space group Pnma. Temperature dependence of magnetization revealed that the compound undergoes an antiferromagnetic transition (AFM) with a Neel temperature of T_N~140 K [26, 27]. The AFM ordering belongs to A-type antiferromagnetic (A-AFM) implying Ferromagnetic (FM) correlations in the planes that are coupled antiferromagnetically perpendicular to the planes [28]. Transport properties showed a band gap of 1.1 eV indicating the insulating nature of the compound. Thus, the structure plays a key role in determining the transport and magnetic properties of RMO.

1.3.3. Magnetic properties

Magnetic properties of the manganites are governed by exchange interactions between the Mn spins. These interactions are comparatively large between two Mn spins separated by an oxygen atom and are affected by the overlap between the Mn 3d-orbitals and the O 2p-orbitals. The Super Exchange (SE) interactions depend on the orbital configuration following the rules of Goodenough-Kanamori [29]. Generally, for Mn^{4+}-O-Mn^{4+} the interaction is AFM, whereas for Mn^{3+}-O-Mn^{3+} it may be FM or AFM, such as in $LaMnO_3$ where both FM and AFM interactions coexist.

A peculiar and interesting case of hole doped manganites, $R_{1-x}A_xMnO_3$ (A = divalent ions) is that of Mn^{3+}-O-Mn^{4+} angle for which the Mn ions can exchange their valence by a simultaneous jump of the e_g electron of Mn^{3+} to the O 2p- orbital and from the O 2p-orbital to the empty e_g orbital of Mn^{4+}. This mechanism of double exchange originally proposed by Zener [30] ensures a strong ferromagnetic interaction as shown in Fig. 1.3. Anderson and Hasegawa [31] interpreted that the probability of the e_g electron transfer from Mn^{3+} to neighboring Mn^{4+} is termed as transfer integral, t which is related to the angle between the Mn spins (θ) and is given by $t_0 \cos(\theta/2)$. The process of electron transfer lifts the degeneracy of the configurations Mn^{3+}-O-Mn^{4+} and Mn^{4+}-O-Mn^{3+} leading to two energy levels, $E_t = E_0 \pm t_0 \cos(\theta/2)$. The energy gain of the parallel spin configuration i.e. $\theta = 0$ which maximizes t for the anti parallel configuration and $\theta = \pi$ reveals the ferromagnetic character of the double exchange interaction. But, the usual exchange interaction $\cos(\theta)$ and the double exchange angular dependence of $\cos(\theta/2)$ are dissimilar. This different angular dependence in conjunction with the competition between double exchange ferromagnetism and super exchange antiferromagnetism is at the origin of the complex magnetic phase diagram of manganites versus the doping level (x). Particularly, for small doping levels, canted AF phases were predicted by de Gennes [32]. As a result, the energy gain of first-order in the canting angle for double exchange which overcomes the energy increases of second-order in the canting angle for super exchange AFM.

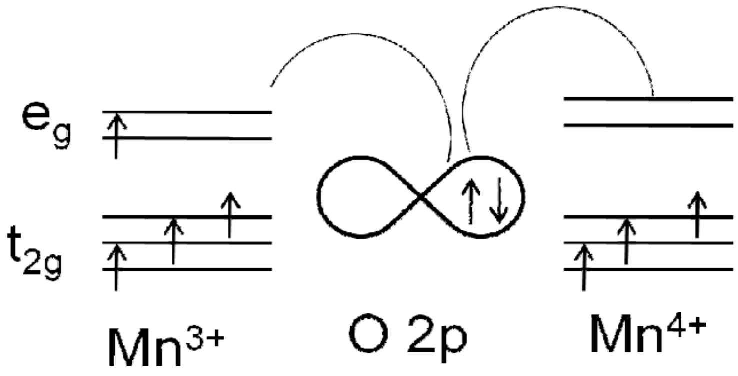

Figure 1.3. Double exchange mechanism between Mn^{3+} and Mn^{4+} via oxygen ion.

Ferromagnetic metallic (FMM) phases with high Curie temperatures (T_C) are required for potential applications. In the first approximation, one can neglect the Mn^{3+}-Mn^{3+} interaction since it is either FM or AFM depending on the orbital configuration and both FM and AFM interactions currently coexist in the same compound such as in $LaMnO_3$. Then, supposing the Mn^{4+}-Mn^{4+} AFM super exchange and Mn^{3+}-Mn^{4+} FM double exchange interaction to be of same magnitude, the mean field approximation leads to $T_C \cong 2x(1-x)-x^2$, which is maximum for $x=1/3$. The fact that the FM phases are generally found around x=1/3 in manganites is in agreement with this crude model.

1.3.4. Electronic properties

The transfer of e_g electron from Mn^{3+} to Mn^{4+} by double exchange is the basic mechanism of electrical conduction in the manganites. In those with strong double exchange, the e_g electrons become delocalized in the ferromagnetic phase for a certain range of doping centered on x=1/3 and a FMM state is established at low temperatures [33]. The electronic structure of such a FM phase is schematically shown in Fig. 1.4. In contrast to the 3d ferromagnetic metals such as Ni or Fe where the up- and down-spin bands are both occupied, they are separated by 1 eV or more and the upper band is empty, leading to a half-metallic behavior. Thus, the conduction band of a half-metallic ferromagnet is fully spin-polarized and is of large potential interest for spin electronics [34].

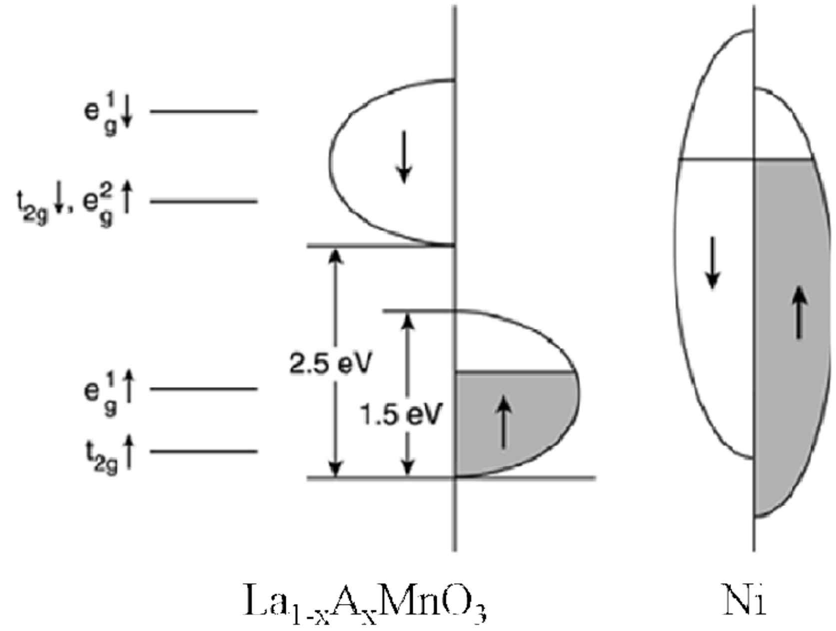

Figure 1.4. Schematic diagram for the band structure of divalent ion substituted $LaMnO_3$ and Ni element [33].

The electronic structure of $La_{1-x}A_xMnO_3$ (A = Ca, Sr and Ba) has been theoretically investigated by the local spin-density approximation [35-37]. Whereas $LaMnO_3$ is found to be an AFM insulator with a gap in the half-filled e_g band resulting from the JT distortion, a half-metallic ferromagnetic ground state is obtained for x =1/3, with the electronic structure near the Fermi level mainly consisting of substantially hybridized bands derived from majority spin Mn e_g states and O 2p states. The manganites with $x<0.5$ have a conduction band more than half-filled whereas those with $x>0.5$ have a conduction band less than half-filled and thus the respective charge carriers are holes and electrons. They are currently labeled as hole-doped and electron-doped manganites, respectively. When increasing above 0.5, the number of ferromagnetic DE links decreases and that of AF coupled Mn^{4+} increases. This favors AF or canted AF phases in which the motion of charge carriers is hindered. For certain doping levels (x=0.5) corresponding to Mn^{3+}-Mn^{4+} species with a 1:1 ratio, an ordering of charge carriers takes place while their long-range Coulomb interaction overcomes their kinetic energy [38, 39]. This Charge Ordered Insulating (CO-I) state is favored by the presence of small size cations at the A site: for example in $Pr_{1-x}Ca_xMnO_3$ [40]. The transition to the CO phase is a first order phase transition accompanied by an abrupt increase in resistivity and abrupt changes in the lattice parameters with lowering temperature. It is also closely related to the orbital ordering through the Jahn–Teller effect of Mn^{3+} [41].

1.3.4.1. Metal to Insulator Transition (MIT)

The hole doped $R_{1-x}A_xMnO_3$ i.e. $La_{1-x}A_xMnO_3$ ($A=Ca^{2+}$, Sr^{2+}, Ba^{2+}) with x=0.33 exhibits a transition from a high temperature paramagnetic (PM) semiconducting or insulating (I) phase to a low temperature metallic of FM phase (FM-M). For instance, single crystals of $La_{0.825}Sr_{0.175}MnO_3$ show the MIT transition around 270 K in a zero applied magnetic field [42] as displayed in Fig. 1.5.

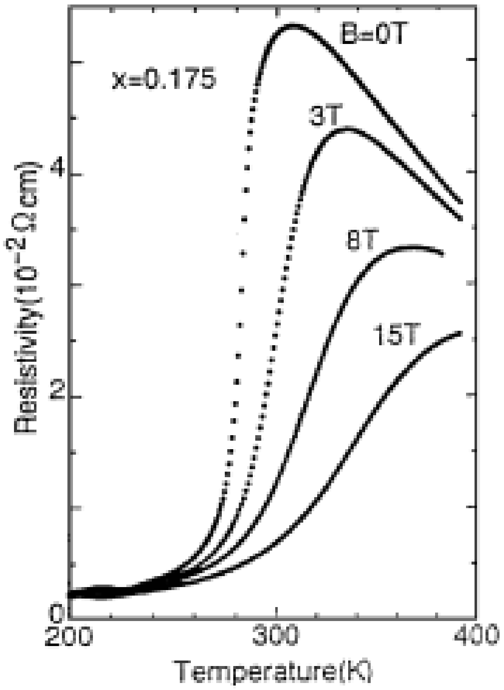

Figure 1.5. Typical graphs for MIT in $La_{0.825}Sr_{0.175}MnO_3$ [42].

In the semiconducting phase, the electrical resistivity generally exhibits strong temperature dependence. Different ρ(T) laws have been used [43-45] in fitting experimental data, the most popular ones being:

(i) Arrhenius type thermal activation law $\rho = \rho_0 \exp(E_0/k_BT)$, with a typical gap value of about 0.1 eV; its origin is due to the existence of a pseudo gap at the Fermi level in the PM phase.

(ii) Hopping of adiabatic polaron $\rho = \rho_0 T \exp(E_0/k_BT)$; this happens due to the local lattice distortion accompanying the moving charge carriers (Jahn-Teller polaron).

(iii) Mott Variable Range Hopping (VRH), $\rho = \rho_0 \exp(T_0/T)^{1/4}$; this is the localization of the charge carriers by the magnetic disorder.

After a particular range of temperatures, it is practically impossible to discriminate among these different ρ(T) laws. At low T, the spontaneous alignment of the

Mn spins below the Curie temperature (T_C), allows a delocalization of the e_g electrons, leading to a low resistivity FM phase with $\rho \approx \rho_o + aT^2$ for $T << T_C$. This alignment of the Mn spins can be induced for $T \geq T_C$, or reinforced for $T \leq T_C$, by applying an external magnetic field [45].

1.3.4.2 Colossal Magneto Resistance (CMR)

Resistivity of some materials changes by the application of external magnetic field. The change in the electrical resistance of a material produced on applying a magnetic field is known as Magneto Resistance (MR) and is given by,

$$MR = \frac{\Delta\rho}{\rho_0} = \frac{\rho(H) - \rho(0)}{\rho(0)}$$

where $\rho(H)$ and $\rho(0)$ are the resistivity at a given temperature in an applied and zero magnetic fields, respectively. MR can be negative or positive. All the metals show some MR, which is a few percent. If MR is large, this MR is referred as Giant Magneto Resistance (GMR) [46] and was first observed in magnetic super lattices (e.g., Fe/Cr). Afterwards, several bimetallic or multi metallic layers containing ferromagnetic and antiferromagnetic or non magnetic metals have been found to exhibit GMR. The maximum effect is obtained close to T_C where the initial magnetic susceptibility diverges as $T \to T_C$. Thus, these manganites have a rather very large negative magneto resistance and are known as CMR effect. The magnetic resistance in these materials peaks at about T_C. This phenomenon has potential technological applications in magnetic recording, actuators and sensors.

1.4. VIBRATIONAL PROPERTIES OF $RMnO_3$

The ideal perovskite (ABO_3) with a geometrical tolerance factor (t) of one exhibits cubic structure with space group (Pm-3m) and Z=1 as shown in Fig. 1.6 (a). All the five atoms of the unit cell occupy centrosymmetric sites and none of the Γ-point phonon modes ($4F_{1u}+F_{2u}$) is Raman active. However, in general ABO_3 compounds have a distorted perovskite-like structure. In this case, tolerance factor differs from unity ($t\neq1$). The distortions compensate as either by displacements of the cations along certain directions and (or) by tilting of the oxygen octahedra [47] as shown in Fig 1.6 (b).

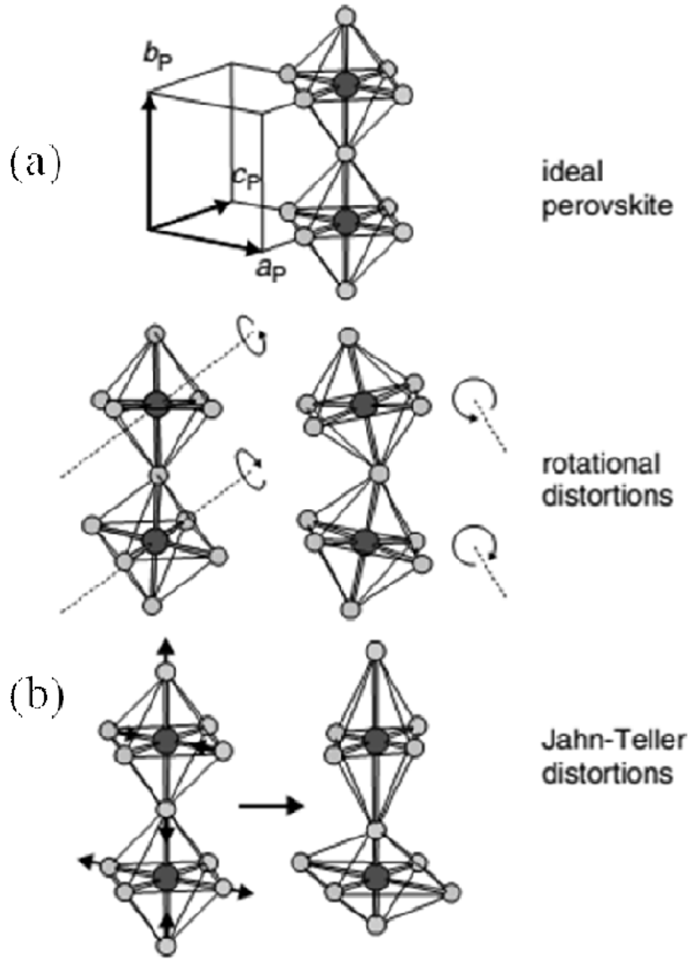

Figure 1.6. (a) Ideal and (b) Distorted perovskite ABO_3 with distortions of BO_6 octahedra [47].

It turns out that there are 24 possible structures that can be formed by tilting alone [48]. These types of distortions in perovskite materials occur due to mismatching of ionic radii of cations. Another type of distortion in the perovskite structure can be induced by the Jahn-Teller (JT) effect. The JT effect is defined as “for a non-linear molecule in an electronically degenerate state, distortion must occur to lower the symmetry, remove the degeneracy and lower the energy” [49]. This JT distortion mainly depends on the B-site ion in the distorted ABO_3 perovskite. Mn^{4+} ($3d^3$) ion in octahedral coordination has a t_{2g} ground state and e_g in the excited state and there are no electrons present in the e_g orbital. Hence no JT distortions occur. All six Mn-O bonds can be of equal length. In contrast, the Mn^{3+} ($3d^4$) ion which is a JT ion occupying B-site has a single electron in the e_g orbital. As a consequence of this, the JT effect causes extension or compression of Mn-O bond lengths. The JT distortions can be compatible with the perovskite-like structure. In such a case the JT distortions are static or coherent and the JT effect does not result in the appearance of new Raman spectral features. In other cases, the crystal structure may not be compatible with the JT distortions. The JT effect produces dynamic and (or) incoherent local distortions which can be detected by standard diffraction techniques. It is plausible to expect that in these cases new Raman band(s) related to the local JT distortions will appear in addition to the Raman modes characteristic of the average structure.

Since the past few decades, the doped rare earth manganites ($R_{1-x}A_xMnO_3$) attracted significant interest as their structural, electrical and magnetic properties exhibited a strong interdependence. This is clearly seen near T_c (Fig. 1.5) where concomitant magnetic and electronic transitions are observed [50]. There are arguments that the interrelations, to a great extent, result from structural instability of the perovskite-like lattice due to a delicate balance between the localization of lattice distortions around the Jahn-Teller Mn^{3+} ions and their delocalization or reordering due to magnetic-order-supported Mn^{3+}-Mn^{4+} charge transfer. Raman spectroscopy of $RMnO_3$ oxides in two crystal structures are discussed in the following sections.

1.4.1. Raman spectra of orthorhombic RMnO₃

The distorted orthorhombic $RMnO_3$ (R = La, Pr, Nd, Sm, Eu, Gd, Tb, Dy or Y) compounds have P*nma* (D^{16}_{2h}) space group. The orthorhombic unit cell with Pnma space group contains four formula units per unit cell (Z = 4). Out of a total of 60 phonon modes, 24 lattice modes are found to be Raman allowed modes and they are ($7A_g$+$5B_{1g}$+$7B_{2g}$+$5B_{3g}$) [51]. The Mn^{3+} ions are at centrosymmetric sites, therefore they do not participate in giving rise to any Raman-active bands. The JT distortions are compatible with this structure (the three pairs of Mn-O bonds are of different length) and therefore can be considered as static or coherent. For example, $YMnO_3$ and $LaMnO_3$ exhibit orthorhombic structure and a typical Polarized Raman spectrum for orthorhombic $YMnO_3$ single crystal at RT [52] is shown in Fig. 1.7.

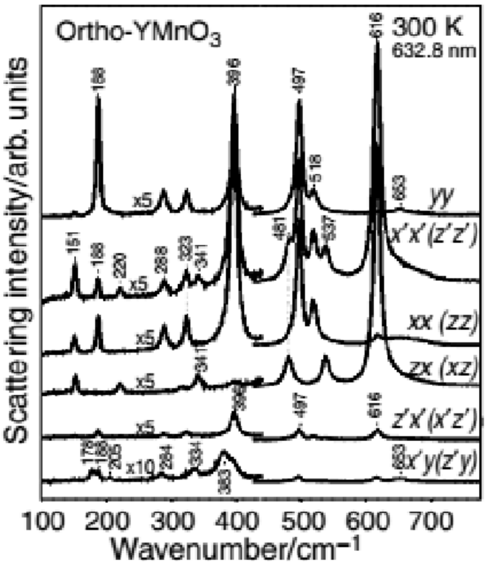

Figure 1.7. Typical polarized Raman spectroscopy of ortho-$YMnO_3$ at RT [52].

Raman spectra obtained in different directions are also included in the same Figure. The experimental modes obtained are compared with modes from lattice dynamics calculations. The most pronounced modes are A_g and B_{2g} which corresponds to symmetry stretching of oxygen motions. These modes do not change significantly with temperature variation. In the case of $LaMnO_3$, B_{2g} mode at 612 cm^{-1} softens at 140 K, which is identified as anti ferromagnetic transition temperature [53].

1.4.2. Raman spectra of hexagonal $RMnO_3$

For either smaller ionic radius of R (R = Ho, Er, Tm, Yb, Lu, Y) or depending on synthesis conditions like annealing at high pressure or high temperature, $RMnO_3$ compounds crystallize in hexagonal structure with space group $P6_3cm$ (C^3_{6v}) with Z = 6. The hexagonal $RMnO_3$ compounds exhibit multiferroic properties due to the coexistence of magnetic and ferroelectric orderings [54, 55]. However, this doesn’t happen with orthorhombic $RMnO_3$ because only magnetic ordering occurs and not ferroelectric ordering. Therefore, these orthorhombic $RMnO_3$ and divalent ion substituted $RMnO_3$ attract many research groups attention to explore the multiferroic properties by inducing magneto coupling effects. Recent studies on orthorhombic $RMnO_3$ reveals the existence of the coupling between the ferroelectric and magnetic orders. This coupling can be identified in the variation of Raman spectra with temperature studied by Raman spectroscopy [53].

According to group theoretical analysis, hexagonal $RMnO_3$ with space group $P6_3cm$ exhibit 60 phonon modes at Γ-point [56]. They are

$$\Gamma = 10A_1+5A_2+10B_1+5B_2+15E_1+15E_2$$

Among the 60 modes, 38 modes are Raman active. These are:

$$\Gamma_{Raman} = 9A_1+14E_1+15E_2$$

The modes of A_1 and E_1 symmetries are also infrared active, whereas the modes of A_2, B_1, and B_2 symmetries are silent (inactive) modes.

$$\Gamma_{Infrared} = 9A_1+14E_1$$

$$\Gamma_{Silent} = 5A_2+10B_1+5B_2$$

$$\Gamma_{Acoustic} = A_1+E_1$$

Raman spectrum for $YMnO_3$ in the hexagonal structure recorded at room temperature [57] is shown in Fig. 1.8.

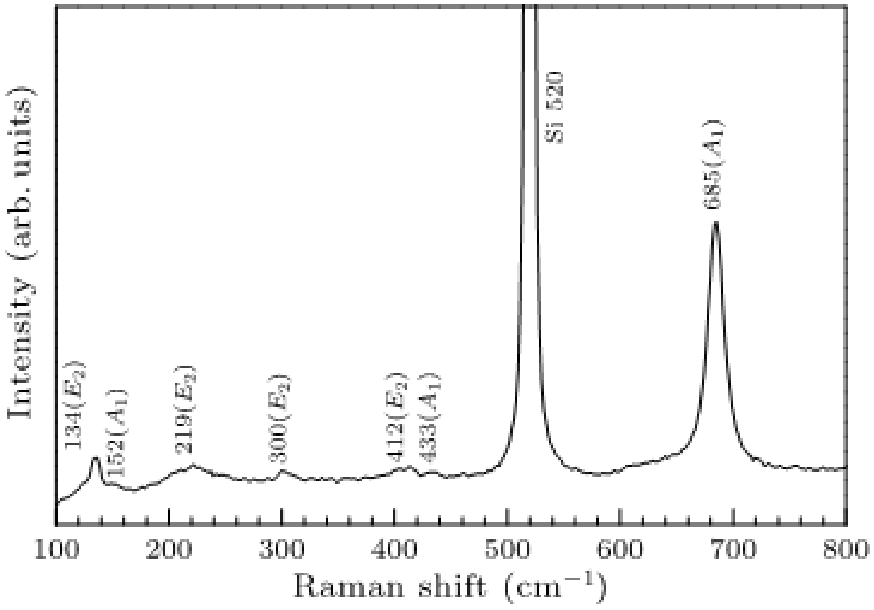

Figure 1.8. Typical Raman spectrum of hexagonal $YMnO_3$ at room temperature [57].

1.5. A SHORT REVIEW ON $DyMnO_3$

1.5.1. Structure of $DyMnO_3$

$DyMnO_3$ (DMO) exhibits either orthorhombic or hexagonal structure depending upon the synthesis conditions. It is reported that DMO prepared at low temperatures shows orthorhombic structure and is found to be electrically insulating in nature. DMO prepared at high temperatures (close to its melting point ~1700°C) adopts hexagonal structure. The insulating orthorhombic DMO shows antiferromagnetic ground state. Neutron diffraction measurements in the orthorhombic DMO by Kimura et al. [58], showed a series of three magnetic transitions viz., sinusoidal incommensurate antiferromagnetic ordering of Mn^{3+} ions from PM state at ~39 K, spiral commensurate antiferromagnetic ordering from the incommensurate antiferromagnetic ordering whose propagation vector remains unchanged below 18 K hence named as lock-in transition of Mn^{3+} ions and antiferromagnetic ordering of Dy^{3+} spins are ordered at ~6 K. In the case of hexagonal structure $DyMnO_3$, these ordering temperatures are seen at ~70 K and ~7 K respectively [59]. These are quite large values in temperature due to geometrical frustration as compared to orthorhombic structure.

1.5.2. Multiferroic properties of $DyMnO_3$

Multiferroic means that electrical and magnetic properties coexist and are mutually coupled together. The intimate coupling between the two orders gives rise to giant Magneto Electric (ME) effect [60], for instance polarization (P) switching in multiferroics hosting a Spiral Spin Order (SSO) of Mn spins [61]. In general, these Type 2 multiferroics with magnetic ordering for ferroelectricity can be further classified in two groups according to the details of microscopic mechanism. The first group includes those having a non collinear spiral spin order, making broken space inversion symmetry and thus a spontaneous ferroelectric (FE) polarization via the well-known inverse Dzyaloshinski-Moriya Interaction (DMI) [62]. The polarization is formulated as $\mathbf{P \sim e_{ij}(S_i \times S_j)}$ where e_{ij} is the vector connecting two neighboring spins S_i and S_j [63]. A unique property of these multiferroics in this group is the magnetic field driven polarization switching, leading to ME effect which has been repeatedly revealed in $TbMnO_3$ and $DyMnO_3$ [64].

The second group has a specific collinear spin configuration and consequently an improper ferroelectricity may be driven by the so called exchange striction mechanism. The polarization can be expressed as **P ~ $\mathbf{S_i.S_j}$**. This is explained in case of $Ca_3Co_{1-x}Mn_xO_6$ and orthorhombic $HoMnO_3$ [65-69]. The FE polarization generated via this exchange striction mechanism is usually much larger than that from the DMI mechanism; therefore this is the largest among all the Type 2 multiferroics. In addition to these two mechanisms, there is still one more worth mentioning, namely the spin dependent p-d type hybridization and the polarization is written as $P \sim (S_i.e_{il})^2.e_{il}$ where e_{il} is the vector connecting spin, S_i and the neighbor ligand ions [70]. The AFM interactions between Mn ions via oxygen with and without DMI are shown in Figs. 1.9 (a) and (b) [71] respectively.

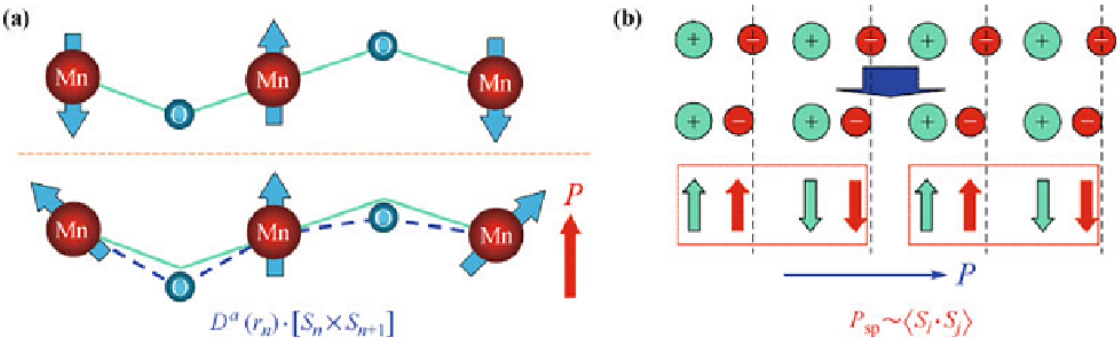

Figure 1.9. (a). Schematic drawing of Mn-O-Mn chain in $RMnO_3$. The upper panel shows the AFM Mn-O-Mn without DM interactions at $T < T_N$. Bottom panel displays, the spin- non collinear Mn-O-Mn due to DM interactions which produces the polarization of oxygen ions perpendicular to the chains for temperatures below T_{FE} (b). Two up arrows and two down arrows spin chain constituted by two magnetic species in alternative arrangements. The coherence ionic shifts due to the symmetry exchange striction and induced polarization (P) are shown [71].

1.5.3. Coupling of Dy and Mn sub lattices in $DyMnO_3$

In $DyMnO_3$, both the Dy ions and Mn ions are magnetic and in particular the Dy spin has quite a large magnetic moment (10.62 μ_B) than Mn spins (4.90 μ_B). Upon decreasing the temperature (T), the high-T paramagnetic state changes into an incommensurate (ICM) sinusoidal antiferromagnetic (AFM) state corresponding to Mn spins at $T_N = 39$ K, below which the collinear Mn spin order is first developed along the b-axis with propagation vector Mn = (0, **b**, 0) where **b** lies between 0.36 and 0.385 varying with temperature at $T < T_N$. Slightly below T_N, the Dy-spins at the R-site also develop an AFM order along the c-axis with the same propagation vector (τ) as that of the Mn-spin order, i.e., $\tau_{Dy} = \tau_{Mn}$, due to the strong coupling between the Dy-spin sub lattice and the Mn-spin sub lattice (Dy-Mn spin interaction). This indicates that the AFM Dy-spin ordering is induced by the Mn-spin order.

When temperature (T) falls down further to $T_{FE} = 18$ K, an additional magnetic transition occurs and which corresponds to the development of a SSO of the Mn along the b-axis, with the fixed propagation vector $\tau_{Mn}=0.385$ b. The Dy-spins also construct a spiral spin order as a consequence of the strong coupling between the Dy-spin sub lattice and the Mn-spin sub lattice, under the premise of $\tau_{Dy}=\tau_{Mn}=0.385$b. The proposed magnetic structure projected on the bc-plane is schematically illustrated in Fig. 1.10 (a). As discussed above, the spiral spin order of Mn ions allows a nonzero FE polarization, contributed from the cross product term $\mathbf{P_{so}} \sim \mathbf{e_{ij}} \times (\mathbf{S_i}\times\mathbf{S_j})_{Mn}$ along the c axis. Whether the spiral spin order of Dy ions makes a contribution to polarization P remains to be identified yet. A surprising consequence of the magnetic structures is the coherence of spin configurations for Mn and Dy sub lattices. As shown in Fig. 1.10 (a), the magnetic structures below T_{FE} show that along the b-axis, the Mn spins between two neighboring Mn spin chains are anti-parallel, so also the two neighboring Dy spin chains. The spin–lattice coupling between the Mn spin chain (red arrows) and the near neighbor Dy spin chain, can be expressed as $\mathbf{\sim(-1)^i(S^i_{Dy} \,.\, S^i_{Mn})}$, where i is an integer counting the Mn/Dy chain series along the c-axis. Therefore, the site dependent configuration averaging over the whole lattice can be termed as $[S_{Dy}\cdot S_{Mn}]$n. That is the spin lattice contributes to develop the ferroelectricity implying a non-zero spin-phonon coupling (P_{sp}). In fact, Dy spin ordering occurs below T_{Dy} = 6.5 K independent of Mn spin ordering. This indicates that the Dy spin order takes a commensurate AFM structure with propagation vector τ_{Dy} = 0.5b, irrelevant with the spiral spin order of Mn ions, as schematically illustrated in Fig. 1.10 (b). This independent Dy spin order implies the dominance of the Dy-Dy spin interaction over the Dy-Mn spin coupling at low $T<T_{Dy}$. The consequence of the competition between the two types of interactions may be the disappearance of component P_{sp} gradually at T → 0 K. The Mn spiral spin structure (in particular the wave-vector) would be modulated by the Dy-Mn spin coupling in case of the independent Dy spin order, which is nevertheless different from that in the case of the Dy spiral spin order at $T_{Dy}<T<T_{FE}$. The reason expected is that the polarization component, P'_{so} induced by the Mn spin–orbit coupling for temperatures below the Neel temperature of Dy would be different from P_{so} at $T>T_{Dy}$.

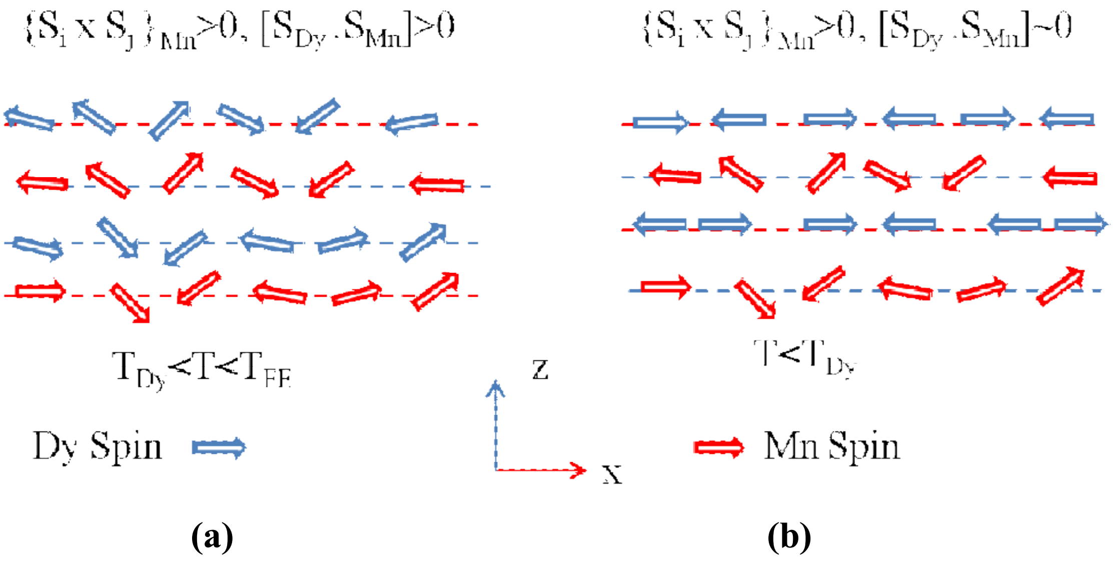

Figure 1.10. Ordered spin configurations of Dy, Mn moments at temperatures (a) $T_{Dy}< T<T_{FE}$ and (b) $T<T_{Dy}$ [71].

1.6. REFERENCES

[1] N.A. Spaldin and W. Pickett, J. Solid State Chem., **176**, (2003), 615.

[2] Multifunctional Materials by Materials innovation growth team, Reports 2006.

[3] D.I. Khomskii, J. Magn. Magn. Mater., **306**, (2006), 1.

[4] Nicola A. Hill, J. Phys. Chem. B, **104**, (2000), 6694.

[5] M. Fiebig, J. Phys. D, **38**, (2005), R123.

[6] H. Schmid, Ferroelectrics, **162**, (1994), 317.

[7] D.I. Khomskii, Bull. Am. Phys. Soc., **C21.002**, (2001).

[8] C.N.R. Rao and C.R. Serrao, J. Mater. Chem., **17**, (2007), 4931.

[9] R. Ramesh and N. A. Spaldin, Nat. Mater., **6**, (2007), 21.

[10] S.W. Cheong and M. Mostovoy, Nat. Mater., **6**, (2007), 13.

[11] N.A. Spaldin and M. Fiebig, Science, **309**, (2005), 391.

[12] J.C. Yang, Q. He, P. Yu and Y.H. Chu, Annu. Rev. Mater. Res., **45**, (2015), 249.

[13] I. Sosnowska and V.A. Zvezdin, J. Magn. Magn. Mater., **140**, (1995), 167.

[14] Y. Wang, L. Zhou, M.F. Zhang, X.Y. Chen, J.M. Liu and Z.G. Liu, Appl. Phys. Lett., **84**, (2004), 1731.

[15] G. Catalan and J.F. Scott, Adv. Mater., **21**, (2009), 2463.

[16] T. Kimura, S. Kawamoto, I. Yamada, M. Azuma, M. Takano and Y. Tokura, Phys. Rev. B, **67**, (2003), 180401.

[17] C. Ederer and N.A. Spaldin, Phys. Rev. B, **71**, (2005), 060401 (R).

[18] T. Kimura, T. Koto, H. Shintani, K. Ishizaka, T. Arima and Y. Tokura, Nature, **426**, (2003), 55.

[19] M. Kenzelmann, A.B. Harris, S. Jonas, C. Broholm, J. Schefer, S.B. Kim, C.L. Zhang, S.W. Cheong, O.P. Vajk and J.W. Lynn, Phys. Rev. Lett., **95**, (2005), 087206.

[20] T. Kimura, G. Lawes, T. Goto, Y. Tokura and A.P. Ramirez, Phys. Rev. B, **71,** (2005), 224425.

[21] V.M. Goldschimdt, Akad. Oslo I. Mat-Natur, **2,** (1926), 7.

[22] J.R. Sun, G.H. Rao and J.K. Liang, Appl. Phys. Lett., **70**, (1997), 1900.

[23] H.Y. Hwang, S.W. Choeng, R.G. Radaelli, M. Marezio and B. Batlog, Phys. Rev. Lett., **75**, (1995), 914.

[24] E. Pollert, S. Krupicka and E. Kuzwicova, J. Phys. Chem. Solids, **43,** (1982), 1137.

[25] G. Zhao, K. Conder, H. Keller and K A. Muïller, Nature, **381,** (1996), 676.

[26] J.B.A.A. Elemans, B. Van Laar, K.R. Van Der Veen and B.O. Loopstra, J. Solid State Chem., **3**, (1971), 238.

[27] J.B. Goodenough, Annu. Rev. Mater. Sci., **28**, (1998), 1.

[28] J.M.D. Coey, M. Viret and S. Von Molnair, Adv. in Phys., **48**, (1999), 167.

[29] J.B. Goodenough, Phys. Rev., **100**, (1955), 564.

[30] C. Zener, Phys. Rev., **81**, (1951), 440.

[31] P.W. Anderson and H. Hasegawa, Phys. Rev., **100**, (1955), 675.

[32] P.G. de Gennes, Phys. Rev., **118**, (1960), 141.

[33] K.H. Ahn and A.J. Millis, Phys. Rev. B, **58,** (1998), 3697.

[34] J.F. Gregg, I. Petej, E. Jouguelet and C.J. Dennis. Phys. D: Appl. Phys., **35**, (2002), R121.

[35] P. Fulde, Electron Correlations in Molecules and Solids, 2nd ed. (Springer-Verlag, Berlin 1995).

[36] W.E. Pickett, Rev. Mod. Phys., **61**, (1989), 433.

[37] W.E. Pickett and D.J. Singh, Phys. Rev. B, **53**, (1996), 1146.

[38] Y. Tokura, Y. Tomioka, H. Kuwahara, A. Asamitsu, Y. Morimoto and M.J. Kasai, Appl. Phys., **79**, (1996), 5288.

[39] P. Schiffer, A.P. Ramirez, A.W.P. Baoand and S.W. Cheong, Phys. Rev. Lett., **75**, (1995), 3336.

[40] Y. Tomioka, A. Asamitsu, H. Kuwahara, Y. Moritomo and Y. Tokura, Phys. Rev B, **53**, (1996), R1689.

[41] A.P. Ramirez, J. Phys.: Condens. Matter, **9,** (1997), 8171.

[42] R. VonHelmolt, J. Wecher, B. Holzapfel, L. Schultz and K. Sanwer, Phys. Rev. Lett., **71**, (1993), 2331.

[43] G. Snyder, J.R. Hiskes, S. DiCarolis, M.R. Beasley and T.H. Geballe, Phys. Rev. B, **53**, (1996), 14434.

[44] M. Zhuang, W. Zhang and N. Ming, Phys. Rev. B, **56,** (1997), 14547.

[45] E. Dagotto, T. Hotta and A. Moreo, Physics Reports, **344,** (2001), 1.

[46] C.N.R. Rao and B. Raveau " Colossal Magnetoresistance , Charge Ordering and Related Properties Of Manganese Oxides" ,World Scientific,(1998)

[47] M.N. Iliev and M.V. Abrashev, J. Raman Spectrosc., **32**, (2001), 805.

[48] G. Burns and A.M. Glazer. Space Groups for Solid State Scientists (2nd edn.), Academic Press: New York, 1993.

[49] H.A. Jahn and E. Teller, Proc. Roy. Soc. London, Ser., **161,** (1937), 220.

[50] R. Mahendran, R. Mahesh, A.K. Raychaudhuri and C.N.R. Rao, Solid State Commun., **94**, (1995), 515.

[51] K. Yadagiri and R. Nithya, RSC Adv., **6**, (2016), 95417.

[52] M.N. Iliev, M.V. Abrashev, H-G. Lee, V.N. Popov, M.V. Abrashev, A. Hamed, R.L. Meng and C.W. Chu, Phys. Rev. B, **57,** (1998), 2872.

[53] M.N. Iliev, M.V. Abrashev, V.N. Popov and V.G. Hadjiev, Phys. Rev. B, **67**, (2003), 212301.

[54] G.A. Smolenskii and I.E. Chupis, Sov. Phys. Usp., **25**, (1982), 475.

[55] K.F. Wang, J.M. Liu and Z.F. Ren, Adv. Phys. **58**, (2009), 321.

[56] M.N. Iliev, H-G. Lee, V.N. Popov, M.V. Abrashev, A. Hamed, R.L. Meng and C.W. Chu, Phys. Rev. B, **56,** (1997), 2488.

[57] Liu Yue-Feng,Wang Bei, Zheng Hai-Wu, Liu Xiang-Yang, Gu Yu-Zong and Zhang Wei-Feng, Chin. Phys. Lett., **27**, (2010), 056801.

[58] T. Kimura, Annu. Rev. Mater. Res., **37**, (2007), 387.

[59] S. Mansouri, S. Jandl, J. Laverdière, P. Fournier, A.A. Mukhin, V.Y. Ivanov, A.M Balbashov, J. Phys. :Condens. Matter., **25**, (2013), 066003.

[60] Y. Tokura, S. Seki and N. Nagaosa, Rep. Prog. Phys., **77,** (2014), 076501.

[61] Y. Tokura and S. Seki, Adv. Mater., **22**, (2010), 1554.

[62] I.A. Sergienko and E. Dagotto, Phys. Rev. B, **73**, (2006), 094434.

[63] I.A. Sergienko, C. Sen and E. Dagotto, Phys. Rev. Lett., **97**, (2006), 227204.

[64] M. Kenzelmann, A. B. Harris , S. Jonas , C. Broholm , J. Schefer , S. B. Kim , C. L. Zhang , S.-W. Cheong, O. P. Vajk and J. W. Lynn, Phys. Rev. Lett. **95**, (2005), 087206.

[65] Y.J. Choi, H.T. Yi, S. Lee, Q. Huang, V. Kiryukhin and S.W. Cheong, Phys. Rev. Lett., **100**, (2008), 047601.

[66] Y.J. Guo, S. Dong, K.F. Wang and J.M. Liu, Phys. Rev. B, **79**, (2009), 245107.

[67] P.P. Rout, S.K. Pradhan, S.K. Das and B.K. Roul, Physica B, **407**, (2012), 2072

[68] C.L. Lu, J. Fan, H.M. Liu, K. Xia, K.F. Wang and P.W. Wang, Appl. Phys. A, **96**, (2009), 991.

[69] H. Murakawa, Y. Onose, S. Miyahara, N. Furukawa and Y. Tokura, Phys. Rev. Lett., **105**, (2010), 137202.

[70] C. Lu and J.M. Liu, J. Materiomics, **2**, (2016), 213.

[71] Na Zhang, Shuai Dong and Jun-Ming Liu, Front. Phys., **7**, (2012), 408.

CHAPTER – 2

EXPERIMENTAL DETAILS

2.1. INTRODUCTION

Polycrystalline compounds whose properties were investigated as a function of temperature, magnetic field and frequency were synthesized from the respective oxides using solid state reaction. The conventional solid state reaction was chosen over other available methods used for the preparation of a variety of compounds studied in the present work. Various experimental techniques were performed to measure their properties whose results are described in the ensuing chapters. Methodology of the synthesis procedure and experimental details of the techniques along with the necessary theories are given in this chapter.

2.2. SYNTHESIS PROCEDURE

The most important part of experimental condensed matter physics research is the preparation of single phase bulk compounds with known composition in order to get desired properties. The bulk compounds can be prepared with different shapes and sizes like polycrystalline powders, single crystals, amorphous solids, thin and thick films, etc. There are several methods that include Solid State Reaction (SSR) or ceramic, Co-precipitation, Sol-gel, Hydrothermal method, Vapor Phase Transport (VPT), Physical Vapor Deposition (PVD), Chemical Vapor Deposition (CVD), Pulsed Laser Deposition (PLD), Chemical Solution Deposition (CSD), Metal-Organic

Chemical Vapor Deposition (MOCVD), Sputtering, Flux Growth Technique, and Electrochemical Methods etc. In general, in solid state physics, solid state reaction is adopted for synthesis of oxide materials owing to its feasibility in terms of reproducibility and easy operation to get good mono phasic compounds, all the compounds under the present investigation are prepared using SSR route. Details of the technique are given below:

Many polycrystalline materials are prepared by employing SSR method from the mixture of their constituent solid oxide powders. The preparations of materials through this method require high temperature to accelerate the slow solid–solid diffusion [1-3]. This method may not be good for all applications due to low kinetics, high temperature, low homogeneity phase which means that it may contain secondary phase, uncontrolled the particle size of low surface area [4]. However, this conventional route is widely employed due to its simplicity and low manufacturing costs involved.

Various steps are involved in the conventional solid state reaction route. The final product obtained in the solid state reaction route can usually be in the form of a powder or polycrystalline piece.

Main steps in the solid state reaction process:

1. Appropriate high purity starting materials in fine powders are taken in stoichiometric proportions.
2. Mix the powder thoroughly using agate mortar and pestle or ball milling (for large quantity sample) for several hours to get homogeneous mixtures.
3. Heat the solid powder mixture (calcinations) at elevated temperatures in air using muffle furnace.
4. Repeat the heat treatments twice or trice with intermittent grinding.

5. The black powder was compressed into circular pellets which were then sintered at elevated temperatures (~1300 °C) for prolonged durations to obtain pellets with high density for subsequent physical property measurements.

The final temperature and duration of sintering may vary depending on the nature and properties of the compounds under preparation.

Advantages of SSR:

The solid reactants react chemically without the presence of any solvent at high temperatures yielding a product which is stable.

- ✓ The major advantage of solid state reaction method is the final product in solid form is structurally pure with the desired properties depending on the final sintering temperatures.
- ✓ This method is environment friendly and no toxic or unwanted waste is produced after completion of the solid state reaction.

Disadvantages of SSR:

- ➢ High temperatures are generally required (>500°C), because it takes a significant amount of energy to overcome the lattice energy so a cation or anion can diffuse into a different site.
- ➢ The desired compound may decompose at high temperatures.
- ➢ With increase of the temperature, diffusion rates will become uncontrollable.
- ➢ Generally temperatures of the reaction are not raised to their melting point, so reactions take place in the solid state (sub solidus).

For the present work, a box furnace was used for thermal treatments (like annealing and sintering) of all the compounds. The box furnace has Silicon Carbon (SiC) rods as heating elements that can produce high temperatures up to ~1400°C.

2.3. CHARACTERIZATION TECHNIQUES

2.3.1. X-Ray diffraction technique

Powder X-ray diffraction (XRD) technique is used to identify crystalline structures and composition of phases present in a solid material. Each crystalline material has its own characteristic powder X-ray diffraction pattern, which serves as a fingerprint for its identification. The powder X-ray method serves to indicate the completeness of a chemical reaction and the presence or absence of unwanted side products and impurity phases. The X-ray diffraction pattern consists of a set of lines or peaks, each of different intensity satisfying Bragg's equation. The diffraction directions are determined solely by the shape and size of the unit cell whereas the intensities of diffracted beams are determined by the type of atom and the coordinates of the atoms within the unit cell. Thus, from the position of the peaks in a typical X-ray powder diffraction pattern, the structural information such as size and shape of the unit cell can be obtained and from the intensities, information regarding the atomic coordinates within the unit cell can be obtained.

For the work presented in this thesis, STOE diffractometer (Germany) was used for phase identification of all the synthesized compounds.

The STOE make θ-θ diffractometer operates from 10° to 168°. Precise angular positions can be set by a stepper motor with reproducibility. Manual control for angle movement is also available. The radius of the measuring circle is 260 mm. The diffractometer can operate in the θ-2θ, 2θ-ω scan modes. The tube housing accommodates an X-ray tube of a long, fine focus type with spot size 12 mm x 0.4 mm. The X-ray tube used in the line focus mode is a ceramic tube with a Cu target.

The tube is powered by a 4 kW air cooled generator. The target is cooled by chilled water supply line using a dedicated chiller unit. Chilled water is made to circulate so as to cool the Cu target. The X-rays that emanate from the tube at a takeoff angle of 6° are sent through "Soller slits" for controlling vertical beam divergence without sacrificing the intensity. Such a Soller slit assembly is also available at the diffracted beam end. The sample holder is a zero background Si plate and in the present case it is a Silicon (911) single crystal wafer which can be positioned at the center of the diffractometer circle with the help of a knife edge. A 10 mm diameter groove is made at the center of this plate for loading powder samples.

The zero background plate ensures a negligibly small background. The incident and diffracted X-ray beam divergence can be adjusted by a computer controlled precision slit from 0.01 to 2 mm. A secondary monochromator (plane graphite) is also provided for rejecting any stray X-ray contamination. A substantial intensity of the diffracted beam is made possible because of the Bragg-Brentano para-focusing geometry [5]. In this geometry, the specimen is placed at the center of the diffractometer circle. The X-ray source, the sample and the detector lie tangentially along the focusing circle as shown in the schematic Fig. 2.1. The detector is always at an angle of 2θ and the sample is at θ with respect to the incident beam. In the Bragg-Brentano geometry, the diffraction vector is normal to the (911) planes and does not satisfy Bragg's law. Therefore there will be no diffraction peaks from the sample holder. A NaI (Tl) scintillation detector optically coupled to a photo multiplier tube is used for receiving the diffracted beam.

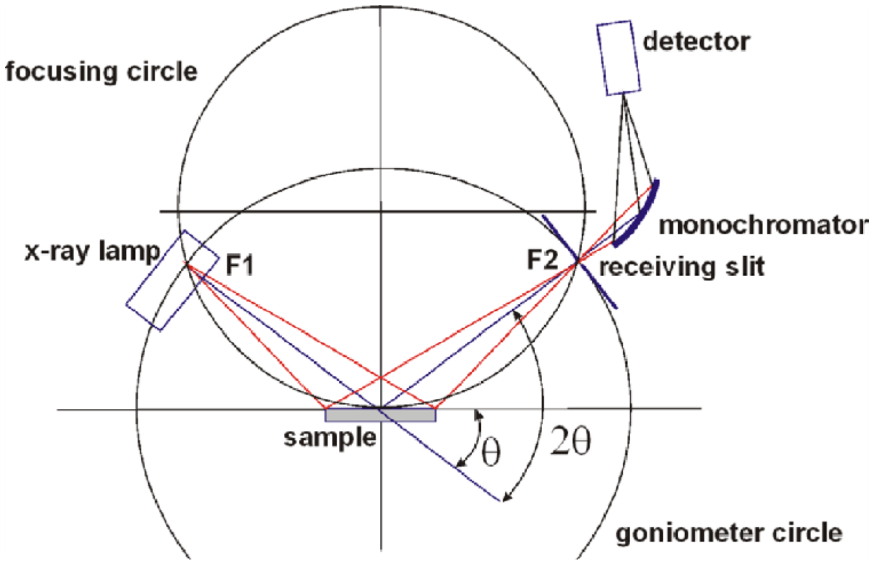

Figure 2.1. Schematic diagram of Bragg-Brentano geometry

Diffraction data collection details

Powder X-ray diffraction patterns of the compounds were collected at room temperature using STOE (Germany) diffractometer and details of the data collection are given below:

Instrumental parameters:

Geometry: Bragg-Brentano parafocusing
Goniometer radius: 260 mm
Wavelength: Cu-K_{α} radiation, 1.5406 A°
Power supply: 1.2 kW (40 kV and 30 mA)
Scan mode: Reflection
Scan type: 2θ-Omega
Detector: Scintillation detector, NaI (Tl)
Slits: Fixed divergence and receiving slits
Divergence slit: 0.3 mm
Receiving slit: 0.4 mm
Monochromator: Secondary (flat pyrolitic graphite)
Cu $K_{\alpha 2}$ peak stripping: No

Measurement parameters for Rietveld refinement:

Sample holder: grooved (911) Si single crystal wafer with zero background intensity

2θ range: 20° to 90°
Step interval: 0.05°
Step time: 50 sec / step

2.3.1.1. Rietveld Refinement (RR)

Rietveld refinement of the powder diffraction data can provide in depth information of the structural details of the material. In this method, [6-9] the square of the difference between the observed diffraction intensity and the calculated diffraction intensity at every point in the diffraction pattern is minimized with a weight factor using a non-linear least squares algorithm. Let y_i^c and y_i^{obs} represent the calculated and the observed intensity at a point i in the diffraction pattern then,

$$\varphi = \sum_{i=1}^{n} w_i (y_i^{obs} - y_i^c)^2$$

is a function to be minimized. $w_i = [y_i]^{-1}$ is the weight factor. Minimization is carried out with respect to a number of parameters like background, sample displacement, sample transparency, zero shift, peak profile, unit cell dimensions, scale factor, preferred orientation, positional parameters, occupancy and atomic displacement (isotropic and anisotropic). During the time of the refinement, the parameters are floated sequentially and allowed to vary till stability is achieved. Every time the calculated pattern is compared with the experimental pattern and also examined by observing the trend in residual parameters like profile residual Rp, weighted profile residual R_{wp} and goodness of fit χ^2. When the algorithm is stable, these residuals decrease and approach a steady minimum value indicating that the refinement can be terminated. Rietveld refinement using the GSAS package is used for refining structural parameters in this thesis [10, 11].

2.3.2. Elemental analysis techniques

2.3.2.1. Scanning Electron Microscopy (SEM)

SEM is a tool which gives information about the 3-dimensional microstructure morphology. The SEM instrument consists of electron gun, electromagnetic lenses and detector. The electron gun produces electron beam, which is focused or collected by electromagnetic lenses and detector, detects the signal after the interaction of electron beam with sample. To produce image of a specimen, focused electron beam is scanned across a specimen with a scanning coil and point of specimen struck by electron beam emits secondary electrons [12].

2.3.2.2. Energy Dispersive X-ray Spectroscopy (EDS)

EDS is one of the analytical techniques used for analysis of elements or chemical characterizations in a material. It is one of the variants of X-ray fluorescence spectroscopy. This depends on the investigation of a sample through interaction between the electromagnetic radiation and matter, analyzing emitted X-rays by matter while hitting the electron beam. The main principle of this characterization is that each electron has a unique atomic structure allowing X-rays that are characteristic of an element's atomic structure to be identified uniquely from one another.

The EDS system is comprised of basic components, X-ray detector, pulse processor and analyzer that must be designed to work together to achieve optimum results. The pulse processor measures the electronic signal to determine the energy of each X-ray detected. Finally the analyzer displayed the X-ray data [13].

In the present thesis, compositional homogeneity was verified using Scanning Electron Microscopy (SEM), Cam Scan 3200 (England) combined with Energy Dispersive X-ray (EDX) facility, NCA Penta FETX3 (Oxford instruments).

2.3.2.3. X-ray Photoelectron Spectroscopy (XPS)

XPS is a quantitative technique that measures the elemental composition, chemical state of the element that exists in the material. XPS spectra are obtained by irradiating a material with a beam of X-rays while spontaneously measuring the kinetic energy and number of electrons that escape from the sample surface. XPS is done under ultra high vacuum conditions. Since the energy of the X-rays (E_{ph}) used is a known quantity, we can determine the binding energy of the emitted electron (E_b) by using the equation:

$$E_b = E_{ph} - E_k - \varphi$$

Here E_b is the binding energy of the emitted electron, E_{ph} is the energy of the X-ray source used, E_k is the kinetic energy of the emitted electron and φ is work function of the spectrometer. A typical XPS spectrum is a plot of number of electrons detected versus the binding energy of the detected electrons. Each element has a characteristic binding energy, so it gives directly the information about the oxidation state of the elements present in the sample [14, 15].

For the present work, XPS spectra were recorded to estimate binding energies of the elements present in the investigated materials. XPS measurements were performed using a PHOIBOS 150 spectrometer (SPECS Surface Nano Analysis GmbH, Germany) equipped with a monochromatic Al K_α (1486.7 eV) X-ray source. XPS spectra were analyzed using XPSPEAK 4.1 software [16].

2.3.3. Raman Spectroscopy

Raman scattering was discovered in 1928 by Sir Chandrasekhar Venkata Raman, using sunlight as a source, telescope as a collector and his eyes as a detector. For this discovery, he got noble prize in 1930.

Raman spectroscopy is a spectroscopic technique based on inelastic scattering of monochromatic light (laser source). Inelastic scattering means that the frequency of photons in monochromatic light changes upon interaction with a sample. Photons of the laser light are absorbed by the sample and then reemitted. Frequency of the reemitted photons is shifted up or down in comparison with original monochromatic frequency, which is called Raman Effect. This shift provides information about vibrational, rotational and other low frequency transitions in molecules. Raman spectroscopy can be used to study solid, liquid and gaseous samples.

The Raman effect is based on molecular deformations in electric field, E determined by molecular polarizability (α). The laser beam can be considered as an oscillating electromagnetic wave with electrical vector E. Upon interaction with the sample it induces electric dipole moment, $P = \alpha E$ which deforms molecules. Because of periodical deformation, molecules start vibrating with a characteristic frequency (υ_m). The monochromatic laser light with frequency (υ_0) excites molecules and transforms them into oscillating dipoles. Such oscillating dipoles emit light of three different frequencies as shown in Fig. 2.2. They are:

1. A molecule absorbs a photon with the frequency υ_0. The excited molecule returns back to the same basic vibrational state and emits light with the same frequency υ_0 as an excitation source. This type of interaction is called an elastic Rayleigh scattering.
2. A photon with frequency υ_0 is absorbed by a Raman-active molecule which at the time of interaction is in the basic vibrational state. Part of the photon's energy is transferred to the Raman-active mode with frequency υ_m and the resulting frequency of scattered light is reduced to $\upsilon_0 - \upsilon_m$. This Raman frequency is called Stokes frequency (Stokes lines).

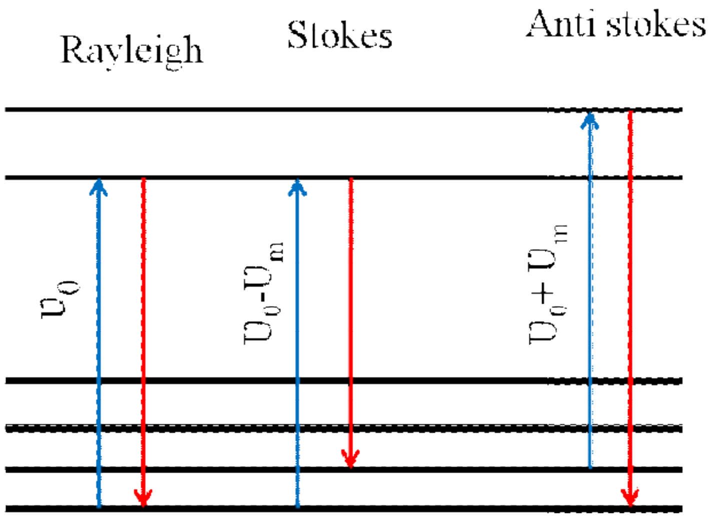

Figure 2.2. Raman scattering transitional schemes.

3. A photon with frequency υ_0 is absorbed by a Raman-active molecule which is already in the excited vibrational state at the time of interaction. Excessive energy of excited Raman active mode is released, molecule returns to the basic vibrational state and the resulting frequency of scattered light goes up to $\upsilon_0+\upsilon_m$. This Raman frequency is called Anti Stokes frequency (Anti-Stokes lines).

The concerning 99% of all incident photons in spontaneous Raman scattering undergo elastic Rayleigh scattering. This type of signal is useless for practical purposes of molecular characterization. Only about 1% of the incident light produces inelastic Raman signal with frequencies $\upsilon_0\pm\upsilon_m$. Spontaneous Raman scattering is very weak and special measures should be taken to distinguish it from the predominant Rayleigh scattering. Instruments such as notch filters, tunable filters, laser stop apertures, double and triple spectrometric systems are used to reduce Rayleigh scattering and obtain high-quality Raman spectra [17-19].

Raman spectra were recorded on sintered pellets at room temperature with a Renishaw InVia micro-Raman spectrometer (Renishaw, UK) in a back scattering geometry with a single monochromator equipped with an edge filter down to 50 cm^{-1}. Excitation wavelength of 514.5 nm Ar^{+} laser was used. Raman scattered radiation was collected by Pielter cooled charge coupled detector (CCD). Depending on the nature of the materials, laser powers and data acquisition times were varied to obtain a better signal to noise ratio. Raman spectra were recorded in the range 40 cm^{-1}–1000 cm^{-1} with a scan rate of 2 $cm^{-1}sec^{-1}$. Spatial homogeneity was verified by collecting the scattered data from different spots. The Raman modes were found to remain the same in all the spectra indicating the homogeneity of the compounds.

2.3.4. Electrical Resistivity

Four-probe method was used for resistivity measurements by van der Pauw technique. For semiconducting materials, a four-probe method for the resistivity measurements is often performed. In the four-probe method, separate pairs of wires are used for providing the current through the sample and measuring the voltage across it. The advantage of such a four-wire method over the conventional two-wire method is that the contact resistance due to electrical contacts with the material and the wire resistance can be avoided. Another effect that may arise during the resistance measurement is due to the dissimilar metal contact, which results in a thermal voltage. This can be nullified by changing the direction of the current. For a four-probe measurement, sample geometries and contacts type are important. In studying the bulk materials, measurements are usually made on rod-shaped samples. Contacts are soldered, evaporated or glued using electrically conducting paint to the faces of the rod-shaped sample. Commonly the contacts are given in-line. An alternative four-probe method is van der Pauw method [20]. In this technique ideally the sample is of the clover-leaf shape as displayed in Fig. 2.3 (i). But it is successfully applied to quite arbitrarily shaped samples also as shown in Fig. 2.3 (ii). The method for obtaining the resistivity is as follows.

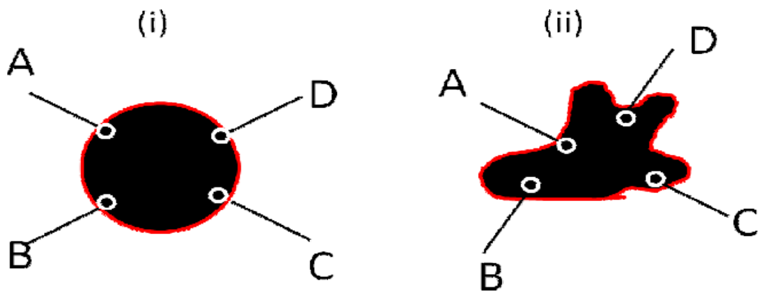

Figure 2.3: Arrangement of electrical contacts for four probe resistivity measurement using van der Pauw method.

1. A current I_{AB} is supplied to contacts A and B, the resulting voltage V_{CD} is measured between contacts C and D. Thus the measured resistance is

$$R_{AB,CD} = \frac{V_{CD}}{I_{AB}}$$

2. A current I_{BC} is driven from contact B to contact C and the resulting voltage V_{AD} is measured between contacts A and D. The resistance is

$$R_{BC,DA} = \frac{V_{DA}}{I_{BC}}$$

3. Then the resistivity can be calculated using the formula:

$$\rho = \frac{\pi d}{\ln 2} \frac{\left(R_{AB,CD} + R_{BC,DA}\right)}{2} f$$

where f is a function which depends on the ratio $\frac{R_{AB,CD}}{R_{BC,DA}}$ or on the geometry of the contacts, often known as the van der Pauw factor and d is the sample thickness.

Keithely 6221 dc and ac current source and Agilent 34420A Voltmeter were used to measure the resistance.

2.3.5. Magnetization measurements

2.3.5.1. dc Susceptibility

The basic principle of operation of VSM is that the changing of magnetic flux will produce a voltage in the pickup coil. The time dependent voltage induced can be written as

$$V_{coil} = \frac{d\phi}{dt} = \frac{d\phi}{dz}\frac{dz}{dt}$$

where φ is magnetic flux, z is the vertical position of the sample with respect to the coil and t is the time. For sinusoidal oscillating sample position, the induced voltage can be written as,

$$V_{coil} = 2\pi fCmASin(2\pi ft)$$

where C is a coupling constant, m is dc magnetic moment of sample, A is amplitude of oscillation and f is frequency of oscillation [21].

The measurement is done by oscillating the sample near a pickup coil (detection coil) and synchronously detecting the voltage induced. Quantum Design uses a gradiometer pickup coil which operates at large oscillating amplitude; the system is able to resolve magnetization change of 10^{-8} emu at a data rate of 1 Hz [22].

dc magnetization measurements with respect to temperature and magnetic field were performed using a Magnetic Property Measurement System (MPMS) 3 Ever cool from Quantum Design Inc., San Diego, CA., equipped with a 7 x 10^4 Oe superconducting magnet. Temperature dependent M–H loops were collected in a field sweeping from −70 to +70 kOe with different scan rates by first demagnetizing the sample by heating it to 300 K in a zero field before cooling it to the desired temperature. Magnetization versus temperature measurements in various applied magnetic fields were carried out in a temperature range from 2 K to 300 K in two experimental conditions: for Field Cooled (FC) measurements - at first the desired field was applied at 300 K and sample was cooled down to 2 or 5 K, for Zero Field Cooled (ZFC) measurements - the sample was cooled without applying any external field and the desired field was turned-on at the lowest temperature. Magnetic moment was picked-up while heating the sample in both ZFC and FC modes.

2.3.5.2. ac Susceptibility

MPMS can be used as both dc magnetometer and ac susceptometer. It consists of drive, detection coil, thermometer and electronics. ac drive coil set provides an alternating excitation field and the detection coil inductively measures the sample moment and excitation field. Drive coil can generate alternating field of ± 10 Oe and frequency in range of 0.1 Hz–1 kHz. The ac magnetic measurements were performed using an ac susceptibility option from Quantum Design Inc., San Diego, CA [22].

2.3.6. Mossbauer Spectroscopy (MS)

Mossbauer spectroscopy is a versatile technique which can be used to provide information in many areas of science such as Physics, Chemistry, Biology and Metallurgy. It can give very precise information about the chemical, structural, magnetic and time-dependent properties of a material [23]. Mossbauer Effect discovered by Rudolph Mossbauer in 1957 for which he received Nobel Prize in Physics in 1961 refers to “recoilless gamma ray emission and absorption by atomic nuclei in a solid”.

Energy levels of an atomic nucleus are influenced by their surrounding chemical environment. Interactions of the nucleus with its neighboring electrons include a variety of energy level transitions, often associated with the emission or absorption of a gamma ray. The gamma rays emitted by one nucleus can be absorbed by the surrounding nucleus resulting in nuclear resonance. The nuclear interactions known as hyperfine interactions involve small energy changes. Thus, a study of the changes in the energy levels can provide information about the atom's local environment within a system. There are three types of hyperfine interactions: isomer shift or chemical shift, nuclear quadrupole splitting and magnetic splitting. The isomer shift arises from the electron density at the nucleus. If the absorbing nucleus is identical to the nucleus that emitted the gamma ray then the energies of the nuclear transition are equal and resonant absorption is observed. If the chemical environment is different, the nuclear energy levels shift in the resonance energy which is known as isomer shift (δ). If there is a non-spherical charge distribution, then a gradient of the electric field produces quadrupole moment. In the presence of an asymmetrical electric field (produced by an asymmetric electronic charge distribution or ligand arrangement) this splits the nuclear energy levels, known as quadrupole splitting. The third and last hyperfine interaction is the magnetic splitting which arises from an interaction between the nucleus and the surrounding magnetic field. The magnetic field splits nuclear energy levels with a spin I into (2I+1) sub energy levels. Presence of all these interactions contributes to the nuclear resonance. Resonance spectrum also known as Mossbauer spectrum is a plot of gamma ray intensity as a function of velocity of a radiation source. The gamma ray intensity reduces at velocities where gamma rays are absorbed and hence resonance occurs. A typical Mossbauer spectrum for nuclei with identical surroundings is shown in Fig. 2.4. Figures 2.5 and 2.6 show Mossbauer spectra with quadrupole and magnetic splitting respectively. The number of resonance lines and their intensities will provide information about the chemical environment.

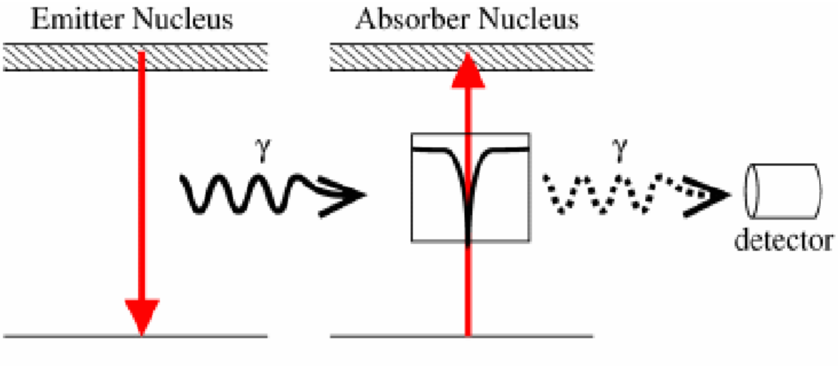

Figure 2.4: Simple Mossbauer spectrum from identical source and absorber [24].

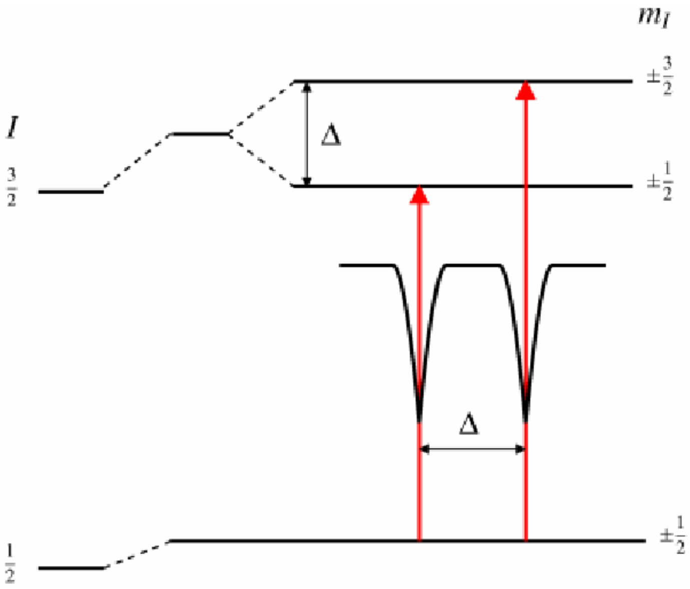

Figure 2.5. Quadruple splitting for a 3/2 to ½ transition.

In the presence of a magnetic field the nuclear spin moment experiences a dipolar interaction known as Zeeman splitting. There are many sources of magnetic fields that can be experienced by the nucleus. This magnetic field splits nuclear levels with a spin of I into (2I+1) sub states. This is shown in Fig. 2.6 for ^{57}Fe. Transitions between the excited state and ground state can only occur where $\Delta m_I = 0$ or 1. This gives six possible transitions for a 3/2 to 1/2 transition, giving a sextet as illustrated Fig. 2.6.

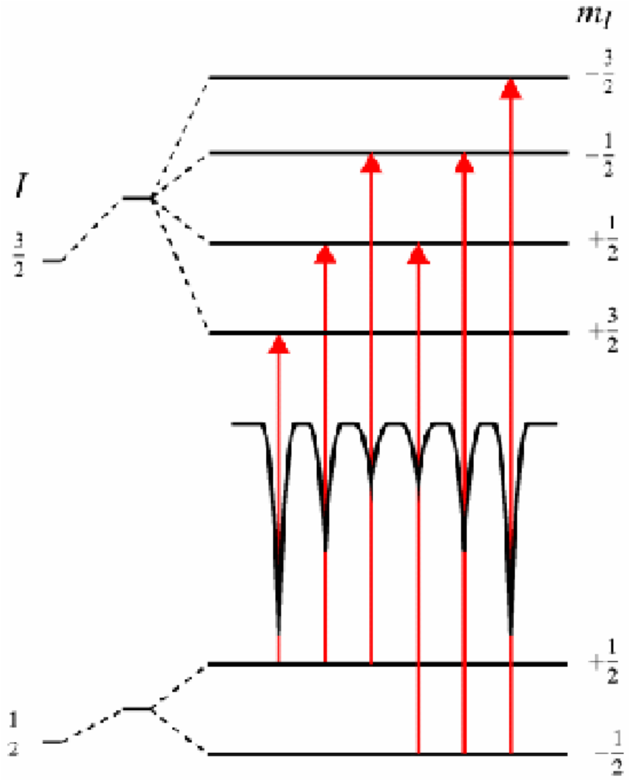

Figure 2.6. Mossbauer spectrum corresponding to nuclear energy levels splitting in the presence of magnetic field.

The line positions are related to the splitting of the energy levels, but the line intensities are related to the angle between the Mossbauer gamma-ray and the nuclear spin moment. The outer, middle and inner line intensities are related by

$$3:\frac{4\sin^2\theta}{1+\cos^2\theta}:1$$

The outer and inner lines are always in the same proportion but the middle lines can vary in relative intensity between 0 and 4 depending upon the angle the nuclear spin moments make with the gamma-ray. In polycrystalline samples with no applied field this value averages to 2 but in single crystals or under applied fields the relative line intensities can give information about moment orientation and magnetic ordering [25-28].

The study of magnetic properties of materials has been one of the most frequent applications of Mossbauer spectroscopy. Most of the studies have utilized the 14.4 k eV transition in ^{57}Fe. There are several reasons for the popularity of this isotope in the study of magnetic materials. The major reason is the presence of iron as a constituent in most of the scientifically and technologically important materials. Even other materials not containing iron, still they can be studied by the introduction of very small amounts of ^{57}Fe as a substitutient. The iron isotope has also nuclear properties such as low energy, long life time; adequate nuclear moments and usually strong bonding lattice (high Debye temperature) and long lived parent activity ^{57}Co that facilitate the measurements.

For $Dy_{0.55}Sr_{0.45}Mn_{1-x}Fe_xO_3$ system of compounds, ^{57}Fe Mossbauer measurements were carried out in transmission mode with a ^{57}Co (Rh) radioactive source in constant acceleration mode using a standard PC based Mossbauer spectrometer equipped with a WissEl velocity drive. Velocity calibration of the spectrometer was carried out with a natural iron absorber at room temperature.

2.3.7. Dielectric spectroscopy

Dielectrics are insulating materials which exhibit electric polarization in the presence of an electric field. The amount of polarization caused is described by a dimensionless quantity called the dielectric constant. Dielectrics have been studied for decades due to both their technology application and the fundamentally interesting relationships among their crystal chemistry, crystal structures and physical properties.

In the presence of an electric field, the positive and negative charges of a dielectric are displaced from their equilibrium positions by very small distances throughout the volume of the dielectric. This results in the formation of a large number of dipoles each having some dipole moment in the direction of the field. Then the material is said to be polarized with a polarization (P). The polarization is defined as dipole moment per unit volume. In the presence of electric fields, different types of polarizations are observed as shown in Fig. 2.7 [29].

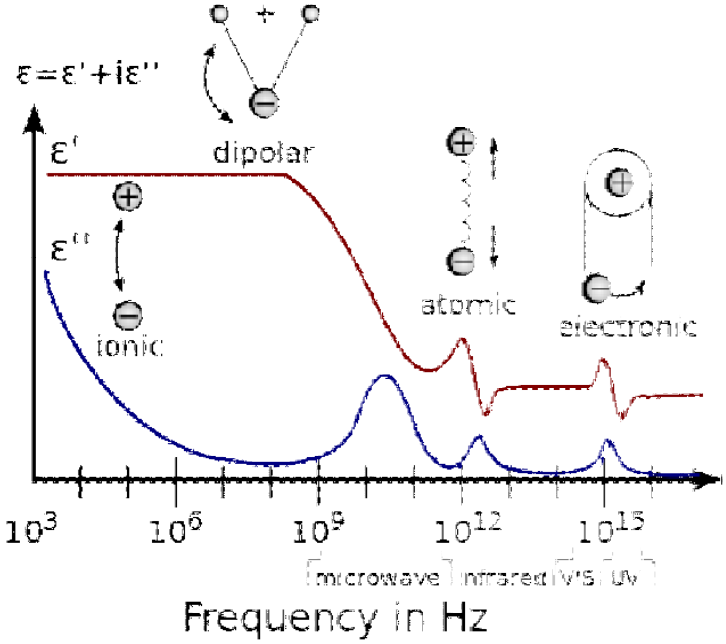

Figure 2.7. Frequency dependence of dielectric permittivity showing contributions from various ploarizations [29].

The various polarizations are:

1. **Electronic polarization**

This type of polarization is produced in neutral atoms due to the displacement of the nucleus with respect to the electron cloud in the presence of an external electric field. It is observed at high frequencies.

2. **Atomic/ Ionic polarization**

Ionic polarization develops due to displacement of a charged ion relative to other ions in a solid. The ionic contribution is important at low frequencies.

3. **Dipolar polarization**

   The dipolar polarization is observed in the polar substances with a permanent dipole moment. The dipoles can orient themselves in the presence of an external electric field.

4. **Space charge polarization**

   Space charge polarization arises due to the accumulation of charges at the interface or at the grain boundary of a polycrystalline material. The charge carriers can migrate over appreciable distances through the bulk of the material in response to the applied field-giving rise to re-distribution of charges in the dielectric medium [30].

Dielectric bahaviour of the materials depends on the polarization. Dielectrics take a finite time for the polarization to reach its maximum value. This is due to the forces between adjacent molecules which tend to prevent the alignment along the external field. This phenomenon is called dielectric relaxation. There are a number of equivalent ways in which dielectric information may be expressed. Relaxation behavior is generally expressed in terms of ε^* and electric conduction behavior in terms of σ^*, Z^* and M^*. Complex dielectric function ε^* which is expressed as $\varepsilon'+i\varepsilon''$ can be measured using Broadband dielectric spectroscopy, a technique to characterize dielectric materials. Dielectric relaxation processes are usually analyzed using model functions. To estimate relaxation times from dielectric spectra, the dielectric constant or relative permittivity is subsequently determined from the measured bulk capacitance:

$$\mathrm{C} = \frac{\epsilon_0 \epsilon_r \mathrm{A}}{\mathrm{d}}$$

where C is capacitance, A is the area of the material, d is the thickness or in other words, is the distance between the two plates of the capacitor, ε_0 is the permittivity of free space (8.854 x 10^{-12} F/m) and ε_r is the relative permittivity which is a complex quantity and is given by ε_r or $\varepsilon^* = \varepsilon' + i\varepsilon''$. The real part of ε_r, i.e. ε' describes a relationship between ac signals transmission speed and the dielectric materials capacitance and is known as dielectric constant. The energy loss from the original signal as it passes through the dielectric material is given by the imaginary part of the relative permittivity, ε_r i.e., ε''. The interaction of electromagnetic radiation with dielectric materials is studied by dielectric spectroscopy. Dielectric information may be presented in a number of equivalent ways. The dielectric functions used for the present work which are derived from ε^* are given below:

$$\mathrm{M}^* = \frac{1}{\epsilon^*}$$

$$\mathrm{Z}^* = \frac{\mathrm{M}^*}{\mathrm{i}\omega\mathrm{C}_0}$$

$$\sigma^* = \mathrm{i}\omega\mathrm{C}_0\epsilon^*$$

Dielectric spectroscopy data presented in this thesis were collected using a broadband dielectric spectrometer (NOVOCONTROL Technologies, GmbH Co. Germany, Model Concept 80) in a temperature range ~120 K – 300 K in the frequency range 0.5 Hz -10^7 Hz.

2.4. REFERENCES

[1] H. Fukuoka, T. Isami and S. Yamanaka, Chem. Lett., **8**, (1997), 703.

[2] Y. Inaguma, C. Liquan, M. Itoh, T. Nakamura, T. Uchida, H. Ikuta and M. Wakihara, Solid State Commu., **86**, (1993), 689.

[3] A. Safari, R.K. Panda and V.F. Janas, Key Eng. Mater., **122**, (1996), 35.

[4] R.J. Bell, G.J. Millar and Drennan, Solid State Ionics, **131**, (2000), 211.

[5] B.D. Cullity, Elements of X-Ray diffraction, Addison-Wesley Publishing Company, Inc. (1956).

[6] D. Kriegner, Z. Matej, R. Kuzela and V. Holy, J. Appl. Cryst., **48**, (2015), 613.

[7] H.M. Rietveld, Acta Cryst., **22**, (1967), 151.

[8] H.M. Rietveld, J. Appl. Cryst., **2,** (1969), 65.

[9] R.A. Young, Introduction to the Rietveld method, R.A. Young, Ed., The Rietveld method, Oxford University Press, Oxford, New York (1993).

[10] A.C. Larson and R.B. Von Dreele, "General Structure Analysis System (GSAS)", Los Alamos National Laboratory Report, LAUR 86-748, (1994).

[11] B.H. Toby, EXPGUI, a graphical user interface for GSAS, J. Appl. Cryst., **34**, (2001), 210.

[12] A.J. Garratt-Reed and D.C. Bell, Energy-Dispersive X-Ray Analysis in the Electron Microscope, BIOS Scientific Publishers Limited, (2003).

[13] Gary J. Long, Mossbauer Spectroscopy Applied to Inorganic Chemistry, Springer Science, Business Media New York, (1984).

[14] John F. Watts, and John Wolstenholme, Front Matter in An Introduction to Surface Analysis by XPS and AES, John Wiley & Sons, Ltd., Chichester, UK., (2003).

[15] M.P. Seah, Surf. Interface Anal., **2**, (1980), 222.

[16] R. Kwok, XPSPEAKV4.1, 2000, http://www.phy.chuk.end.hkl./surfacr/XPSPEAK.

[17] W.H. Weber and R. Merlin, Raman scattering in Materials Science, (2006).

[18] John R. Ferraro, Kazuo Nakamoto and Chris W. Brown, Introductory Raman Spectroscopy, Elsevier, (2003).

[19] Raman Spectroscopy Basics, Princeton Instruments.

[20] L.J. van der Pauw, Phillips Res. Rep., **13**, (1958), 1.

[21] B.D. Cullity and C.D. Graham, Introduction to Magnetic Materials, Second Edition, John Wiley & Sons, Inc., Hoboken, NJ, USA, (2008).

[22] Manual of MPMS® SQUID VSM, Quantum Design.

[23] Gary J. Long, Mossbauer Spectroscopy Applied to Inorganic Chemistry, Springer Science, Business Media New York, (1984).

[24] Introduction to Mossbauer Spectroscopy, Royal Society of Chemistry, Cambridge CB4 0WF3.

[25] R.H. Herber, J. Chem. Educ., **42**, (1965), 180.

[26] R.H. Herber, Ann. Rev. Phys. Chem., **17,** (1966), 26.

[27] V.V. Ovchinnikov, Mössbauer Analysis of The atomic and Magnetic Structure of Alloys, Cambridge International Science Publishing, UK, (2006).

[28] U. Gonser, Mossbauer Spectroscopy, Springer-Verlag Berlin Heidelberg New York (1975).

[29] Introduction to Solid State Physics by C. Kittle, (2004).

[30] Kwan Chi Kao, Dielectric Phenomena in solids, Elsevier Academic Press, (2004).

CHAPTER – 3

STRUCTURE AND OTHER PHYSICAL PROPERTIES OF MONOVALENT POTASSIUM SUBSTITUTION AT Dy SITE IN $DyMnO_3$ – $Dy_{1-x}K_xMnO_3$

3.1. INTRODUCTION

Multiferroic materials have attracted many researchers attention due to their potential applications such as electronic switching, magnetic recording, information storage, spintronics and sensor etc. The multiferroic materials display magneto electric phenomenon where spontaneous electric polarization is induced by magnetic transitions and thus they belong to Type 2 multiferroics. This magnetoelectric coupling is of importance for certain applications in devices. Some of the Rare earth (R) perovskite manganites ($RMnO_3$) [1-4] exhibit a variety of magnetic transitions at low temperatures leading to magneto electric coupling effect. $DyMnO_3$ (DMO) is one such material exhibiting an anomalous variation in dielectric constant at an antiferromagnetic transition temperature corresponding to Mn spins whose propagation vector reaches a constant value [5]. Moreover, the magnetoelectric effect was related to structural instabilities. DMO is an interesting system as it can crystallize either in a $GdFeO_3$-type distorted orthorhombic structure or a hexagonal structure depending on the synthesis conditions such as temperature, environment etc. [6-8]. Moreover, DMO has a very complex magnetic phase diagram at low temperatures. In the literature, structural [9], magnetic [10], vibrational [11] properties of DMO have been reported for both orthorhombic and hexagonal structures. From the magnetic scattering experiments of DMO, the antiferromagnetic ordering of Dy spins is ~ 5 K and that of Mn spins is ~ 39 K [12]. Extensive research has been carried out on the DMO compound with Sr [13], Ca [14], Ho [15] and Y [16] substitutions at the Dy site. 50at. % Sr substituted for Dy site in orthorhombic DMO [13] showed spin glass nature at low temperature. Yoshii et al. [14] from the magnetic and dielectric properties of $Dy_{0.5}Ca_{0.5}MnO_3$ reported charge ordering of Mn ions at low temperatures. Magnetic ground state properties of DMO are changed with Holmium substitution for Dy. The ground state of DMO which is a cycloidal magnetic state changed to E-AFM for $HoMnO_3$ whereas mixed compounds of $Dy_{1-x}Ho_xMnO_3$ displayed phase separation [15]. Ferrimagnetic ordering of Dy ions was found to decrease from 8 K for DMO to 4 K for $Dy_{0.5}Y_{0.5}MnO_3$. This was understood to be due to Dy sublattice dilution effect in $Dy_{1-x}Y_xMnO_3$ [16].

In view of the above mentioned properties, we explored the ground state properties of DMO by first reducing the structural distortions by substituting larger size ion and secondly, producing mixed valent Mn ions favoring double exchange interaction. We have undertaken monovalent substitution at Dy site in $DyMnO_3$ to investigate structural, vibrational, transport and magnetic properties. In addition to these properties, low temperature frequency dependence of dielectric and impedance properties at several temperatures were described in this chapter. However, due to experimental constraints, we could not perform dielectric measurements at low temperatures where a series of magnetic transitions were observed.

3.2. METHODOLOGY OF SYNTHESIS AND EXPERIMENTAL DETAILS

Polycrystalline compounds of $Dy_{1-x}K_xMnO_3$ (x=0, 0.1, 0.2 and 0.3) were prepared using solid state synthesis method. High purity (99.99%) oxide powders of Dy_2O_3, K_2CO_3 and MnO_2 taken in appropriate ratios were mixed thoroughly using an agate mortar and pestle and then calcined at 1000 ˚C and 1300 ˚C for 12 hrs. in an alumina crucible in air. The heat treatments were repeated with intermediate grindings until crystalline phase compounds were obtained. Phase formation of the compounds after each heat treatment was tracked by collecting X-ray diffraction data at room temperature. After ensuring the single phase formation, the powder was compressed using tungsten carbide die and plunger into circular pieces with dimensions of 10 mm diameter and 2 mm thickness. The compacted pellets were then sintered at 1300 ˚C for 24 hrs. to increase the density of the pellets for electrical resistivity and dielectric spectroscopy measurements.

Phase identification of the sintered pellets was carried out by powder X-ray diffraction technique with STOE (Germany) diffractometer in Bragg-Brentano parafocusing geometry at ambient temperature using Cu K_α radiation (1.5406 Å). Diffraction data for refinement analysis were collected in the angular range of 20˚ to 90˚ with an equal interval of 0.05˚ and a step time of 50 sec/step. Refinement of whole powder diffraction pattern was carried out using GSAS software [17]. Raman spectra were recorded using Renishaw micro-Raman spectrometer at room temperature in the backscattering geometry. An excitation wavelength of 514.5 nm with a laser power of 10% (2mW) was used for all the compounds. Compositional homogeneity was verified using Scanning Electron Microscopy (SEM), (Oxford instruments make; Model: CamScan 3200) combined with Energy Dispersive X-ray

(EDX) facility, (Oxford instruments make; Model: INCAPenta FETX3). Binding energies of manganese were estimated from X-ray Photoelectron Spectroscopy (XPS) measurements performed using a PHOIBOS 150 spectrometer (SPECS Surface Nano Analysis GmbH, Germany) equipped with a monochromatic Al K_α (1486.7 eV) X-ray source.

Electrical resistivity of $Dy_{1-x}K_xMnO_3$ (x=0, 0.1, 0.2 and 0.3) was measured by four-probe method in a liquid helium Dewar using a dipstick arrangement down to 160 K. Sub ambient temperature is limited by a maximum measurable resistance of 10^6 Ohms. SQUID based VSM (Quantum Design make; model: MPMS 3 Ever Cool SQUID) magnetometer was used to record Zero Field Cooled (ZFC) and Field Cooled (FC) dc magnetization data (M-T) in the temperature range, 2-400 K at different fixed fields. Magnetization (M-H) curves were recorded at several temperatures under sweeping magnetic field –7 T to +7 T using the same magnetometer. ac susceptibility data were also collected in the temperature range, 4-100 K in low ac magnetic fields of 1 Oe and 5 Oe and a zero-bias external dc magnetic field at various frequencies.

Dielectric properties were studied using a broadband dielectric spectrometer, (NOVOCONTROL Technologies, GmbH Co. Germany make; Model: Concept 80) in the temperature range ~125 K – 300 K and frequency range 0.5 Hz -10^7 Hz.

3.3. RESULTS AND DISCUSSION

3.3.1. X-ray diffraction

From the powder XRD, no impurities, within the detection limits of the diffractometer could be detected. Entire pattern of the compounds could be indexed to orthorhombic structure with Pnma space group using Rietveld refinement by GSAS package. None of the compounds showed preferred orientation. Linear interpolation function (function 7) was used to fit the background, while Pseudo-Voigt (type 2 in GSAS) function was found to represent the diffraction peaks fairly well. Steps in the refinement were as per the sequence given in the GSAS manual. At the final cycles of refinement, fractional occupancies were refined, but this did not improve either the R-factors or the visual fit hence occupancy parameters were unchanged. Figure 3.1 (a) shows experimental X-ray diffraction pattern of DMO along with the results of the final refinement. Lattice constants of DMO from the final refinement are a = 5.7840 (1) Å, b = 7.3883 (1) Å and c = 5.2756 (0) Å which follow the relation $b/(\sqrt{2}) < c < a$.

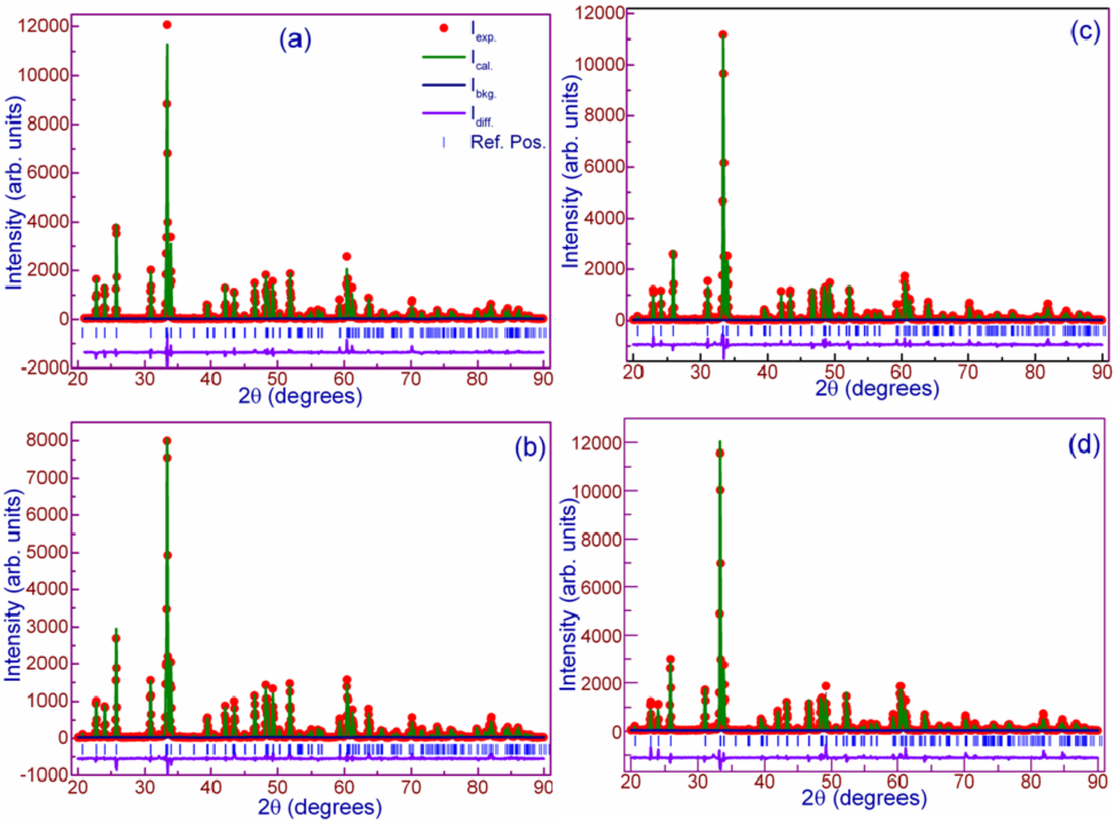

Figure 3.1. X-ray powder diffraction patterns of $Dy_{1-x}K_xMnO_3$. (a) x = 0.0, (b) x = 0.1, (c) x = 0.2 and (d) x = 0.3. Experimental data are presented by closed circles and calculated intensity is plotted by solid lines. The difference between the experimental and calculated is also included by a solid line below the patterns. Vertical blue color lines correspond to Bragg reflection positions as per the lattice constants with Pnma space group.

These lattice parameters of DMO agree with those reported in JCPDS database [18]. Since the quality of the existing JCPDS card (25-0330) for DMO is only indexed, we submitted our X-ray powder diffraction data to International Centre for Diffraction Data (ICDD) and the data are accepted for inclusion in the ICDD database under star (*) quality [19]. In the distorted perovskite, the unit cell is larger than the simple cubic unit cell and the distortions resemble that of $GdFeO_3$-type perovskite (Space group Pnma and Z=4) distortions. Due to smaller ionic size of Dy (1.027 Å), polyhedra tilt about all three principal crystallographic directions to fill the space created by the smaller ion (Dy) in an otherwise cubic unit cell adopted by an ideal perovskite (Space group Pm3m and Z=1). As a consequence, displacements of Dy and oxygen ions produce orthorhombic distortions such as Mn-O-Mn bond bending and octahedral tilts. This can be inferred from the decrease of the <Mn-O-Mn> angle to 144.713° in contrast to 180° in the undistorted cubic structure. DMO has only Mn^{3+} ions which are JT active and hence additional distortions are produced in the Mn-O bond lengths. Consequently, the six equal bond lengths are split into three pairs of unequal bond lengths. Each Mn site has a distribution of four short bonds with oxygen and two long bonds with oxygen showing elongation in the ac plane. In DMO, Dy, due to its small size is 8-fold coordinated with oxygen ions as compared to La where La is 12-fold coordinated [20]. 8-fold coordination was arrived at based on our refinement results. The same exercise of refinement was performed for the potassium substituted compounds and X-ray diffraction patterns corresponding to all the compounds are also shown in separate panels in the Fig. 3.1 (b-d).

Lattice constants, fractional atomic coordinates along with Wyckoff positions for all the compounds after the final refinement are summarized in Table 3.1. Quality of the diffraction pattern fitting is judged by a set of Reliability factors (R-factors) viz., the goodness of fit χ^2, structure factor $R(F^2)$, profile factor R_p, weighted profile factor wR_p and Durbin and Watson statistical parameter D_{wd}. R-factors after the final the refinement are also included in the same Table. Substitution of larger size,

Table 3.1. Structural parameters from the refined data of $Dy_{1-x}K_xMnO_3$. Dy, K and O(1) are at (4c) position: (x, ¼, z), Mn is in a special position (4b): (0, 0, ½) and O(2) is in a general position (8d): (x, y, z).

Parameters		**Composition, x**			
		0.0	**0.1**	**0.2**	**0.3**
Space group		Pnma			
Lattice parameters (Å)	*a*	5.783993	5.792277	5.757226	5.744169
	b	7.388287	7.386155	7.403611	7.405681
	c	5.275582	5.276251	5.279975	5.278595
Unit cell volume (Å^3)		225.446	225.732	225.054	224.549
Dy/K Fractional atomic O1 coordinates O2	x	0.080109	0.080687	0.077851	0.077467
	z	0.983761	0.983401	0.983576	0.983449
	x	0.469045	0.482108	0.461613	0.457863
	z	0.11002	0.115660	0.123688	0.132861
	x	0.180673	0.179024	0.177344	0.179894
	y	0.548879	0.548430	0.551833	0.558297
	z	0.195885	0.204968	0.202080	0.197239
Reliability factors	χ^2	2.962	2.254	3.923	4.343
	$R(F^2)$	9.24	5.98	8.71	7.69
	R_p	10.04	9.26	11.70	12.20
	wR_p	13.37	12.86	16.01	16.30
	D_{wd}	1.270	1.168	0.982	0.922

monovalent potassium (1.55 Å – 12 fold coordination) for smaller size Dy^{3+} ion (1.027 Å – 8 fold coordination) partially converts some of the JT active trivalent manganese ions (0.645 Å) to tetravalent manganese ions (JT inactive) of smaller size (0.58 Å) to preserve the total charge balance in the samples. The average ionic size at Dy site increases from 1.027 Å for x=0.0 to 1.211 Å for x=0.3 while the average ionic size at Mn site reduces from 0.645 Å for x=0 to 0.576 Å for x=0.3. As a result of this, we see that for an initial concentration of 10 at. % K, volume of the unit cell increases and subsequent substitution brings down the volume because for every K^{1+} substitution, two smaller Mn^{4+} ions are created. However, distortions in bond lengths are much more distinctive when x=0 as expected due to the presence of active JT Mn^{3+} ions.

Table 3.2 lists some of the relevant inter atomic distances together with bond angles derived from the diffraction data with standard deviations in parenthesis. Although there are octahedral tilts which increase with x, coordination of manganese and dysprosium ions is preserved. With substitution, changes in the JT distortion of the oxide octahedron around Mn^{3+} cation are evident from the Mn-O bond distances.

Table 3.2. Inter atomic distances (Å) and bond angles (degrees) in Mn-O octahedron for $Dy_{1-x}K_xMnO_3$ with standard deviations mentioned in parenthesis.

Parameters	**Composition, x**			
	0.0	**0.1**	**0.2**	**0.3**
$d_{Mn\text{-}O1}$	1.94479 (3)	1.94752 (3)	1.97139 (4)	1.99110 (4)
$d_{Mn\text{-}O2}$	1.94179 (2)	1.90434 (3)	1.91487 (4)	1.94872 (4)
$d_{Mn\text{-}O2}$	2.15187 (3)	2.18036 (3)	2.17317 (5)	2.15592 (5)
∠Mn-O1-Mn	143.521 (1)	142.936 (1)	139.730 (1)	136.822 (1)
∠Mn-O2-Mn	145.905 (0)	147.029 (0)	145.593 (0)	143.670 (0)

However, the distortions within Mn-oxygen octahedra are also reducing since concentration of JT ion (Mn^{3+}) is decreasing with x. $Dy_{0.7}K_{0.3}MnO_3$ shows more regular octahedra as compared to the pristine compound. The apical bond length (Mn-O1) increases and approaches one (the longer) of the axial Mn-O2 bond distances for x=0.3 which indicates that the distortions within the octahedra are small as compared to the parent compound. The suppression of distortions for large K content is remarkable as compared to that of DMO, and this may be inferred to be due to the presence of less number of JT active ions, Mn^{3+}. This is quantified by D_{JT} parameter which estimates the deformation of MnO_6 octahedra based on the bond lengths and is calculated using the relation:

$$D_{JT} = \frac{\Delta d_{Mn-O2}}{\langle d_{Mn-O2} \rangle} \tag{3.1}$$

Here Δd_{Mn-O2} is the change in the axial bond distances and $\langle d_{Mn-O2} \rangle$ is the average bond distance in the ac plane. D_{JT} is 0.101 for x=0.3 in contrast to 0.103 for x=0.0. All the parameters that influenced the polyhedral distortions in the structure with substitution are plotted against K content in Fig. 3.2 (a) to (d). Some of the Dy-O distances decrease while others increase as seen from the Fig. 3.2 (d).

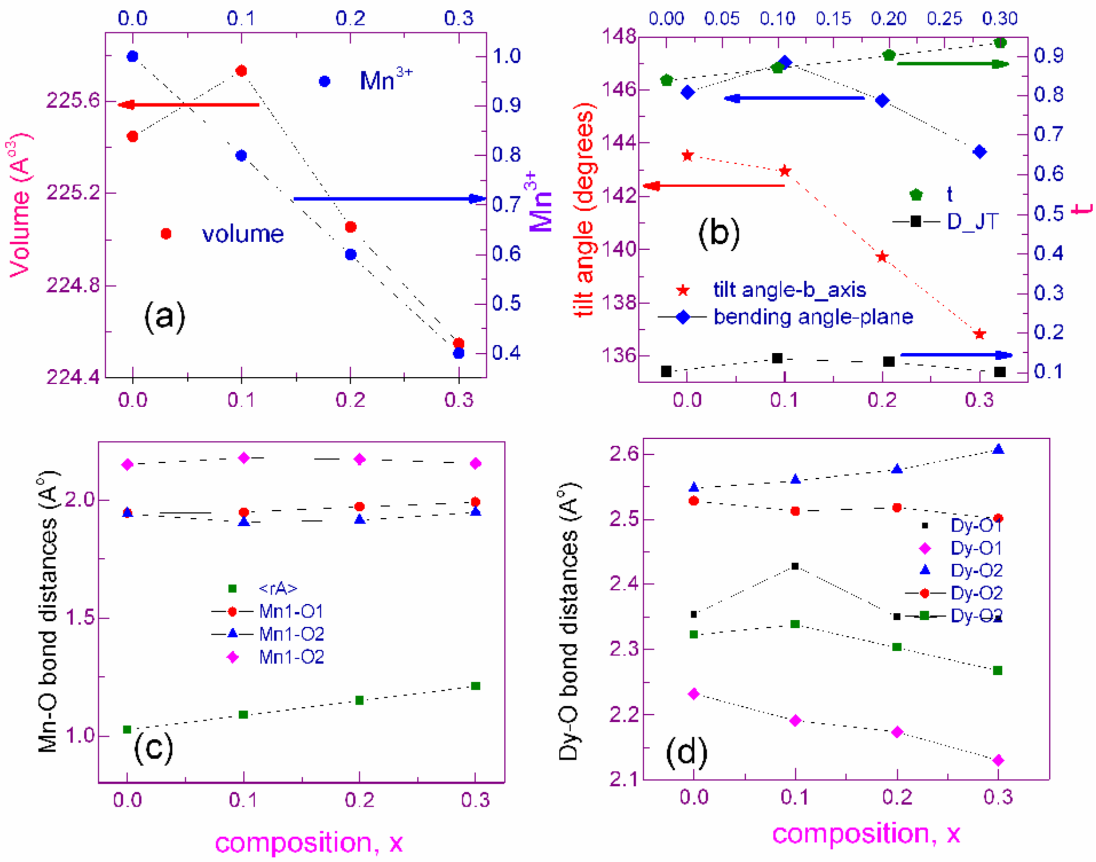

Figure 3.2. Comparison of the refined structural parameters for all the compositions of x in $Dy_{1-x}K_xMnO_3$.

Due to changes in the ionic sizes of Dy and Mn, atomic positions of Dy, Mn and oxygen are changed giving rise to more complicated oxygen ion environment. The most prominent distortion from the ideal cubic perovskites is in the tilting of the polyhedra along b-axis and bending of Mn-O2-Mn in the ac plane in the Pnma symmetry.

3.3.2. Raman spectroscopy

$DyMnO_3$ has an orthorhombic structure with space group Pnma, D_{2h}^{16} (mmm) with four formula units per unit cell - 24 Raman active modes are expected. Raman active modes using SAM module of Bilbao crystallographic server [21], normal modes at the zone centre are enumerated and are listed in Table 3.3

Table 3.3. Irreducible representations for Raman active modes in the orthorhombic structure with Pnma space group.

Atoms	**Wyckoff position**	**Site symmetry**	**A_g**	**B_{1g}**	**B_{2g}**	**B_{3g}**
Dy & O1	4c	C_s	2	1	2	1
Mn	4b	C_i	-	-	-	-
O2	8d	C_1	3	3	3	3

The irreducible representation for Raman active modes, Γ_{Raman} for Pnma space group is given by:

$$\Gamma_{Raman}(\mathrm{Pnma}) = 7A_g + 5B_{1g} + 7B_{2g} + 5B_{3g} \tag{3.2}$$

Mn atoms occupying a special position (0, 0, ½) with site symmetry C_i do not contribute to Raman modes (Table 3.3). Only dysprosium and oxygen ions give rise to Raman active modes. Hence Raman modes are due to oxygen polyhedral vibrations and translations of oxygen atoms in the unit cell. Peak centers of the Raman mode frequencies have been obtained using Peakfit program by fitting the Raman spectra using Lorentzian function. 14 Raman bands could be identified from Raman spectrum of DMO (Fig. 3.3) in the wave number range 50 to 1000 cm^{-1} as listed in Table 3.4 and they are consistent with those reported in the literature [22 - 24].

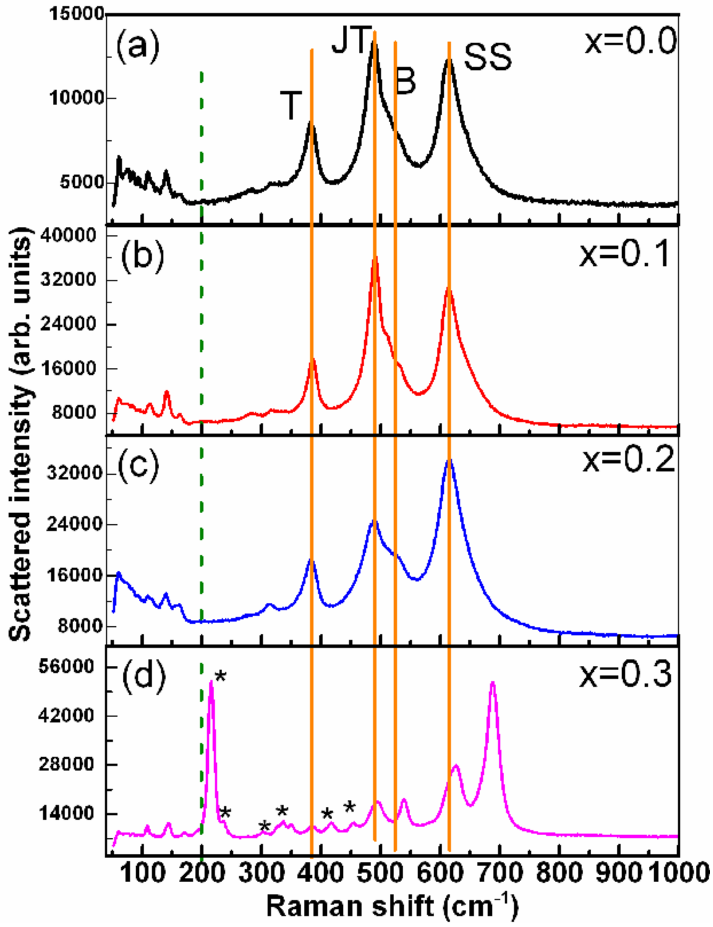

Figure 3.3. Unpolarized, room temperature Raman spectra for $Dy_{1-x}K_xMnO_3$ displaying Raman active phonon modes with respect to potassium content, x=0, 0.1, 0.2 & 0.3. $\lambda_{exc.}$ = 514.4 nm. Mode assignment has been done following Cai et al. [26]. * indicates new Raman lines for x=0.3; SS - Symmetric Stretching mode; B - Bending mode; JT/ASS – Jahn-Teller/Anti Symmetric Stretching mode; T - Tilting mode.

Six external modes appear below 200 cm^{-1}. These low wave number modes could be assigned to the vibrations of heavier rare earth ion shifts. Remaining modes could not be detected either due to weak intensity or accidental degeneracy. Line widths of all bands are high due to polyhedral distortions and spin-phonon coupling

[25]. Assignment of vibrational modes to their respective atomic motions/polyhedral units was carried out following Cai et al. [26]. Out of the four pure modes, the Raman band at 614 cm^{-1} is attributed to a symmetric stretching (SS) of the basal oxygen ions of the octahedra. Asymmetric stretching mode associated with distortions produced due to JT Mn^{3+} ions is observed at 488 cm^{-1}. The vibrational modes arising from polyhedral tilts and bending correspond to 372 cm^{-1} and 522 cm^{-1} respectively. With increasing potassium content, (i.e., reduction in Mn^{3+} ion concentration), the intensity of the band at 488 cm^{-1} which denotes JT distortions reduces. This can be understood from the reduction in the dispersion of octahedral bond lengths (Fig. 3.2 (c)). Also atomic vibrations giving rise to a bending mode which appears as a shoulder to the JT

Table 3.4. Comparison of experimental Raman frequencies corresponding to the vibrational modes in $Dy_{1-x}K_xMnO_3$.

S.No.	**Composition (x)**			
	0.0	**0.1**	**0.2**	**0.3**
1.	61	60	59	60
2.	75	74	74	73
3.	94	96	91	93
4.	111	113	112	109
5.	141	141	139	144
6.	163	163	161	177 216*
7.	274	283	278	238* 302*
8.	320	320	314	326 336*
9.	372	381	375	350
10.	384	387	385	385 416* 454*
11.	488	490	488	494
12.	522	521	529	539
13.	614	614	615	624
14.	642	642	650	688

mode gets decoupled and shifts to a higher frequency for x=0.3. Frequency of the SS mode remains unchanged with x except for x=0.3; where a mode hardening is observed. This is followed by an intensity reversal between SS and JT modes. Frequency of the Raman band corresponding to octahedral tilt remains the same but its intensity reduces gradually. The remaining bands arise due to coupled vibrations of Dy and O1 in the xz plane and along the y-axis. Raman spectra for the substituted compounds are shown in Fig. 3.3 (b to d). The overall features of the spectra of the substituted compounds are similar to those of the parent compound except for x=0.3 where sharp peaks are observed. All the six bands below 200 cm^{-1} are preserved.

Figure 3.4 displays the dependence of mode frequencies on potassium composition; x. Except for some peaks, there is a slight upward shift of the Raman frequencies with increasing K content, which is attributed to lattice contraction upon replacement of Dy by K. It is worth noting here that the line width of the Raman

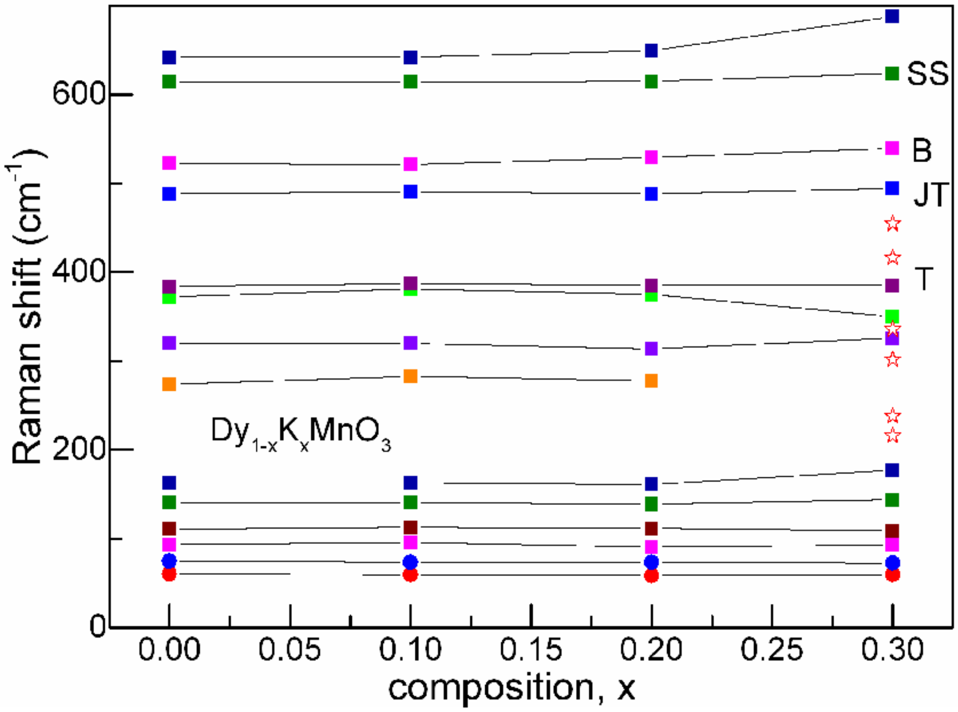

Figure 3.4. Comparison of Raman modes for the solid solution, $Dy_{1-x}K_xMnO_3$ (x = 0.0-0.3).

bands for x=0.3 has reduced which may facilitate magnetic interactions among Mn ions. Frequency of the bending mode increases showing hardening with x. Asymmetric mode found at 488 cm^{-1} increased to 494 cm^{-1} for x=0.3. However, local symmetry might have changed as new peaks appear for x=0.3. A remarkable feature is the large intensity of the low energy band for x=0.3. For x=0.3, a high intense Raman band along with a small shoulder at 216 cm^{-1} was observed. Since the bond distances do not change abruptly across the solid solution range studied, Raman band frequency changes are small except for the bands discussed above.

3.3.3. Microstructure analysis

Scanning Electron Microscopy (SEM)

The SEM images of $Dy_{1-x}K_xMnO_3$ solid solution are shown in Fig. 3.5. The grain sizes in a given material are uniform. The density was found to decrease with increase in the potassium content in the substituted compounds.

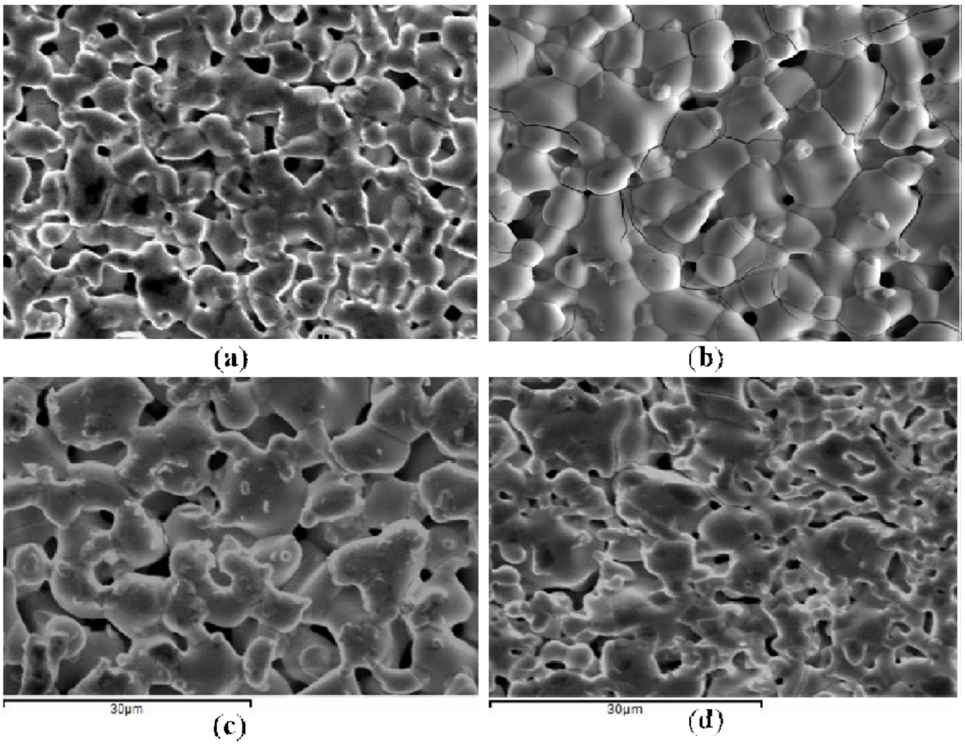

Figure 3.5. SEM images for $Dy_{1-x}K_xMnO_3$ (a) x=0.0 (b) x=0.1 (c) x=0.2 and (d) x=0.3.

Energy-Dispersive X-ray Spectroscopy (EDS)

Energy Dispersive X-ray spectra of $Dy_{1-x}K_xMnO_3$ (x=0.0-0.3) shown in Fig. 3.6 revealed the presence of all the ions present in the studied compounds without loss of elements during the high temperature synthesis.

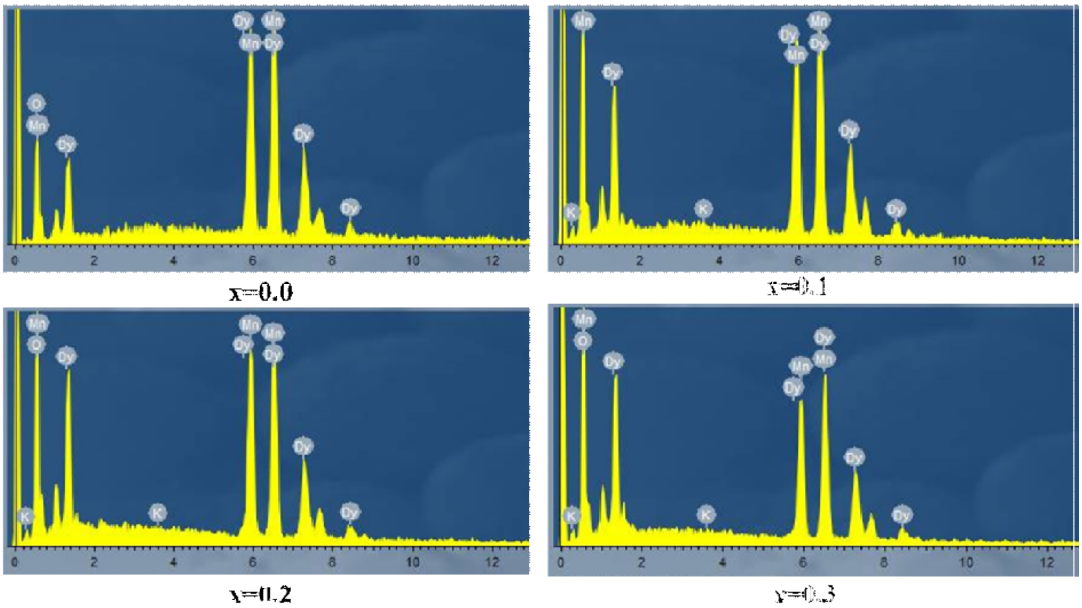

$x=0.0$ $x=0.1$

$x=0.2$ $x=0.3$

Figure 3.6. Energy dispersive X-ray spectra corresponding to the potassium substituted compounds revealing the presence of all the elements.

3.3.4. X-ray Photoelectron Spectroscopy (XPS)

Figure 3.7 (a) displays the normalized satellite peaks of $2p_{3/2}$, $2p_{1/2}$ of Mn ion for different concentrations of potassium. In the parent compound $DyMnO_3$, Mn ion is found in trivalent state with binding energies 641.8 eV for $2p_{3/2}$ and 653.9 eV for $2p_{1/2}$. This Mn ion is transferred into mixed oxidation states i.e., Mn^{3+} and Mn^{4+} ions when potassium is substituted at Dy site. Using XPS PEAKS 4.1 software [27], the satellite peaks of Mn ion in potassium substituted $DyMnO_3$ are fitted as shown in Figs. 3.7 (b) to (d) and binding energies of Mn^{3+} and Mn^{4+} are found and are presented in Table 3.5.

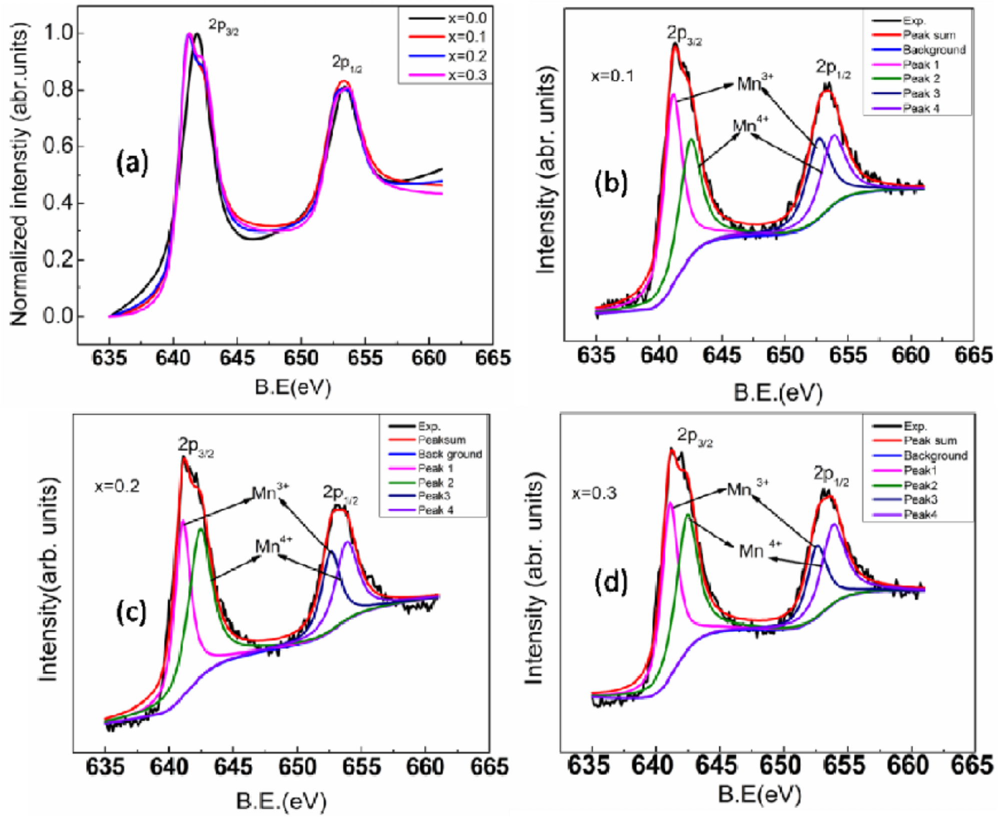

Figure 3.7. XPS spectra of Mn ion for $Dy_{1-x}K_xMnO_3$ (x=0.0-0.3:0.1) (a) Normalized XPS spectra of $Dy_{1-x}K_xMnO_3$ (x=0.0-0.3). (b-d) XPS spectra for individual compositions of x=0.1, 0.2 and 0.3 respectively.

Table 3.5: Binding energies of Mn^{3+} and Mn^{4+} ions along with their energy differences and ratio.

x in $Dy_{1-x}K_xMnO_3$	**$2p_{3/2}$ (eV)**				**$2p_{1/2}$ (eV)**			
	Mn^{3+}	**Mn^{4+}**	**Mn^{4+}-Mn^{3+}**	$\frac{Mn^{3+}}{Mn^{4+}}$	**Mn^{3+}**	**Mn^{4+}**	**Mn^{4+}-Mn^{3+}**	$\frac{Mn^{3+}}{Mn^{4+}}$
0.0	641.8				653.4			
0.1	641.1	642.5	1.3	4	652.8	653.9	1.1	4
0.2	641.1	642.4	1.3	1.5	652.7	654.3	1.6	1.5
0.3	641.1	642.5	1.4	0.6	652.7	653.9	1.2	0.6

3.3.5. Transport Properties

Although heterovalent Mn ions with (e_g^1) and without (e_g^0) mobile electrons are available in the substituted oxides, variation of electrical resistivity of these oxides showed semiconducting behavior in the whole temperature range measured as seen in the main panel of Fig. 3.8. No insulator – metal transition was observed within the temperature range of measurement. The random occupation of active and inactive JT Mn ions with different ionic radii induces distortions in the lattice in addition to the JT distortions and hence DE was not observed. Occupancy of the multiple ions Dy and K at the same lattice site (Wyckoff position-4c) also introduces distortions in the lattice. Overall, these distortions are coupled via an oxygen ion to Mn^{3+} ions with a lone electron occupying e_g orbital. As a consequence, electron-lattice interaction is strong [28]. With JT distortions being anisotropic so does the electron-lattice interac-

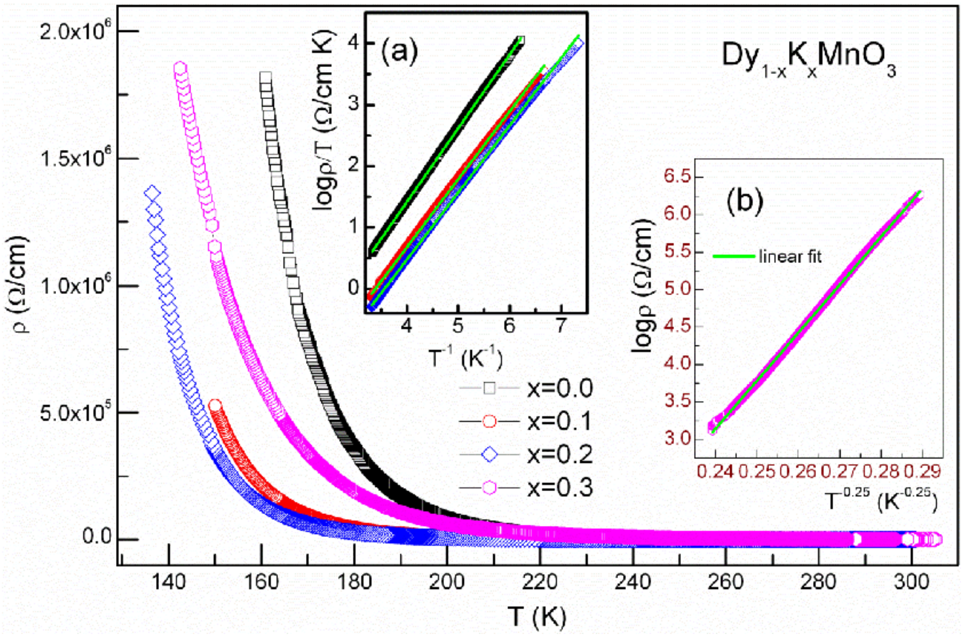

Figure 3.8. Variation of resistivity (**ρ**) as a function of temperature for $Dy_{1-x}K_xMnO_3$ (x=0.0, 0.1, 0.2 & 0.3) is displayed in the main panel. Inset (a) shows a plot of log (ρ/T) against inverse temperature (symbols) along with the linear fit (solid lines) to small polaron conduction for x=0.0, 0.1 and 0.2. (b) A linear fit of the resistivity data to VRH expression for x=0.3.

tions. Thus the strong electron-phonon interaction favors formation of polarons and hence polaron model is invoked to understand conductivity mechanism in these oxide materials. This is the basis for the analysis of the ρ(T) data using polaron models [29, 30]. It is interesting to note that the electrical resistivity decreased with increasing x up to x=0.2. For the subsequent increase in x to 0.3, resistivity increased. This behavior may be due to the reduction in the ratio of Mn^{3+}/Mn^{4+} with increase in potassium content. The ρ(T) behavior of DMO, $Dy_{0.9}K_{0.1}MnO_3$ & $Dy_{0.8}K_{0.2}MnO_3$ has been attributed to Small Polaron Hopping (SPH) conduction mechanism since Mn^{3+} electrons are majority of charge carries in these two compounds. The variation of ρ(T) with temperature was analyzed by SPH equation:

$$\rho(T) = \rho_0 T e^{\frac{E_a}{k_B T}} \tag{3.3}$$

Best fits to SPH equation are shown in insets of Fig. 3.8 (a). From the fitting parameters, activation energies for hopping (E_a) are found to be 103.85 meV, 95.81 meV and 94.6 meV for x=0, 0.1 and 0.2 respectively. The values of E_a are decreased with increase in x. The lower values of activation energy may be ascribed to the enhancement of hopping of the conduction electrons to neighboring sites due to increase in the hole concentration. From the hopping energy, activation energy to produce hopping sites can be estimated using the equation below:

$$E_a = W_H + \varepsilon_0 \tag{3.4}$$

Here W_H is thermal activation energy to produce sites to facilitate hopping and ε_0 is the activation energy necessary to produce a stationary number of carriers which is obtained from temperature dependence of thermopower. Assuming 6.5 meV [31] for producing charge carriers, polaron activation energy (W_H) is obtained as 97.35 meV, 89.31 meV and 88.10 meV for x=0, 0.1 and 0.2 respectively. A decreasing trend in the W_H values for thermal energy to produce hopping sites is consistent with the creation of Mn^{4+} ions with potassium substitution. The polaron binding energy (E_b) which is twice of W_H, according to Holstein model is estimated to be 194.7 meV, 178.62 meV and 166.2 meV for x=0, 0.1 and 0.2 respectively. Polaron binding energy is decreasing with monovalent potassium ion substitution.

ρ(T) corresponding to x=0.3 could not be fitted well to the adiabatic nearest neighbor hopping model of small polaron equation. Due to randomization of different heterovalent cations on the crystallographic equivalent lattice sites with unequal energies leading to polarons with a complex neighbor sites, small polarons were no longer stable for transport in the lattice. Linear fit to Mott's equation for VRH which is given by:

$$\rho(T) = \rho_0 e^{\left(\frac{T_0}{T}\right)^{1/4}} \quad (3.5)$$

yielded a good fit (inset of Fig. 3.8 (b)). Here T_o is related to localization length (α) and density of states at the Fermi level, $N(E_F)$ by the relation:

$$T_0 = \frac{16\alpha^3}{k_B N(E_F)} \quad (3.6)$$

From the slope of ρ(T) versus $T^{-1/4}$ plot, values for T_o and $N(E_F)$ were calculated to be 1.6×10^7 K and 6.4×10^{22} states/eV cm^3 assuming the localization length (α) to be Mn-Mn distance as reported by Palstra et.al., [32] for similar materials. The above resistivity analysis showed a different transport behavior with high concentration of tetravalent manganese ions as compared to other compounds with high concentration of trivalent manganese ions.

3.3.6. Magnetic studies

Temperature dependent molar susceptibility in the Zero Field Cooled (χ_{ZFC}) and Field Cooled (χ_{FC}) protocols for all the materials was measured under several external magnetic fields. Representative graphs for the temperature dependence of both χ_{ZFC} and χ_{FC} for DKMO are presented in Figs. 3.9 (a) to (d). While the data of χ_{ZFC} (T) for x=0.0 to 0.2 merge with χ_{FC} (T) data in a wide temperature range, for the high potassium content, x=0.3, χ_{ZFC} (T) data measured under low fields (50 to 500 Oe) show a sharp peak below which χ_{ZFC} and χ_{FC} curves bifurcate with χ_{FC} increasing sharply with decreasing temperature whereas χ_{ZFC} curves show a downturn. Nevertheless, for higher magnetic fields, χ_{FC} (T) matches with that of χ_{ZFC} (T).

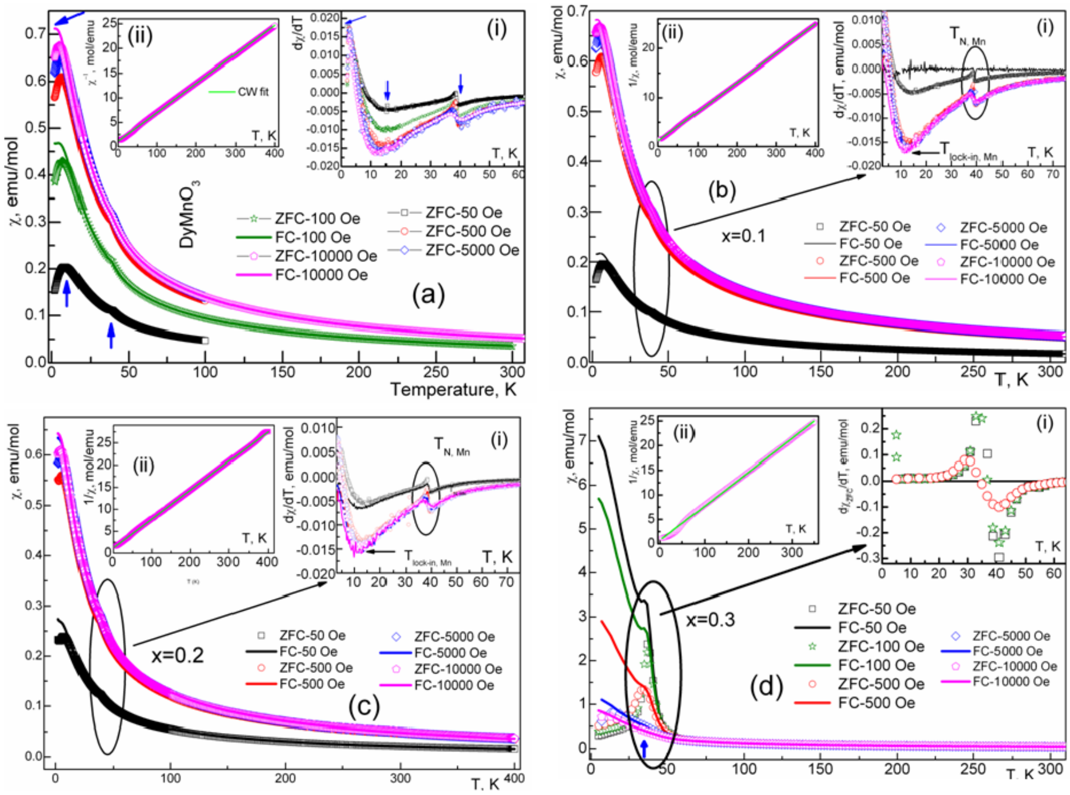

Figure 3.9. Magnetization versus temperature measured in ZFC and FC cycles under various applied magnetic fields for x=0.0 (a), x=0.1, (b) x=0.2 (c) and x=0.3 (d) in $Dy_{1-x}K_xMnO_3$. Inset (i) shows a plot of first derivative susceptibility with respect to temperature depicting the magnetic transitions explained in the text. Inset (ii) shows CW fit (solid line) to FC magnetization data (symbols) measured at 1 Tesla field.

All the compounds essentially showed a paramagnetic behavior with temperature down to ~50 K below which different kinds of transitions are found. Moreover, with increasing x, the high temperature anomalies remain the same while the low temperature anomaly shifts to still lower temperatures. Before we discuss the effects of substitution on the magnetic properties of DKMO, let us first identify the origin for the features exhibited by the pristine compound, DMO by comparing with the previous reported results [33]. The molar susceptibility of DMO is characterized by a small kink, a broad peak and an upward increase with respect to temperature which are indicated by arrow marks in Fig. 3.9 (a). The temperatures involving these apparent magnetization changes are estimated from a plot of first derivative of the susceptibility with temperature as depicted in the inset (i) of Fig. 3.9 (a). Neutron diffraction studies by Kimura et al. [33] on DMO revealed three types of magnetic transitions at ~39 K, 18 K and < 10 K involving manganese ions and Dy ions respectively. They have attributed the transition at 39 K to a sinusoidal antiferromagnetic ordering of Mn ions, T_N (Mn) where magnetic wave vector is incommensurate with the atomic displacement vector. With further reduction in the temperature, the magnetic modulation wave vector reaches a constant value for temperatures below 18 K. This transition temperature is ascribed to an incommensurate to commensurate transition where manganese ions are locked so it is termed as lock-in transition of manganese ions, $T_{lock-in}$ (Mn). Finally the rare earth ions (Dy) undergo antiferromagnetic ordering, T_N (Dy) at low temperatures (< 10 K). All the transitions observed in our parent $DyMnO_3$ [34] that are illustrated in the inset (i) of Fig. 3.9 (a) are in good agreement with the neutron scattering observations reported by Kimura et al. [33] and magnetization results reported by Harikrishnan et al. [35]. It is to be noted that the long range antiferromagnetic ordering of layer type (A type AFM) among manganese spins observed in the prototype colossal magneto resistance material, $LaMnO_3$ at around 140 K [36] has been shifted to 40 K in $DyMnO_3$. The reduction in the Neel temperature of Mn ions was because of the buckling of Mn-O-Mn bond caused due to the lattice distortions when the larger La ions were replaced by smaller Dy ions. This resulted in the weaker exchange interactions between Mn ions. Interestingly, similar features were observed in the magnetization data of the substituted samples also, Figs. 3.9 (b) to (d). Nevertheless, the compound corresponding to x=0.3 showed a prominent single peak in χ_{ZFC} data measured at low applied magnetic fields with χ_{FC} rising at low temperatures. The appearance of peak corresponds to T_N (Mn). Moreover, the irreversibility between χ_{ZFC} and χ_{FC} curves is more for this compound. Such irreversibility in the magnetization data measured under ZFC and FC protocols does not signify any long range magnetic ordering transition and rather is a feature of spin-glass-like state. On increasing the applied magnetic field, this peak shifted to lower temperatures and is broadened (Fig. 3.9 (d)).

As discussed earlier, in this compound, concentration of Mn^{4+} ions is more than that of Mn^{3+} ion concentration. Antiferromagnetic super exchange coupling between JT active Mn^{3+} ions is weaker as compared to inactive JT Mn^{4+}-Mn^{4+} ions. This is because, nature of the super exchange coupling between Mn^{3+} ions depends on the orientation of 3d orbitals of the Mn^{3+} ions in addition to the angle between the two manganese spins whereas, the SE coupling between Mn^{4+} ions depends on the angle between their spins. Thus the strength of exchange interactions between Mn^{4+}-Mn^{4+} are larger as compared to that between Mn^{3+}-Mn^{3+} ions. The values of ordering temperatures determined from the derivative curves shown in insets of the respective plots in Fig. 3.10 for x=0.0 and 0.3 are presented in Table 3.6.

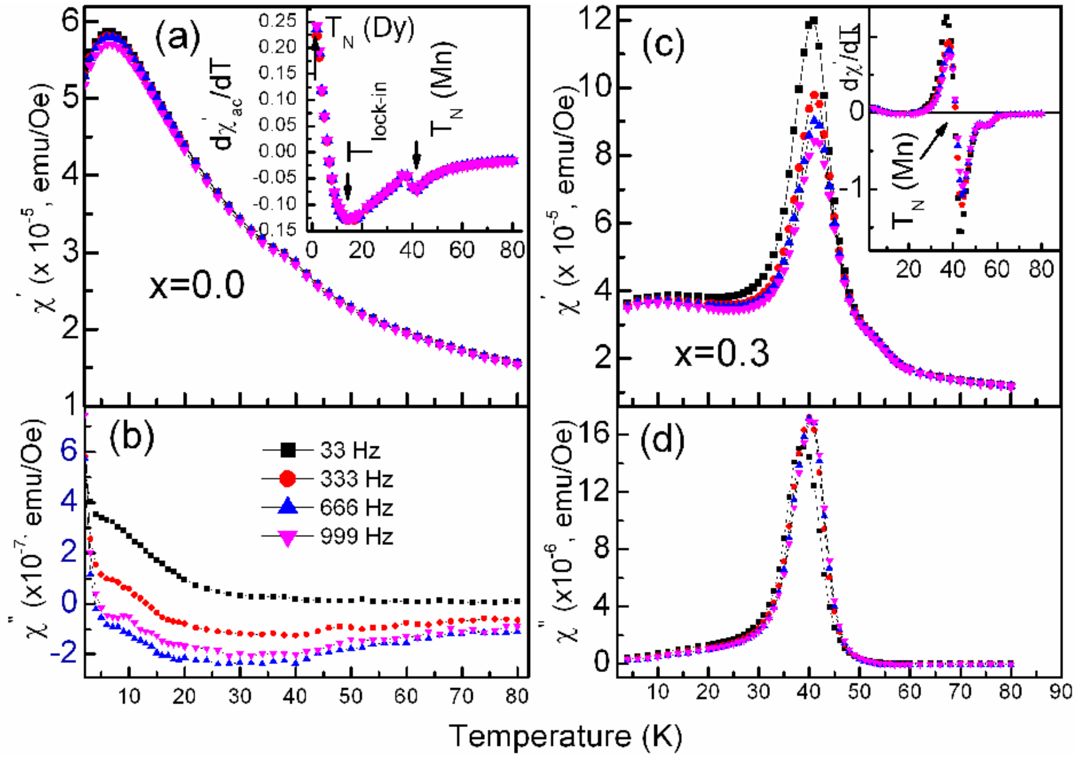

Figure 3.10. (a) Real (χ') and (b) imaginary (χ'') parts of ac susceptibility of DMO and (c) and (d) for x=0.3 as a function of temperature measured at four frequencies of 33, 333, 666 and 999 Hz. The temperatures corresponding to the magnetic transitions explained in the text are marked by arrows in the dχ'/dT versus T plots shown in insets of the upper panel of (a) for DMO (c) for x=0.3.

Table 3.6. Derived parameters from CW fit and M-H loops for $Dy_{1-x}K_xMnO_3$ are tabulated. The transition temperatures correspond to inflection points observed in dχ_{FC}/dT curve at 1 Tesla. Values of Coercive field (H_c) and remnant magnetic moment (M_r) are obtained from hysteresis loops registered at 2.2 K. M_{5T} corresponds to the magnetic moment value measured at 5 T external magnetic field.

x	Temperature (K)				$\mu_{eff.}$ (μ_B)		H_c (Oe)	M (μ_B/f.u.)	
	From dχ/dT curve			CW fit	Expt.	Cal.			
	T_N (Mn)	$T_{lock-in}$ (Mn)	T_N (Dy)	θ				M_r	M_{5T}
0.0	39	12	3.6	-23	11.66	11.69	1520	0.174	4.75
0.1	39	12	3.2	-19	11.59	10.34	700	0.105	4.33
0.2	39	12	3.5	-20	11.08	10.05	980	0.140	3.84
0.3	42	-	-	-18	10.90	9.75	7575	0.75	3.08

Above T_N (Mn), the susceptibility data followed a Curie-Weiss (CW) behavior given below:

$$\chi = \frac{C}{T+\theta} \tag{3.7}$$

Here C is a Curie constant, θ is a Curie-Weiss temperature and T is the measurement temperature. Linear fits to CW law are shown in the respective insets (ii) in Figs. 3.9 (a) to (d). A linear fit to inverse susceptibility data of all the compounds measured at different fields showed an increase in the effective magnetic moment with the increase in the applied magnetic field. For example, for x=0.0, the effective magnetic moment increased from 9.62 μ_B to 11.66 μ_B for the data collected at 100 Oe and 1 T respectively. High field magnetic moment is close to the moment calculated by considering the individual moments of Dy^{3+} and Mn^{3+}. The effective moment value of 11.66 μ_B determined from the fitting the χ(T) data at 1 T field agrees well with the calculated value of 11.69 μ_B by considering Dy^{3+} and Mn^{3+} moments alone. For low applied magnetic fields, existence of antiferromagnetic correlations among magnetic ions cancels the moments leading to reduction in the observed magnetic moment values. Effective magnetic moments ($\mu_{eff.}$) obtained from the fit of the inverse χ_{FC}(T) data (at 1 T) to CW law for all the compounds are included in the Table 3.6. The values of μ_{eff} decrease with increasing x and vary from 11.66 μ_B to 10.90 μ_B. The negative sign of the CW temperatures (θ) suggested that the exchange interactions are antiferromagnetic in nature supporting the observations in the magnetization data. Calculated effective magnetic moment ($\mu_{eff,}$ (cal.)) is estimated from the following expression by considering the fraction of magnetic ions present in the chemical formula of the compounds:

$$\mu_{\text{eff.}}(\text{cal.}) = \sqrt{(1-x)\mu^2_{Dy^{3+}} + x\mu^2_{Mn^{3+}} + 2x\mu^2_{Mn^{4+}}} \qquad (3.8)$$

where x = potassium concentration, $\mu_{Dy^{3+}}$, $\mu_{Mn^{3+}}$ and $\mu_{Mn^{4+}}$ are free ion magnetic moments of Dy^{3+} (10.62 μ_B), Mn^{3+} (4.89 μ_B) and Mn^{4+} (3.87 μ_B) ions respectively. The calculated values of $\mu_{\text{eff,}}$ (cal.) are also included in the same table for comparison. The experimental effective magnetic moments are higher than the calculated values except for DMO, point to the presence of ferromagnetic correlations between magnetic spins. This fact is evidenced by the observation of hysteresis loops shown in Fig. 3.11.

Generally, the processes involved in the irreversibility of ZFC and FC curves arise from the complex interplay between strong magnetic ion interactions. In order to probe the dynamics of such interacting systems, the ac magnetic susceptibility has been studied in the temperature range of 2 K to 100 K and in the frequency range of 33 Hz to 999 Hz. External ac fields of 1 Oe and 5 Oe amplitude with a zero dc bias field was applied to study the dynamic behavior of the compounds. Susceptibility was found to be independent of ac field and henceforth all our analysis was carried on the ac χ (T) data recorded at 1 Oe field. Figure 3.10 demonstrate the behavior of the real, χ' and imaginary, χ'' parts of ac susceptibility with temperature for the parent compound, DMO and for x=0.3. χ' (T) of DMO exhibits a broad peak at a low temperature. The frequency dependent χ' (T) collapses into a single curve where the temperature of the broad peak is nearly independent of the frequency thereby ruling out the possibility of spin glass state in the case of the parent compound. χ' (T) curve resembles that of dc susceptibility curve χ (T) with similar features. Plots of the first derivative of χ' with respect to temperature shown in inset of Fig. 3.10 (a) reveals the magnetic transitions and are in supportive of dc magnetization data. However, magnitude of the peak observed for x=0.3 decreased slightly for higher frequencies; nevertheless the peak temperature remains almost the same implying the absence of spin glass.

Isothermal magnetization as a function of applied magnetic fields at the lowest temperature (~2 K) for all the compounds is presented in Fig. 3.11. M-H curves measured for temperatures below the ordering temperature of manganese ions (40 K) show hysteresis loops whose area increases with decreasing temperature implying the presence of ferromagnetic interactions.

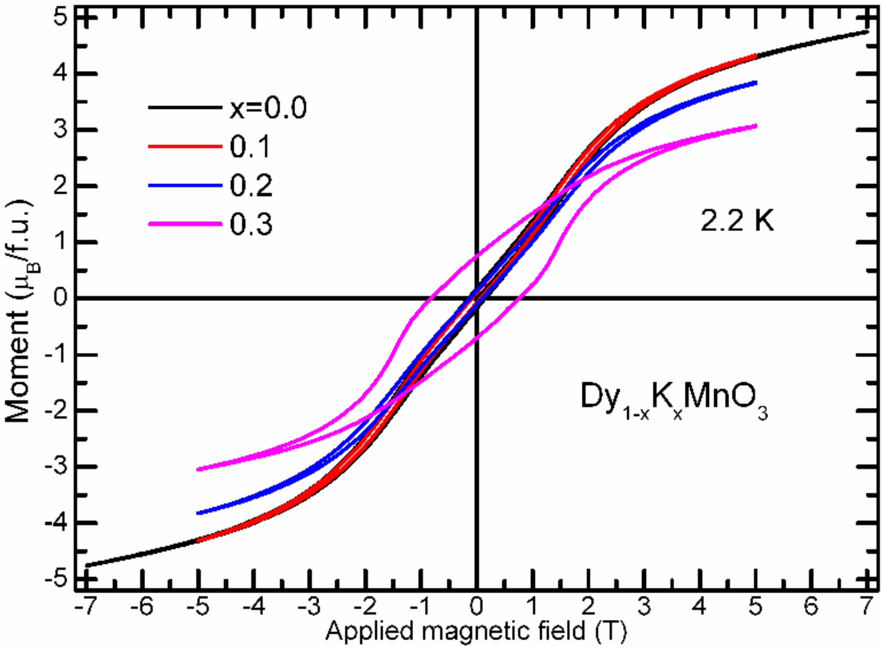

Figure 3.11. Hysteresis loops recorded at 2.2 K in fields from -7 to +7 Tesla for DKMO. It is remarkable to see large coercive field for x=0.3 as compared to other compounds.

However, the magnetization of the compounds did not saturate even at 7 T field indicating that there is no long range ferromagnetic order in the magnetic structure. M-H curves are linear for temperatures above 40 K signifying the random distribution of magnetic spins leading to paramagnetic state. Several parameters such as coercive field (H_c), remnant magnetization (M_r) and magnetization at an applied magnetic field of 5 T (M_{5T}) obtained from M-H curves are tabulated in Table 3.6.

Large values of the coercive field imply the existence of ferromagnetic interactions between the magnetic ions. Thus magnetization curves are superposition of both the antiferromagnetic and ferromagnetic contributions arising from a canted spin state. Spin moment arrangements between rare earth ions and transition metal ions were also found in $Nd_{1-x}Y_xMnO_3$ [37]. Hemberger et al. [38] explained the temperature dependence of magnetization data of $La_{1-x}Gd_xMnO_3$ based on the canting of manganese spins.

3.3.7. Dielectrics Properties

Variation of dielectric constant (ε') and dielectric loss (ε") of the complex dielectric permittivity ($\varepsilon^* = \varepsilon' + i\varepsilon''$) for x=0.1 and x=0.2 in $Dy_{1-x}K_xMnO_3$ with the frequency of the applied electric field measured at different temperatures are presented in Figs. 3.12 (a), (b) and (c), (d) respectively. Values of ε' and ε" are high in the low frequency range and this value is decreasing with increasing frequency. The high dielectric constant in low frequency region may be associated with the electrode polarization where charge carriers are blocked at the sample/electrode interface leading to a separation of positive and negative charges which gives rise to additional polarization. This large electrode polarization or charge build up as a function of frequency gives rise to dielectric dispersion which is also known as Maxwell-Wagner polarization [39-41]. As frequency increases dielectric constant decreases on account of the fact that space charge accumulation is insignificant between the sample and electrodes. At high frequencies, dipoles cannot follow the applied electric field and the dielectric constant becomes independent of the frequency. As the temperature increases, the dielectric constant and loss increase due to thermally activated charge carriers.

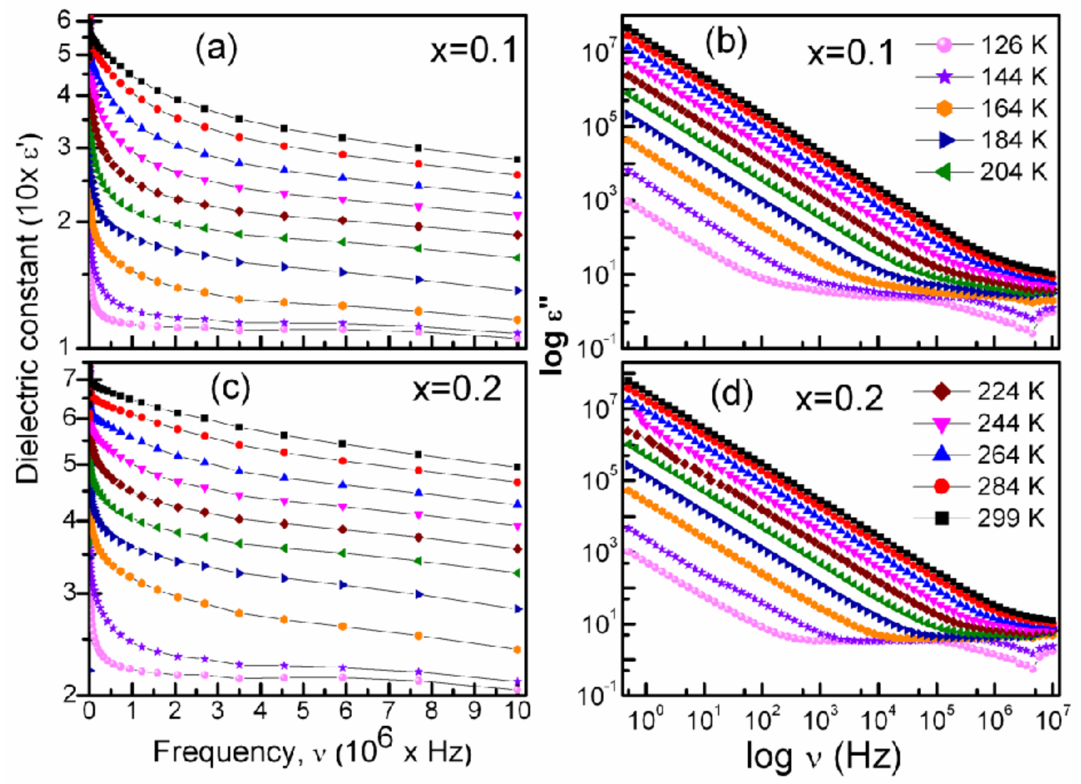

Figure 3.12. (a) and (c) display frequency dependence of dielectric constant (ε') for x=0.1 and x=0.2 and (b) and (d) show dielectric loss (ε'') with respect to the frequency for x=0.1 and x=0.2 of $Dy_{1-x}K_xMnO_3$ respectively in the temperature range 126-299 K.

Figure 3.13 (a) & (b) show a log-log plot of variation of ac conductivity (σ′) with respect to frequency for x= 0.1 an x= 0.2 at several fixed temperatures. It is to be noted that all the curves show similar behavior. The isotherms display the following features: (1) by considering conductivity isotherm at 126 K, it is observed that σ′ is frequency independent in the low frequency range (0.5 Hz – 100 Hz) and is attributed to dc conductivity (σ_{dc}); (2) as frequency increases, σ′ also increases with frequency; (3) when the temperature is increased, σ_{dc} increases in the low frequency region and then increases with increasing frequency following a power law [42]. (4) the curves show dispersion at low frequency range and merge at high frequencies as the temperature of the isotherm increases; However, the crossover regime from σ_{dc} to high frequency conductivity occurs at higher frequencies; and (5) at lower temperatures, there is an additional contribution to conductivity which increases at high frequencies. The frequency dependent conductivity reveals hopping conduction process.

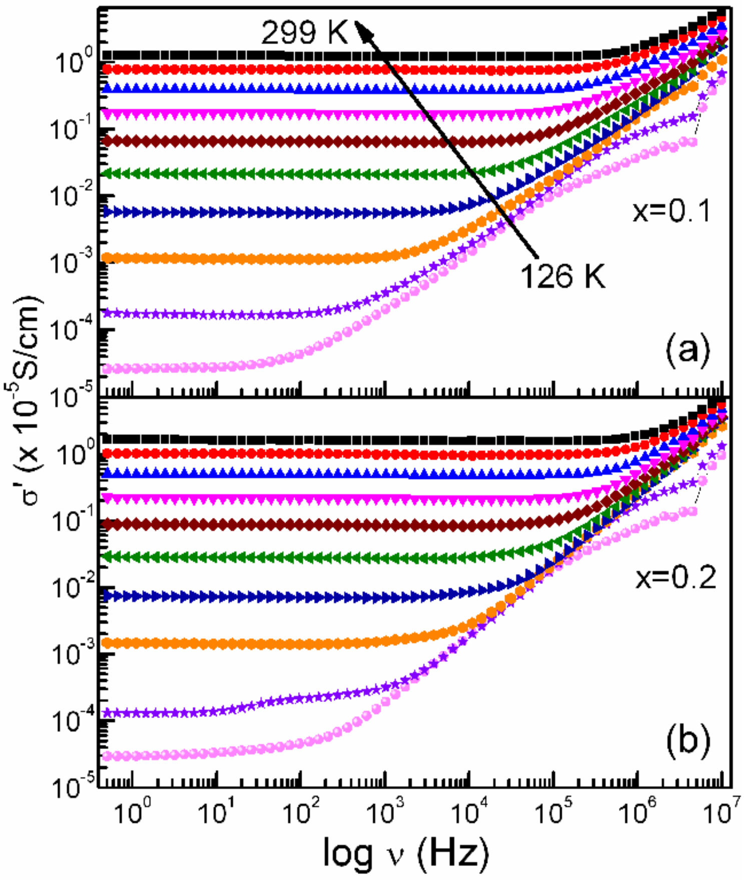

Figure 3.13 Variation of real part (σ') of the complex conductivity, σ^* with frequency of the applied electric field for (a) x=0.1 and (b) x=0.2 in $Dy_{1-x}K_xMnO_3$. The arrow indicates increasing temperature.

The reciprocal of the permittivity gives complex electrical modulus: M^* (= M'+iM") = $1/\varepsilon^*$ which corresponds to the relaxation of the electric field. The spectra of $M^*(\nu)$ represent the bulk electrical properties of materials. Figure 3.14 illustrate the frequency dependent behavior of (a) real (M') and (b) imaginary (M") parts of complex modulus (M^*) measured at different temperatures for x=0.1. The conductivity relaxation manifests as a peak in the imaginary part of the modulus spectra, (M"(ν)).

M′ increases with increase in the frequency and decreases with increase in temperature. Thus there is dispersion in M′(ν) curves at all the frequencies.

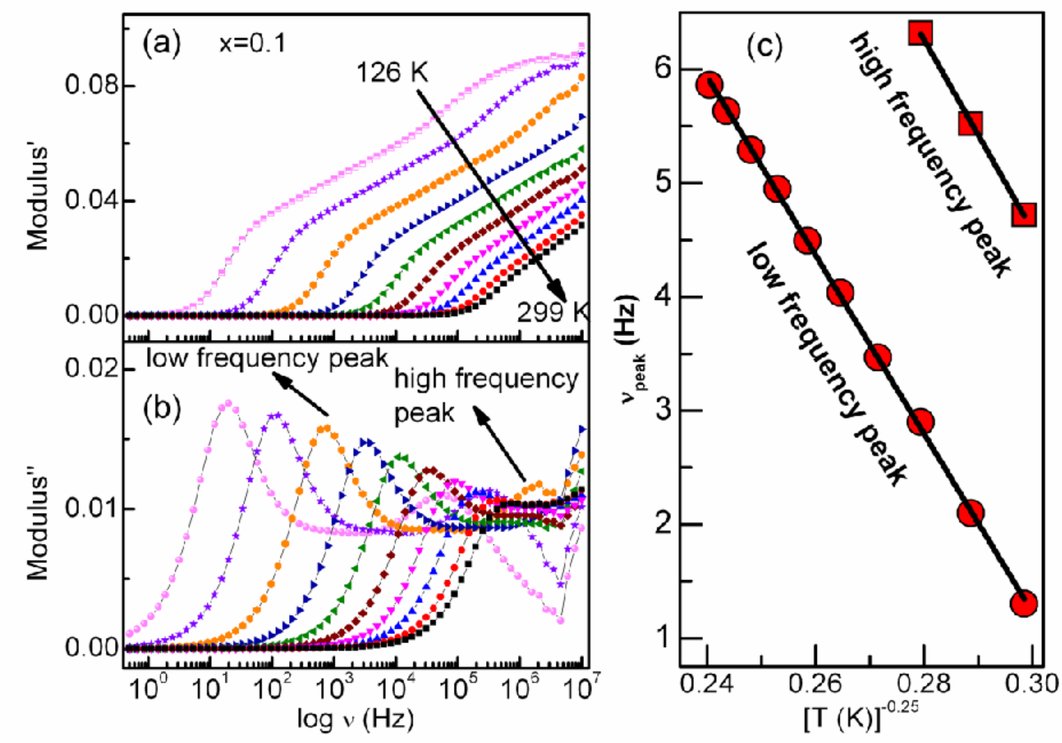

Figure 3.14 Frequency dependence of (a) real (Modulus′) and (b) imaginary (Modulus″) parts of complex modulus (M^*) for $Dy_{0.9}K_{0.1}MnO_3$ in the studied temperature range between 126 and 299 K. (c) Linear fit to peak frequencies according to VRH conduction mechanism given by equation (3.9).

As observed from the Fig. 3.14 (b), M″(ν) at 126 K exhibits an asymmetric peak (ν_{peak}) at low frequency. With increase in the temperature of the measurement, the ν_{peak} shifts to higher frequencies whose asymmetry increases. Grains and grain boundaries present in the polycrystalline materials respond to external frequencies culminating into slope changes in M′ vs. frequency spectra (Fig. 3.14 (a)) and the corresponding to these slope changes, there appears peaks in the imaginary part of the modulus (M″(ν)) spectra shown in Fig. 3.14 (b) whose peak frequencies shift to higher values as temperature of the measurement increases. In the low temperatures (126 K, 144 K and 164 K), double peaks appear in the M″(ν) spectra at low and high frequencies and at high temperatures (T ≥ 184K), M"(ν) spectra display only a single peak. As the temperature increases there is a gradual decrease in the height of the peaks and the peak frequencies shift to high frequencies as well. Low frequency peak is attributed to dielectric relaxations while the second peak at high frequency arises from conduction type relaxations in materials [43]. However, the peaks are broad due to short time dynamic behavior of charge carriers. The peak frequency (ν_{peak}) is plotted against temperature as shown in Fig. 3.14 (c). The peak frequency follows the variable range hopping conduction behavior [44],

$$f = f_0 e^{\left(\frac{T_0}{T}\right)^{1/4}} \tag{3.9}$$

where f_0 is the pre-exponential factor and T_0 is a constant given by equation (3.6). Using the following Mott's equations, hopping energy (W) and hopping range (R) for the hopping conduction are calculated:

$$W = 0.25 k_B T_0^{1/4} T^{3/4} \tag{3.10}$$

$$R = \frac{a}{3}\left(\frac{T_0}{T}\right)^{1/4} \tag{3.11}$$

Here T is the measurement temperature, a is the minimum distance between Mn ions in the unit cell. By substituting value of T_0 in the equations (3.10) and (3.11), hopping energies and hopping ranges at various temperatures are obtained. Hopping energies are found to increase with increase in the temperature and hopping distances decrease with increase in the temperature. Following similar analysis, W and R for x=0.2 are calculated from the modulus spectra shown in Fig. 3.15. Values of W and R for both the compounds are tabulated in Table 3.7.

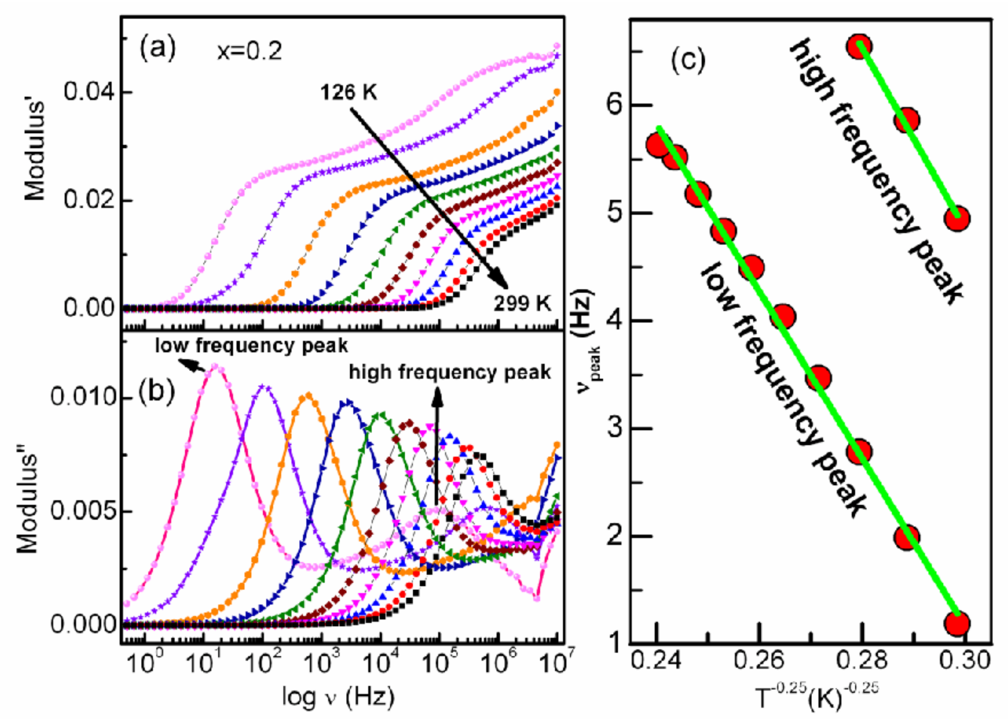

Figure 3.15. Frequency dependence of (a) real (Modulus′) and (b) imaginary (Modulus") parts of complex modulus (M^*) for $Dy_{0.8}K_{0.2}MnO_3$ in the studied temperature range between 126 and 299 K. (c) Linear fit of maximum frequencies to VRH behavior.

Table 3.7. Hopping energies and hopping distances calculated from for polarons from VRH analysis of modulus and impedance spectra of $Dy_{1-x}K_xMnO_3$.

x	Hopping energy (meV) T : 126 K - 299 K			Hopping range (Å) T : 126 K - 299 K		
	Modulus		Impe.	Modulus		Impe.
	Low frequency peak	High frequency peak (126 K – 164 K)		Low frequency peak	High frequency peak (126 K – 164 K)	
0.1	64 - 122	68 - 83	62 - 119	31 - 25	33 - 31	30 - 24
0.2	63 - 120	68 - 83	64 - 122	30 - 24	33 - 31	31 - 25

Figure 3.16 presents complex modulus plots at all the measured temperatures for (a) x=0.0 and (b) x=0.2. Two semicircles of unequal size are observed for lower temperatures (<184 K) and a single peak for high temperatures (> 164 K). Different capacitances corresponding to grain and grain boundaries give rise to the semicircles. Frequency dependent behavior of the real part Z′ of complex impedance Z^*(=Z′+iZ")

in the temperature 126-299 K is shown in Fig. 3.17 (a) and (b) for x=0.1 and x=0.2. It was found from the graph that the Z'(Ω) which is independent in the low frequency range decreases with increase in the frequency and also decrease with increase in the temperature. The decrease in Z' with temperature indicates a rise in the conductivity. Morever, Z'(T) merged in the high frequency region resulting from the increase in the conductivity. This observed sudden increase in Z'(ν) with decrease in frequency that occurs at different frequencies depending on the temperature indicates relaxation behavior [45]. This manifests as a maximum peak in Z"(ν) spectra and Fig. 3.18 demonstrates this behavior.

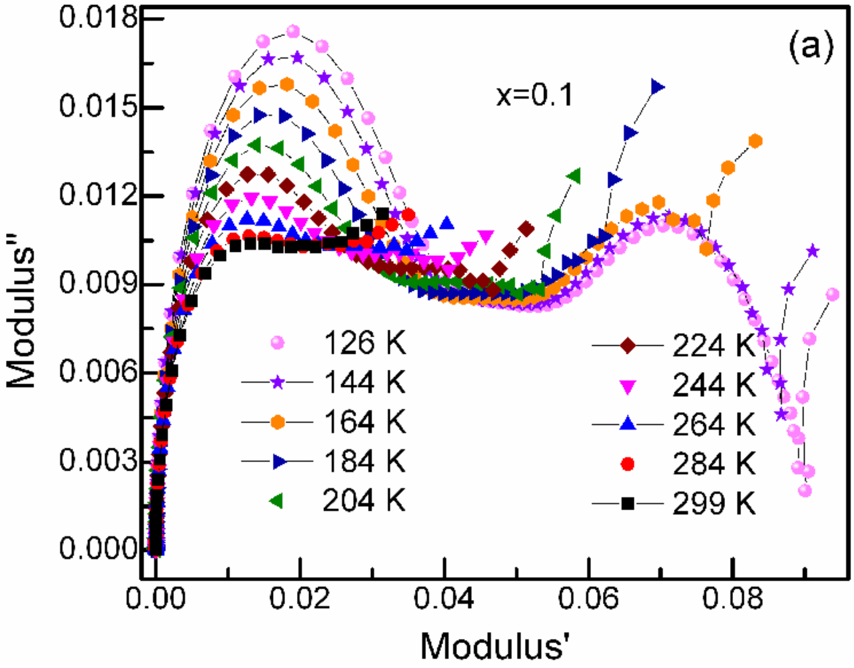

Figure 3.16. Continued.

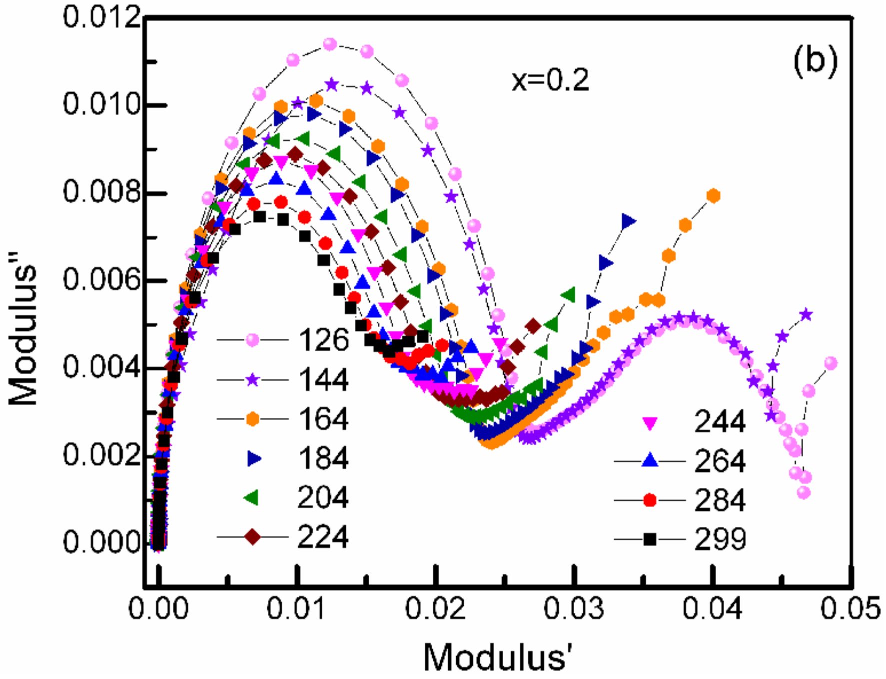

Figure 3.16. Cole-Cole plots for (a) $Dy_{0.9}K_{0.1}MnO_3$ and (b) $Dy_{0.8}K_{0.2}MnO_3$ in the studied temperature range between 126 and 299 K.

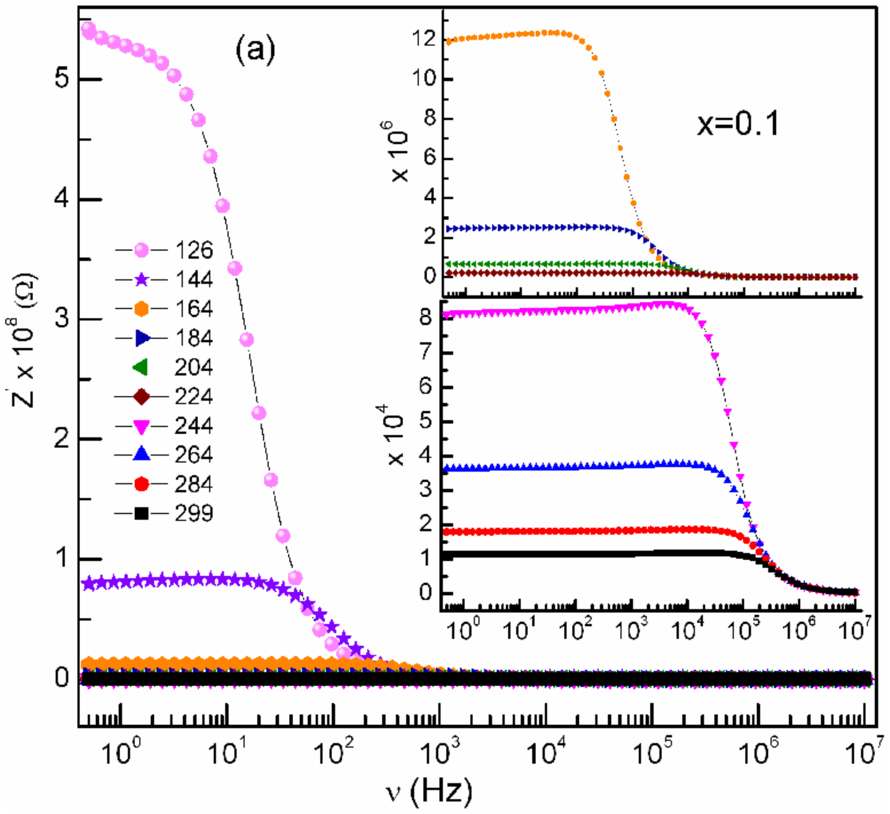

Figure 3.17. Continued.

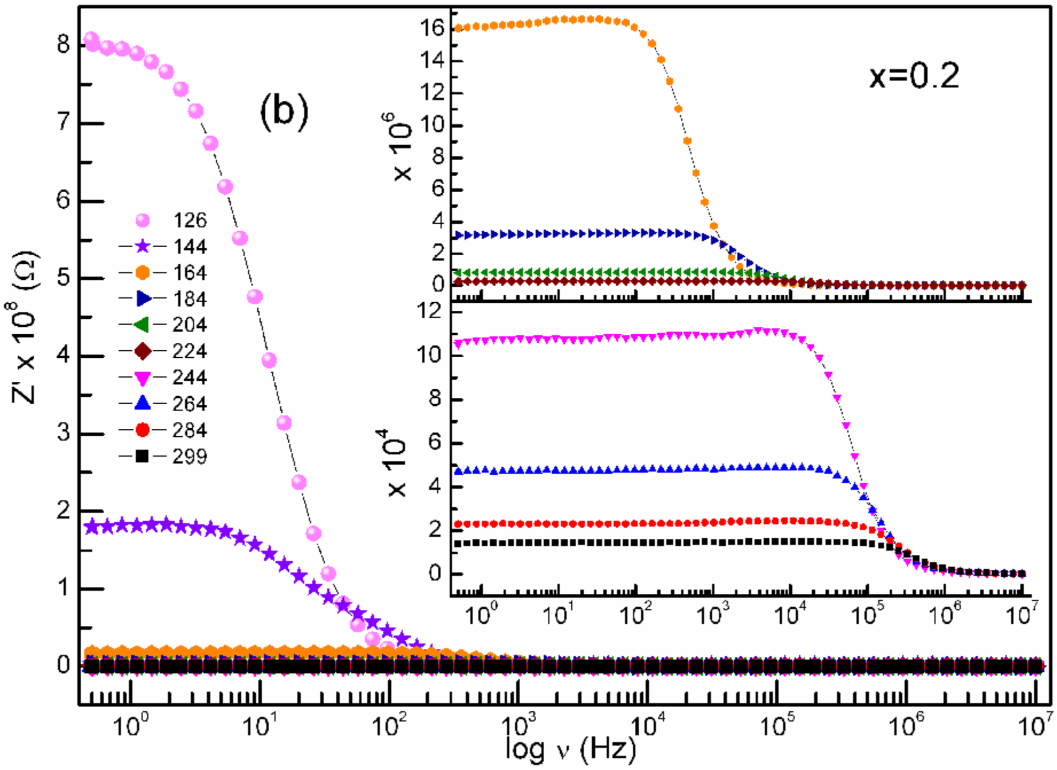

Figure 3.17. (a) Real component of impedance against frequency at different temperatures for (a) x=0.1 and (b) x=0.2.

Figure 3.18 (a-d) shows the imaginary part of impedance Z"(Ω) versus frequency for x=0.1 at different temperatures as mentioned in the respective panels. It is observed that the peak is shifted gradually towards the high frequency with increasing temperature implying that relaxation processes depend on the thermal energy. The frequency corresponding to the maximum value of Z" was found to follow VRH conduction mechanism. Hopping energies for the conduction are calculated from the eq. (3.10) and from T_o values obtained by fitting the peak frequency (ν_{peak}) as per VRH behavior as shown in Fig. 3.18 (e). By performing similar analysis for x=0.2 whose spectra are displayed in Fig. 3.19 (a-e), the hopping energies and hopping distances are calculated and are included in the Table 3.7.

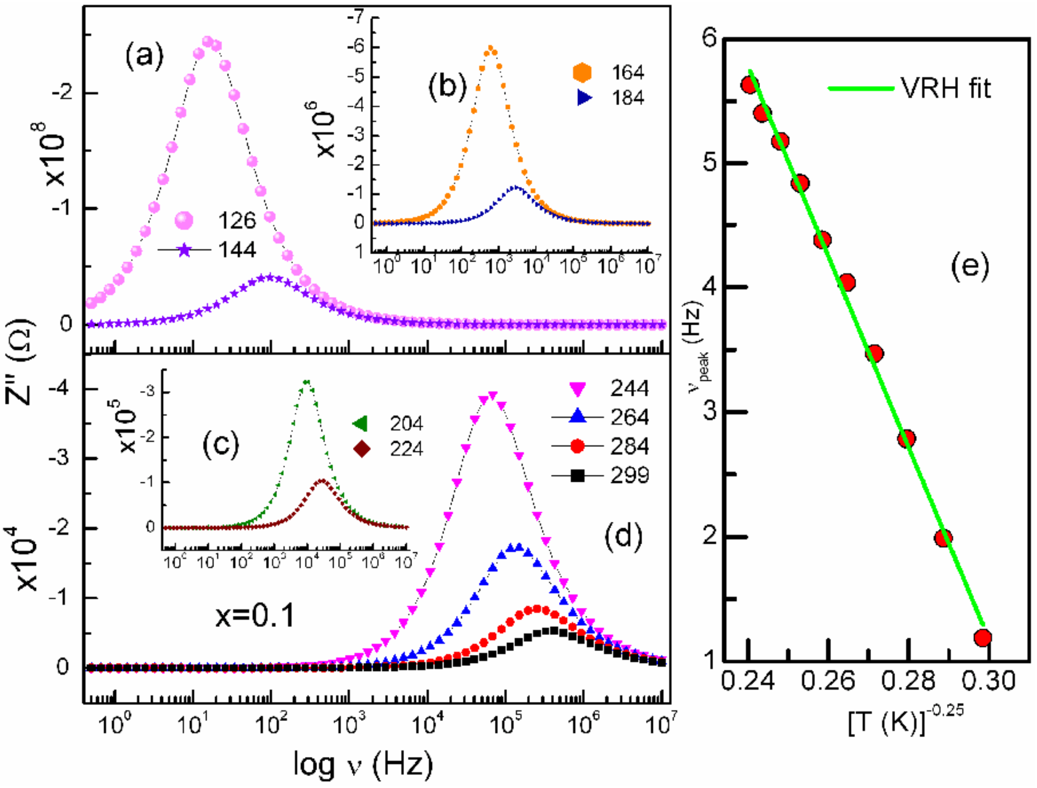

Figure 3.18. (a-d) display frequency dependence of imaginary part of impedance (Z''(Ω)), (e) shows peak frequency versus temperature with VRH fitting for $Dy_{0.9}K_{0.1}MnO_3$.

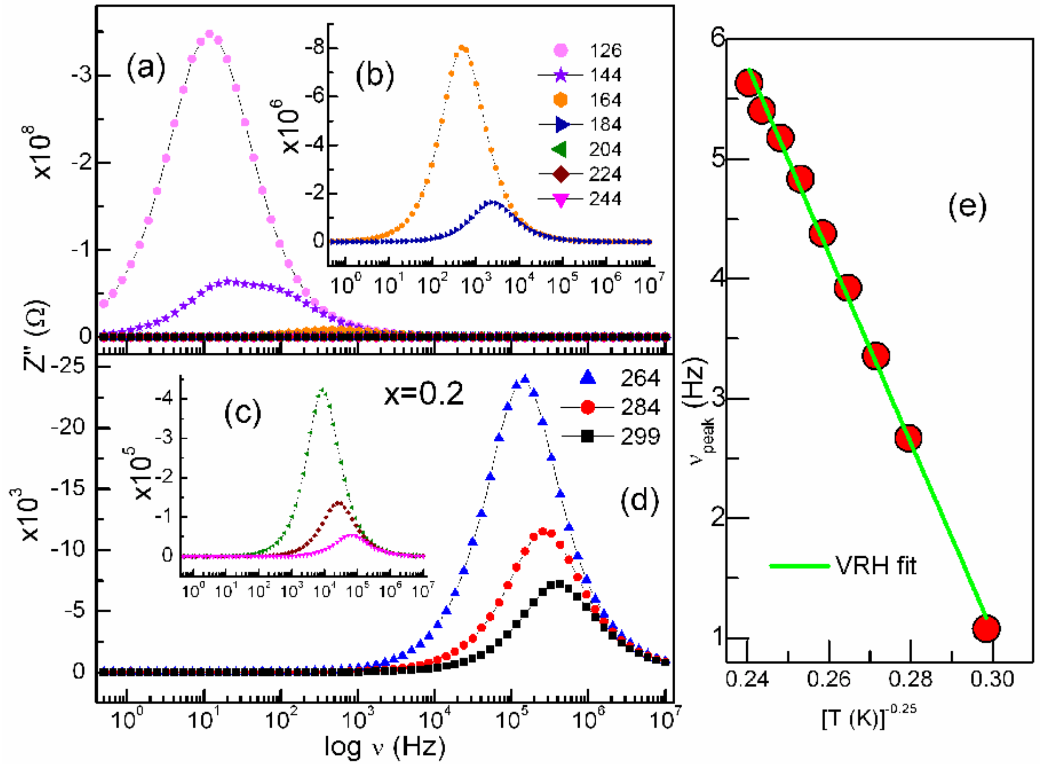

Figure 3.19. (a-d) display frequency dependence of imaginary part of impedance (Z''(Ω)), (e) shows peak frequency versus temperature with VRH fitting for $Dy_{0.8}K_{0.2}MnO_3$.

Figure 3.20 indicates imaginary part of impedance, Z''(Ω) versus real part of impedance, Z′(Ω) (referred to as Cole-Cole plots or Nyquist plots) measured at different temperatures for x=0.1. All the plots contain a single semicircle whose centre lies below the Z' axis revealing the non-Debye type relaxations. For clarity, Nyquist plots are shown in separate panels. Radii of all the semicircles decrease as temperature increases showing semiconducting nature. The decrease in the impedance is attributed to the thermally activated conduction mechanism.

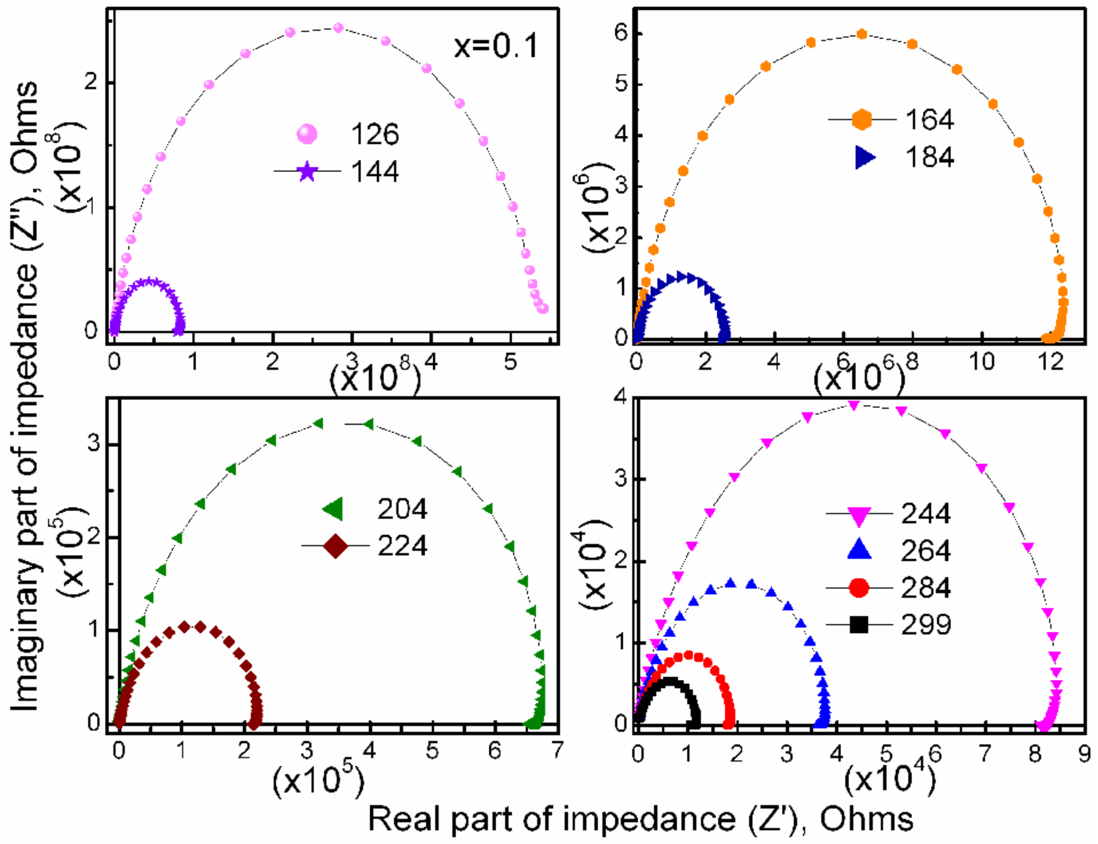

Figure 3.20. Nyquist plots for x=0.1 at fixed temperatures.

Fig. 3.21 illustrates Nyquist plots for x=0.2. In contrast to complex plots of x=0.1, the shape of the plots changed from semi-circular to skewed arc shaped curves at high temperatures (284 K and 299 K) signifying different relaxation mechanisms operating in the frequency range studied. In general, in the polycrystalline materials, it is known that grains and grain boundaries contribute to conductivities depending on

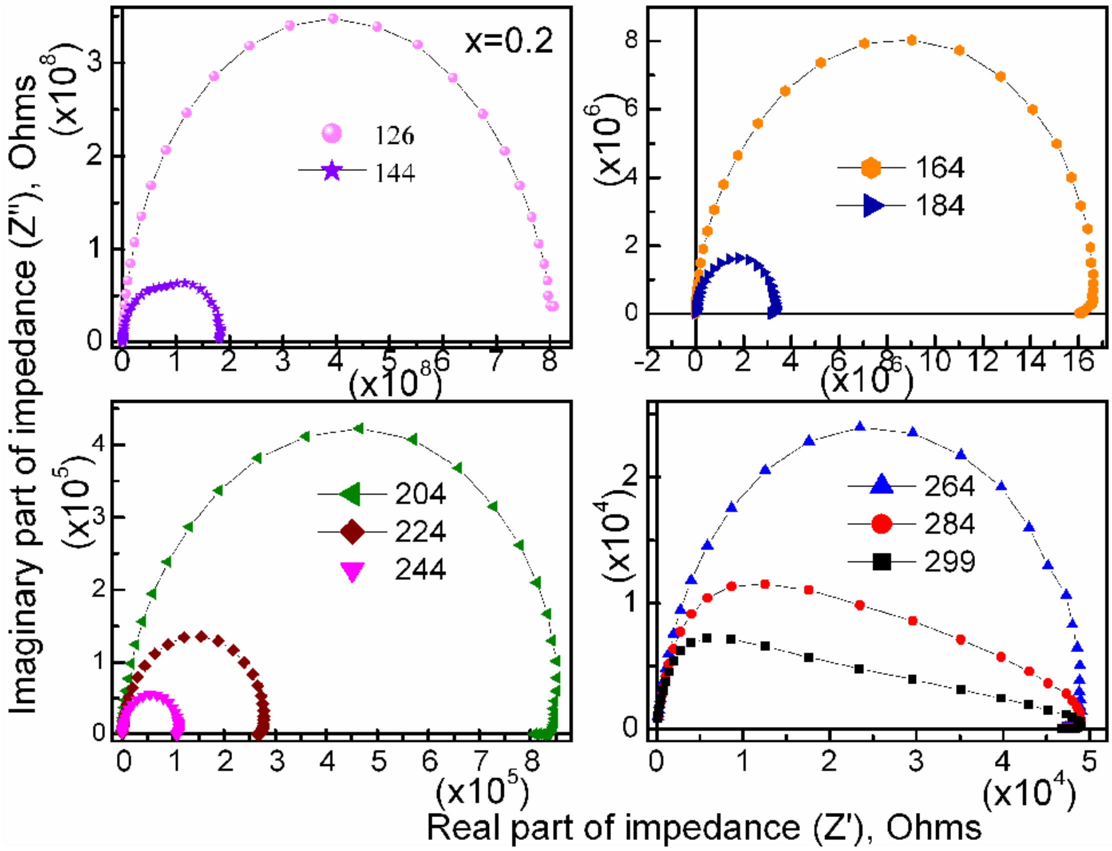

Figure 3.21. Nyquist plots for x=0.2 at fixed temperatures as mentioned in the respective graphs.

the external temperature. Grain and grain boundary contributions to conductivity could be obtained by fitting Nyquist plots to an equivalent circuit consisting of resistance and capacitance elements using EIS software. An R-C parallel equivalent circuit shown in Fig. 3.22 (a) yielded a semicircle in the complex plane is used to model the Nyquist plots. While some of the fitted complex plots measured at low temperatures (126 K to 204 K) match with the experimental data well in the whole impedance range, plots measured at temperatures above 204 K showed deviations at low frequency range on the real axis.

Figure 3.22 (b) shows a representative plot of fitted and simulated impedance spectra along with the experimental data collected at 126 K for x=0.1. From the matched plots, values of the grain and grain boundary resistances were obtained. The resistance of grains (R_g) was found to be lower than that of grain boundary resistance (R_{gb}). Both resistance values decrease with increase in temperature. On account of the deviations, the analysis of the plots requires a more detailed analysis to get quantitative information.

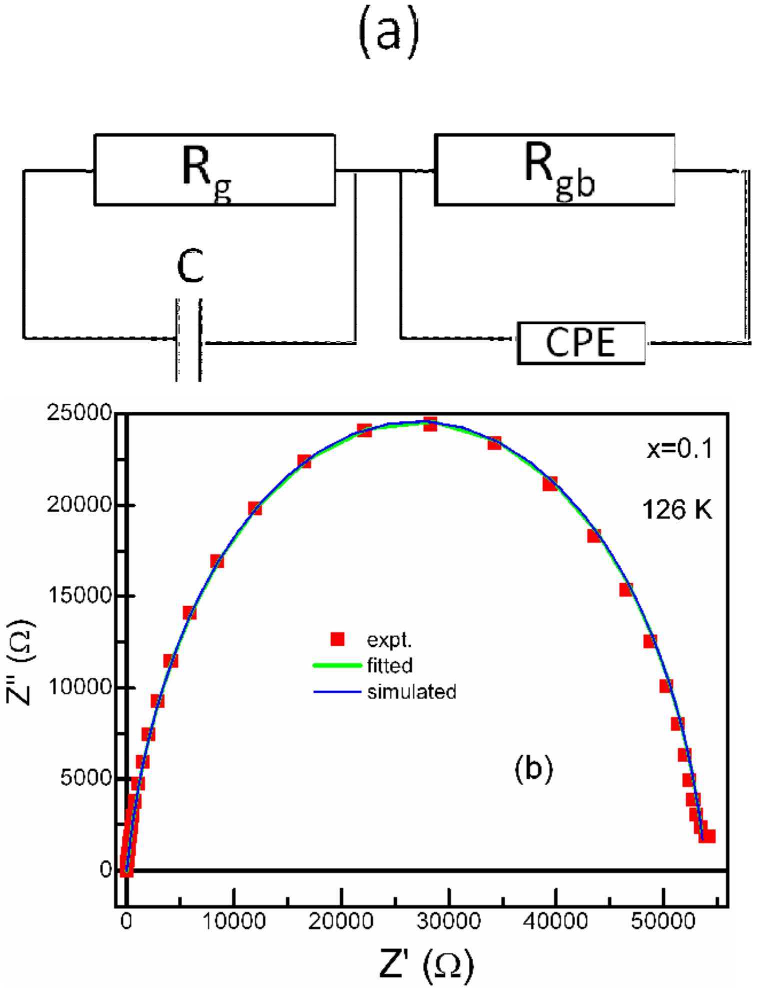

Figure 3.22. (a) Circuit diagram used for fitting the complex impedance data for x=0.1. (b) Cole-Cole plot at 126 K along with fitted and simulated curves using EIS software.

3.4. CONCLUSIONS and SUMMARY

The polycrystalline compounds of $Dy_{1-x}K_xMnO_3$ (x=0.0 - 0.3: 0.1) were synthesized using the conventional solid state reaction route. Rietveld analysis confirmed the single phase formation in orthorhombic structure with Pnma space group. Structural distortions in $DyMnO_3$ resemble that of $GdFeO_3$-type structure. These distortions were caused due to the presence of smaller Dy ion and active JT Mn^{3+} ions. Although ionic size of K is larger than Dy, for each potassium substitution, two tetravalent manganese ions (whose ionic size is smaller than Mn^{3+}) are generated for charge compensation. As a consequence, unit cell volume decreases with increasing x. Furthermore, concentration of JT ions reduces with increasing K, leading to a reduction in octahedral bond deformations. This was evident from a comparison of equatorial and axial bond lengths of Mn-O octahedra in the case of x=0.3. Moreover, decoupling of some of the Raman bands corroborates this conclusion. Raman band frequencies increase with potassium substitution which involves stretching vibrations of Dy-O, Mn-O-Mn bending and octahedral tilts. EDX analysis reveals that the cationic composition of the compounds is close to the nominal one. The XPS results show evidence for Mn ion which is in the mixed oxidation states and holes production increases with increasing of potassium concentration.

Analysis of the transport measurements of the compounds showed semiconducting behavior following hopping conduction mechanism. While the compounds with x=0.0 to 0.2 showed SPH mechanism, x=0.3 followed VRH mechanism. Temperature dependent dc and ac magnetization results revealed the presence of three types of magnetic transitions which agree well with the neutron scattering results. The corresponding slope changes were illustrated well in the plots of first derivative of magnetization versus temperature. The three magnetic transitions observed in all the compounds correspond to antiferromagnetic transitions of Mn and Dy ions as cited in the literature. While antiferromagnetic ordering of Mn spins was observed around 40 K and is robust with potassium substitution, ordering temperature of Dy spins was found to reduce with substitution. dc magnetization measurements were complimented by ac susceptibility studies. Frequency independent ac susceptibility against temperature indicated the absence of spin glass state. Different features observed in the magnetization data indicated various magnetic interactions in the compounds leading to a complex ground state. Field dependent magnetization of all the compounds exhibited hysteresis loops with high coercive fields for temperatures below the Neel temperature of Mn spins. However, the magnetic moment at 50 kOe magnetic field was found to decrease with increase in the potassium content. The presence of hysteresis loops may be ascribed to the parasitic ferromagnetism arising due to canting of Mn spins besides Dy and Mn exchange interactions. Neutron scattering measurements may provide more insight into the microscopic interactions in the substituted compounds.

The ac electrical properties of $Dy_{1-x}K_xMnO_3$ are studied in the temperature range 126 K - 299 K for x=0.1 and 0.2. With increase in the potassium content, there is a slight increase in both the dielectric constant and loss suggesting that conducting type relaxations exist in the materials. The frequency dependence of the real component of the complex conductivity as a function of temperature showed dispersion at low frequencies and merge at high frequencies. The modulus spectrum suggests that two types of relaxations exist in the compounds. Impedance spectra also revealed non-Debye type relaxation. From the Nyquist plots at low temperatures whose data could be fitted well with the circuit diagram, the grain and grain boundary resistances were obtained. The grain resistance was found to be less than that of the grain boundary resistance and both resistances decreased with increase in the temperature.

3.5 REFERENCES

[1] N.A. Spaldin and M. Fiebig, Science, **309**, (2005), 391.

[2] W. Eerenstein, N.D. Mathur and J.F. Scott, Nature, **442**, (2006), 759.

[3] S.W. Cheong and M. Mostovoy, Nature Materials, **6**, (2007), 13.

[4] A.F. Vaz, J. Hoffman, C.H. Ahn and R. Ramesh, Advanced Materials, **22**, (2010), 2900.

[5] T. Kimura, S. Ishihara, H. Shintani, T. Arima, K.T. Takahashi, K. Ishizaka and Y. Tokura, Phys. Rev. B, **68**, (2003), 060403.

[6] Y. Chen, H. Yuan, G. Li, Ge Tian and S. Feng, J. Crystal Growth, **305**, (2007), 242.

[7] S. Harikrishnan, S. Robler, C.M. Naveen Kumar, H.L. Bhat, U.K. Robler, S. Wirth, F. Steglich and Suja Elizabeth, J. Phys.: Condens. Matter, **21,** (2009), 096002.

[8] V.Yu. Ivanov, A.A. Mukhin, A.S. Prokhorov, A.M. Balbashov and L.D. Iskhakova, Phys. of the Solid State, **48**, (2006), 1726.

[9] T. Mori, K. Aoki, N. Kamegashira, T. Shishido and T. Fukuda, Mater. Lett., **42,** (2000), 387.

[10] S. Harikrishnan, C.M. Naveen Kumar, S.S. Rao, H.L. Bhat, S.V. Bhat and Suja Elizabeth, J. Appl. Phys., **104**, (2008), 023902.

[11] M.N. Iliev, M.V. Abrashev, J. Laverdiere, S. Jandl, M.M. Gospodinov, Y.Q. Wang and Y.-Y. Sun, Phys. Rev. B, **73**, (2006), 064302.

[12] R. Feyerherm, E. Dudzik, N. Aliouane and D.N. Argyriou, Phys. Rev. B, **73**, (2006), 180401.

[13] S. Harikrishnan, C.M. Naveen Kumar, H.L. Bhat, Suja Elizabeth, U.K. Robler, K. Dorr, S. Robler and S. Wirth, J. Phys.: Condens. Matter, **20**, (2008), 275234.

[14] K. Yoshii, Y. Hiramitsu, Y. Yoneda, Y. Okajima, Y. Nishihata, J. Mizuki and N. Ikeda, Ferroelectrics, **379**, (2009), 183.

[15] N. Zhang, S. Dong, Z. Fu, Z. Yan, F. Chang and J. Liu, Scientific Reports, **4,** (2014), 1.

[16] C. Abughayada, B. Dabrowski, M. Avdeev, S. Kolesink, S. Remsen and O. Chmaissem, J. Solid State Chem., **217**, (2014), 127.

[17] B.H. Toby, EXPGUI, a graphical user interface for GSAS, J. Appl. Cryst., **34**, (2001), 210.

[18] JCPDS (Joint Committee on Powder Diffraction Standards) Card No. 25-0330.

[19] K. Yadagiri and R. Nithya, accepted in ICDD database (2016).

[20] J.B. Goodenough, "Localized to Itinerant Electronic Transition in Perovskite Oxides", 2001, (Springer).

[21] http://www.cryst.ehu.es/rep/sam.html.

[22] L.M. Carrón, A. de Andrés, M.J.M. Lope, M.T. Casais and J.A. Alonso, Phys. Rev. B, **66**, (2002), 174303.

[23] J. Laverdiere, S. Jandl, A.A. Mukhin, V.Yu. Ivanov, V.G. Ivanov and M.N. Iliev, Phys. Rev. B, **73**, (2006), 214301.

[24] K. Yadagiri and R. Nithya, RSC Adv., **6**, (2016), 95417.

[25] M. Viswanathan, P.S. Anil Kumar, V.S. Bhadram, Chandrabhas Narayana, A.K. Bera and S.M. Yusuf, J. Phys.: Condens. Matter, **22**, (2010), 346006.

[26] X. Cai, L. Shi, S. Zhou, J. Zhao, Y. Guo and C. Wang, J. Appl. Phys., **116**, (2014), 103903.

[27] R. Kwok, XPSPEAK V4.1 2000, http://www.phy.cuhk.end.hkl/Surface/XPSPEAK/

[28] A.J. Millis, P.B. Little Wood and B.I. Shraiman, Phys. Rev. Lett., **74**, (1995), 5144.

[29] T. Holstein, Ann. Phys., (N.Y) **8**, (1959), 343.

[30] D. Emin and T. Holstein, Ann. Phys., **53**, (1969), 439.

[31] J.M. De Teresa, K. Dorr, K.H. Muller and L. Schul, Phys. Rev. B, **58**, (1998), R5859.

[32] T.T.M. Palstra, A.P. Ramirez, S-W. Cheong, B.R. Zegarski, P. Schiffer, and J. Zaanen, Phys. Rev. B, **56**, (1997), 5104.

[33] T. Kimura, G. Lawes, T. Goto, Y. Tokura and A.P. Ramirez, Phys. Rev. B, **71**, (2005), 224425.

[34] K. Yadagiri, R. Nithya, Neeraj Shukla and A.T. Satya, AIP Advances, **7**, (2017), 035003 (1-10).

[35] S. Harikrishnan, S. Robler, C.M. Naveen Kumar, H.L. Bhat, U.K. Robler, S. Wirth, F. Steglich and Suja Elizabeth, J. Phys.: Condens. Matter, **21,** (2009), 096002.

[36] C. Ritter, M. R. Ibarra, J.M. De Teresa, P.A. Algarabel, C. Marquina, J. Blasco, and J. Garcı´a, S. Oseroff and S-W. Cheong, Phys. Rev. B, **56**, (1997), 8902.

[37] S. Landsgesell, A. Maljuk T.C, Hansen, O. Prokhnenko, N. Aliouane and D.N. Argyriou, Phys. Rev. B, **80,** (2009), 014412.

[38] J. Hemberger, S. Lobina, H.A. Krug von Nidda, N. Tristan,. V.Yu. Ivanov, A.A. Mukhin, A.M. Balbashov and A. Loidl, Phys. Rev. B, **70,** (2004), 024414.

[39] J.L. Zhang, P. Zheng, C.L. Wang, M.L. Zhao, J.C. Li and J.F. Wang, Appl. Phys. Lett., **87**, (2005), 142901.

[40] S.F. Shao, J.L. Zhang, P. Zhang, W.L. Zhong and C.L. Wang, J. Appl. Phys., **99**, (2006), 084106.

[41] T.T. Fang and H.K. Shiau, J. Am. Ceram. Soc., **87**, (2004), 2072.

[42] A.K. Jonscher, Dielectric Relaxation in Solids, (Chelsea, London, 1983).

[43] J. Liu, C-G. Duan, W-G. Yin, W.N. Mei, R.W. Smith and J.R. Hardy, J. Chem. Phys., **119**, (2003), 2812.

[44] N.F. Mott and E.A. Davis, Electronic Process in Non Crystalline Materials, (Clarendon, Oxford, 1979).

[45] D.C. Sinclair and A.R. West, J. Appl. Phys., **66**, (1989), 3850.

CHAPTER – 4

STRUCTURAL PHASE TRANSITION AND OTHER PHYSICAL PROPERTIES OF DIVALENT ION (Ba^{2+}) SUBSTITUTION AT Dy SITE IN $DyMnO_3$ – $Dy_{1-x}Ba_xMnO_3$

4.1. INTRODUCTION

Multiferroic materials exhibit both ferromagnetic and ferroelectric properties in a single phase. These materials triggered extensive research due to the fascinating physics and potential applications like new electronic devices, memory devices and sensor applications [1-3]. $RMnO_3$ (R: Rare earth element) also belong to multiferroic materials. These manganites are divided into two groups due to the rare earth ionic size dependence on the crystal structure. The first group of $RMnO_3$ (R= La to Dy) compounds show orthorhombic structure and the second group of $RMnO_3$ (Ho–Lu) compounds display hexagonal structure. For divalent ion (A) substitutions at La site in $La_{1-x}A_xMnO_3$, very interesting properties like insulator to metal and para- to ferro-magnetic transition due to the presence of mixed valent states (Mn^{3+} & Mn^{4+}) of Mn ions were reported. These magnetic and electronic transitions have been attributed to double exchange mechanism between Mn^{3+} and Mn^{4+} ions. For instance, $La_{0.7}Ca_{0.3}MnO_3$ showed simultaneous transitions at 260 K from paramagnetic to ferromagnetic and insulator to metal transitions [4]. Similar studies were carried out on an analogous material, $DyMnO_3$ and related compounds to study hole doping effects such as structure, transport, magnetic and other properties. $DyMnO_3$ owing to its critical ionic radius, can exist in two structures either hexagonal or orthorhombic structure depending on the synthesis conditions. The orthorhombic $DyMnO_3$ exhibited magnetic field induced ferroelectric transition at low temperatures, $T_{FE} < 18$ K [5-7]. This temperature is associated with lock in temperature of Mn spins where the propagation vector of the Mn ions remained constant below this temperature. Sr doped $DyMnO_3$ shows orthorhombic structure like $DyMnO_3$, however; spin glass like nature is displayed by this compound around 35 K [8]. In the case of hexagonal $RMnO_3$ compounds, lattice distortion through off-centering of Mn ions induces multiferroic property. The contribution of off-centered Mn ions leads to ferroelectric polarization in these compounds. The off-centering of Mn ions contributes first in developing ferroelectric polarization then that will be responsible for magnetic behavior of the material. This mechanism is somewhat different as compared with other multiferroic ABO_3 perovskites like $BiFeO_3$ [9] in which magnetism and ferroelectricity phenomena occur independently by A and B cations. Another member of ABO_3 compounds, Barium manganite, $BaMnO_3$ with tetravalent Mn ions crystallized in hexagonal perovskite structure as its Goldschmidt tolerance factor (t) exceeded one due to large ionic radius of Ba^{2+}. The $BaMnO_3$ contains hexagonal stacking of close packed BaO_3 layers with Mn ions occupying interlayer octahedral sites. $BaMnO_3$ exists in more than one crystal structure like 2H, 4H, 6H, 9R, 10R, and 15R, etc., where H and R refer to Hexagonal and Rhombohedral depending on the number of BaO_3 layers present in unit cell [10-11]. Here nH implies that n layers of BaO_3 or n formula units per unit cell. Both end compounds, $DyMnO_3$ and $BaMnO_3$ show multiferroic nature [12-14]. By reducing the structural distortions caused due to smaller Dy ion (Dy^{3+} in 8 fold coordination: 1.0271 Å) [15] in $DyMnO_3$, by partially replacing with a larger Ba ion (Ba^{2+} in 12 fold coordination: -1.41 Å), we have chosen the mixed perovskite oxide system, $Dy_{1-x}Ba_xMnO_3$ to study the structural phase transition from orthorhombic to hexagonal and other physical properties as well.

4.2. SYNTHESIS AND EXPERIMENTAL PROCEDURE

Polycrystalline materials of $Dy_{1-x}Ba_xMnO_3$ (x=0.0-1.0) were synthesized by the conventional ceramic method using the respective oxides; Dy_2O_3, $BaCO_3$ and MnO_2. The oxide powders with nominal compositions: $Dy_{0.9}Ba_{0.1}MnO_3$; $Dy_{0.7}Ba_{0.3}MnO_3$ and $Dy_{0.5}Ba_{0.5}MnO_3$ were taken according to stoichiometric ratios and then ground thoroughly and calcined at 1300 °C for 24 hours for with intermediate grindings. For the preparation of $Dy_{0.2}Ba_{0.8}MnO_3$ and $BaMnO_3$ heating temperatures differed from the previous compounds. For x=0.8, the heating temperature was 1100 °C for 12 hours and in the case of x=1.0, heating temperature was 1050 °C for 12 hours. The resulting compounds were characterized by the powder X-ray diffraction (STOE diffractometer, Germany). Raman spectra of all the materials were recorded at room temperature with 514.5 nm laser using a micro-Raman spectrometer (Renishaw). Electrical resistivity was measured using four probe method from 300 K down to 145 K beyond which compounds exhibited high resistance hence could not be measured. Using MPMS 3 Ever Cool SQUID VSM (Quantum Design) magnetometer, Zero Field Cooled (ZFC) and Filed Cooled (FC) magnetization measurements were carried out in the presence of different fields in the temperature range: 5 K-300 K. Magnetization with respect to magnetic field (M-H) was also recorded at different temperatures.

4.3. RESULTS AND DISCUSSION

4.3.1. Structural studies

The $Dy_{1-x}Ba_xMnO_3$ (x=0.0-1.0) system showed a structural phase transition from orthorhombic to hexagonal at x=0.8 as displayed in Fig. 4.1 (a). The parent compound x=0.0, $DyMnO_3$ exhibited orthorhombic structure. Orthorhombic structure of the pristine compound is retained by the barium substituted compounds till x=0.5. However, lattice parameters and unit cell volume were found to decrease with increase in x and Fig. 4.1 (b) illustrates this behavior. This observation is similar to that found in the potassium system, DKMO which was attributed to the introduction of smaller tetravalent manganese ions by lower valent ion substitution. As concentration of Ba increases to x=0.8 and 1.0, the structure changed to hexagonal from orthorhombic due to the larger ion. The lattice parameters of x=0.8 and x=1.0 proved to be two layer hexagonal structure by adopting formula $\frac{c}{(n \times a)} = 0.4225$ [16] where, n is number of layers, *a* and *c* are lattice parameters. All the unit cell parameters with the corresponding volume are tabulated in Table 4.1.

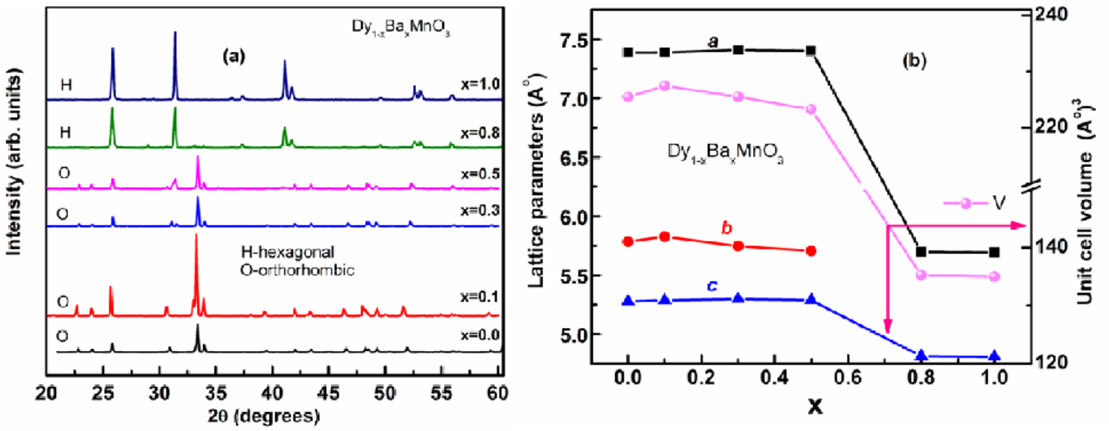

Figure 4.1. (a) X-ray diffraction patterns of $Dy_{1-x}Ba_xMnO_3$ (x=0.0-1.0). (b) Lattice parameters and unit cell volume against concentration of Ba in $Dy_{1-x}Ba_xMnO_3$.

Table 4.1. Lattice parameters and unit cell volume of $Dy_{1-x}Ba_xMnO_3$ (x = 0.0-1.0).

x	***a*** **(Å)**	***b*** **(Å)**	***c*** **(Å)**	**Unit cell volume ($Å^3$)**
0.0	5.7840	7.3880	5.2760	225.45
0.1	5.8161	7.3890	5.2821	226.99
0.3	5.7503	7.4029	5.2788	224.71
0.5	5.7060	7.4010	5.2860	223.20
0.8	5.6969	5.6969	4.8122	135.27
1.0	5.6939	5.6939	4.8079	134.99

4.3.2. Raman Spectroscopy

In order to probe the influence of lattice distortions on phonon frequencies, Raman spectra of $Dy_{1-x}Ba_xMnO_3$ (x=0.0-1.0) were recorded at room temperature. Raman spectra are displayed in Fig. 4.2 (a). As is seen from the Figure, Raman spectra of the compounds up to x=0.5 contains similar Raman band frequencies for orthorhombic structure with Pnma space group. However, for excess of Ba i.e., for x=0.8 & x=1.0 with hexagonal structure several extra Raman modes are observed as compared to other compounds. According to group theory, Raman active modes for orthorhombic structure with Pnma space group are: $\Gamma = 7A_g+5B_{1g}+7B_{2g}+5B_{3g}$ [17-19] and for hexagonal structure with $P6_3/mmc$ space group are: $\Gamma = A_{1g}+E_{1g}+3E_{2g}$ [20-22]. Out of the 24 expected Raman modes for orthorhombic structure; Tilting (T), Asymmetry Stretching mode arising from JT distortions (AS/JT), Bending (B) and Symmetry Stretching (SS) modes have been identified. The rest of two compounds i.e. x=0.8 and x=1.0 with hexagonal structure showed several Raman modes as per the symmetry. The position (peak centre) and line width (half maximum) of Raman peaks were obtained by fitting the profile to Lorentzian function using Peakfit program and their values are listed in Table 4.2. A representative plot for the decomposition of the

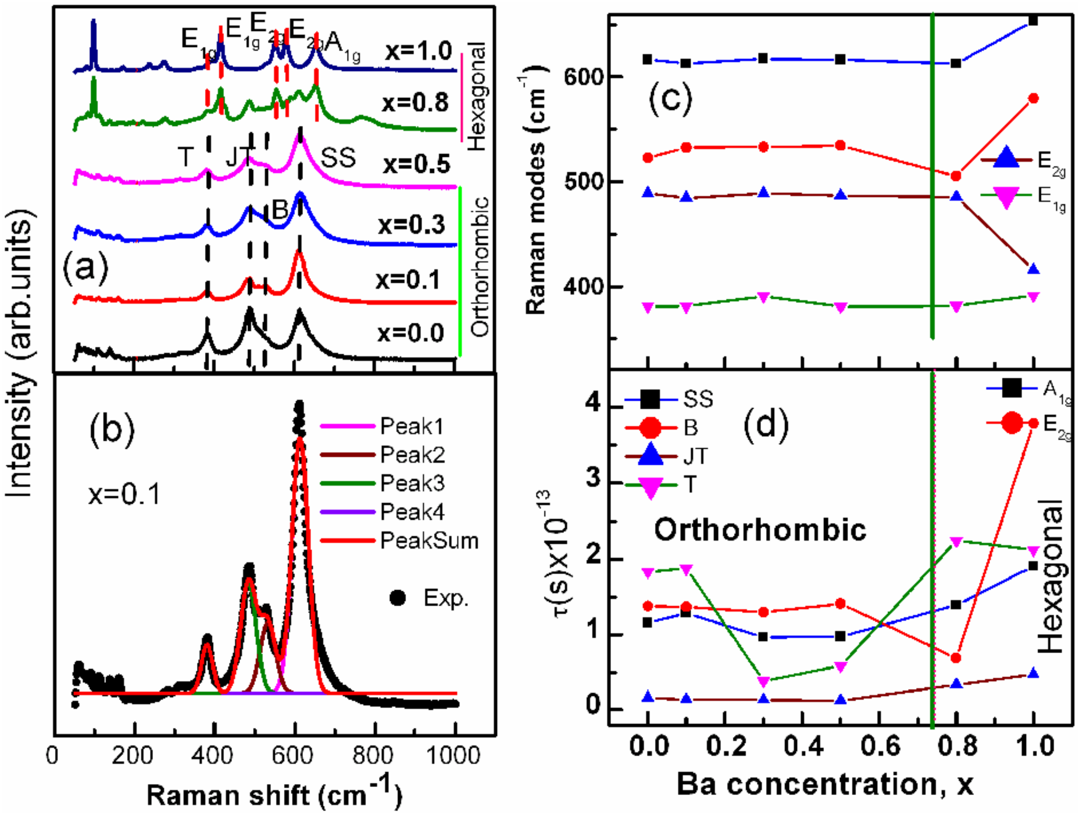

Figure 4.2. Raman spectra of Dy$_{1-x}$Ba$_x$MnO$_3$ (x=0.0-1.0). (a) Raman bands with mode assignment (b). Experimental data (symbols) of Raman spectra of x=0.1 fitted with Lorentzian function. Solid lines represent Lorentzian fit to the data. (c). Plot of Raman mode frequencies against Ba concentration. (d). Phonon life time vs. Ba concentration, x.

peaks is shown in Fig. 4.2 (b) for x=0.1. Figure 4.2 (c) demonstrates variation of peak positions with barium concentration, x. Modes assignment have been marked in Fig. 4.2 (a). From the Figure 4.2 (a), it is noted that the frequencies corresponding to A$_{1g}$ mode around 600 cm^{-1} and E$_{2g}$ mode near 500 cm^{-1} and E$_{1g}$ mode around 380 cm^{-1} are increased with x. On the other hand, E$_{2g}$ mode (~490 cm^{-1}) is decreased with x. In general, Raman line width (Γ) arises from a convolution of all broadening mechanisms, which in turn is due to the life time-shortening mechanism happening for a given crystal. The phonon life time (τ) is controlled by two mechanisms. First mechanism is phonon anharomonic interaction i.e., the phonon decays into multi phonons. Second mechanism is phonon scattering at impurity or defect centers which is called inhomogeneous broadening [23]. The phonon life time can be calculated from the width of the spectral lines from the equation [24]:

$$\Gamma \times \tau = \frac{h}{2\pi} \tag{4.1}$$

Here Γ and τ are phonon line width and phonon life time respectively. Table 4.2 consists of line width and phonon life time for all the concentrations of Ba. It is observed that for x=0.3 and x=0.5, the Raman lines are broader and consequently phonon life time values are less.

Table 4.2. The four essential Raman modes of $Dy_{1-x}Ba_xMnO_3$ (x=0.0-1.0) corresponding to atomic vibrations and polyhedral movements. From the widths of the Raman line, Γ phonon life times are calculated using the equation (4.1). Here h/2π = $5.3x10^{-12}$ cm^{-1}.

x → Raman bands ↓	0.0	0.1	0.3	0.5	0.8	1.0
T mode (cm^{-1})	384	382	382	381	383	392
Γ (cm^{-1})		23	26	28	20	26
τ x 10^{-12} (sec)		0.231	0.204	0.1896	0.265	0.204
AS mode (cm^{-1})	488	485	487	485	487	416
Γ (cm^{-1})		39	49	49	24	11
τ x 10^{-12} (sec)		0.136	0.108	0.108	0.221	0.483
B mode (cm^{-1})	522	527	524	526	531	529
Γ (cm^{-1})		34	53	47	47	15
τ x 10^{-12} (sec)		0.156	0.100	0.113	0.113	0.354
SS mode (cm^{-1})	614	611	614	613	610	654
Γ (cm^{-1})		34	43	44	30	27
τ x 10^{-12} (sec)		0.156	0.123	0.121	0.177	0.197

4.3.3. X-ray Photoelectron Spectroscopy

DMO contains only trivalent manganese ions. In the barium substituted compounds, for every barium ion, one tri-valent manganese ion gets converted to a tetra-valent manganese ion for charge neutrality. Besides, charge balance, hole doping into DMO by Ba substitution at Dy site leads to changes in the chemical environment of atomic species. These alterations manifest themselves in the binding energies whose values can be obtained from XPS data. Thus the oxidation states of the constituent elements can be identified [25] from XPS spectra.

XPS survey scans of all the compounds, $Dy_{1-x}Ba_xMnO_3$ (x=0.0-1.0) are shown in Fig. 4.3 (a). The X-ray photoelectron spectrum of each compound reveals the presence of the constituent elements Dy, Ba, Mn and oxygen in the binding energy range: 0 eV to 1000 eV.

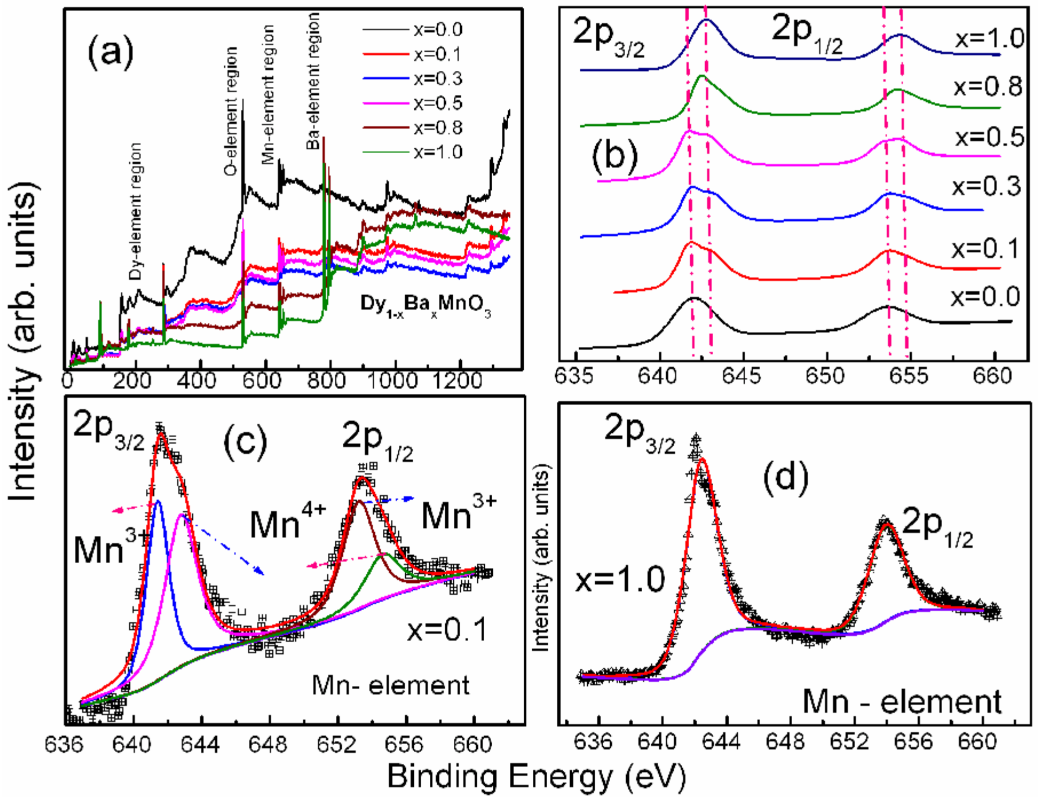

Figure 4.3. (a). Survey scans for all compounds, $Dy_{1-x}Ba_xMnO_3$ (x=0.0-1.0). (b). Demonstrates mixed valent states of $2p_{3/2}$, $2p_{1/2}$ of Mn^{3+} and Mn^{4+} ions. (c) & (d) Fitted XPS spectra for x=0.1 and x=1.0 using XPSPEAK 4.1 software.

As stated earlier, DMO has only one manganese species i.e., Mn^{3+} while the other end member, $BaMnO_3$ too has only one manganese species i.e., Mn^{4+}. Whereas for the substituted series of compounds, $Dy_{1-x}Ba_xMnO_3$ (x=0.1, 0.3, 0.5 and 0.8), Mn ion is found to exist in the mixed oxidation states; Mn^{3+} and Mn^{4+}. Figure 4.3 (b) illustrates the presence of tetravalent Mn ion for x=0.1 and increase of Mn^{4+} ion concentration for higher x in the series. Binding energies of the respective elements were obtained using XPSPEAK 4.1 software. The background was fitted to a Shirley function. A typical fitting for x=0.1 is shown in Fig. 4.3. (c). The Ba 3d, Mn 2p and O 1s binding energies thus obtained are listed in Table 4.3. From these binding energy values, the ratio of trivalent to tetravalent manganese ions (R) is calculated using the following equation:

$$R = \frac{(1-x)\ \text{B.E.of Mn}^{3+}}{x\ \text{B.E.of Mn}^{4+}} \qquad (4.2)$$

Table 4.3. Photoelectron Binding Energies of Ba, Mn and O ions for $Dy_{1-x}Ba_xMnO_3$ compounds.

x	Binding Energy (eV)									
	Ba		Mn							O
	$3d_{5/2}$	$3d_{3/2}$	$2p_{3/2}$			$2p_{1/2}$			$\Delta E^{‡}$	1s
			Mn^{3+}	Mn^{4+}	R	Mn^{3+}	Mn^{4+}	R		
0.0	-	-	641.7			653.3			11.6	529.4
0.1	780.2	795.5	641.4	642.7	8.98	653.2	654.6	8.98	11.8	529.6
0.3	780.3	795.6	641.5	642.9	2.32	653.2	654.5	2.32	11.7	529.8
0.5	780.6	795.3	641.3	642.6	0.98	652.9	654.1	0.99	11.6	529.6
0.8	780.1	795.4	642.0	643.0	0.25	653.7	654.6	0.25	11.6	529.6
1.0	779.5	794.8	642.4			653.9			11.5	529.5

$\Delta E^{‡} = Mn\ (2p_{3/2} - 2p_{1/2})$

The R parameter agrees well with the nominal reduction in the trivalent manganese ions upon Ba substitution. The difference between the Mn $2p_{3/2}$ and $2p_{½}$ (=ΔE) which indicated the spin–orbit splitting of Mn ion [26] is also included in the same Table. For x=1.0, Mn ion exhibited tetravalent state as seen in Fig. 4.3 (d). Binding energy values for Mn and O are in agreement with those reported in the literature for Mn_3O_4 compounds [27].

4.3.4. Transport properties

Temperature behavior of electrical resistivity for $Dy_{1-x}Ba_xMnO_3$ compounds is shown in Fig. 4.4 (main panel). All the samples exhibited semiconducting nature for the studied temperature range (140-300 K). It is reported in the literature [28, 29] that the high temperature transport properties in rare–earth transition metal oxide systems is dominated by thermally activated hopping of small polarons in the lattice. The experimental data are fitted using the equation for SPH conduction given by (3.3) and the fit curves are displayed in inset of Fig. 4.4. Thus the temperature dependence of resistivity of these materials is attributed to small polaron hopping conduction.

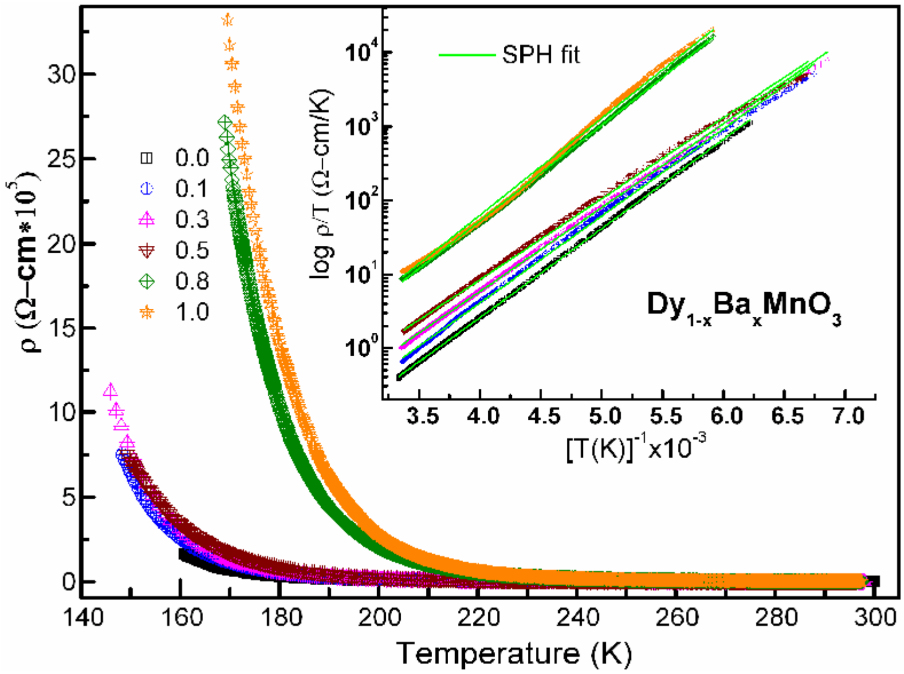

Figure 4.4. Temperature dependence of electrical resistivity of $Dy_{1-x}Ba_xMnO_3$ (x=0.0-1.0) from 300 K down to 145 K. Inset indicates SPH fitting to equation (3.3) in the text for all the compounds.

A plot of the hopping energy (E_a) (left y-axis) and $\log\rho_0$ (right y-axis) against x shown in Fig. 4.5 indicates that polaron hopping energy is decreased with increasing Ba concentration up to x=0.5 and then increased for x>0.5. While the initial reduction in E_a may be ascribed to charge and structural disorders due to the substitution of larger Ba ion at Dy site, the later increase in E_a may be due to two layer hexagonal structure. In contrast to E_a behavior, there is a large increase in the temperature independent resistivity (ρ_0) values up to x=0.5 and then ρ_0 becomes almost independent of x.

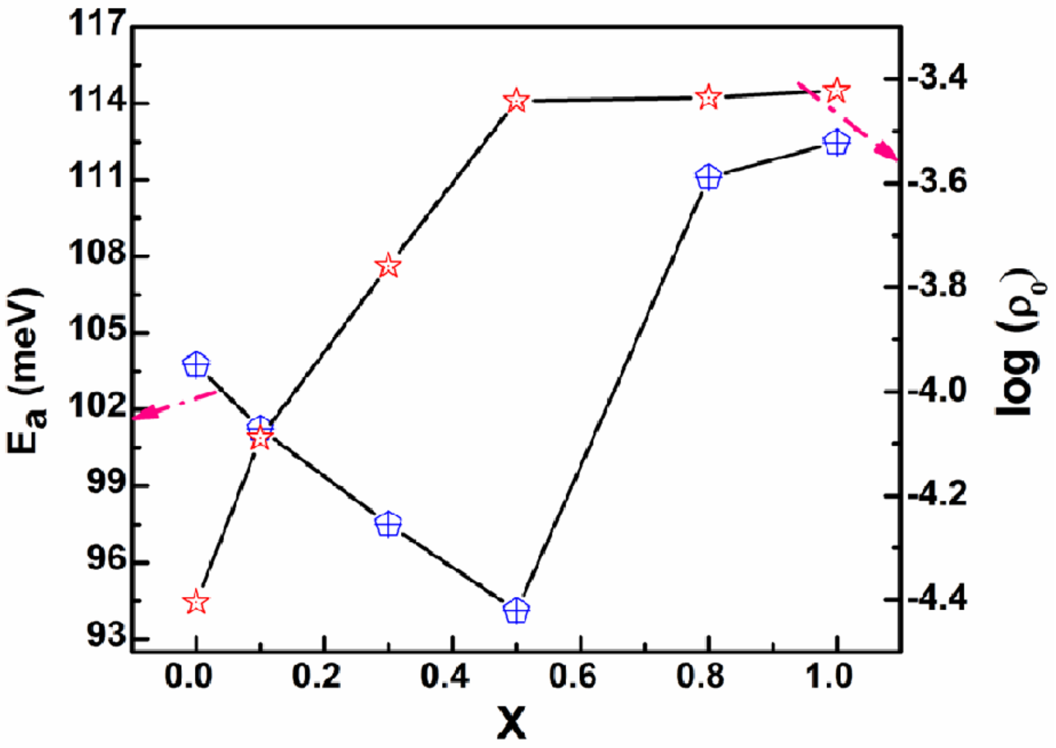

Figure 4.5. Displays hopping energy (E_a) and logarithm of residual resistivity ($\log\rho_0$) Vs. Ba concentration (x) in $Dy_{1-x}Ba_xMnO_3$.

4.3.5. Magnetic studies

The temperature dependent dc molar susceptibilities, $\chi(T)$ of $Dy_{1-x}Ba_xMnO_3$ (x=0.0-1.0) in the ZFC and FC protocols in the temperature range: 5 K - 300 K measured in an applied field of 1 Tesla are shown in Fig. 4.6. No difference between the χ_{ZFC} (T) and χ_{FC} (T) curves is observed down to 10 K. Below this temperature, while

χ_{ZFC} shows a peak at ~6 K, χ_{FC} continues to increase. However, for lower applied fields in compounds with intermediate Ba concentrations (x=0.3 and 0.5), bifurcation between χ_{ZFC} (T) and χ_{FC} (T) starts at a higher temperature (50 K) itself. As the applied field increases, the peaks are broader and their maximum value in the magnetization shifts to lower temperatures.

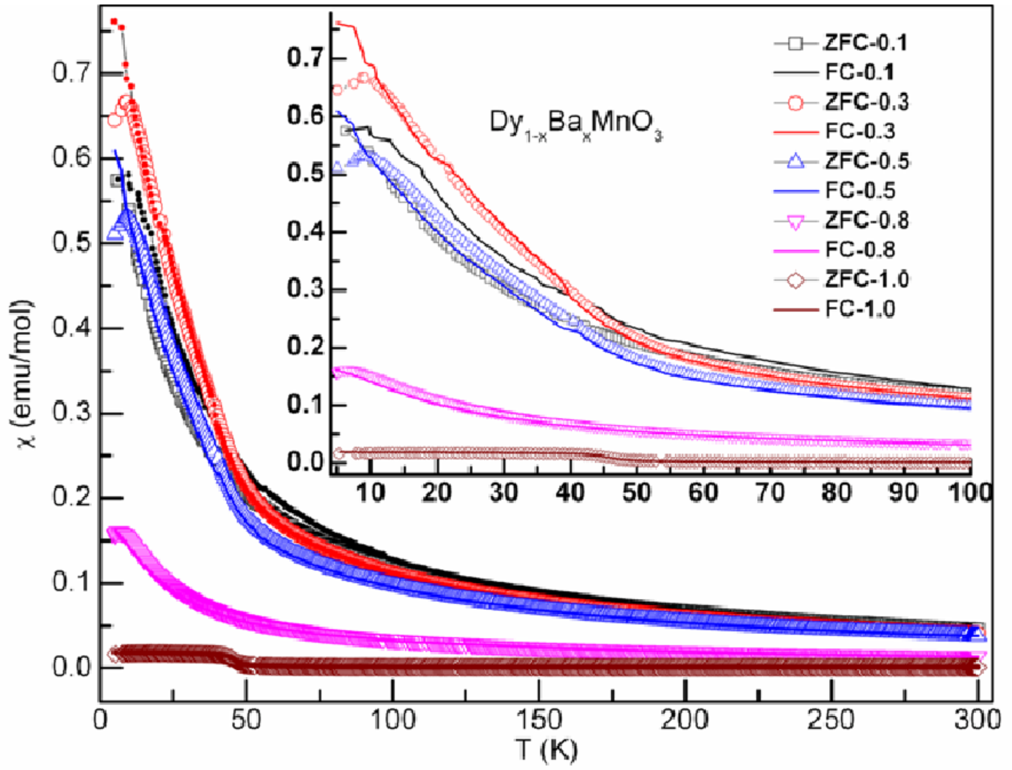

Figure 4.6. Variation of molar susceptibility vs. temperature for $Dy_{1-x}Ba_xMnO_3$ (x=0.1-1.0) in the ZFC and FC modes in an applied field of 1 Tesla.

The magnetic ordering of both Mn and Dy moments is inferred from the neutron scattering measurements performed on $DyMnO_3$ as a function of temperature by Kimura et al. [30]. Only in the pristine DMO compound, three magnetic transitions viz., antiferromagnetic (AFM) ordering of Mn ions [T_N (Mn^{3+})=39 K], lock-in AFM of Mn ions [$T_{lock\text{-}in}$ (Mn^{3+})=12 K], and AFM ordering of Dy spins [T_N (Dy^{3+})=3.6 K], were observed [31]. By disrupting the Dy sublattice by Ba ions, the low temperature anomaly corresponding to Dy spins ordering was further decreased and hence was not observed in the present χ(T) data of the mixed oxides. The substituted compounds contain both tri- and tetra valent manganese ions which are randomly distributed in the lattice. Depending on the occupancy of these ions in the lattice, magnetic interaction paths are anisotropic and it is difficult to ascertain the nature of the ordering of the magnetic ions from magnetization data alone. However, Mn ordering is reported in the literature [30] as well as our own studies on the other substituted compounds viz., $Dy_{1-x}K_xMnO_3$ [32] in the Chapter 3 and $Dy_{1-x}Bi_xMnO_3$ [31] presented in this thesis. Sinusoidal incommensurate antiferromagnetic ordering of manganese ions was observed around 40 K and the incommensurate to commensurate spiral ordering that takes place around 12 K. The transition temperatures corresponding to these changes in the magnetization were determined from the first derivative of susceptibility (dχ/dT) curves with respect to temperature. dχ/dT (T) curves show a single minimum for x=0.1 and 0.8 and two minima for x=0.3 and 0.5 compounds. Hence the high temperature minimum at ~40 K is attributed to antiferromagnetic ordering of Mn ions whereas the low temperature anomaly to lock-in temperature was observed only for some compounds. A plausible explanation for this observation could be due to the following: generation of Mn^{4+} ions upon divalent substitution reduces JT distortions leading to complex magnetic structures. High temperature susceptibility data were fitted to the CW law and from the fitted parameters, effective magnetic moments and Curie temperatures were determined. Calculated effective magnetic moments associated with the substituted compounds can be estimated from the individual atomic moments of Dy^{3+}, Mn^{3+} and Mn^{4+} using the equation:

$$\mu_{\mathrm{eff.}} = \sqrt{(1-x)\mu^2_{Dy^{3+}} + (1-x)\mu^2_{Mn^{3+}} + x\mu^2_{Mn^{4+}}} \qquad (4.3)$$

Here x is the concentration of Ba. As mentioned before, for every Ba ion substitution, one trivalent manganese ion is converted into a tetravalent manganese ion. Since Ba ion is non-magnetic and does not contribute to magnetism, magnetic moments corresponding to magnetic ions viz, Dy^{3+}, Mn^{3+} and Mn^{4+} only are considered to calculate magnetic moments as per the equation (4.3). As Ba concentration increases, magnetic moment decreases. Table 4.4 summarizes the magnetic moment values.

Table 4.4. Calculated magnetic moments ($\mu_{eff.}$ (cal.)) and moments obtained from the CW fit ($\mu_{eff.}$ (expt.)) to high temperature $\chi(T)$ data measured at 1 Tesla field in the field cooled mode. Magnetic moment derived from hysteresis loops measured at 5 K is also included in the table.

x	**Effective magnetic moment (μ_B)**		**Moment (7 T) μ_B/f.u.**
	$\mu_{eff.}$ (cal.)	**$\mu_{eff.}$ (expt.)**	
0.0	11.69	11.66	4.75 (5 T)
0.1	11.16	10.86	4.20
0.3	10.01	10.22	3.70
0.5	8.71	9.93	3.15
0.8	6.27	5.94	1.18
1.0	3.87	-	0.054

Contrary to DMO, magnetization of $BaMnO_3$ shows two anomalies: one at high temperatures as high as 230 K (Fig. 4.7) and the second one around 44 K which agrees well with the reported values by Korneta et al. [33] from magnetization measurements. Due to anomalies found in the magnetization data of BMO, CW law could not be fitted.

Calculated and experimental effective magnetic moments plotted against concentrations are showed in Fig. 4.8. It is observed that magnetic moment decreases due to enhancement of Mn^{4+} moments as well as decrement of Dy^{3+} and Mn^{3+}.

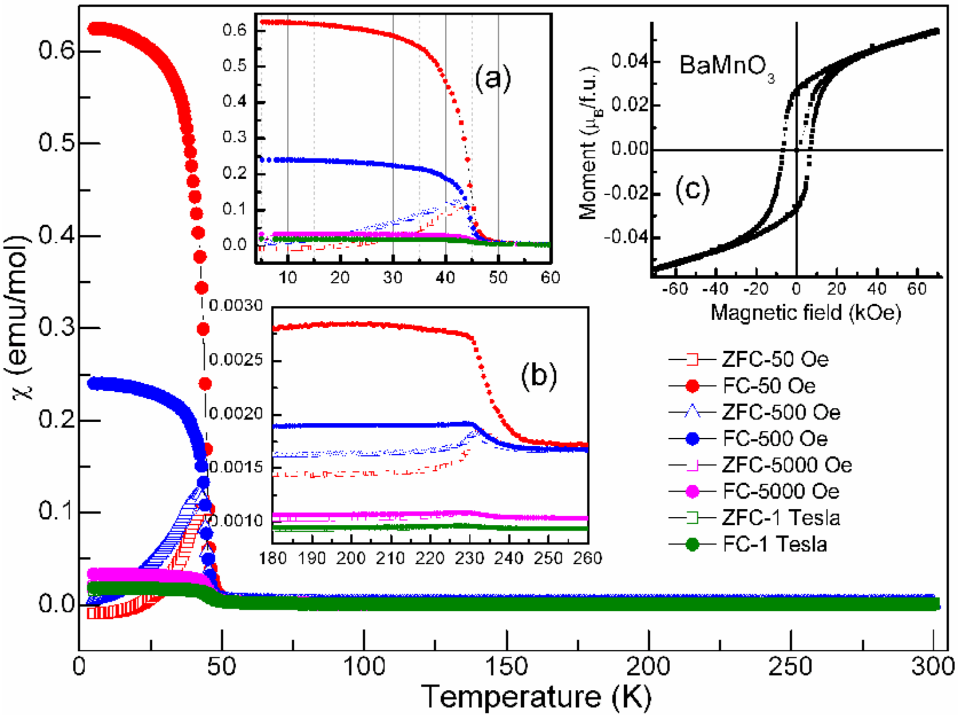

Figure 4.7. Molar magnetic susceptibiltiy as function of temperature in the tempearture range 2 K to 300 K measured in ZFC and FC protocols under different applied magnetic fields for BaMnO$_3$. The magnetic transitions in the low and high temperatures regions are shown insets (a) and (b) respectively. (c) Isothermal magnetization curve recorded at 5 K.

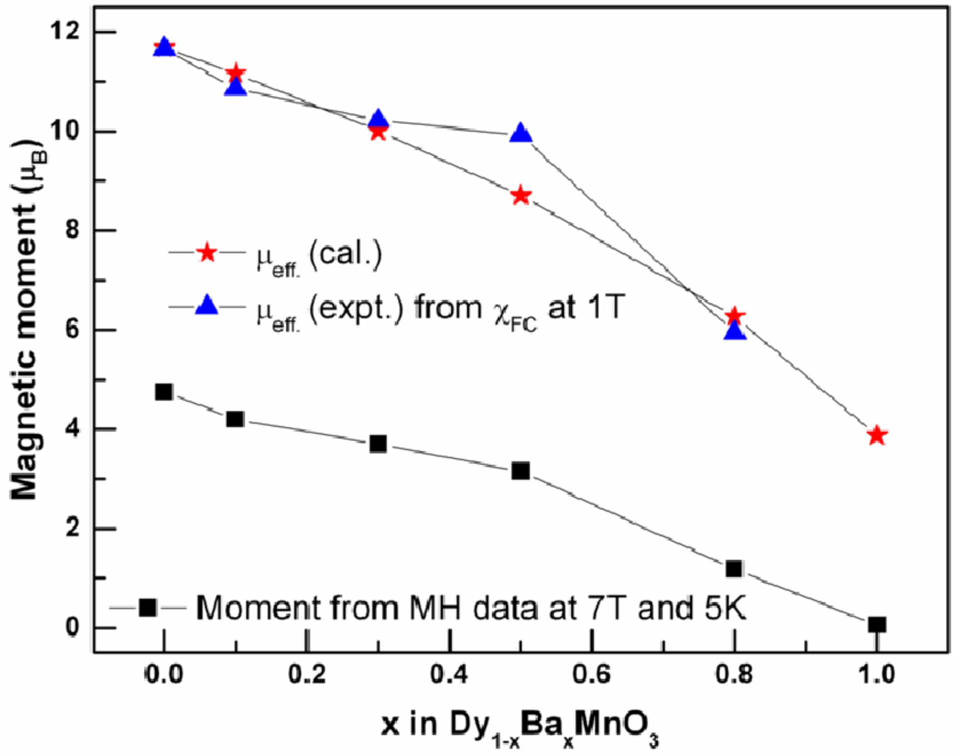

Figure 4.8. Effective magnetic moment ($\mu_{eff.}$ (expt.)) determined from fitting parameters obtained from the CW fit to and χ_{FC} (T) against x.

In order to understand the magnetic behavior observed in the temperature dependent magnetization data, magnetic isotherms were measured at several fixed temperatures above and below the magnetic ordering temperatures. The field dependence of magnetization (M-H) of $Dy_{1-x}Ba_xMnO_3$ (x=0.0-1.0) measured at 5 K is shown in Fig. 4.9. It is clear from the M-H curves that they exhibit hysteresis loops at low temperatures and low fields. The magnetization does not saturate even at 7 T external field. Although magnetization shows a tendency to saturate but the magnetization value at 7 T field is reduced with increase in barium concentration in accordance with the decrease in the moment values as per the experiment and calculations using the equation (4.3). The magnetization moment at 7 T is also included in Fig. 4.8. As temperature of the measurement increases, the hysteresis loops collapse and show a linear variation with field. Representative isothermal plots of $Dy_{0.5}Ba_{0.5}MnO_3$ and $Dy_{0.2}Ba_{0.8}MnO_3$ shown in Figs. 4.10 and 4.11 illustrate this behavior. Lack of saturation and observation of hysteresis loops with finite values of coercive fields indicate the presence of multiple magnetic interaction paths.

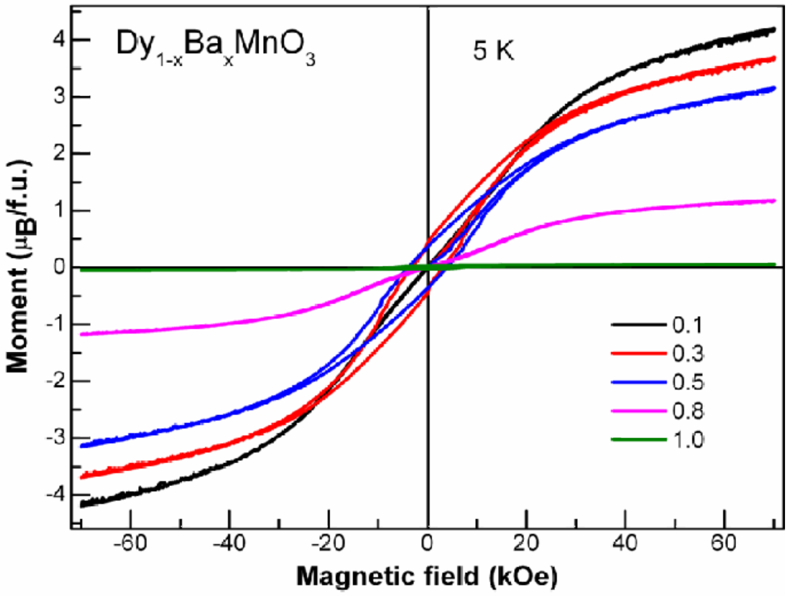

Figure 4.9. Magnetization as a function of magnetic field at 5 K for $Dy_{1-x}Ba_xMnO_3$ (x=0.0-1.0).

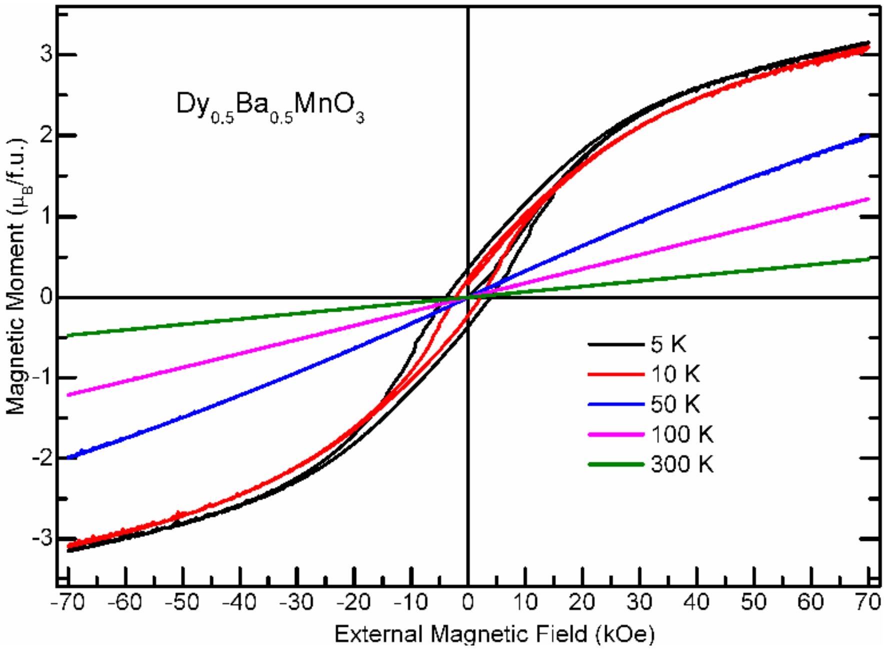

Figure 4.10. M-H curves for $Dy_{0.5}Ba_{0.5}MnO_3$.

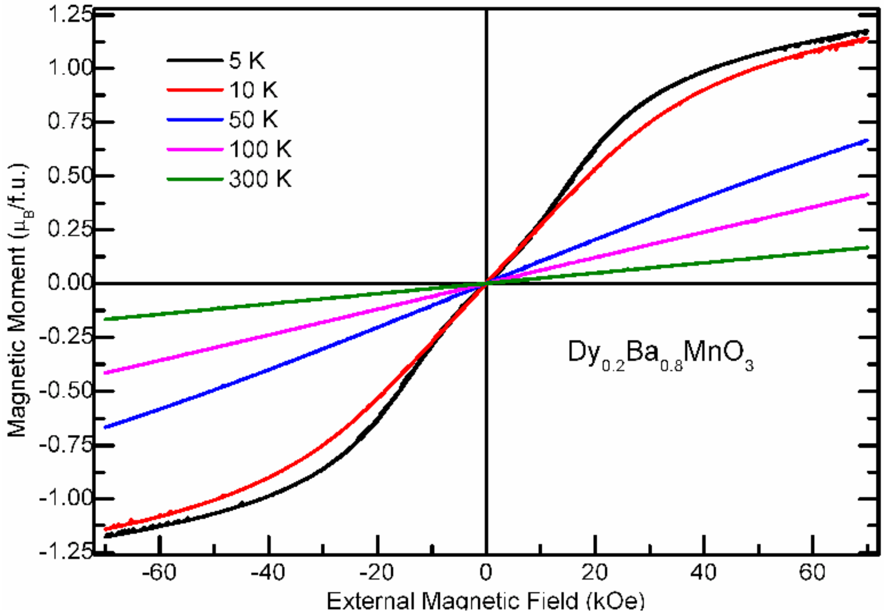

Figure 4.11. M-H curves for $Dy_{0.2}Ba_{0.8}MnO_3$.

4.4. CONCLUSIONS

The investigated compounds of $Dy_{1-x}Ba_xMnO_3$ were prepared by solid state reaction. For x=0.0 to 0.5, the compounds have orthorhombic structure and for x=0.8 and 1.0, the structure changed to hexagonal structure corresponding to 2H. As Ba concentration increases, volume decreases due to the conversion of bigger trivalent ions into smaller tetravalent ions for maintaining charge balance in the compounds. Raman spectroscopy of these materials revealed that structural phase transition is confirmed and Raman modes are identified for orthorhombic structure and hexagonal structure. Phonon life time calculated is found to be in the order of picoseconds. From the XPS spectrum of $Dy_{1-x}Ba_xMnO_3$, Dy, Ba, Mn and O elements in different regions are identified. Mn ion is found in the mixed valent state of Mn^{3+} and Mn^{4+} and its ratio decreased with increasing of Ba concentration. Temperature dependence of electrical resistivity was carried out and results showed insulating behavior with small polaron hopping conduction mechanism. Despite the presence of Mn(III) and Mn(IV) ions that can favor double exchange interaction leading to metallicity, resistivity increased with increase in x. Hopping energy and polaron binding energies were calculated. The magnetic properties as a function of temperature indicated that rare earth (Dy) moments ordering is suppressed and random distribution of manganese ions led to complex ground states. By fitting the high temperature susceptibility to the CW law, effective magnetic moments were obtained and compared with the calculated moments. The reduction in the moments followed the magnetic dilution. Compounds with intermediate x displayed two transitions corresponding to AFM transitions of Mn ions while x=0.1 and 0.8 showed only a single transition. Isothermal magnetization curves showed the presence of multiple interactions between magnetic ions.

4.5. REFERENCES

[1] N.A. Spaldin and M. Fiebig, Science, **15**, (2005), 5733.

[2] M. Fiebig, J. Phys. D, **38**, (2005), R123.

[3] M. Bibes and A. Barthelemy, Nat. Mater., **7**, (2008), 425.

[4] R. Mahendiran, S.K. Tiwary, A.K. Raychaudhuri, T.V. Ramakrishnan, R. Mahesh, N. Rangavittal, C.N.R. Rao, Phys. Rev. B, **53**, (1996), 3348.

[5] T. Kimura, G. Lawes, T. Goto, Y. Tokura and A.P. Ramirez, Phys. Rev. B, **71**, (2005), 224425.

[6] O. Prokhnenko, R. Feyerherm, E. Dudzik, S. Landsgesell, N. Aliouane, L.C. Chapon and D.N. Argyriou, Phys. Rev. Lett., **98**, (2007), 057206.

[7] T. Goto, T. Kimura, G. Lawes, A.P. Ramirez and Y. Tokura, Phys. Rev. Lett., **92**, (2004), 257201.

[8] S. Harikrishnan, C.M. Naveen Kumar, H.L. Bhat, Suja Elizabeth, U.K. Robler, K. Dorr, S. Robler and S. Wirth, J. Phys.: Condens. Matter, **20**, (2008), 275234.

[9] S.W. Cheong and M. Mostovoy, Nature Mater, **6**, (2007), 13.

[10] T. Negas and R.S. Roth, J. Solid State Chem., **3,** (1971), 323.

[11] Laura Miranda, Antonio Feteira, Derek C. Sinclair, Mar Garcia Hernandez, Khalid Boulahya, María Hernando, Aurea Varela, Jose M. Gonzalez-Calbet and Marina Parras , Chem. Mater., **20**, (2008), 2818.

[12] S. Bhattacharjee, E. Bousquet and P. Ghosez, Phys. Rev. Lett., 102, (2009), 117602.

[13] C. Roy and R.C. Budhani, Phys. Rev. B, **58**, (1998), 8174.

[14] E.J. Cussen and P.D. Battle, Chem. Mater., **12**, (2000), 831.

[15] R.D. Shannon, Acta Cryst., **A32**, (1976), 751.

[16] B.L. Chamber land, A.W. Sleight and J.F. Weiher, J. Solid State Chem., **1**, (1970), 506.

[17] K. Yadagiri and R. Nithya, RSC. Adv., **6**, (2016), 95417.

[18] M.N. Iliev, M.V. Abrashev, V.N. Popov and V.G. Hadjiev, Phys. Rev. B, **67**, (2003), 212301.

[19] M.V. Abrashev, J. Backstrom, L. Borjesson, V.N. Popov, R.A. Chakalov, N. Kolev, R.-L. Meng and M.N. Iliev, Phys. Rev. B, **65**, (2002), 184301.

[20] M.N. Iliev, H.-G. Lee, V.N. Popov, M.V. Abrashev, A. Hamed, R.L. Meng and C.W. Chu, Phys. Rev. B, **56**, (1997), 2488.

[21] D.L. Rousseau, R.P. Bauman and S.P.S. Porto, J. Raman Spectrosc., **10**, (1981), 253.

[22] Chaitali Roy and R.C. Budhani, Phys. Rev. B, **58**, (1998), 8174.

[23] Leah Bergman, Dimitri Alexson, Patrick L. Murphy, Robert J. Nemanich, Mitra Dutta, Michael A. Stroscio, Cengiz Balkas, Hyumin Shin and Robert F. Davis, Phys. Rev. B, **59**, (1999), 12977.

[24] B. Di Bartolo, Optical Interactions in Solids*,* Wiley, New York, 1968.

[25] Practical Surface Analysis by Auger and X-ray Photoelectron Spectroscopy, edited by D. Briggs and M.P. Seah (Wiley, New York, 1983).

[26] Elke Beyreuther, Stefan Grafström Lukas M. Eng, Christian Thiele and Kathrin Dörr, Phys. Rev. B, **73**, (2006), 155425.

[27] A. Moses Ezhil Raja, S. Grace Victoria, V. Bena Jothy, C. Ravidhas, Joachim Wollschlager, M. Suendorf, M. Neumann, M. Jayachandran and C. Sanjeeviraja, Appl. Surf. Sci., **256,** (2010), 2920.

[28] A.J. Millis, Phys. Rev. B, **53**, (1996), 8434.

[29] A.J. Millis, P.B. Littlewood and B.I. Shraiman, Phys. Rev. Lett., **74**, (1995), 5144.

[30] T. Kimura, G. Lawes, T. Goto, Y. Tokura and A.P. Ramirez, Phys. Rev. B, **71,** (2005) 224425.

[31] K. Yadagiri, R. Nithya, Neeraj Shukla and A.T. Satya, J. Alloys. Compd, **695**, (2017), 2959.

[32] K. Yadagiri, R. Nithya, Neeraj Shukla and A.T. Satya, AIP Advances, **7**, (2017), 035003 (1-10).

[33] O.B. Korneta, T.F. Qi, M. Ge, S. Parkin, L.E. De Long, P. Schlottmann and G. Cao, J. Phys.: Condens. Matter, **23,** (2011), 435901.

CHAPTER – 5

MULTIFUNCTIONAL PROPERTIES OF ISOVALENT IONS (Bi & Eu) SUBSTITUTION AT Dy SITE IN DyMnO$_3$

5.1. INTRODUCTION

RMnO$_3$ series of compounds exhibit a variety of magnetic phases depending on the R site ion and temperature. The first member of this series, LaMnO$_3$ showed A-AFM order around 140 K which developed due to staggered orbital order [1]. The A-AFM temperature decreases with the decrease in the ionic size of the R ion (r_R). Kimura et al. [2] reported a magnetic phase diagram as a function of r_R. With the suppression of A-AFM order, several spin structures appear resulting in the antiferromagnetic ground states. For example, in the case of orthorhombic DyMnO$_3$, as mentioned earlier in the previous Chapters, high temperature paramagnetic phase changed to incommensurate sinusoidal AFM order which in turn changed to commensurate magnetic structure with the lowering of temperature. Whereas another member of the series, HoMnO$_3$ with a smaller ionic radius at R site, displayed a commensurate magnetic structure that can be identified with “up-up-down-down” spin structure or E-type anti ferromagnetic structure [3]. The modification of magnetic structures is understood to be due to the decrease of bond angle Mn-O-Mn in the crystal structure as a consequence of GdFeO$_3$ - type distortions in addition to JT distortions. Yet in another member, YMnO$_3$, frustrated antiferromagnetic ground state is observed [4, 5]. Thus RMnO$_3$ compounds show complex magnetic ground states and the magnetic interactions have been understood to be due to two types of interactions: super exchange interactions between nearest neighbor (NN) and next nearest neighbor (NNN) Mn ions [6]. Owing to the critical ionic size of dysprosium ion, (1.027 Å) in 8 fold coordination, DMO crystallizes either in orthorhombic structure or hexagonal structure depending upon synthesis conditions and environments [7]. The significant polyhedral distortions caused due to small R ions in the perovskite structure can be altered by substituting larger ions at R-site either partially or fully. Robler et al. [8] reported that orthorhombic DMO showed antiferromagnetic ground state involving Dy^{3+} spins which ordered at 5 K and incommensurate anti ferromagnetic ordering at 39 K corresponding to Mn^{3+} spins in addition to the lock-in transition of Mn spins around 18 K. In contrast, divalent (Sr) substituted DMO single crystals exhibited spin glass nature around 39 K [9]. In the case of tri valent ion (Y^{3+}) substituted DMO single crystals, two magnetic transitions were observed: antiferromagnetic ordering (T_N) around 68 K arising due to Mn-Mn spins and rare earth ion (Dy^{3+}) spins ordering at 3 K [10]. In view of the different properties shown by $RMnO_3$ and related systems, we aim at studying the effects of larger isovalent ions viz., Bi (r_{Bi}^{3+} (8) = 1.17 Å) and Eu (r_{Eu}^{3+} (8) = 1.066 Å) substitution at Dy site in DMO on the structural and physical properties. Among all the manganites, $BiMnO_3$ whose structure stabilized in the monoclinic unit cell showed unique properties like ferromagnetic (T_c) insulating ground state around 105 K with a magnetic moment of 3.1 μ_B / Mn at high fields [11, 12]. In addition to low temperature ferromagnetic behavior, $BiMnO_3$ exhibits ferroelectric transition around 450 K [13] and 760 K [14, 15]. Due to a lone pair of electrons ($6s^2$) present in Bi^{3+}, $BiMnO_3$ shows the multi ferroic properties in a single phase compound. In general, in rare earth manganites, magnetic transitions occur at temperatures where orbital ordering is observed while $BiMnO_3$ showed magnetic transitions much below their orbital ordering temperature [16]. While DMO belongs to prototype magnetoelectric multiferroic materials, $EuMnO_3$ (EMO) which is another member of $RMnO_3$ does not show magnetic induced ferroelectric order. Both compounds have an orthorhombic distorted perovskite structure yet display different physical properties. In this context, we have chosen solid solutions between DMO and EMO, to understand the coupling between the magnetic and electric properties. In view of the diverse properties exhibited by dysprosium and substituted manganites, it is interesting to study the ground state properties of the mixed compounds of $Dy_{1-x}Bi_xMnO_3$ and $Dy_{1-x}Eu_xMnO_3$. In the case of Bi substitution compounds, for the first time we attempted to synthesize 10at.%, 30at.%, 50at.% compounds, but only 10at.% compound could be synthesized. This was due to the evaporation of Bi at these synthesizing temperatures. Compounds with high concentrations of Bi require optimization of thermal parameters such as temperature, heating rate, duration of heating, etc. However, we studied structural, transport, vibrational and magnetic properties of 10at.% bismuth substituted compound and compared with the pristine compound, DMO. On the other hand, solid solubility range existed between DMO and EMO.

5.2. SYNTHESIS AND EXPERIMENTAL DETAILS

Polycrystalline materials of $Dy_{1-x}Bi_xMnO_3$ ($x = 0.0$ and 0.1) and $Dy_{1-x}Eu_xMnO_3$ ($x = 0.0, 0.1, 0.3, 0.5, 0.8$ & 1.0) were synthesized by the conventional ceramic method from the oxides of Dy_2O_3, Bi_2O_3 / Eu_2O_3 and MnO_2 as per stoichiometric ratios. The mixture was ground thoroughly and heated around 1000 ˚C for 12 hours with intermediate grinding. Subsequently, mixture was once again heated at 1300 ˚C for 12 hours. The mixture was then compressed into circular pieces which were sintered at 1300 ˚C for 24 hrs. to obtain dense pellets for resistivity measurements. The resulting compounds were characterized by powder X-ray diffraction (XRD) technique using powder diffractometer (STOE, Germany) with Cu K_α radiation (1.5406 Å). XRD data were analyzed using Rietveld refinement to get structural data. Room temperature Raman Spectra of these materials were recorded with an excitation wavelength of 514.5 nm Ar ion laser using InVia micro-Raman spectrometer (Renishaw, UK). Temperature dependence of electrical resistivity was measured using four probe method from 300 K down to 160 K beyond which compounds exhibited high resistance hence could not be measured. Using MPMS3 Ever cool SQUID-VSM (Quantum Design) magnetometer, temperature dependent dc magnetization data (M-T) were collected in both Zero Field Cooled (ZFC) and Field Cooled (FC) modes at several fields in the range of 50 Oe – 10 kOe in the temperature range of 2 K - 400 K. Magnetization with respect to magnetic field (M-H) was also recorded at different temperatures. Also variation of ac susceptibility as a function of temperature at different frequencies was measured in 1 Oe ac magnetic field and zero-bias external dc magnetic field using the same magnetometer for DMO and Bi substituted compounds.

5.3. RESULTS AND DISCUSSION

5.3.1. Structural studies

a. $Dy_{1-x}Bi_xMnO_3$

XRD patterns of $Dy_{1-x}Bi_xMnO_3$ are displayed in Fig. 5.1. X-ray analysis indicated that all the compounds retained orthorhombic structure with increase in the unit cell volume exhibiting good crystallinity. After initial examination for phase

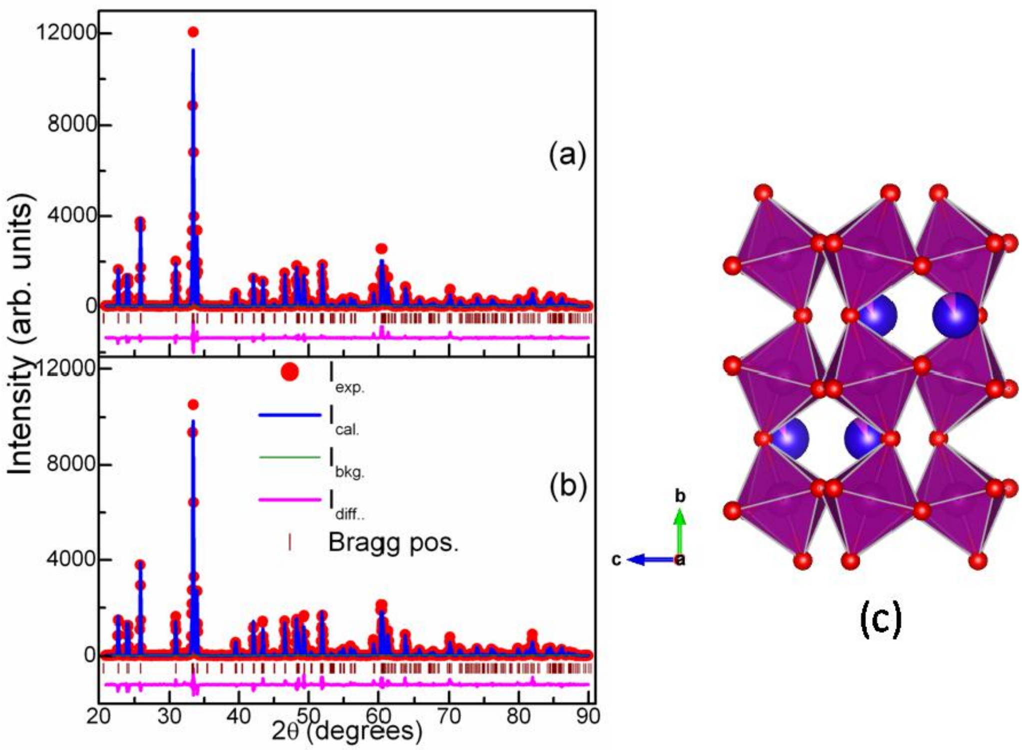

Figure 5.1. Observed X-ray diffraction intensity ($I_{expt.}$, red color solid symbol) and calculated intensity ($I_{cal.}$, blue color solid line) after the final refinement cycle using GSAS software for (a) DMO and (b) DBMO. Green solid line represents the background intensity. Magenta color solid curve shown at the bottom is the difference between $I_{expt.}$ & $I_{cal.}$. Vertical lines indicate the allowed Bragg reflections according to the space group, Pnma. (c) Schematic diagram of the unit cell of DBMO. Since Dy (blue) and Bi (pink) ions occupy the same crystallographic site, they are represented by bicolor as per their occupancy. Oxygen ions are shown by red spheres enclosing Mn ions which are in the purple color octahedra.

purity of the compounds by X-ray diffraction technique, slow scan data were collected for refinement of the starting lattice and structural parameters. No extra peaks were observed in the diffraction patterns either corresponding to starting oxides or intermediate phases, concluding that the compounds are single phase in nature. Initial lattice parameters were obtained by Index and refine program available with WinX-POW software provided by STOE diffractometer. Subsequently these lattice parameters were refined using GSAS suite, EXPGUI [17]. Refinement of the whole powder diffraction pattern was performed for orthorhombic structure with Pnma (62) space group using GSAS. Refinement analysis is initiated once the necessary input parameters for starting GSAS program viz., instrument parameters, initial lattice constants, space group, diffraction data and starting structure model are entered. The instrument file contains type of radiation and polarization used for diffraction. Wavelengths of $K_{\alpha1}$ and $K_{\alpha2}$ and their ratio along with polarization ratio have to be incorporated in the instrument file. These instrument parameters will take care of the $K_{\alpha2}$ component present in the diffraction peaks during refinement. Hence no corrections were being made to the diffraction data in order to eliminate Bragg peaks corresponding to $K_{\alpha2}$. In the beginning of the refinement, lattice constants determined from the Index and Refine were used. The starting structure model was based on the distorted orthorhombic perovskite-type structure with Pnma space group reported by Yadagiri and Nithya [18]. The background intensity was not subtracted from the whole profile intensity before starting the refinement. Background intensity was calculated using standard functions during the refinement analysis. Among the seven background functions available in GSAS, Linear interpolation formula (function 7) was used to fit the background intensity of all the patterns. Pseudo-Voigt function (Type 2 profile function for continuous wavelength in GSAS suite) which is a combination of a Lorentzian and a Gaussian function were used to model the diffraction peaks satisfactorily. Variables in the refinement process included lattice constants, fractional coordinates, crystallographic site occupancies, thermal parameters, diffractometer zero, coefficients corresponding to background and profile functions. The refinement calculation started with the approximate values that were entered in the beginning. Later on each parameter was refined at a time until the calculated pattern matched well with the measured pattern. Site occupancy factors too were floated during refinement, but neither the intensity of the pattern nor the R-factors did show improvement hence the occupancies were kept constant. This confirms the chemical composition of the compounds is close to the nominal composition. In the final cycle of refinement, to achieve a global minimum, multiple parameters were refined. Rietveld Refinement (RR) results of $DyMnO_3$ (DMO) and $Dy_{0.9}Bi_{0.1}MnO_3$ (DBMO) along with the measured XRD patterns are presented in Fig. 5.1 (a) and (b).

All the diffraction peaks could be indexed to orthorhombic structure. Lattice parameters [19], average bond lengths and bond angles of $Dy_{1-x}Bi_xMnO_3$ (x=0.0 and 0.1) calculated from RR are tabulated in Table 5.1. The lattice parameters of DMO agree with that of JCPDS card No. 25-0330 (indexed).

Table 5.1. Structural parameters of $DyMnO_3$ and $Dy_{0.9}Bi_{0.1}MnO_3$.

Parameters	**DMO**	**DBMO**
a, b, c (Å)	5.784 (1) 7.388 (1) 5.276 (1)	5.788 (1) 7.391 (1) 5.277 (1)
V (Å^3)	225.446 (5)	225.748 (6)
t (tolerance factor)	0.839	0.844
<Mn-O1 > (Å)	1.944 (3)	1.950 (3)
<Mn-O2> (Å)	2.048 (3)	2.032 (4)
<Dy-O1> (Å)	2.292 (4)	2.284 (5)
<Dy-O2> (Å)	2.466 (3)	2.478 (4)
Mn-O1-Mn (degrees)	143.593 (0)	142.623 (1)
Mn-O2-Mn (degrees)	145.744 (0)	148.925 (0)
R-factors: χ^2 R (F^2) R_p wR_p DW_d	 2.96 9.24 10.04 13.37 1.27	 4.49 12.99 12.86 16.78 1.09

The present diffraction data of $DyMnO_3$ has been included in ICDD database [19] under star quality. In MnO_6 octahedra, axial Mn-O2 bond lengths are decreased while apical bond lengths of Mn-O1 are increased. As a consequence, the Mn-O-Mn bond buckles more in the ac plane as compared to the one along b-axis where the tilting is reduced by one degree. From the refined atomic coordinates, an orthorhombic unit cell is drawn using VESTA software [20] and Fig. 5.1 (c) illustrates the unit cell of DBMO compound showing polyhedral distortions.

b. $Dy_{1-x}Eu_xMnO_3$

The solid solutions between DMO and EMO retained the orthorhombic structure as seen from Fig. 5.2. RR was performed only for the substituted compounds with x=0.1, 0.3 and 0.5. Figs. 5.3 (a) to (c) illustrate experimental XRD patterns (solid symbols) of $Dy_{0.9}Eu_{0.1}MnO_3$, $Dy_{0.7}Eu_{0.3}MnO_3$ and $Dy_{0.5}Eu_{0.5}MnO_3$ respectively along with refinement results. Lattice parameters and refine structural parameters for DEMO system is presented in Tables 5.2 and 5.3 respectively.

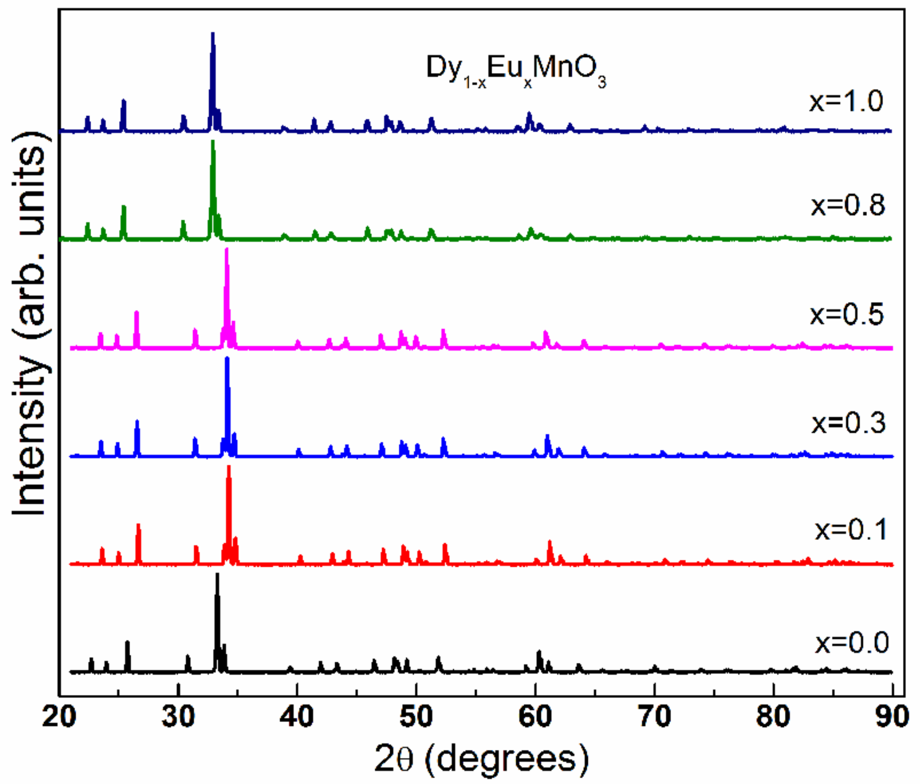

Figure 5.2. X-ray diffraction patterns of $Dy_{1-x}Eu_xMnO_3$ (x=0.0 - 1.0).

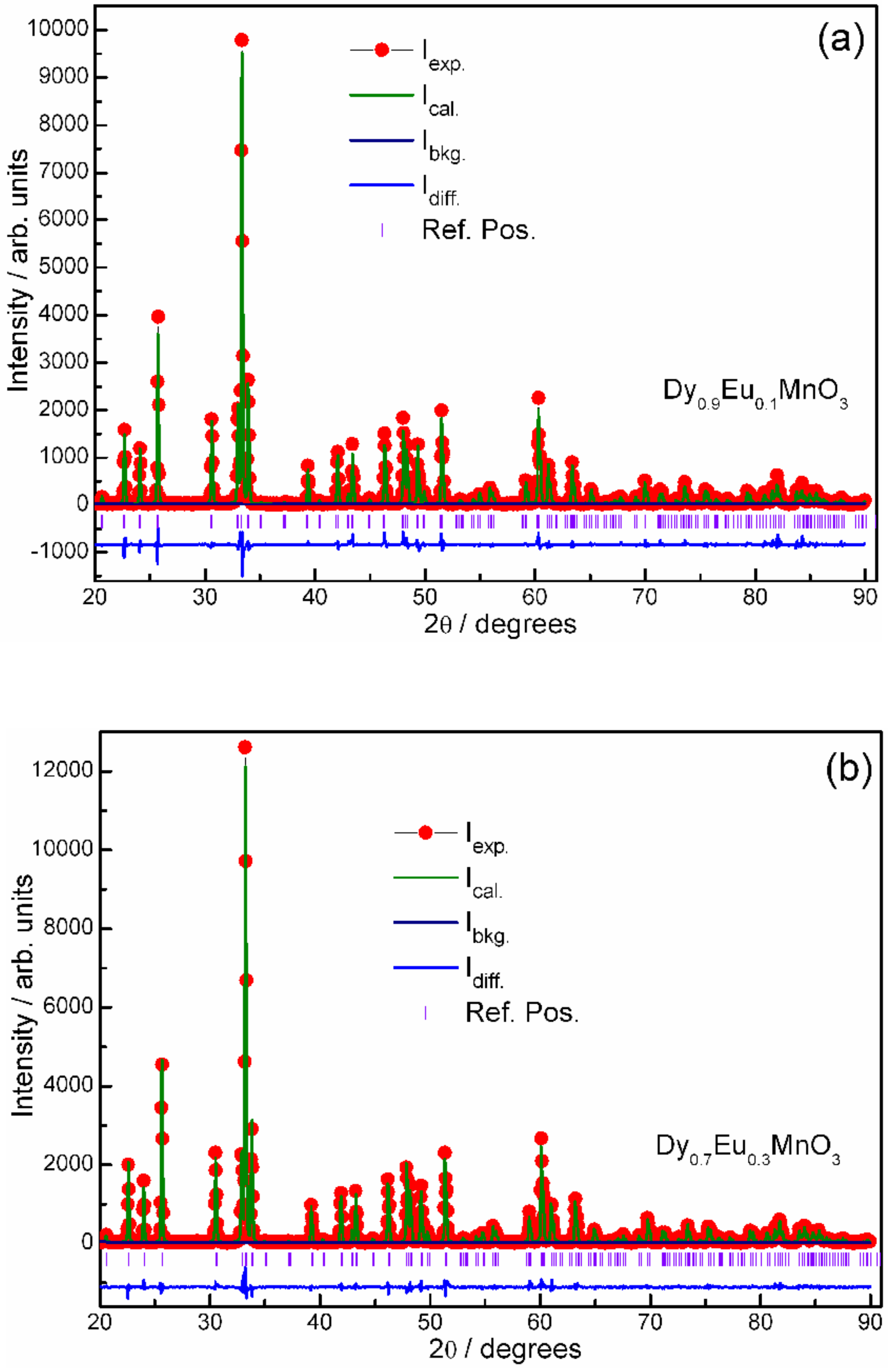

Figure 5.3. Continued.

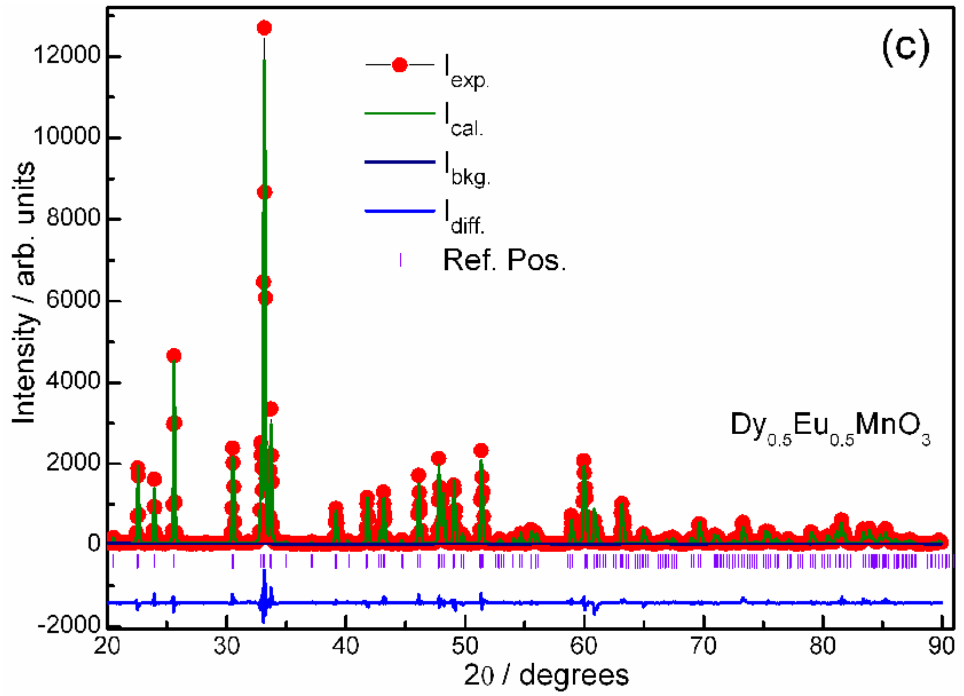

Figure 5.3. (a) - (c) Experimental (solid symbols) and calculated (solid lines) XRD patterns of $Dy_{1-x}Eu_xMnO_3$. Legends corresponding to various solid lines are given in each figure.

Table 5.2. Lattice parameters of $Dy_{1-x}Eu_xMnO_3$.

x	***a*** **(Å)**	***b*** **(Å)**	***c*** **(Å)**	**Volume (Å^3)**
0.0	5.78399 (10)	7.38829 (11)	5.275580 (9)	225.446 (5)
0.1	5.84738 (10)	7.39441 (13)	5.29157 (10)	228.796 (5)
0.3	5.849370 (9)	7.40073 (11)	5.296980 (8)	229.304 (4)
0.5	5.84519 (10)	7.41459 (12)	5.30858 (10)	230.084 (5)
0.8	5.83570 (12)	7.44130 (15)	5.32400 (10)	231.200 (6)
1.0	5.83070 (16)	7.45370 (18)	5.33340 (14)	231.790 (8)

Table 5.3. Refined structural parameters of $Dy_{1-x}Eu_xMnO_3$.

Parameters	**x = 0.10**	**x = 0.30**	**x = 0.50**
t (tolerance factor)	0.840	0.843	0.845
<Mn-O1 > (Å)	1.92698 (17)	1.94526 (5)	1.95291 (5)
<Mn-O2> (Å)	2.06569 (16)	2.07059 (5)	2.06331 (5)
<Dy-O1> (Å)	2.33974 (21)	2.31746 (6)	2.31122 (7)
<Dy-O2> (Å)	2.47218 (19)	2.47226 (6)	2.48137 (6)
Mn-O1-Mn (degrees)	147.205 (4)	144.024 (1)	143.307 (1)
Mn-O2-Mn (degrees)	145.2 (3)	144.5	146.0407
R-factors:			
χ^2	2.93	2.55	2.79
R (F^2)	5.61	4.51	6.29
R_p	10.22	8.41	9.28
wR_p	13.96	11.89	12.39
DW_d	1.30	1.44	1.27

Owing to the larger ionic size of europium, unit cell volume of the series increased and Fig. 5.4 displays the variation of lattice constants and volume against europium concentration. While marginal increase in the unit cell volume for DBMO system was observed, the cell volume of DEMO compounds showed significant increase. Fractional coordinates and lattice constants from the final Rietveld refinement cycle were used to view the crystal structures. Influence of polyhedral distortions obtained from RR analysis in the solid solution series is depicted in Fig. 5.5.

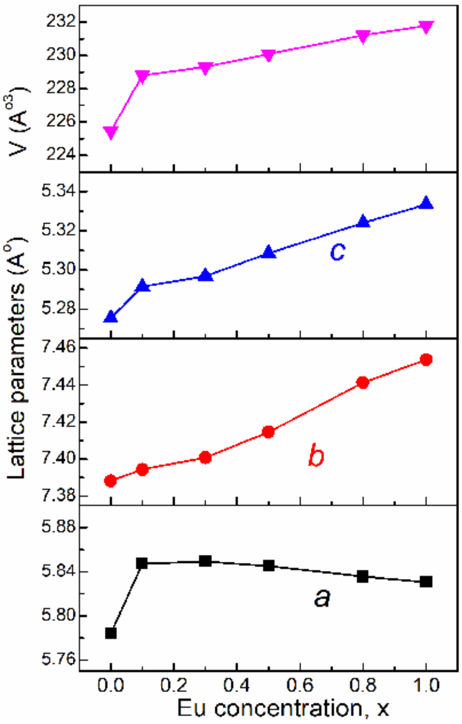

Figure 5.4. Lattice parameters and unit cell volume versus Eu concentration, x.

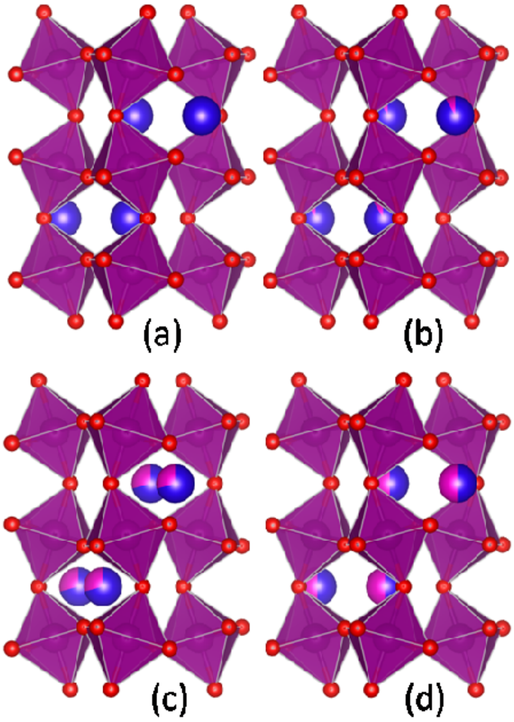

Figure 5.5. (a) Unit cell of $DyMnO_3$ viewed along [100]. Relative positions of atoms in the unit cell corresponding to (b) 10at.%, (c) 30at.% and (d) 50at.% europium substituted $DyMnO_3$. It is to be noted that Dy and Eu occupy the same crystallographic position and hence their occupancy is represented by bicolor spheres. Octahedral units of MnO_6 are shown in purple color.

To determine the stoichiometry in the DEMO compounds, compositional analysis was carried out by Inductively Coupled Plasma-Optical Emission Spectroscopy (ICP-OES) technique. In order to avoid spectral interference from the rare earth ions in ICP-OES technique, Atomic Absorption Spectroscopy was used to analyze Mn. Results obtained from chemical analysis for the two substituted compounds, x=0.1 and 0.3 along with the parent compound are tabulated in Table 5.4. $Dy_{0.5}Eu_{0.5}MnO_3$ could not be dissolved by acid digestion method. As seen from the table, there is a good agreement between the chemical analysis results and calculated results by weight percentage as per the nominal composition.

Table 5.4. Elemental composition results obtained from chemical analysis given under Exp. columns. Calculated values are also included in the table.

Sample / **Elements**	**$DyMnO_3$ (wt.%)**		**$Dy_{0.9}Eu_{0.1}MnO_3$ (wt.%)**		**$Dy_{0.7}Eu_{0.3}MnO_3$ (wt.%)**	
	Exp.	Cal.	Exp.	Cal.	Exp.	Cal.
Dy	62.5	61	55.2	55	45.7	43.4
Eu	<0.3	0	6.0	5.8	19.7	17.4
Mn	20.8	21	19.5	20.8	18.9	21.0

5.3.2. Raman spectroscopy

Raman spectroscopy is a good tool to probe lattice distortions in a material. For the orthorhombic structure with Pnma space group, factor group analysis predicts 24 Raman active bands [21]. Room temperature as well as temperature variation of Raman scattering spectra of manganites were reported by several authors [22-26] where individual phonon modes have been correlated with structural distortions including Jahn-Teller ion (Mn^{3+}) distortions. Figure 5.6 (a) shows the Raman spectra for DBMO compounds. However, experimentally, only three high intense broad bands are observed in the range between 200 cm^{-1} and 1000 cm^{-1} and two Raman bands that appear as a shoulder in the main peaks. Below 200 cm^{-1} wave number, a set of six peaks are present in both the samples which are due to the vibrations of heavier rare earth ions. All the Raman modes could not be observed either due to weak

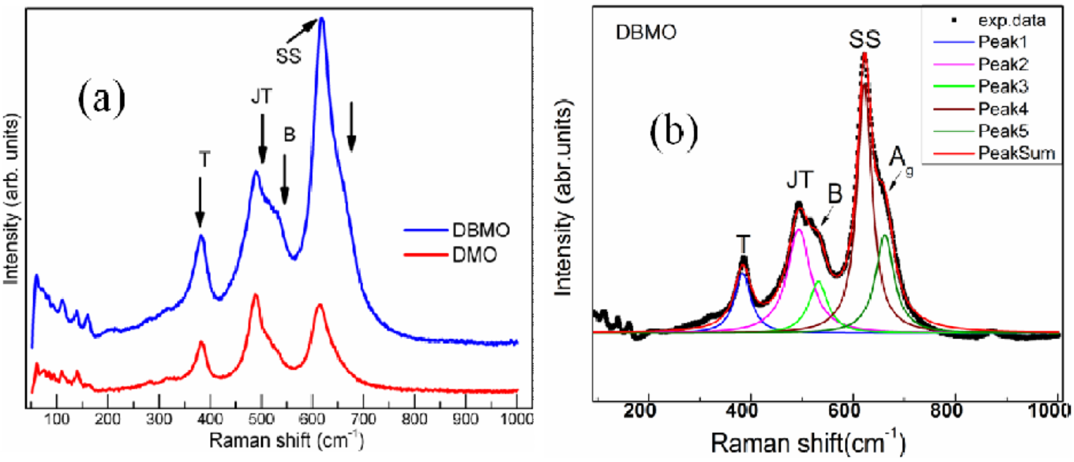

Figure 5.6. (a) Room temperature Raman spectra of $Dy_{1-x}Bi_xMnO_3$ (x=0 and 0.1) with mode assignments. (b) Decomposed spectra for various modes for the substituted compound (x=0.1).

intensity or merging of several modes with close wave numbers. The observed Raman mode frequencies are consistent with those reported in the literature confirming the single phase nature of the compounds under study which was also inferred by the XRD data analysis. Following Cai et al. [25] identification of Raman modes to their respective atomic vibrations/polyhedral units was carried out. Decomposition of modes in the substituted compound, DBMO is shown in Fig. 5.6 (b). Symmetric Stretching (SS) mode found at 617 cm^{-1} for DMO gets hardened (622 cm^{-1}) for DBMO. This could be attributed to the reduction in the bond lengths in the axial plane (ac) of the octahedra, MnO_6. The JT (A_g) mode found at 488 cm^{-1} for DMO also hardens in the case of DBMO at 494 cm^{-1}. JT mode is shifted to high wave number for DBMO because the bond angle of Mn-O2-Mn of MnO_6 is increased with substitution of Bi. The frequency of the Raman band corresponding to the tilting mode also increased from 382 cm^{-1} for DMO to 384 cm^{-1} for DBMO. As a consequence of static octahedral tilt [27] in DBMO as compared to DMO, tilting mode (T) is shifted towards the high wave number. The bending mode (B) is observed at 522 cm^{-1} and 532 cm^{-1} for DMO and DBMO respectively. Overall, hardening of Raman bands is observed for the DBMO system.

In the case of $Dy_{1-x}Eu_xMnO_3$, Raman spectra for all the compounds are illustrated in Fig. 5.7 (main panel). Raman spectra were fitted using Peakfit to obtain Raman mode frequencies and their values for the four modes are tabulated in Table 5.5. Raman band frequencies of the JT, tilting and bending modes decreased with increase in Eu concentration whereas that of SS modes showed only a marginal decrease with increase in x. Inset of Fig. 5.7 shows the experimental findings of variation of Raman mode frequencies with europium concentration.

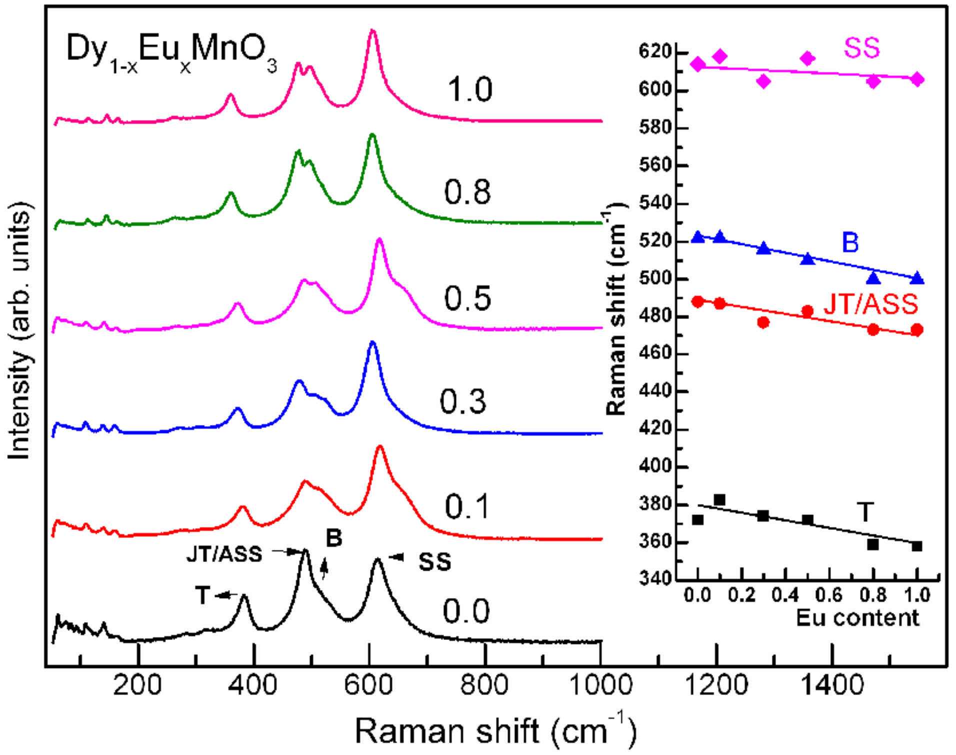

Figure 5.7. Main panel: Raman spectra of $Dy_{1-x}Eu_xMnO_3$ recorded at room temperature. Inset: Variation of Raman mode frequencies with x.

Table 5.5. Raman modes of $Dy_{1-x}Eu_xMnO_3$ (x=0.0-1.0)

x	T mode (A_g)	JT/ASS mode (A_g)	B mode ($A_g + B_{2g}$)	SS mode (B_{2g})
0.0	372	488	522	614
0.1	383	487	522	618
0.3	374	477	516	605
0.5	372	483	510	617
0.8	359	473	500	605
1.0	358	473	500	606

5.3.3. X-ray Photoelectron Spectroscopy

X-ray photoelectron spectra of both the systems viz., $Dy_{1-x}Bi_xMnO_3$ (x=0.0 and 0.1) and $Dy_{1-x}Eu_xMnO_3$ (x=0.1 - 1.0) were recorded in the energy range 0 eV – 1000 eV. Survey scans for DBMO are shown in Figure 5.8 (a). From the spectra it is seen that the elements Dy, Mn, Bi and oxygen are present in the respective binding energy ranges. From the XPS spectra, Mn ions are found to exist in 3+ oxidation state with binding energies ~641.7 eV. The binding values are estimated from the deconvoluted XPS spectra shown in Fig. 5.8 (b) in the energy range 635 to 660 eV using XPS PEAKS 4.1 software. The binding energies 641.7 eV ($2p_{3/2}$) and 653.3 eV ($2p_{1/2}$) for

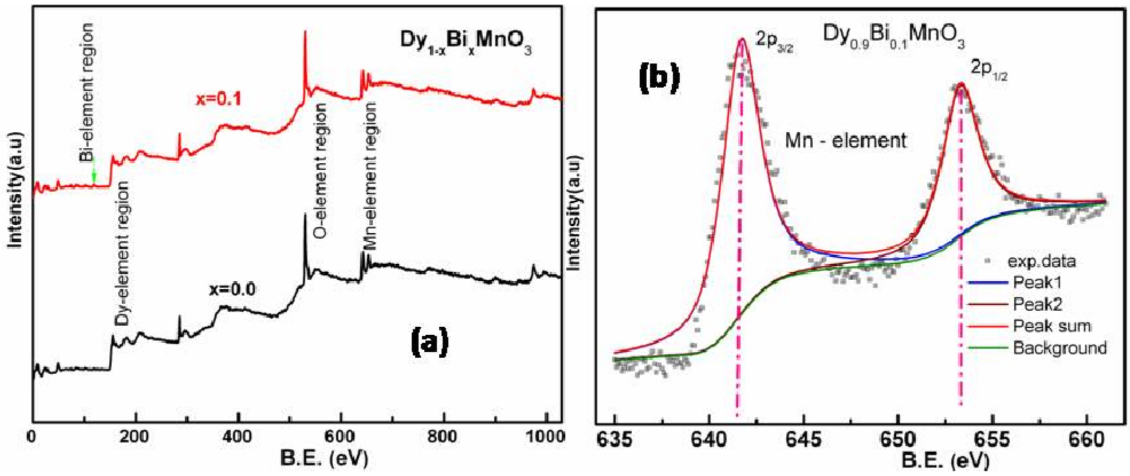

Figure 5.8. (a). Wide spectrum of $Dy_{1-x}Bi_xMnO_3$ (x=0.0 and 0.1), (b) XPS spectrum of Mn 2p for x=0.

x=0.1. The binding energies agree with the reported values of 641.8 eV and 653.0 eV respectively for $2p_{3/2}$ and $2p_{1/2}$ respectively reported by Biesinger et al. [28] for transition metal oxides.

In the case of DEMO system, representative survey scans corresponding to x=0.0, 0.5 and 1.0 are depicted Fig. 5.9 (a). It is seen from the wide spectrum that all the elements are present in their respective binding energy scale. XPS spectra corresponding to manganese are shown in Fig. 5.9 (b). Figs. 5.9 (c) and (d) display a typical deconvoluted spectrum of Mn element for x=0.5 and normalized spectra for DEMO for Eu 3d respectively. The binding energies determined from the fitting the spectra are tabulated in Table 5.6. Binding energies of Eu and Mn calculated from the fitting are found to be in agreement with the respective ions in the trivalent states. Binding energy of oxygen lies between 529.4 to 529.8 eV corresponding to O 1s.

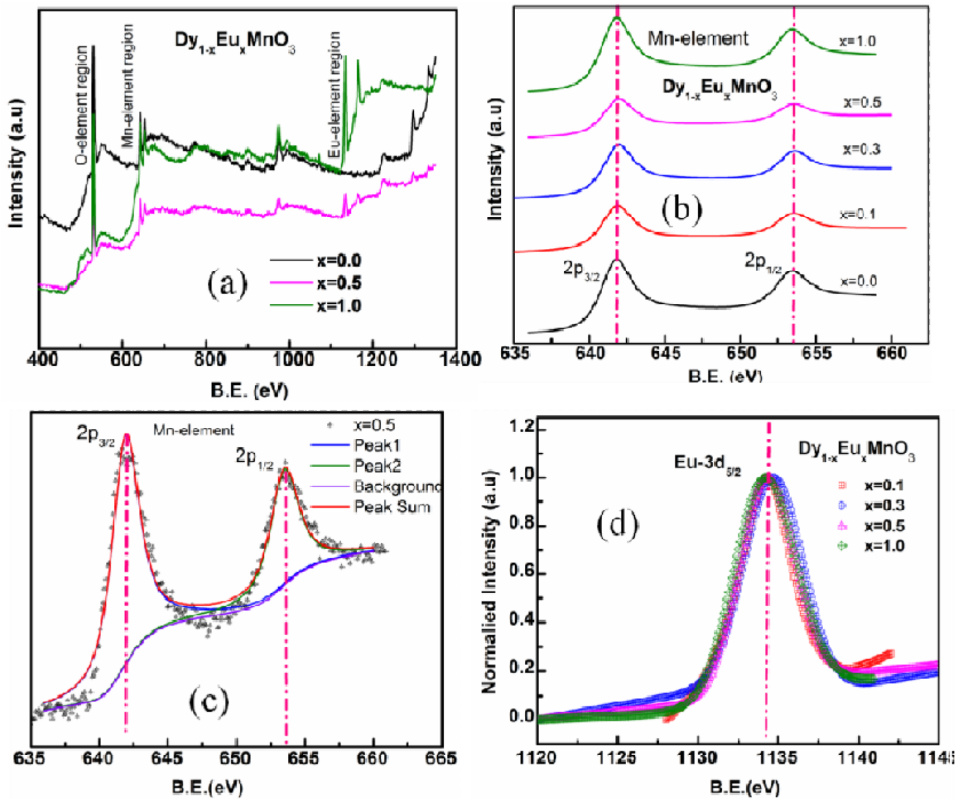

Figure 5.9. (a) Representative survey scan spectra for the two end members and 50at.% substituted in the solid solution series. (b) Mn 2p spectra for all the compounds (c) Deconvoluted spectra for x=0.5 (d) Normalized spectra for Eu 3d.

Table 5.6. Binding energies of $Dy_{1-x}Eu_xMnO_3$.

x	Binding Energy (eV)				
	Eu		Mn		O
	$3d_{5/2}$	$3d_{3/2}$	$2p_{3/2}$	$2p_{1/2}$	1s
0.0	-	-	641.7	653.3	529.4
0.1	1134.33	-	641.8	653.5	529.6
0.3	1134.47	1163.99	641.8	653.5	529.8
0.5	1134.23	1163.68	641.9	653.5	529.7
1.0	1134.31	1164.05	641.7	653.4	529.6

XPS results indeed provide evidence for the existence of trivalent manganese ions in all the substituted compounds of both the systems and trivalent Eu in DEMO.

5.3.4. Transport properties

a. $Dy_{1-x}Bi_xMnO_3$

Electrical resistivity was measured by the four probe method from room temperature down to 160 K beyond this temperature compounds exhibited high insulating character. Figure 5.10 depicts the variation of resistivity with temperature. Both compounds exhibited semiconducting nature. To understand the temperature variation of electrical resistivity in manganites exhibiting colossal magnetoresistance in the paramagnetic insulating region, various models have been used [29]. Palstra et.al., [30] and Jaime et al. [31] have shown evidence for polaron transport in Ca doped $LaMnO_3$ from the transport measurements combined with thermo power studies. Palstra et al. concluded that the small (Holstein)-polarons formed due to distortions of Mn-O octahedra dominates the transport conduction. Using Holstein model [32], activation energy for small polaron hopping (SPH) was determined by fitting the resistivity data to the equation (3.3). Fits to this equation are shown in the inset of the Fig. 5.10. The polaron hopping energy values are 103.85 meV and 98.52 meV for DMO and DBMO respectively. These values suggest that by substitution of Bi^{3+} in DMO, hopping energy is decreased. Since Bi^{3+} ion is having a lone pair of electrons which plays role in reducing the activation energy for hopping to occur. From the hopping energy, activation energy to produce hopping sites, W_H can be determined using the equation (3.4). Thus the values of W_H are 97.35 meV, 92.02 meV for DMO and DBMO respectively. In Holstein model, polaron binding energy (E_b) is twice of W_H, so that E_b is calculated to be 194.70 meV and 184.04 meV respectively for DMO, and DBMO. Eventually, we can conclude that polaron binding energy is decreased with substitution of Bi^{3+}.

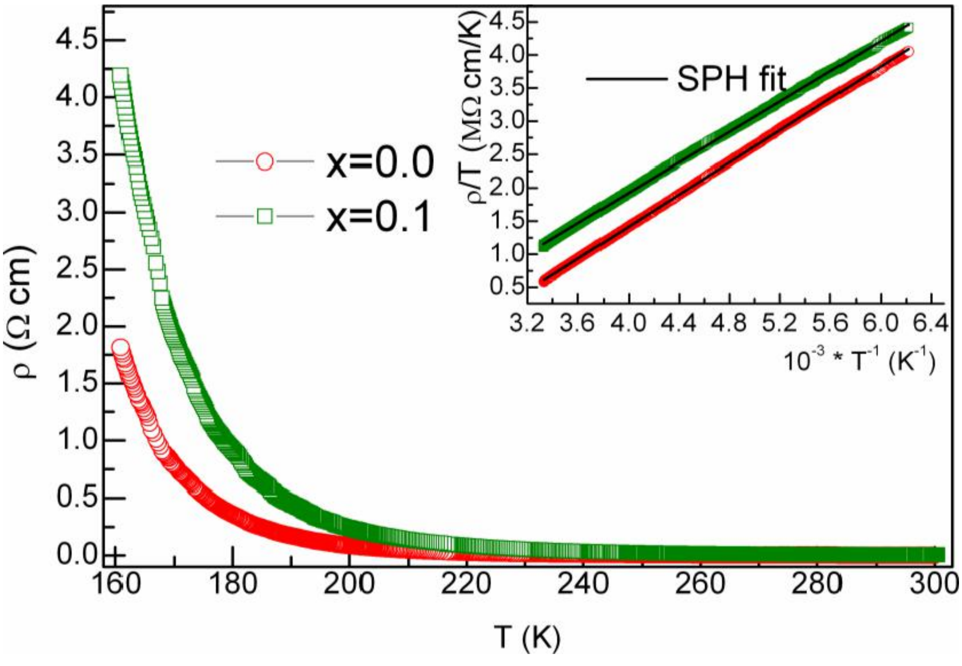

Figure 5.10. Temperature dependent electrical resistivity for $Dy_{1-x}Bi_xMnO_3$ (x=0 and 0.1). Inset illustrates logarithm of resistivity, log (ρ/T) against 1/T. Open symbols represent the experimental data while the solid lines are the result of linear fit to the polaron hopping conduction as described in the text.

b. $Dy_{1-x}Eu_xMnO_3$

Figure 5.11 (a) shows temperature dependence of electrical resistivity, ρ(T) of $Dy_{1-x}Eu_xMnO_3$ from 150 K to 300 K. It is observed that the semiconducting behavior persists in the whole temperature range of measurement. In order to understand the charge transport mechanism for the observed semiconducting behavior, various models such as thermal activation process involving nearest neighbor hopping, hopping of small polarons and VRH were used to fit the ρ(T) data. The equation for thermal activation process with activation energy (E_a) is:

$$\rho(\mathrm{T}) = \rho_0 e^{\frac{E_a}{k_B T}} \tag{5.1}$$

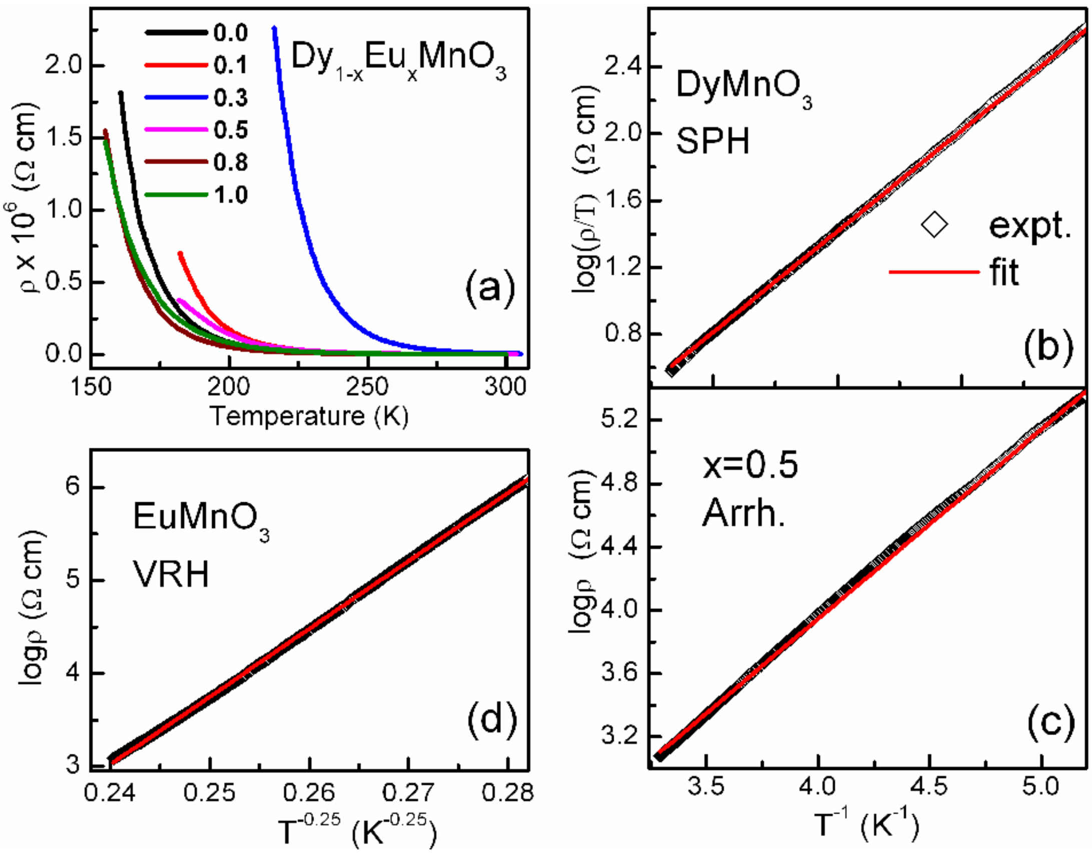

Figure 5.11. (a) Electrical resistivity of $Dy_{1-x}Eu_xMnO_3$ versus temperature for all the compositions of europium (b) SPH fitting for x=0.0 (c) Arrhenius fitting for x=0.5 (d) VRH fitting for x=1.0.

The equations for SPH and VRH conductions are (3.3) and (3.5) respectively. Fitting of the ρ(T) data to all the three models was carried out and the best fits showed that the nature of the electronic transport varied between the two end compounds and from the intermediate compounds as well. It was found that the conduction mechanism for the substituted compounds (x=0.1 to 0.8) is dominated by the activated type of conduction in the whole temperature range whereas the end compounds $DyMnO_3$ and $EuMnO_3$ followed SPH and Mott type VRH mechanisms respectively. Linear fits of ln(ρ/T) with 1/T, lnρ with 1/T and lnρ with $1/T^{1/4}$ are shown in Figs. 5.11 (b), (c) and (d) respectively. The activation energies for the nearest neighbor hopping calculated from the fit parameters are: 110.0, 168.8, 104.4 and 94.4 meV for x= 0.1, 0.3, 0.5 and 0.8 respectively.

It may be noted that different transport mechanisms operate in the solid solutions, $Dy_{1-x}Eu_xMnO_3$. SPH was found in the pristine compound, DMO and then there is a crossover from SPH to activated behavior for the substituted compounds again to VRH for $EuMnO_3$. Various parameters such as average ionic size, grain morphology, charge and structural disorders can directly affect the transport properties. Furthermore, increase in the resistivity with decrease in the temperature observed for all the compounds in the entire temperature range indicates a robust insulating behavior.

5.3.5. Magnetic properties

a. $Dy_{1-x}Bi_xMnO_3$

Temperature dependent molar susceptibility curves for the parent compound, $DyMnO_3$ measured in the ZFC mode under various applied magnetic fields are presented in Fig. 5.12 (I) (main panel) in the temperature range 2-100 K. In all these curves, it is observed that susceptibility increases with decreasing temperature and with increasing magnetic field strength thus exhibiting similar features. A weak feature (marked by arrows in the figure) is seen around 39 K (clearly seen in dχ/dT curves shown in inset) corresponding to sinusoidal incommensurate antiferromagnetic ordering involving Mn^{3+} ions, T_N^{Mn} [33]. A broad peak is observed around 8.4 K for 50 Oe external fields and it downshifts with the applied field to around 5 K for 1 Tesla external field. There is another transition observed ~15 K in the first derivative of dχ/dT versus temperature. Based on the neutron scattering studies by Kimura et al. [34] this transition is attributed to the lock-in-transition of Mn ions, $T_{lock-in}^{Mn}$. However, the long-range antiferromagnetic ordering of Mn^{3+} ions is masked by the huge paramagnetic contribution from the Dy^{3+} ions. Figure 5.12 (II) illustrates the field cooled magnetization data for DMO with temperature for 100 Oe and 1 Tesla field from 2-300 K. It is interesting to see a downturn in the χ_{FC} curves (main panel in Fig. 5.12 (II)) around 2.62 K pointing to the antiferromagnetic ordering of Dy^{3+} moments. This ordering temperature is reduced to low temperatures at 1 Tesla field. The antiferromagnetic ordering of Mn^{3+} ions persists even in the 1 Tesla applied magnetic

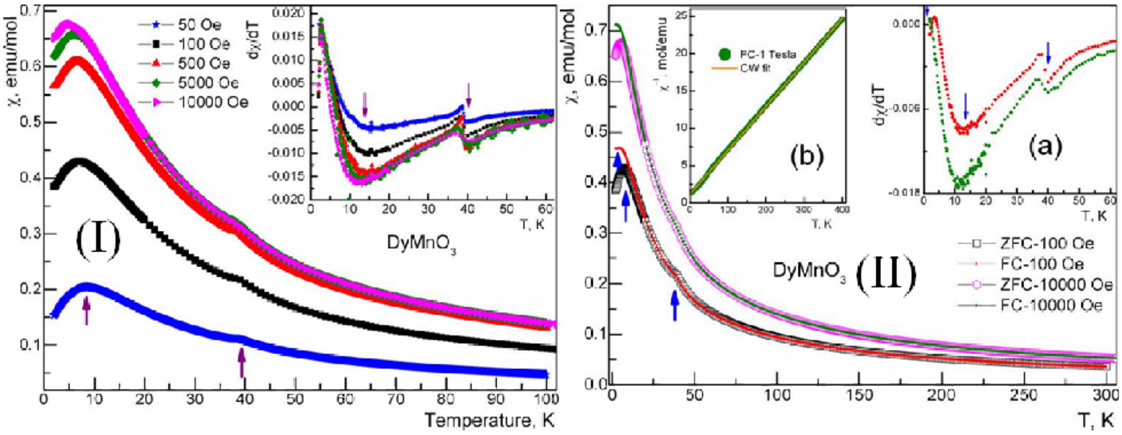

Figure 5.12. (I) Zero Field Cooled susceptibility (χ_{ZFC}) curves measured at different magnetic fields as a function of temperature for $DyMnO_3$. A plot of the first order derivative of magnetization, dχ/dT with respect to temperature is displayed in inset. The arrow marks indicate magnetic transition temperatures whose origins are discussed in the text. Figure 5.4 (II) Plot of Zero Field (χ_{ZFC} – open symbols) and Field Cooled susceptibilities (χ_{FC} – solid lines) as a function of temperature measured under an external magnetic field of 100 Oe and 1 Tesla. All the three magnetic transitions are depicted in the dχ/dT plot shown in inset (a). Curie-Weiss fit to the field cooled data measured at 1 Tesla is shown in inset (b).

field as seen in the first derivative susceptibility curves (arrow mark) shown in inset (a) of Fig. 5.12 (II).

The magnetization results of the parent compound, DMO are similar to those reported for orthorhombic DMO by Harikrishnan et al. [35]. In order to gain insight into the nature of the magnetic transitions observed in the dc magnetization data, ac susceptibility at different frequencies was measured in small ac fields. Real (χ') and imaginary (χ'') components of ac susceptibility (χ) between 2 K and 80 K measured at various ac frequencies and 1.0 Oe ac magnetic field for DMO are displayed in upper and lower panels of Fig. 5.13 respectively. There is no peak shift observed in the frequency. All the three magnetic transitions (marked by arrows) are clearly seen in the first derivative of ac susceptibility with temperature as a shown in inset of Fig. 5.13.

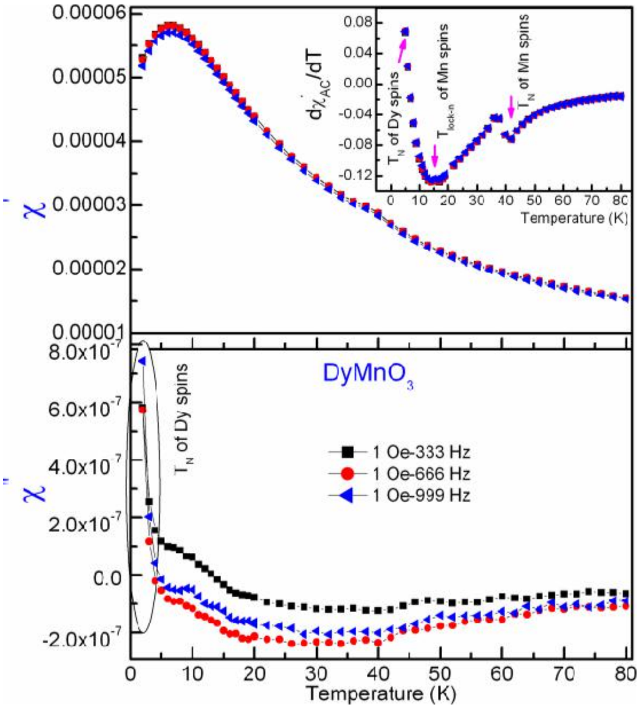

Figure 5.13. Temperature dependence of in-phase (χ') (top panel) and out-of-phase (χ'') (bottom panel) components of ac susceptibility as a function of temperature in the frequency range 333 Hz to 1000 Hz at a driving ac field of 1 Oe with a zero-bias dc magnetic field. Inset displays the first temperature derivative of χ' measured at different frequencies. The arrows indicate the location of all the three magnetic transitions which agree with those observed in the dc magnetization measurements.

Bismuth substituted compound, $Dy_{0.9}Bi_{0.1}MnO_3$ also exhibits similar features that have been observed in the pristine compound, DMO. While the antiferromagnetic transition of Mn^{3+} ions occur at the same temperature, the lock-in transition temperature of Mn^{3+} ions and antiferromagnetic transition temperature of Dy^{3+} spins ordering temperature are reduced slightly. This reduction could plausibly be attributed to the polyhedral distortions caused due to the substitution which affects the 3d-4f interaction. Results of temperature dependence of magnetization data of $Dy_{0.9}Bi_{0.1}MnO_3$ are summarized in Figs. 5.14 (I) and (II). Effective magnetic moments are calculated by fitting the field cooled molar susceptibility data to Curie – Weiss (CW) law given by the equation (3.7). The Curie-Weiss fits to the inverse susceptibility data in the whole temperature range at 1 Tesla field for both compounds are shown in inset (b) in the Figs. 5.12 (II) and 5.14 (II).

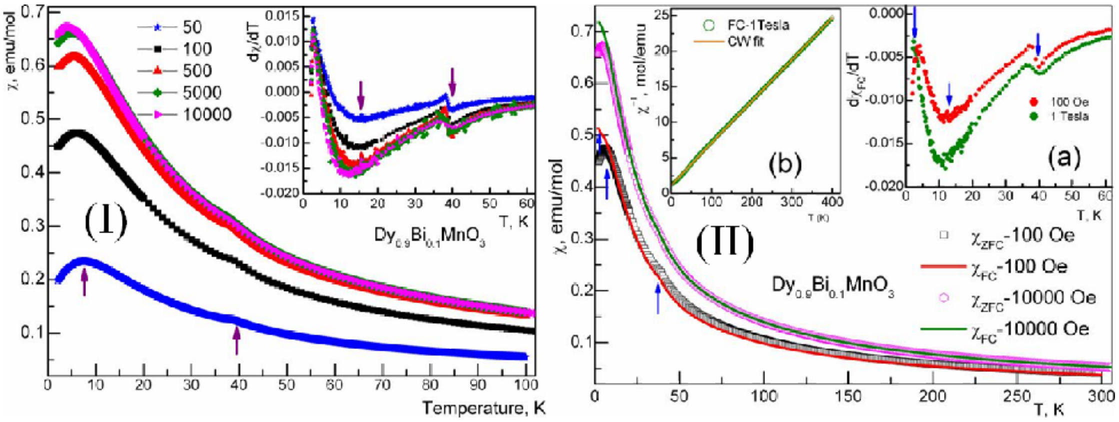

Figure 5.14. (I) χ_{ZFC} (T) of DBMO measured at different applied magnetic fields (main panel). $d\chi/dT$ is shown in inset. Figure 5.6 (II) χ_{ZFC} and χ_{FC} as a function of temperature measured at 100 Oe ad 1 Tesla external magnetic fields. Inset (a) shows first derivative of susceptibility and (b) shows CW fit to the 1 Tesla χ_{FC} data.

The magnitudes of C and θ were used to determine the effective magnetic moment, $\mu_{eff.}$ (expt.) and Curie – Weiss temperature, θ. Thus, the obtained values of $\mu_{eff.}$ (expt.) and θ are 11.66 μ_B, –18.8 K and 11.65 μ_B, –19.2 K for DMO & DBMO respectively. There is no significant change in the effective magnetic moment for 10 at.% bismuth substitution of DMO. Assuming the magnetic contributions from the rare earth and Mn ions to the paramagnetic moment, effective magnetic moment which is a sum of the individual atomic magnetic moments of Dy^{3+} (10.62 μ_B) and Mn^{3+} (4.89 μ_B) is calculated from the equation:

$$\mu_{eff.}\,(\text{cal.}) = \sqrt{(1-x)\left(\mu_{Dy^{3+}}\right)^2 + \left(\mu_{Mn^{3+}}\right)^2} \qquad (5.2)$$

Here x is concentration of Bi^{3+} (x= 0 & 0.1). The calculated effective magnetic moments, $\mu_{eff.}$ (cal.) thus calculated are 11.69 μ_B and 11.2 μ_B for x=0.0 and 0.1 respectively. Experimental effective magnetic moment of DMO is in agreement with the calculated moment value. The higher observed value of 11.65 μ_B for DBMO as compared to 11.2 μ_B implies the presence of localized magnetic moments. Negative values of the Curie–Weiss temperature (θ) indicate that antiferromagnetic interactions between magnetic moments are dominant at low temperatures.

In Figures 5.15 (a) & (b), isothermal magnetization curves at representative temperatures are presented. Magnetization does not saturate up to 7 Tesla magnetic fields. Expanded view of the M-H curves in the low field region is shown in insets in the respective panels revealing hysteresis. It is to be noted that both compounds exhibit similar features and a clear ferromagnetic behavior could be observed for temperatures below 40 K i.e. for temperatures below the Neel temperature of Mn, T_N^{Mn}. Values of coercive field (H_c) and remnant magnetization (M_r) of 1520 Oe, 0.174 μ_B/f.u. for DMO and 1365 Oe, 0.165 μ_B/f.u. for DBMO are observed in M-H loops collected at 2 K and these values are reduced to ~400 Oe and ~0.048 μ_B/f.u. at 8 K for both compounds. The ferromagnetic state may be ascribed to the coexistence of short range parallel arrangement of Dy and Mn spins. At low temperatures, the magnetic spins of Dy and Mn are strongly correlated via apical oxygen ions as compared to weaker Dy-Dy and Mn-Mn interactions. When the temperature is increased from 2 K to 8 K, which is above T_N^{Dy}, Dy^{3+} spins change their direction while the direction of Mn^{3+} spins does not alter. This results in the reduction of the coercive field. As temperature of the measurement increases beyond T_N^{Mn}, both Dy and Mn spins order randomly leading to a paramagnetic state. This paramagnetic state could be ascertained by the linear M-H curves at 45 K and 300 K as shown in Figs. 5.15 (a) and (b). The evolution of the magnetic transitions in M-H data is consistent with the temperature dependence of dc and ac magnetization data.

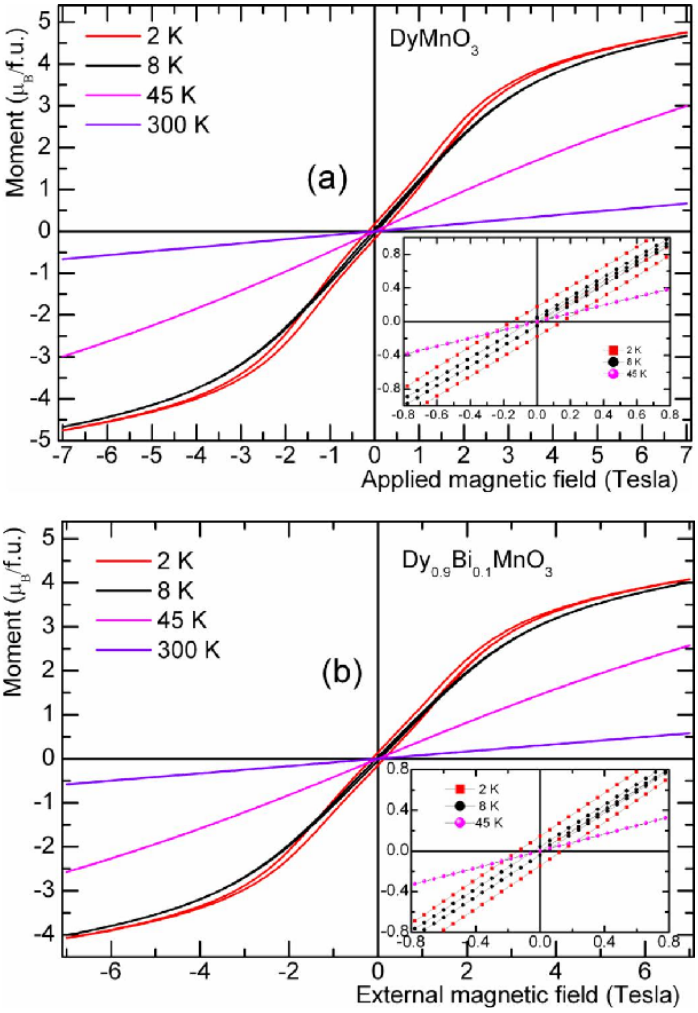

Figure 5.15. Magnetic hysteresis (M-H) curves for (a) DMO and (b) DBMO in the magnetic field range -7 T to +7 T at selected temperatures. Hysteresis loops are observed for temperatures below 40 K without saturation of magnetic moment. Paramagnetic behavior is seen for temperatures above 40 K.

b. $Dy_{1-x}Eu_xMnO_3$

Molar susceptibility of $Dy_{1-x}Eu_xMnO_3$ (x=0.1 - 1.0) as a function of temperature at different applied fields is shown in Fig. 5.16.

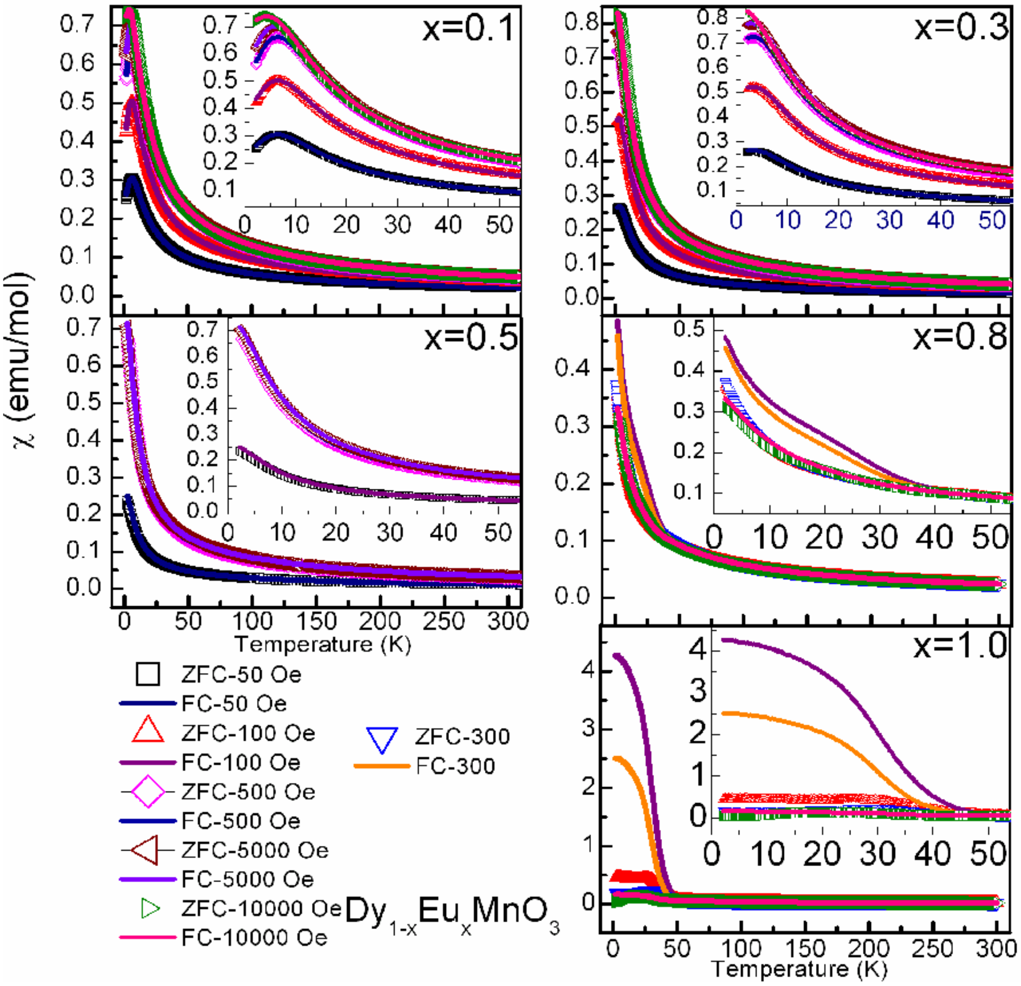

Figure 5.16. Molar susceptibility curves measured in the zero field cooled and field cooled cycles for DEMO compounds with x 0.1 to 1.0 as mentioned in the respective graphs.

There are several features to note:

1. As can be seen in Figs. 5.16 (a), (b) and (c), the χ_{ZFC} and χ_{FC} curves measured under various strengths of the magnetic field overlap whose magnitude increased with decreasing the temperature in the entire temperature range for compounds with x = 0.1, 0.3 and 0.5 respectively. However, there appears a peak in both the χ_{ZFC} and χ_{FC} curves at all the fields whose temperature de-

creases slightly with filed strength indicating the existence of a magnetic transition. Further, the magnetic transition temperature is reduced with increasing the europium concentration, x up to x=0.5. In view of broad peaks, transition temperatures were identified from the first derivative of the susceptibility curves, dχ/dT versus temperature. Thus the estimated transition temperatures are ~12 K, ~10 K and ~5 K for x=0.1, 0.3 and 0.5 respectively. Figure 5.17 reports typical dχ/dT – T plots for selected compounds.

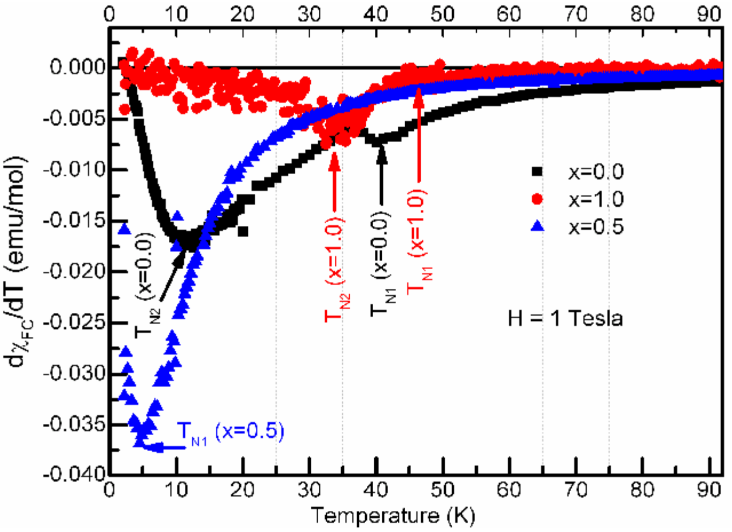

Figure 5.17. First derivative of molar susceptibility with temperature for the compounds, $Dy_{1-x}Eu_xMnO_3$, x=0.0, 0.5 and 1.0 as indicated in the figure.

2. In the case of x=0.8, χ_{ZFC} and χ_{FC} curves merge down to 50 K below which they deviate with magnitude of χ_{FC} greater than χ_{ZFC}. However, the susceptibility data measured at 1 Tesla field does not show any deviation between χ_{ZFC} and χ_{FC}. Irrespective of the applied field strength both χ_{ZFC} and χ_{FC} continue to increase with decrease in the temperature without any anomalies. In the absence of signatures for a typical antiferromagnet whose magnetization decreases as temperature decreases, the magnetic response may be ascribed to random arrangement of magnetic spins. These experimental findings point to the paramagnetic nature of this compound in the entire temperature range.

3. For $EuMnO_3$, χ_{ZFC} and χ_{FC} curves merge with each other down to ~50 K, below which χ_{ZFC} displayed a peak while χ_{FC} increased. A large bifurcation in the curves was observed at low temperatures and low fields. $d\chi/dT$ curve revealed two types of transitions as marked by arrows in the Fig. 5.17 around 50 K and 35 K. By comparing with literature, a small broad anomaly at <50 K may be ascribed to the onset of incommensurate antiferromagnetic ordering of Mn ions (T_{N1}) and the low temperature anomaly around 35 K may be associated with the collinear arrangement of Mn^{3+} ions in the antiferromagnetic state (T_{N2}). Nevertheless, magnetization at low temperatures tends to increase/saturate with lowering temperature resembling that of a ferromagnet. This may imply the existence of ferromagnetic correlations inside the antiferromagnetic state. Hence the low temperature magnetic ground state may be A-type AFM. This is corroborated with the observation of large coercive fields from M - H curves whose results will be discussed in the ensuing sections.
4. $\chi(T)$ data of all the compounds follow Curie-Weiss behavior in the paramagnetic state. The CW fit parameters thus obtained from the fit were used to determine the values of $\mu_{eff.}$ at various fields. For a given compound, with increase in the field strength, $\mu_{eff.}$ was found to increase. Fig. 5.18 demonstrates this behavior (plot with left Y – bottom X axes). Also $\mu_{eff.}$ decreases with Eu substitution at Dy site. The effective magnetic moment is calculated from the chemical formulae of the compounds from the relation:

$$\mu_{eff.}(cal.) = \sqrt{(1-x) \times \mu_{Dy^{3+}}^2 + x \times \mu_{Eu^{3+}}^2 + \mu_{Mn^{3+}}^2} \qquad (5.3)$$

Here magnetic moment of Eu^{3+} is equal to 3.46 μ_B. The values of $\mu_{eff.}$ (Cal) thus calculated are found to reduce with increase in the europium concentration, x in DEMO. It may be remarked here that $\mu_{eff.}$ (expt.) obtained from 1 Tesla data is close to the calculated value. Moreover, both $\mu_{eff.}$ values are showing similar behavior (plot with right Y – top X axes) as seen in Fig. 5.18.

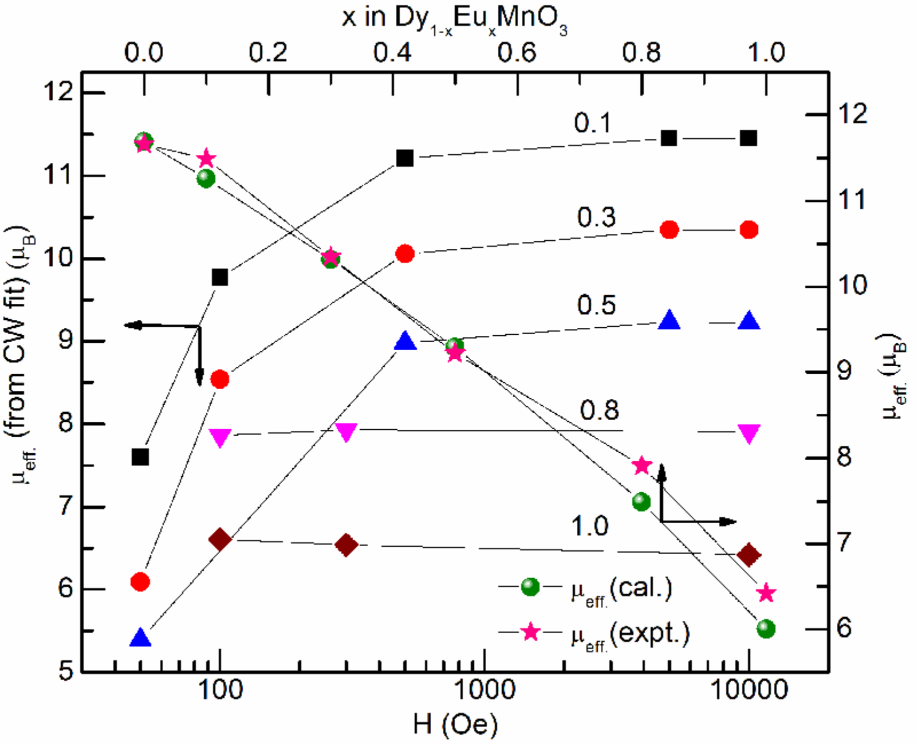

Figure 5.18. Semi log graph between the experimental effective magnetic moment vs. applied field (left Y axis and bottom X axis) for the compounds mentioned in the plot. Comparison of the effective magnetic moments with respect to europium content, x (right Y axis and Top X axis) for all the compounds.

As discussed in the earlier sections, the origin for a series of magnetic transitions observed in DMO was attributed to antiferromagnetic coupling between Mn ions. Comparison of the experimental findings of the substituted compounds with those of the end compounds, DMO and EMO, the following conclusions can be made:

a. The x=0.1, 0.3 and 0.5 compounds with a single anomaly in the $\chi(T)$ data exhibit a magnetic transition from paramagnetic to antiferromagnetic structure with up-up-down-down spin arrangement or E-type magnetic ordering. This type of ordering was observed in rare earth manganites with large ionic radius [36].

b. x=0.8 compound does not undergo any type of magnetic ordering.

c. EMO indicates the onset of IC-AFM for $T \leq 50$ K and C-AFM around 35 K which agrees with the neutron diffraction measurements carried out by Ferreira et al. [37] revealing A-AFM.

Further, to clarify the observations of the temperature dependence of magnetization data and to identify the magnetic nature of these materials, isothermal magnetization measurements at different fixed temperatures were performed. M–H curves for all the compounds at selected temperatures are presented in Fig. 5.19. A linear relationship between the magnetic moment and magnetic field was observed at high temperatures (300 K and 100 K) for all the compounds. It is seen from the Fig. 5.20, that the isothermal curves measured at 2 K for the compounds with x=0.1 to 0.8 show S shape wherein the moment increases gradually in the low magnetic field region without hysteresis followed by a slope change which again increases with increase in the field strength. As temperature of the measurement increases, M-H curves show linear behavior. These S type curves have a very low remnant magnetization and do not exhibit coercivity. On the other hand, EMO has a large coercive filed. Hysteresis curves of DMO and EMO with appreciable coercive fields show no sign of saturation up to 7 T. However, the remnant magnetization is small, 0.174 μ_B/f.u. and 0.214 μ_B/f.u. for DMO and EMO respectively. These features indicate the short range ferromagnetic correlations within the antiferromagnetic state.

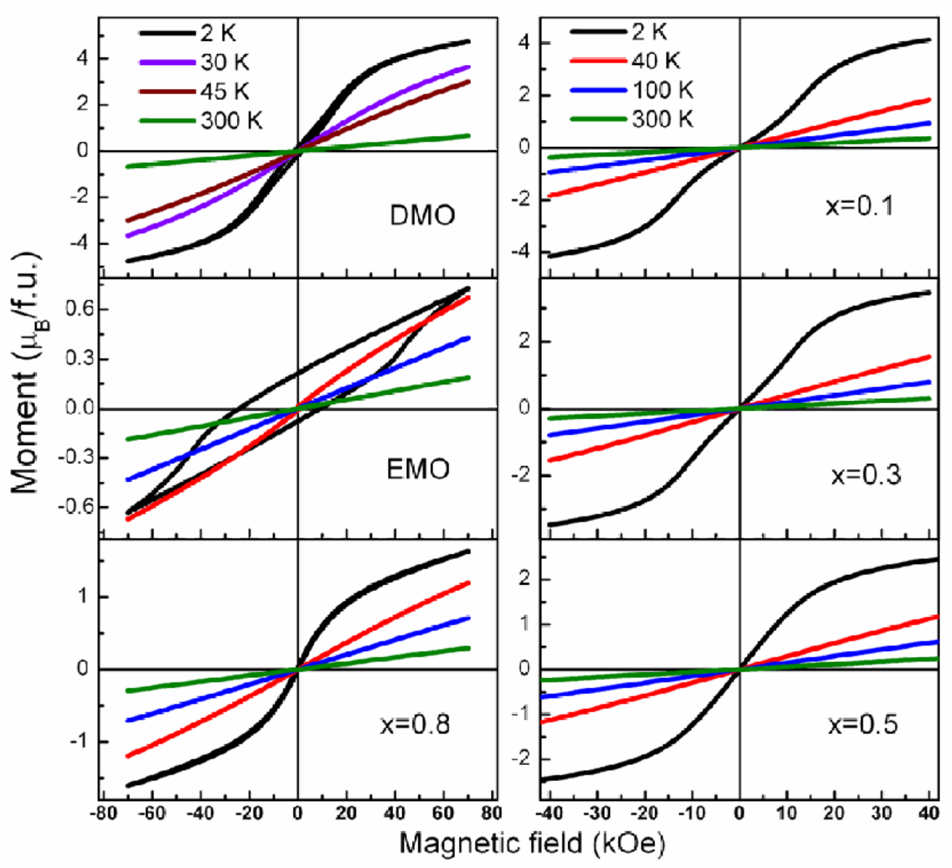

Figure 5.19. Magnetization loops a function of applied magnetic field measured at different fixed temperatures for all the europium concentrations.

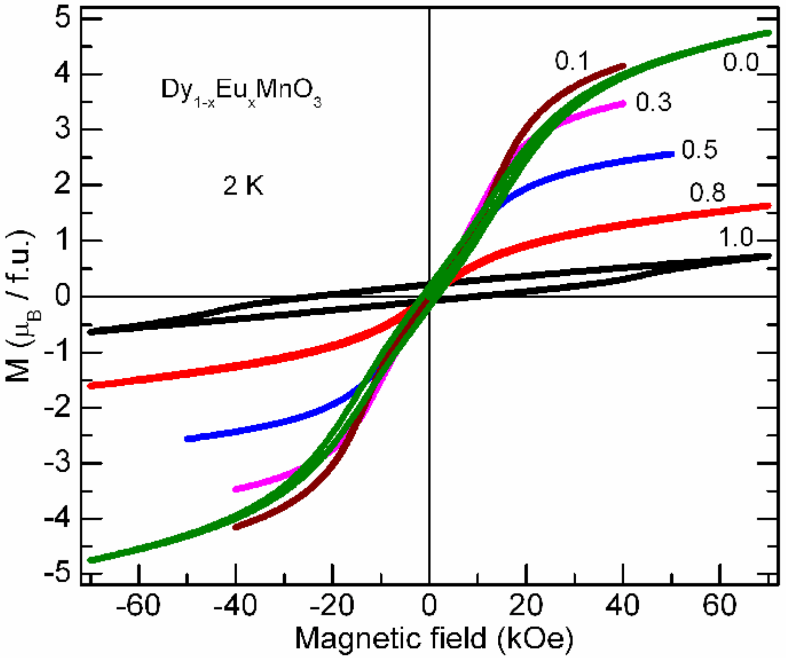

Figure 5.20. Magnetic moment (M) against applied magnetic field recorded at 2 K for $Dy_{1-x}Eu_xMnO_3$ (x=0.0-1.0). Reduction of magnetic moment by Dy sub lattice dilution with a non magnetic Eu ion is evident from the curves.

5.4. CONCLUSIONS

Polycrystalline $Dy_{1-x}Bi_xMnO_3$ (x=0.0 & 0.1) and $Dy_{1-x}Eu_xMnO_3$ (x=0.0-1.0) compounds were prepared by solid state reaction. All the compounds crystallize in the orthorhombic structure but with changes in the bond lengths and bond angles of metal-oxygen to accommodate the larger Bi and Eu ions. Raman spectroscopy studies compliment this structural variation. Contributions from the atomic vibrations to the observation of Raman bands have been established and assigned to symmetry stretching and anti symmetry stretching, bending and tilting modes. These modes are hardened in the case of Bi^{3+} substitution of $DyMnO_3$. In contrast, Raman band frequencies of tilting and bending modes in DEMO decreased showing softening. The transport results reveal that all the compounds show semiconducting nature. While DBMO follows SPH conduction similar to DMO, Eu substituted compounds showed activated type of conduction. EMO showed VRH type conduction. Hopping energy ($E_{hop.}$) is calculated and it is observed that $E_{hop.}$ decreases for DBMO. Consequently, polaron binding energy is decreased. Activated energy for DEMO also was found to reduce. Temperature dependence of the first derivative of magnetization of DBMO measured at several applied fields revealed anti ferromagnetic transitions involving Mn and Dy ions. All DEMO compounds showed only one type of magnetic transition i.e., antiferromagnetic nature corresponding to Mn ions. The fitted Curie – Weiss temperatures also suggest the existence of antiferromagnetic interactions in all the materials. The magnetic field dependent magnetization at various temperatures revealed paramagnetic nature down to 8 K below which hysteresis loops are observed. The presence of strong ferromagnetic correlations between Dy and Mn spins through apical oxygen ions results in the large coercive fields. For temperatures above the antiferromagnetic temperature of manganese ions (39 K) M-H curves show almost straight lines implying an absence of any ferromagnetic interactions in the compounds. Different magnetic transitions: from high temperature paramagnetic state to intermediate temperature antiferromagnetic state to low temperature ferromagnetic states are observed in the M-H data.

5.5. REFERENCES

[1] J.M.D. Coey, M. Viret and S. Von Molnar, Adv. Phys., **48**, (1999), 167.

[2] T. Kimura, S. Ishihara, H. Shintani, T. Arima, K.T. Takahashi, K. Ishizaka and Y. Tokura, Phys. Rev. B, **68**, (2003), 060403.

[3] N. Lee, Y.J. Choi, M. Ramazanoglu, W. Ratcliff II, V. Kiryukhin and S.-W. Cheong, Phys. Rev. B, **84,** (2011), 020101R.

[4] Y. Chen, H. Yuan, G. Li, Ge Tian and S. Feng, J. Crystal Growth, **305**, (2007), 242.

[5] K. Singh, S. Patnaik, S.D. Kaushik and V. Siruguri, Phys. Rev. B, **81**, (2010), 184406.

[6] C. Zener, Phys. Rev., **82**, (1951), 403.

[7] S. Harikrishnan, C.M. Naveen Kumar, S.S. Rao, H.L. Bhat, S.V. Bhat and Suja Elizabeth, J. Appl. Phys., **104**, (2008), 023902.

[8] S. Robler, S. Harikrishnan, U.K. Robler, Suja Elizabeth; H.L. Bhat, F. Steglich and S. Wirth, J. Phys: Conf. Series, **200**, (2010), 012168.

[9] S. Harikrishnan, C.M. Naveen Kumar, H.L. Bhat, Suja Elizabeth, U.K. Robler, K. Dorr, S. Robler and S. Wirth, J. Phys.: Condens. Matter, **20**, (2008), 275234.

[10] S. Harikrishnan Nair, C.M.N. Kumar, H.L. Bhat, Suja Elizabeth and Th. Bruckel, Phys. Rev. B, **83**, (2011), 104424.

[11] A. Moreira dos Santos, S. Parashar, A.R. Raju. Y.S. Zhao, A.K. Cheetham and C.N.R. Rao, Solid State Commun., **122**, (2002), 49.

[12] F. Sugawara, S. Iiida, Y. Syono and S. Akimoto, J. Phys. Soc. Jpn., **25**, (1968) 1553.

[13] D.I. Khomskii, J. Magn. Magn. Mater., **306**, (2006), 1.

[14] Wei-Tin Chen, Falak Sher, Neil D. Mathur, Christopher M. Kavanagh, Finlay D. Morrison and J. Paul Attfield, Chem. Mater., **24**, (2012), 199.

[15] J.L. Garcı´a-Munoz, C. Frontera, M.A.G. Aranda, C. Ritter, A. Llobet, M. Respaud, M. Goiran, H. Rakoto, O. Masson, J. Vanacken and J.M. Broto, J. Solid State Chem., **171**, (2003), 84.

[16] A.M.D. Santos, A.K. Cheetham, T. Atou, Y. Syono, Y. Yamaguchi, K. Ohoyama, H. Chiba and C.N.R. Rao, Phys. Rev. B, **66**, (2002), 064425.

[17] A.C. Larson and R.B. Von Dreele, General Structure Analysis System (GSAS) (Los Alamos National Laboratory Report LAUR 86–748), (2003).

[18] K. Yadagiri and R. Nithya, Powder Diffra., **4**, (2016), 1.

[19] K. Yadagiri and R. Nithya, accepted in ICDD database

[20] K. Momma and F. Izumi, J. Appl. Crystallogr., **44**, (2013), 1272.

[21] K. Yadagiri and R. Nithya, RSC Adv., **6**, (2016), 95417.

[22] L.M. Carrón, A. de Andrés, M.J.M. Lope, M.T. Casais and J.A. Alonso, Phys. Rev. B, **66**, (2002), 174303.

[23] M.N. Iliev, M.V. Abrashev, V.N. Popov and V.G. Hadjiev, Phys. Rev. B, **67**, (2003), 212301.

[24] M.V. Abrashev, J. Bäckström, L. Börjesson, V.N. Popov, R.A. Chakalov, N. Kolev, R.-L. Meng and M.N. Iliev, Phys. Rev. B, **65**, (2002), 184301.

[25] Xuan Cai, Lei Shi, Shiming Zhou, Jiyin Zhao, Yuqiao Guo and Cailin Wang, J. Appl. Phy., **116**, (2014), 103903.

[26] M.N. Iliev and M.V. Abrashev, Phys. Rev. B, **5**, (1998), 2872.

[27] M.C. Weber, J. Kreisel, P.A. Thomas, M. Newton, K. Sardar and R.I. Walton, Phys. Rev. B, **85**, (2012), 054303.

[28] M.C. Biesinger, B.P. Payne, A.P. Grosvenor, L.W.M. Lau, A.R. Gerson and R.St.C. Smart, Appl. Surf. Sci., **257**, (2011), 2717.

[29] D.C. Worledge, G. Jeffrey Snyder, M.R. Beasley, T.H. Geballe, Ron Hiskes and Steve DiCarolis, J. Appl. Phys., **80**, (1996), 5158.

[30] T.T.M. Palstra, A.P. Ramirez, S.W. Cheong, B.R. Zegarski, P. Schiffer and J. Zaanen, Phys. Rev. B, **56**, (1997), 5104.

[31] M. Jaime, M.B. Salamon, M. Rubinstein, R.E. Treece, J.S. Horwitz and D.B. Chrisey, Phys. Rev. B, **54**, (1996), 11914.

[32] J.M. De Teresa, K. Dorr, K.H. Muller, L. Schultz and R.I. Chakalova, Phys. Rev. B, **58**, (1998), R5928.

[33] K. Yadagiri, R. Nithya, Neeraj Shukla and A.T. Satya, AIP Advances, **7**, (2017), 035003 (1-10).

[34] T. Kimura, G. Lawes, T. Goto, Y. Tokura and A.P. Ramirez, Phys. Rev. B, **71**, (2005), 224425.

[35] S. Harikrishnan, S. Robler, C.M. Naveen Kumar, H.L. Bhat, U.K. Robler, S. Wirth, F. Steglich and Suja Elizabeth, J. Phys.: Condens. Matter., **21**, (2009), 096002.

[36] Na Zhang, S. Dong, Z. Fu, Z. Yan, F. Chang and J. Liu, Sci. Rep., **4**, (2014), 6506 (1-7).

[37] W.S. Ferreira, J. Agostinho Moreira, A. Aldeida, M.R. Chaves, J.P. Araujo, J.B. Oliveira, J.M. Machado Da Silva, M.A. Sa, T.M. Mendonca, P. Simeao Carvalho, J. Kreisel, J.L. Ribeiro, L.G. Vieira, P.B. Tavares and S. Mendonca, Phys. Rev. B, **79,** (2009), 054303.

CHAPTER – 6

INVESTIGATION OF MULTIFUNCTIONAL PROPERTIES OF CO - SUBSTITUTION AT Dy AND Mn SITE OF $DyMnO_3$ - $Dy_{0.55}Sr_{0.45}Mn_{1-x}Fe_xO_3$

6.1. INTRODUCTION

Divalent Sr substituted $NdMnO_3$ ($Nd_{0.5}Sr_{0.5}MnO_3$) exhibits Paramagnetic Metallic (PM-M) to a Ferro Magnetic Metallic (FM-M) transition around 255 K [1]. With further reduction in the temperature, FM-M state changes to Charge Ordered Anti Ferro Magnetic Insulating (CO-AFM-I) state around 155 K. Neutron diffraction reports by Abdel-Latif et al. [2] on $Nd_{0.65}Sr_{0.35}Mn_{0.4}Fe_{0.6}O_3$ revealed weak ferromagnetic transitions around 287 K and 520 K. With an aim to induce ferromagnetism in an analogous compounds, we have undertaken co-substitution of Sr and Fe at Dy and Mn sites in $DyMnO_3$ and we have chosen $Dy_{0.55}Sr_{0.45}Mn_{1-x}Fe_xO_3$ (x=0.0 to 1.0; 0.2) system and investigated structural and other physical properties. Synthesis followed by physical property studies are described in the following sections.

6.2. EXPERIMENTAL PROCEDURE

Polycrystalline materials of $Dy_{0.55}Sr_{0.45}Mn_{1-x}Fe_xO_3$ (x=0.0-1.0:0.2) (DSMFO) were synthesized by the conventional ceramic method using high purity raw oxide powders: Dy_2O_3, $SrCO_3$, Fe_2O_3 and MnO_2 taken according to stoichiometric ratios. The powders were mixed thoroughly by grinding for 2 hrs. in an agate mortar and pestle. The mixture was then calcined at 1300 °C for 24 hours with intermediate grinding. The resulting compounds were characterized by the powder X-ray diffraction (STOE diffractometer, Germany) technique at room temperature. Raman spectra of the materials were recorded at room temperature using a micro Raman spectrometer (Renishaw) and the excitation wavelength used was 514.5 nm from a Ar-ion laser source. ^{57}Fe Mossbauer measurements were carried out in a transmission mode with a ^{57}Co (Rh) radioactive source in constant acceleration mode using a standard PC based Mossbauer spectrometer equipped with a Wiss El velocity drive. Velocity calibration of the spectrometer was carried out with a natural iron absorber at room temperature [3-5]. Electrical resistivity of DSMFO was measured by a four probe technique. Magnetic properties were carried out using MPMS 3 Ever Cool SQUID VSM (Quantum Design) magnetometer. Temperature dependent magnetization (M-T) data in experimental conditions as described in the Chapter 2 were collected. Isothermal magnetization measurements (M-H) were performed as function of magnetic field at various temperatures. Temperature and frequency dependent dielectric properties of $Dy_{0.55}Sr_{0.45}MnO_3$, $Dy_{0.55}Sr_{0.45}Mn_{0.6}Fe_{0.4}O_3$ and $Dy_{0.55}Sr_{0.45}FeO_3$ were carried out using the broadband spectrometer.

6.3. RESULTS AND DISCUSSION

6.3.1. X-ray diffraction

Polycrystalline DSMFO materials crystallized with orthorhombic structure. Figure 6.1 displays X-ray diffraction patterns of DSMFO. Miller indices (hkl) of the major diffraction peaks for the pristine compound (x=0.0) have been given in the figure. Compounds with x=0.8 and 1.0 have manganite as a major phase and a minor secondary phase. The peaks corresponding to the secondary phase are marked by asterisk for x=1.0.

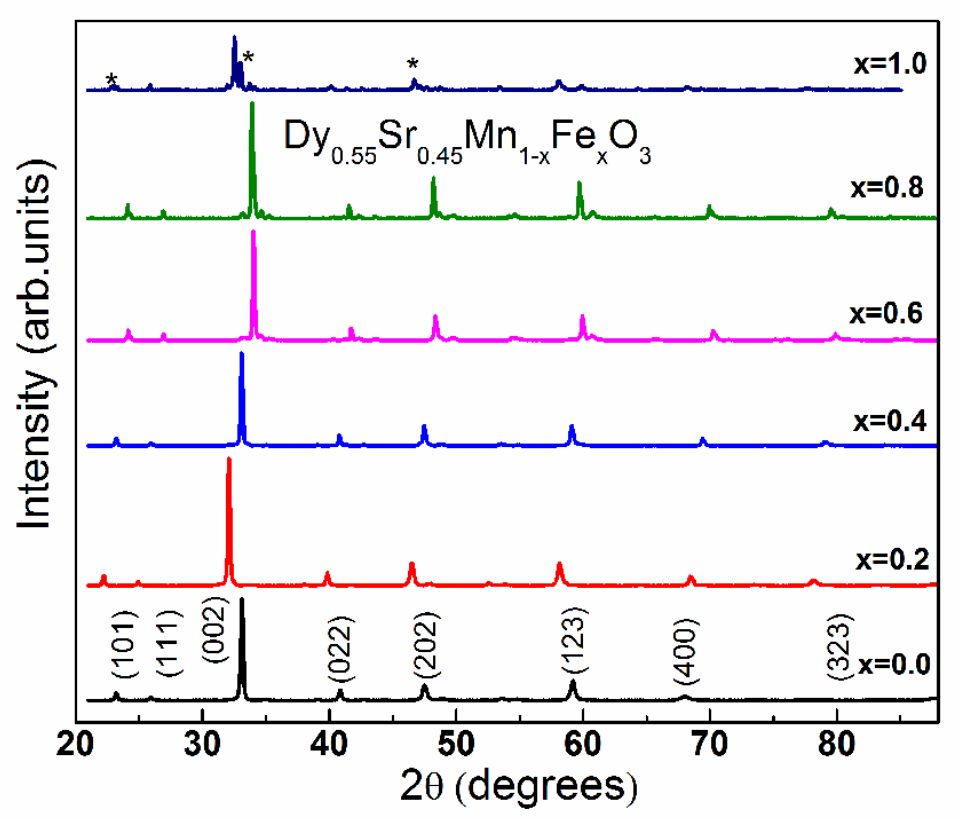

Figure 6.1. Experimental X-ray diffraction patterns of $Dy_{0.55}Sr_{0.45}Mn_{1-x}Fe_xO_3$ collected in an angular range of 2θ from 20° to 90° during a normal scan. Major reflections for the orthorhombic structure have been indexed for x=0.0.

Powder diffraction patterns of pristine compound, $Dy_{0.55}Sr_{0.45}MnO_3$ and $Dy_{0.55}Sr_{0.45}Mn_{0.8}Fe_{0.2}O_3$ were analyzed for their structural properties and communicated to ICDD [6]. These two compounds exhibited orthorhombic structure. The other substituted compounds with x=0.4 and 0.6 retained the orthorhombic structure. As mentioned above, compounds with higher concentrations of iron i.e., x=0.8 and 1.0 contained minor impurity phases. Lattice parameters and unit cell volume for manganite phase are tabulated in Table 6.1. It is observed that orthorhombic unit cell volume increased with increasing of iron substitution in this series.

Table 6.1. Lattice parameters for $Dy_{0.55}Sr_{0.45}Mn_{1-x}Fe_xO_3$.

x	*a* (Å)	*b* (Å)	*c* (Å)	V (Å^3)
0.0	5.421	7.625	5.402	223.285
0.2	5.419	7.636	5.403	223.585
0.4	5.412	7.641	5.409	223.667
0.6	5.534	7.626	5.322	224.633
0.8	5.539	7.641	5.304	224.528
1.0	5.589	7.633	5.311	226.603

6.3.2. Raman spectroscopy

Room temperature Raman spectra of DSMFO are shown in Fig 6.2. In contrast to DMO, the RT Raman spectra of DSMFO consist of broad bands between 400 cm^{-1} to 800 cm^{-1}. The different Raman spectra could be due to changes in the JT distortions of the MnO_6 octahedra [7-10] leading to changes in the local atomic site symmetries resulting in the observed spectra. As Fe concentration increases in DSMFO, peak broadening decreases with increasing the mode frequencies.

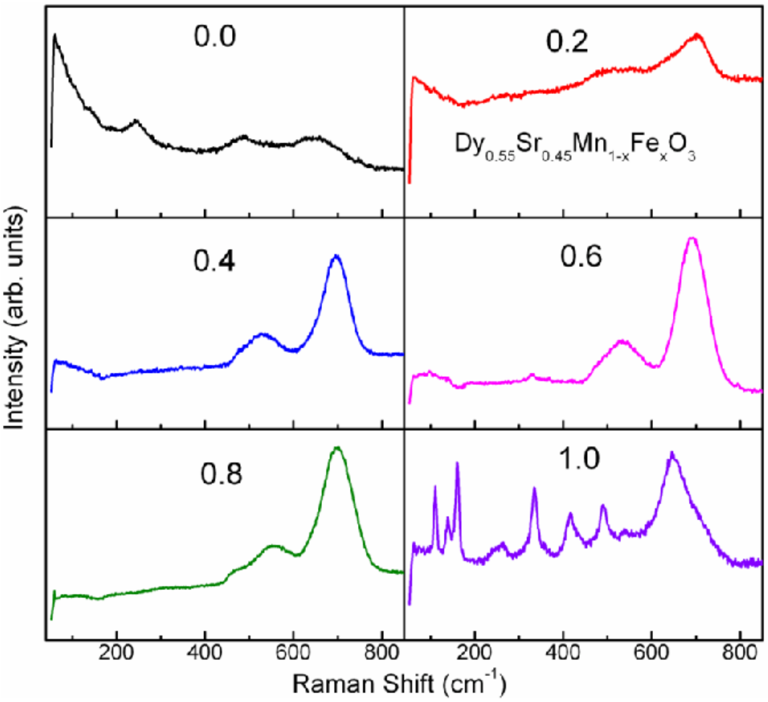

Figure 6.2. Raman spectra of $Dy_{0.55}Sr_{0.45}Mn_{1-x}Fe_xO_3$ solid solutions.

6.3.3. Electrical Resistivity

Figure 6.3 shows resistivity behavior as a function of temperature, ρ(T) for DSMFO. All the compounds display semiconducting nature in the whole temperature range of measurement. With increase in the Fe content in DSMFO, resistivity increased. To find the conduction mechanism in these oxides, analysis of the data was carried out using nearest neighbor, small polaron and variable rage hopping models [11-16]. The entire ρ(T) data could not be fitted to a single model. There are deviations in the fits suggesting that there are different types of conduction processes operating in different temperature ranges. In the temperature range, 300 K to 160 K, ρ(T) data of all the compounds could be fitted well to the variable range hopping equation (3.3) implying the dominant conduction mechanism. The values of the constant, T_0 obtained from the fitting parameters are of the order of 10^6 K.

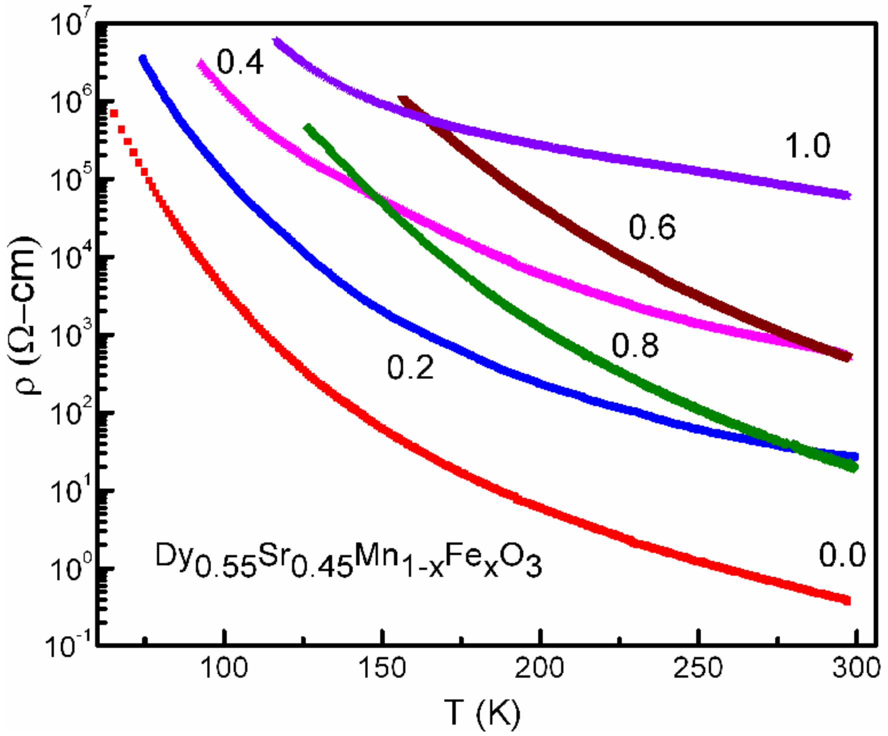

Figure 6.3. Variation of electrical resistivity (ρ) for $Dy_{0.55}Sr_{0.45}Mn_{1-x}Fe_xO_3$ compounds with x = 0.0, 0.2, 0.4, 0.6, 0.8 and 1.0 with temperature.

6.3.4. Mossbauer spectra

Selected ^{57}Fe Mossbauer spectra of DSMFO recorded at room temperature are displayed in Fig. 6.4. Compounds with x=0.2 and 0.4 exhibit quadrupole spliting in the center of the spectra. A sextet resonant absorption pattern appeared for higher iron concentrations indicating an additional phase with a magnetic hyperfine interaction. Values of Isomer Shift (IS) and Quadrupole multiplet Splitting (QS) are presented in Table 6.2. If the values of IS lie between 0.3 to 0.6 mm/sec then trivalent state is assigned to Fe ions and IS values smaller than 0.3 mm/sec correspond to tetravalent iron ions [17]. By comparing with the standard values, it is found that the compounds with x=0.2 and 0.4 have only Fe^{3+} ions whereas compounds with higher concentration of iron consist of both tri and tetra valent iron ions [18-20].

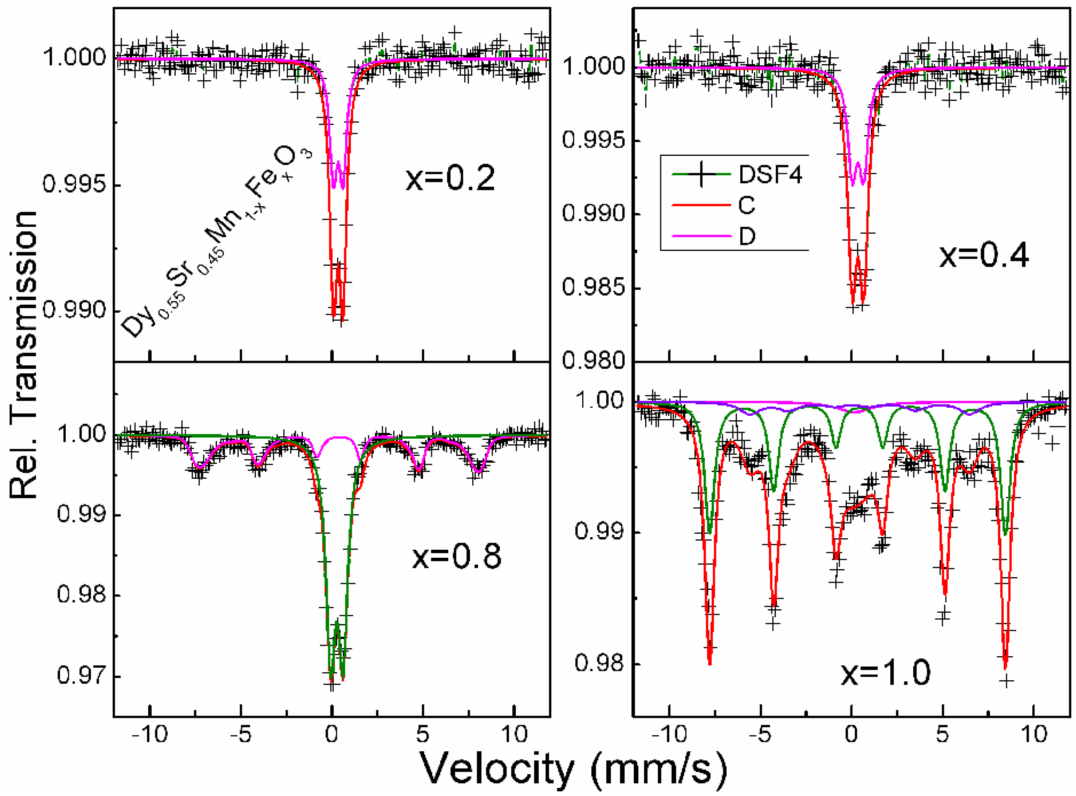

Figure 6.4. Room temperature Mossbauer spectra of $Dy_{0.55}Sr_{0.45}Mn_{1-x}Fe_xO_3$ (x=0.2, 0.4, 0.8 and 1.0) showing gradual changes in the resonance profile with increasing iron concentration.

Table 6.2. Mossbauer spectroscopy parameters: Isomer Shift (IS), Quadrupole Splitting (QS) and line width (Full Width Half Maximum-FWHM).

x	IS (mm/s)	QS (mm/s)	FWHM (mm/s)	Hyperfine field (Tesla)	Relative Area (%)	Oxidation state of Fe
0.2	0.33±0.01	0.52±0.01	0.48±0.02	---	100	Fe^{3+}
0.4	0.34±0.01	0.63±0.02	0.59±0.03	---	100	Fe^{3+}
0.6	0.62±0.08	0.17±0.06	0.23±0.00	---		Fe^{3+}
	0.56±0.07	0.35±0.10	0.42±0.04	39.23±0.02		
	0.19±0.03	0.17±0.06	0.57±0.08	---		Fe^{4+}
0.8	0.26±0.01	0.68±0.01	0.62±0.01	---	64.6	Fe^{4+}
	---	---	0.45	45.95	---	Fe^{3+}
1.0	0.36±0.01	0.1±0.01	0.63±0.12	50.4±0.1	58.8	Fe^{3+}
	0.22±0.03	0.44±0.05	1.34±0.08	37.4±0.2	24.1	Fe^{4+}
	0.23	0.6	2.38±0.16	---	17.1	

6.3.5. Magnetic studies

Temperature dependence of magnetization of DSMFO is carried out at different fields and Fig. 6.5 shows molar susceptibility curves measured in the ZFC (χ_{ZFC}) and FC (χ_{FC}) protocols in different magnetic field strengths varying from 50 Oe to 10,000 Oe for DSMFO. All the materials exhibited paramagnetic nature in the high temperature region (> 100 K) and display variety of magnetic structures below 100 K. By applying lower fields i.e. 50 Oe, in all compounds, deviation in ZFC and FC curves was seen whereas this deviation disappeared for higher fields.

The salient features of the magnetization curves are as follows:

a. For low values of iron concentration (x=0.0 and 0.2), both χ_{ZFC} and χ_{FC} curves overlap with a broad peak in χ_{ZFC} whose peak temperature reduced with decreasing the measuring temperature. Compounds with x=0.4 and 0.6 do not display any maximum in the susceptibility curves. It was observed that for x=0.0, Mn^{3+} spin ordering was found around 38 K as determined from the dχ/dT versus T curves shown in inset of Fig. 6.5.

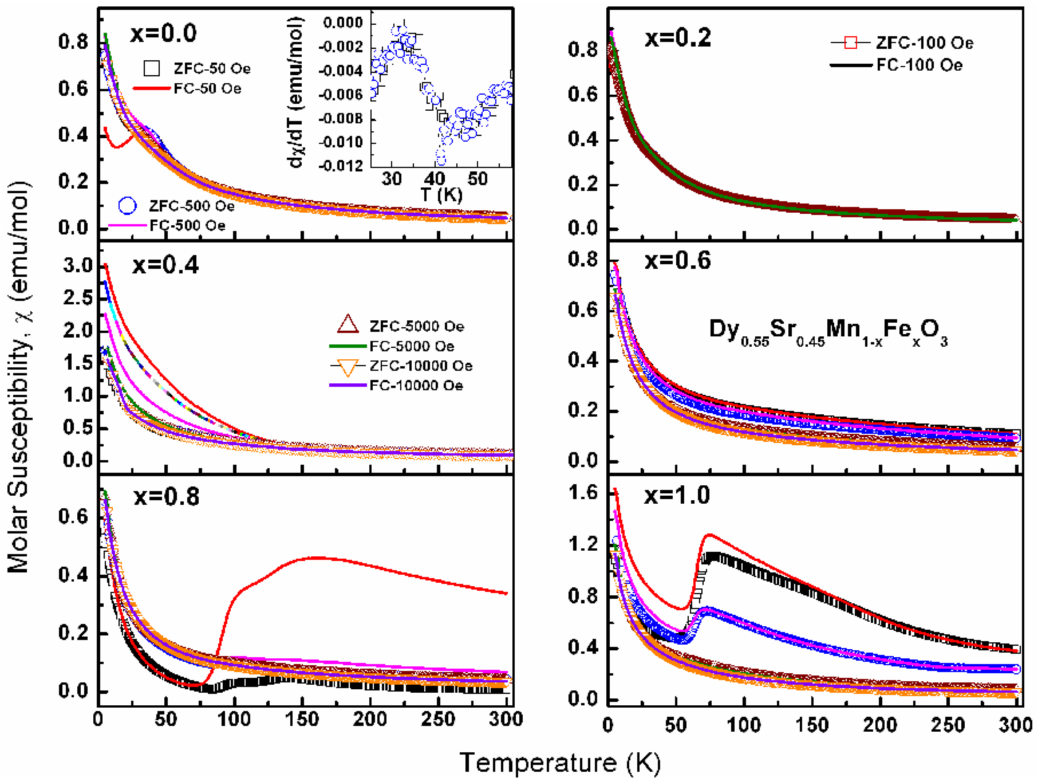

Figure 6.5. Temperature variation of magnetization $Dy_{0.55}Sr_{0.45}Mn_{1-x}Fe_xO_3$ at various fixed applied magnetic fields.

b. In the case of compounds with x=0.8 and 1.0, the paramagnetic (PM) susceptibility decreased around 100 K and 75 K respectively indicating onset of an antiferromagnetic (AFM) transition: PM to AFM transition. Below this transition, again the susceptibility started to increase around 80 K and 55 K suggesting the development of ferromagnetic correlations (AFM to a mixed state) among the magnetic ions existing in multiple oxidations states viz., Dy^{3+}, Mn^{4+}, Fe^{3+} and Fe^{4+}. The presence of ferromagnetic clusters is complimented by hysteresis loops observed at 300 K for these two compounds. The transition temperatures corresponding to PM → AFM and AFM → mixed state are reduced with increasing iron content [21].

c. In order to estimate the effective magnetic moment, χ_{FC} (T, 1 Tesla) data in the paramagnetic state was fitted to the CW law. A representative plot of the inverse susceptibility as a function of temperature is shown in Fig. 6.6 for x=0.0.

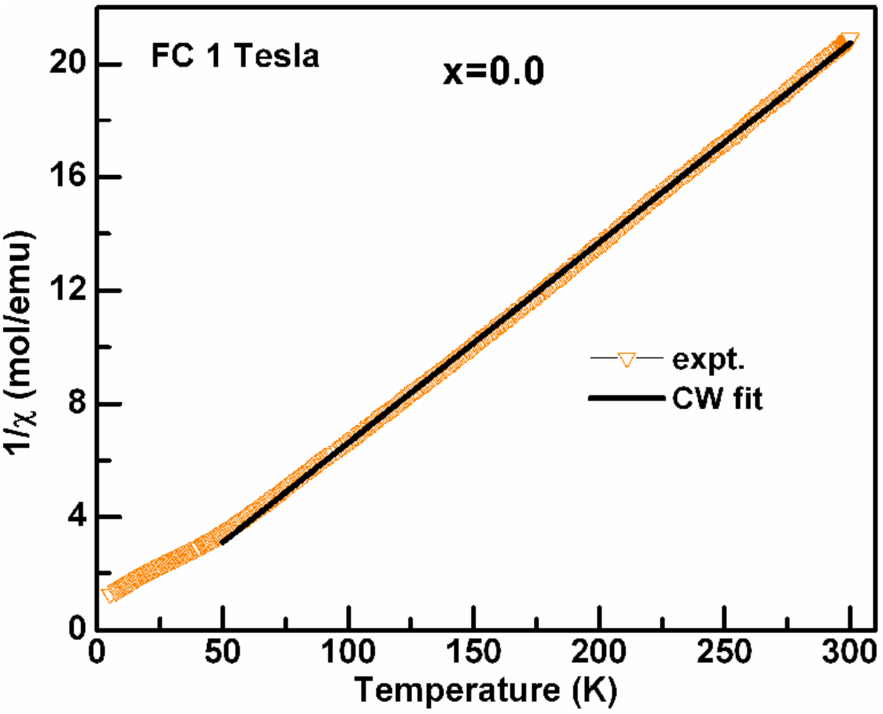

Figure 6.6. Thermal variation of inverse susceptibility data measured at 1 Tesla applied field in the field cooled cycle along with CW fit for x=0.0.

Calculated effective magnetic moments for the whole series are calculated by using individual magnetic moments of Dy^{3+}, Mn^{3+}, Mn^{4+}, Fe^{3+} and Fe^{4+} using the two formulae given below:

For x =0.0 - 0.4:

$$\mu_{eff.}(cal.) = \sqrt{0.55(\mu_{Dy^{3+}})^2 + (0.55 - x)(\mu_{Mn^{3+}})^2 + 0.45(\mu_{Mn^{4+}})^2 + x(\mu_{Fe^{3+}})^2} \quad (6.1)$$

and for x =0.6 – 1.0:

$$\mu_{eff.}(cal) = \sqrt{0.55(\mu_{Dy^{3+}})^2 + (1.0 - x)(\mu_{Mn^{4+}})^2 + 0.55(\mu_{Fe^{3+}})^2 + (x - 0.55)(\mu_{Fe^{4+}})^2} \quad (6.2)$$

where x is the concentration of iron in $Dy_{0.55}Sr_{0.45}Mn_{1-x}Fe_xO_3$. Here values of 5.92 μ_B and 4.9 μ_B were used for Fe^{3+} (high spin state) and Fe^{4+} ions respectively in the calculations.

By comparing the calculated and experimental effective magnetic moments as shown in Fig. 6.7, it was observed that $\mu_{eff.}$ (expt.) is always higher than the predicted values; thus the ratio ($\mu_{eff.}$ (expt.) / $\mu_{eff.}$ (cal.)) is always greater than one. This may be ascribed to ferromagnetic cluster formation [22].

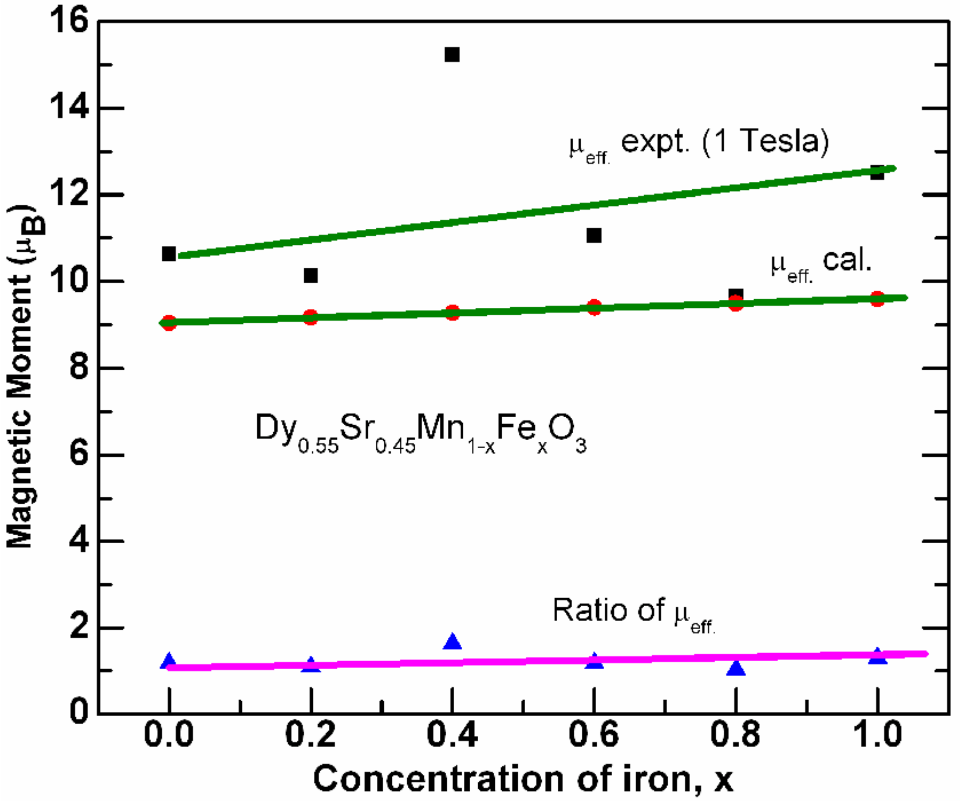

Figure 6.7. Dependence of effective magnetic moments ($\mu_{eff.}$ (expt.) and $\mu_{eff.}$ (cal.)) as a function of x in $Dy_{0.55}Sr_{0.45}Mn_{1-x}Fe_xO_3$. Ratio of magnetic moments ($\mu_{eff.}$ (expt.) / $\mu_{eff.}$ (cal.)) is also included in the same graph.

Field dependence of magnetization carried out at different temperatures for all the compounds in the series is presented in Fig. 6.8. It may be noted from M-H curves that for the compounds with different values of iron content, the magnetization at 7 T decreased with increase in x up to x=0.4 and there afterwards, the moment value remained to be ~ 3 μ_B. Magnetization isotherms recorded at 5 K and 300 K for all the compounds are shown in Figs. 6.9 and 6.10 respectively. It is interesting to note that hysteresis loops are present even at 300 K for x=0.6, 0.8 and 1.0.

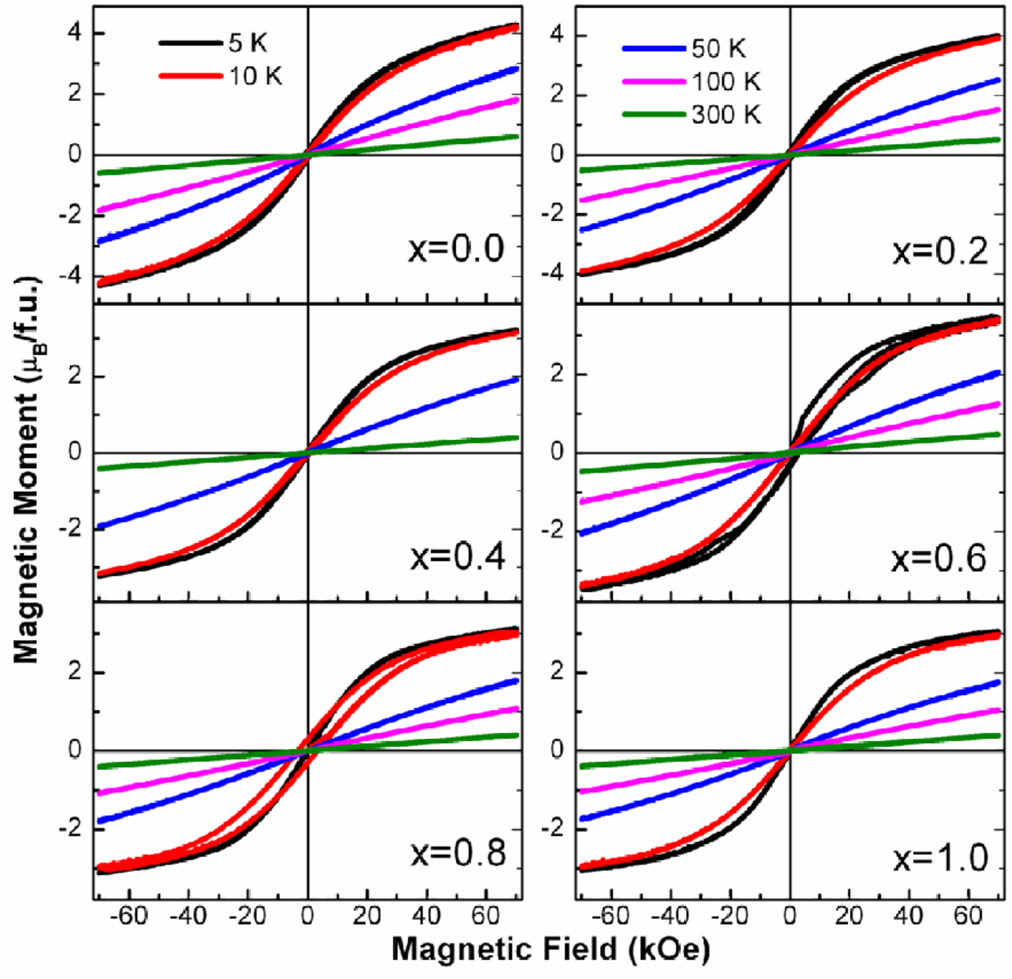

Figure 6.8. Isothermal magnetization behavior with respect to magnetic field at several temperatures for all x in $Dy_{0.55}Sr_{0.45}Mn_{1-x}Fe_xO_3$.

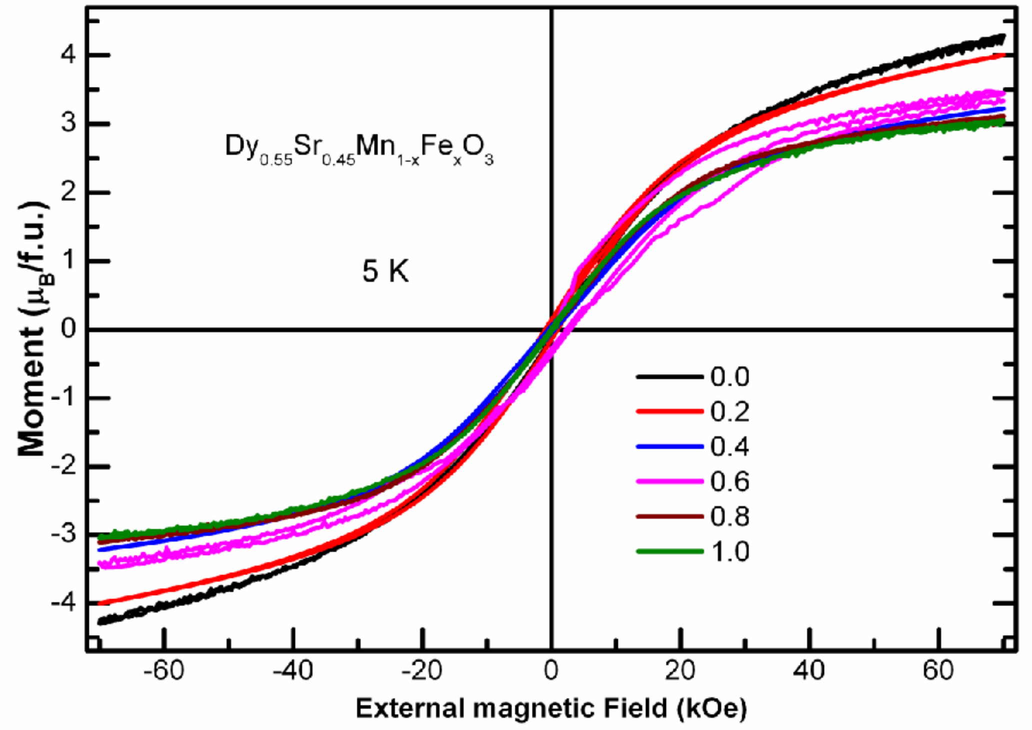

Figure 6.9. M-H curves recorded at 5 K for all x in $Dy_{0.55}Sr_{0.45}Mn_{1-x}Fe_xO_3$.

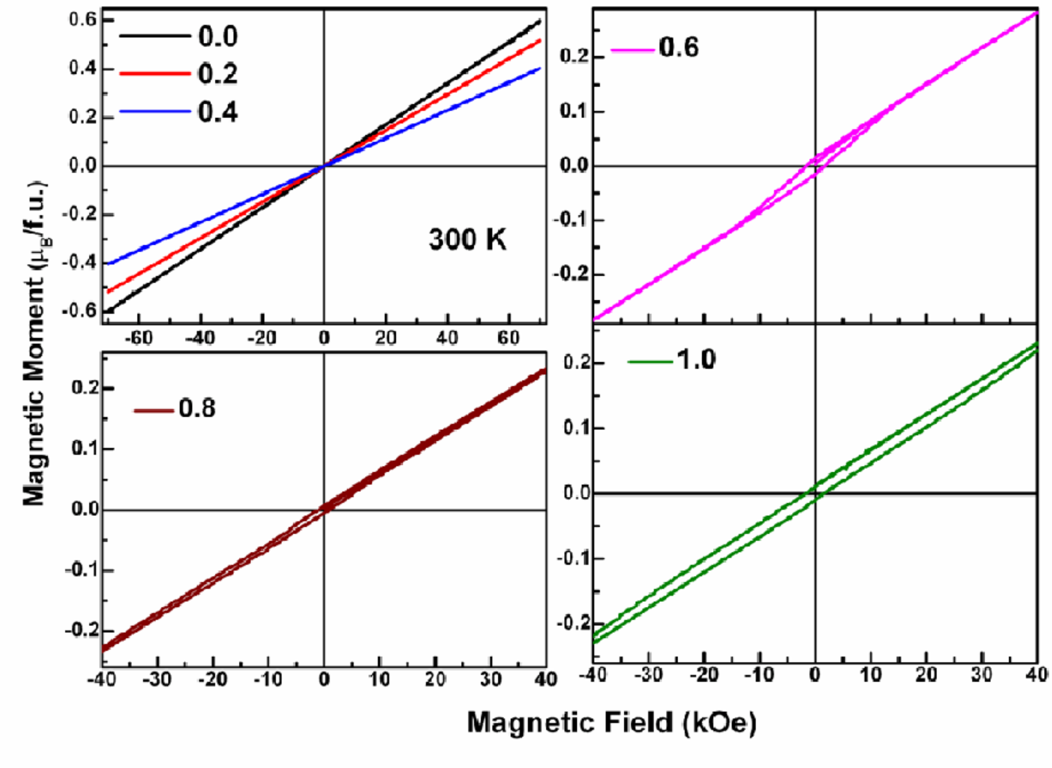

Figure 6.10. RT magnetization curves for all x in $Dy_{0.55}Sr_{0.45}Mn_{1-x}Fe_xO_3$.

6.3.6. Dielectric properties

Frequency dependence of dielectric constant (ε') and dielectric loss (ε") for selected compounds: $Dy_{0.55}Sr_{0.45}MnO_3$, $Dy_{0.55}Sr_{0.45}Mn_{0.6}Fe_{0.4}O_3$ and $Dy_{0.55}Sr_{0.45}FeO_3$ at several fixed temperatures are shown in Figs. 6.11 (a), 6.11 (b) and 6.11 (c) respectively.

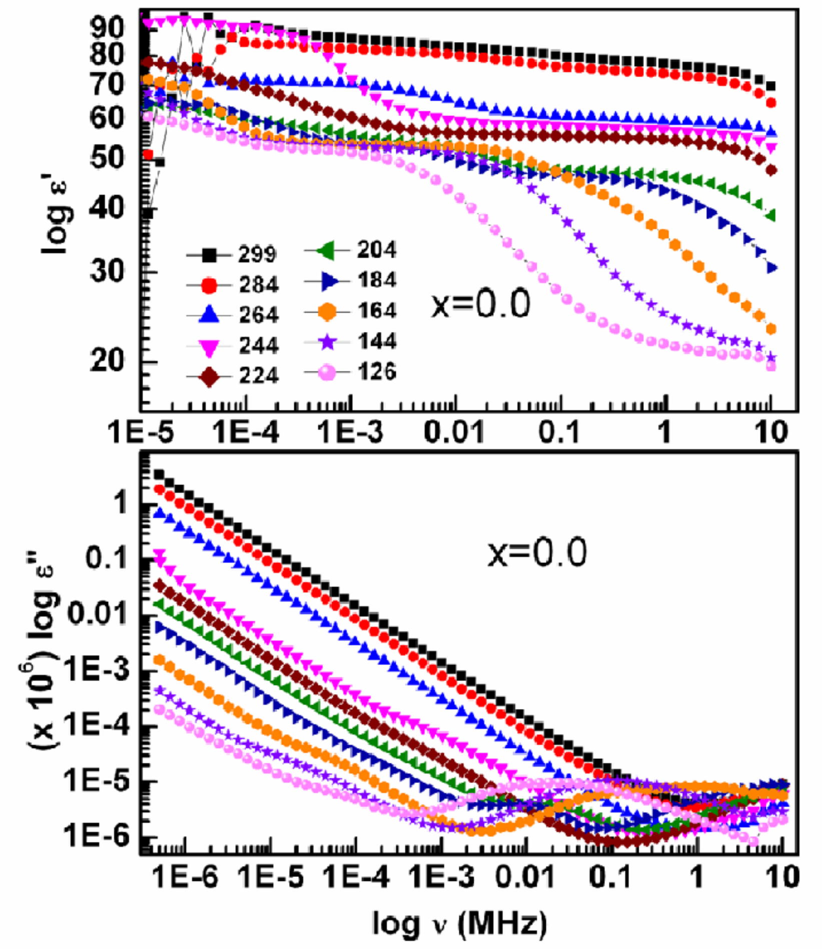

Figure 6.11. (a) log-log plot of frequency dependence of dielectric constant (ε') and dielectric loss (ε") at different fixed temperatures for $Dy_{0.55}Sr_{0.45}MnO_3$.

From all the figures, it is observed that both the dielectric constant, ε' and dielectric loss, ε" decrease with increase of the frequency which is a typical behavior shown by a dielectric material. The frequency dependent dielectric behavior of materials depends on the type of polarization mechanism operating at that frequency. At low frequencies, ionic contributions dominate whereas at high frequencies, electronic polarization dominates. The high ε' observed in the present compounds in the low frequency regime may be associated with the electrode polarization where charge carriers are blocked at the sample electrode interface leading to separation of charges which gives rise to additional polarization [23, 24]. As the temperature increased, the dielectric constant as well as dielectric loss increased due to thermal activation of charge carriers. Due to scatter in the data at low frequencies, corresponding to both the end compounds, quantitative comparison could not be made, however, ε' values are found to increase with iron concentration.

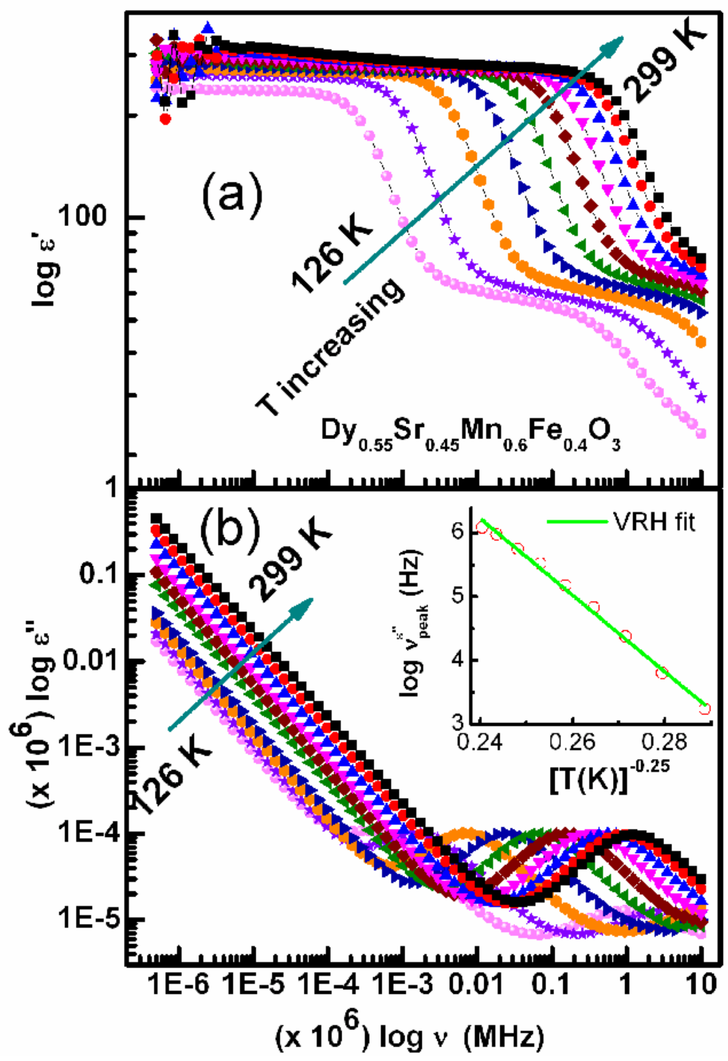

Figure 6.11. (b) log-log plot of frequency dependence of (a) dielectric constant (ε') and (b) dielectric loss (ε'') at different fixed temperatures for $Dy_{0.55}Sr_{0.45}Mn_{0.6}Fe_{0.4}O_3$.

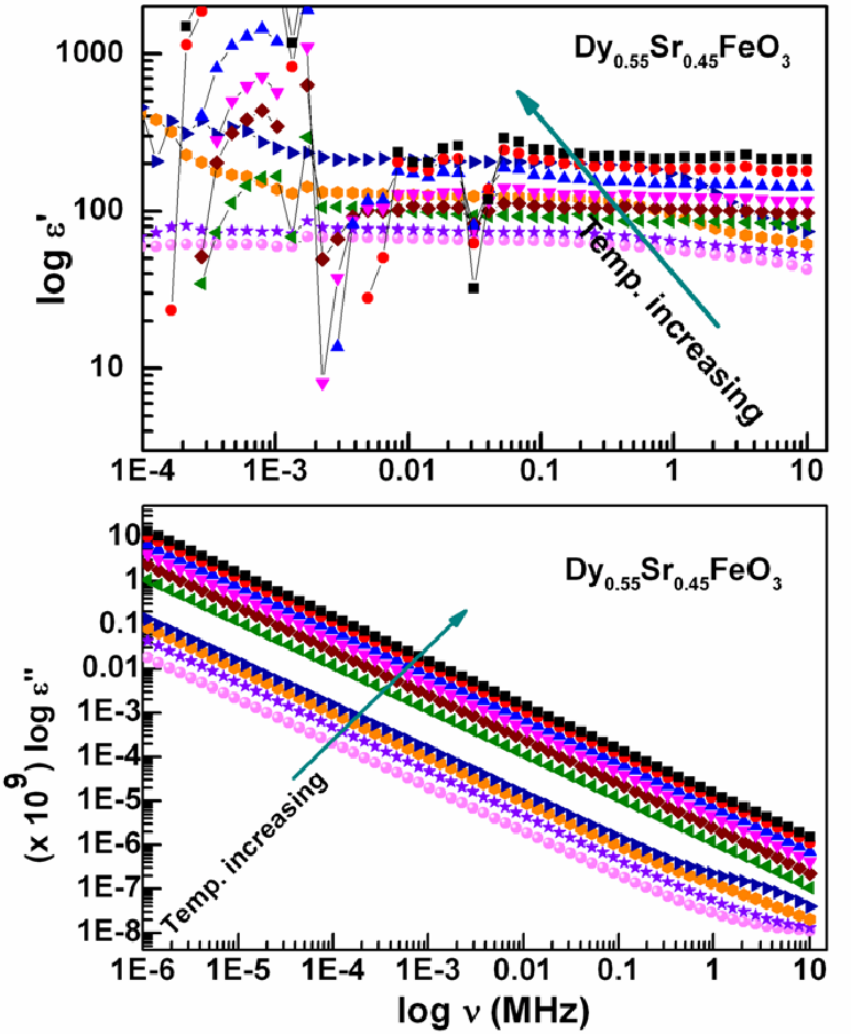

Figure 6.11. (c) log-log plot of frequency dependence of dielectric constant (ε') and dielectric loss (ε") at different fixed temperatures for $Dy_{0.55}Sr_{0.45}FeO_3$.

A step like decrease in the dielectric constant was observed for x=0.4 and corresponding relaxation peaks were observed in the dielectric loss spectra. It may be observed from Figs. 6.11 (a) and (b) that in the dielectric loss spectra, the peak frequency shifted to higher frequency values with increasing temperature. This behavior implies a thermally activated relaxation process. While the dielectric constant of the compound with x=1.0 decrease with increase in the frequency without any loss peaks in the investigated frequency and temperature range. Thus the substitution of Mn by Fe introduced significant changes in the dielectric properties. The temperature dependence of the peak frequency for x=0.4 was found to follow VRH equation given by

$$f = f_0 e^{\left(\frac{T_0}{T}\right)^{0.25}} \tag{6.3}$$

here f_0 is pre frequency factor, T_0 is a constant related to localization length (Eq. 3.5) and T is the temperature of the measurement. A plot of log ν_{peak} (ε'') vs. $T^{-0.25}$ shown in inset of Fig 6.11 (b) yielded a straight line over a considerable temperature range. A value of 2 x 10^6 K was obtained for T_0 which agrees with the values obtained for disordered materials [25, 26].

Figure 6.12 display the frequency dependence of the real part of the ac conductivity, $\sigma_{ac}(\nu)$ measured in the temperature range 299 K to 126 K for $Dy_{0.55}Sr_{0.45}MnO_3$, $Dy_{0.55}Sr_{0.45}Mn_{0.6}Fe_{0.4}O_3$ and $Dy_{0.55}Sr_{0.45}FeO_3$ as mentioned in the respective panels. In the low frequency regime, σ_{ac} is mainly frequency independent and is associated with the dc conductivity, σ_0 (σ_{dc}). At higher frequencies, σ_{ac} increases with frequency.

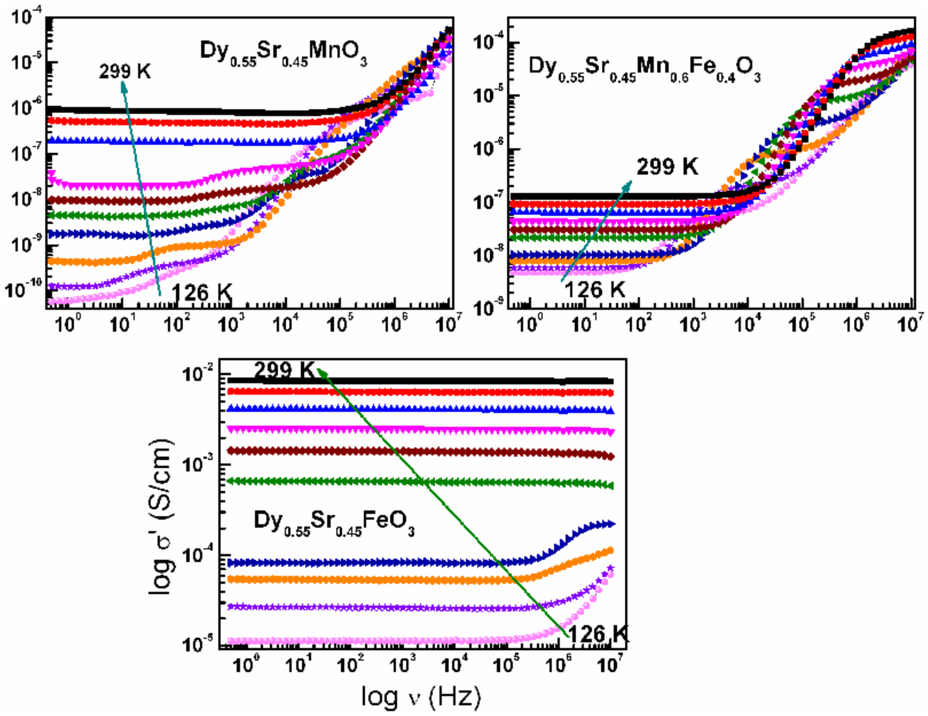

Figure 6.12. A log-log plot of ac conductivity as a function of frequency at different temperatures.

With increase in the temperature of the measurement, both σ_0 and σ_{ac} conductivity values increase. The increase in these values implies the semiconducting nature of the compounds. However, the shape of the conductivity isotherm curves in the high frequency range changes for compounds with x=0.0 and 0.4 which may be resulting from multiple conduction processes occurring. In the end compound, $Dy_{0.55}Sr_{0.45}FeO_3$, dc conductivity part extends to a larger frequency range indicating its possible use as resistors for high frequency applications. In general, in polycrystalline materials, due to the presence of grains and grain boundaries, conductivities vary depending on the microstructure. As a consequence of this, dielectric properties arising from the grains and grain boundaries will be different and their contributions could be obtained from impedance measurements.

In order to understand space-charge relaxation phenomena in dielectric materials, electric modulus is introduced by Macedo et al. [27]. It is widely used to describe the ionic conductivity. Generally, electrical modulus corresponds to the relaxation of the electric field in the material when the electric displacement does not change. Therefore, electric modulus represents pure dielectric relaxation process. Along with formalism of permittivity and impedance, electric modulus studies for identification of grain and grain boundary effects was carried out to distinguish dielectric relaxation and conduction type relaxation in materials [28]. The corresponding dielectric modulus plots are presented in Figs. 6.13 (a) and 6.13 (b) for x=0.0, 0.4 and 1.0 as mentioned in the respective graphs. Frequency dependence of the real part of the modulus, M' at various temperatures is shown in Fig 6.13 (a) while Fig. 6.13 (b) displays imaginary part of M'' against frequency.

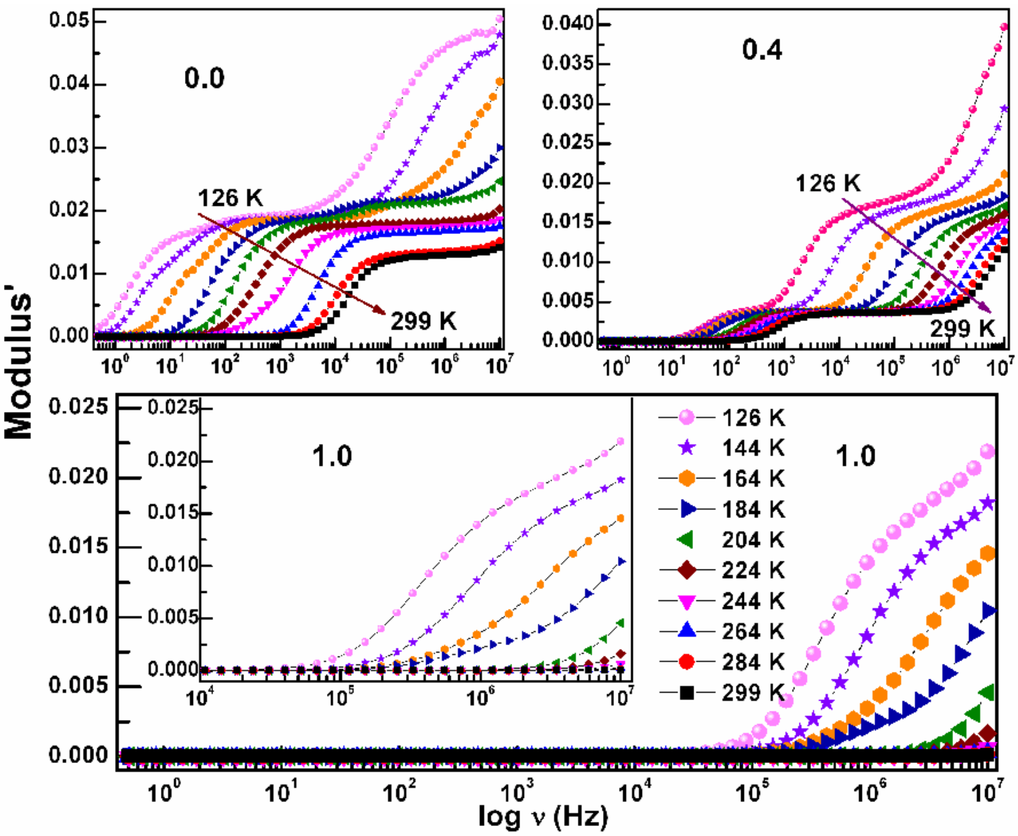

Figure 6.13. (a) Real component of modulus (M') spectra of $Dy_{0.55}Sr_{0.45}Mn_{1-x}Fe_xO_3$ for x=0.0, 0.4 and 1.0 as mentioned in the respective panels at different temperatures.

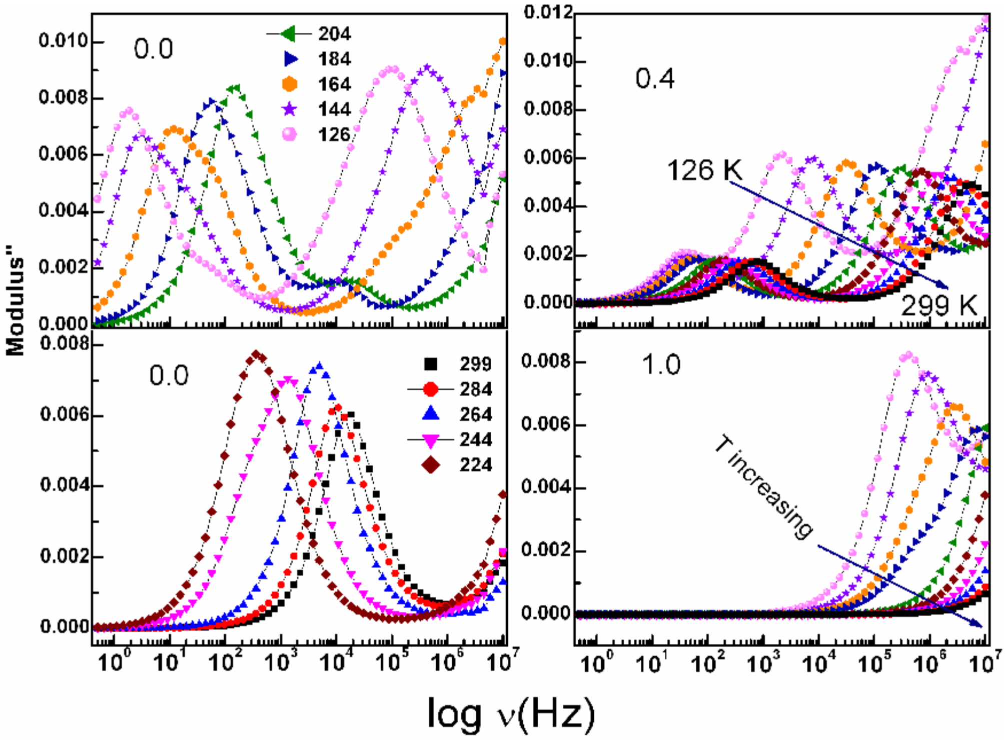

Figure 6.13. (b) Imaginary part of modulus (M") spectra of $Dy_{0.55}Sr_{0.45}Mn_{1-x}Fe_xO_3$ for x=0.0, 0.4 and 1.0 as mentioned in the respective panels at different temperatures.

The pristine compound, $Dy_{0.55}Sr_{0.45}MnO_3$ showed dispersion at all frequencies whereas substituted compound and end compound with x=0.4 and 1.0 showed dispersion for frequency >10 Hz. Furthermore, magnitude of M' decreases with increasing temperature. The imaginary component, M'' of these compounds is shown in Fig. 6.13 on a semi log plot. The slope changes in M' - ν plot are developed into peaks in the M'' of the compounds with x=0.0 and 0.4 while the compound with x=1.0 shows only a single peak consistent with the frequency behavior of M'. The peak frequency (ν_{peak}) shifts to higher frequencies with rise in the temperature suggesting the thermally activated nature of the relaxation time. It was found that the temperature variation of the peak frequency followed VRH behavior and Figs. 6.14 (a) and (b) depict this behavior. Activation energies for hopping conduction are temperature dependent and are calculated from the equation (3.10) using the fit parameter T_0.

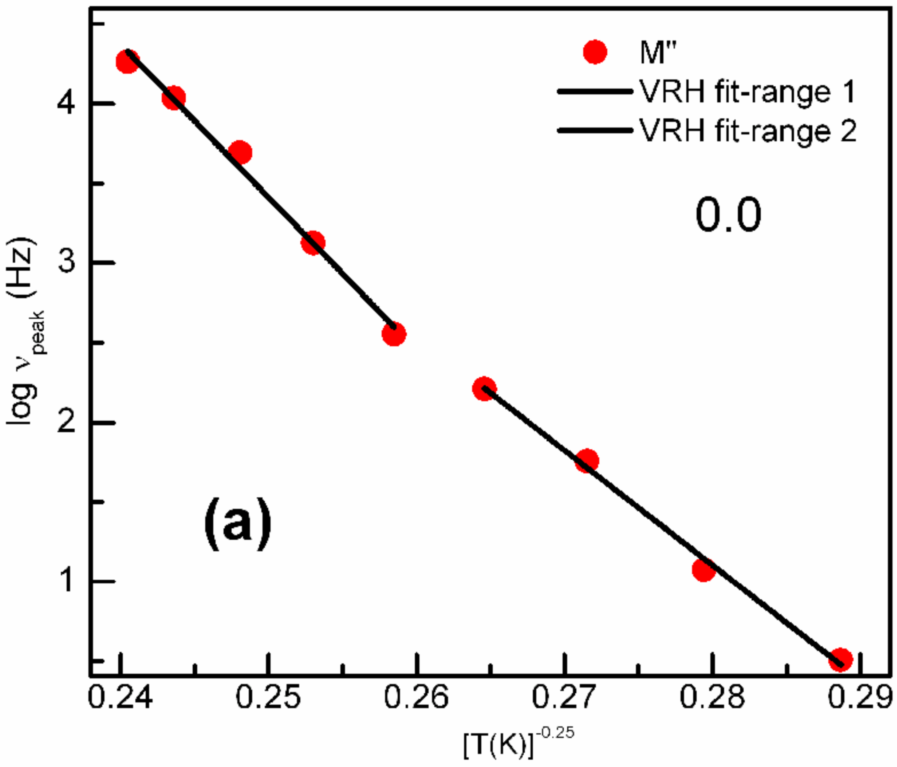

Figure 6.14. Continued.

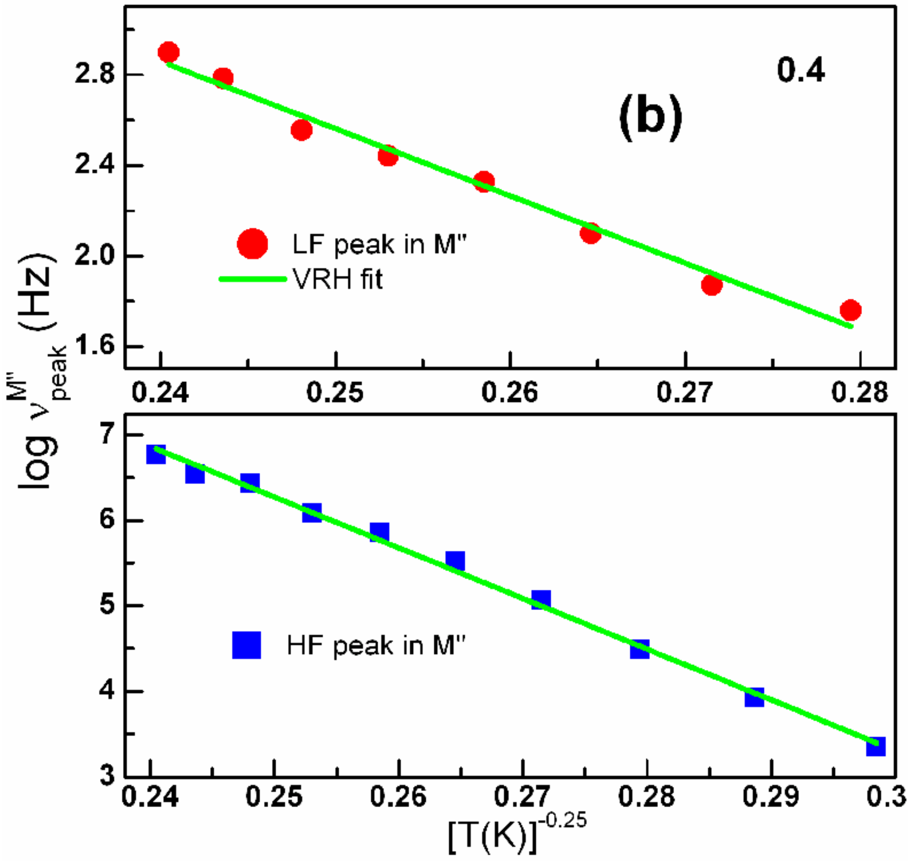

Figure 6.14. Plots of log ν_{peak} (peak frequency observed in the imaginary part of the modulus spectra) versus ($1/T^{0.25}$) for $Dy_{0.55}Sr_{0.45}Mn_{1-x}Fe_xO_3$ (a) x=0.0 and (b) x=0.4. The straight lines indicate best fits to the VRH conduction.

Figure 6.15 show the results of impedance in the frequency range 0.5 Hz to 10 MHz and in the temperature range 125 K to 300 K for x=0.0, 0.4 and 1.0 respectively in separate panels. The experimental observations that were found in the permittivity, ac conductivity and modulus in the investigated frequency and temperature range for all the studied compounds are reflected in the impedance spectra. The real and imaginary components are shown in Fig. 6.15 (a) and (b) respectively.

Slope changes in Z'-ν manifested as peaks in the Z"- ν plot. The magnitudes of both Z' and Z" decrease with an increase in frequency as well as temperature in the entire range indicating the semiconducting behavior of the materials. Asymmetric broadening of the peak is observed with rise in temperature suggests a distribution of relaxation times. The frequency range over which Z' is constant increases and shifts to higher frequency values with increase in the temperature.

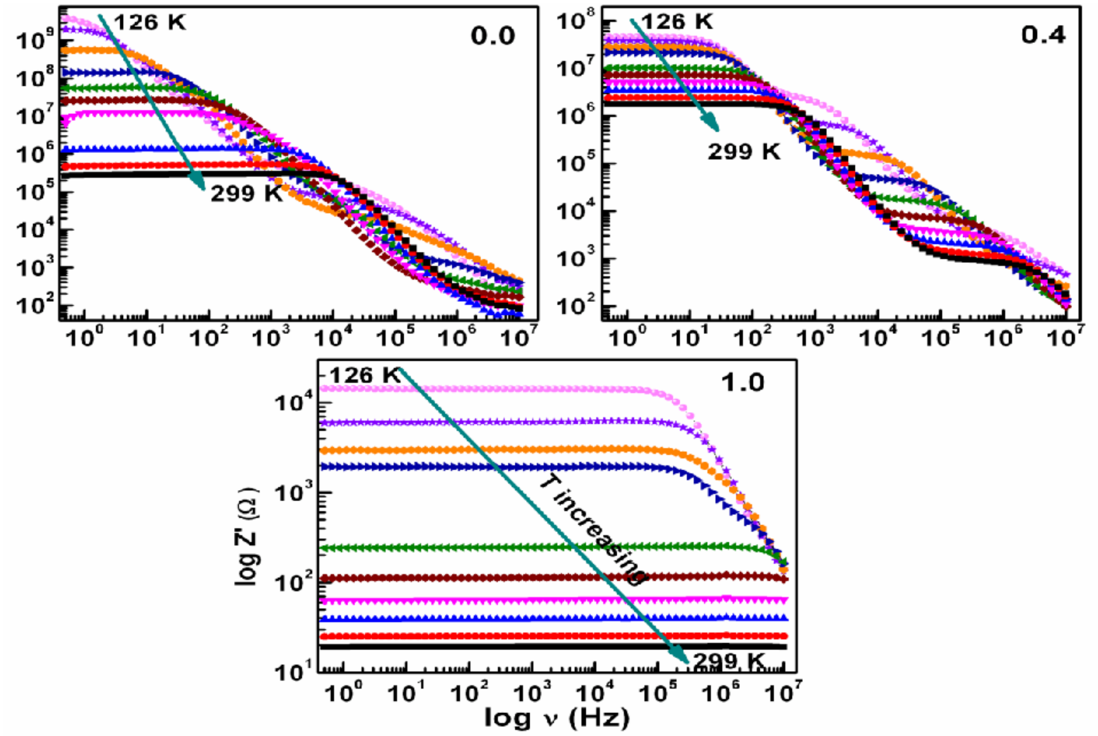

Figure 6.15. (a) Real component of impedance (Z') spectra of $Dy_{0.55}Sr_{0.45}Mn_{1-x}Fe_xO_3$ for x=0.0, 0.4 and 1.0 as mentioned in the respective panels at different temperatures.

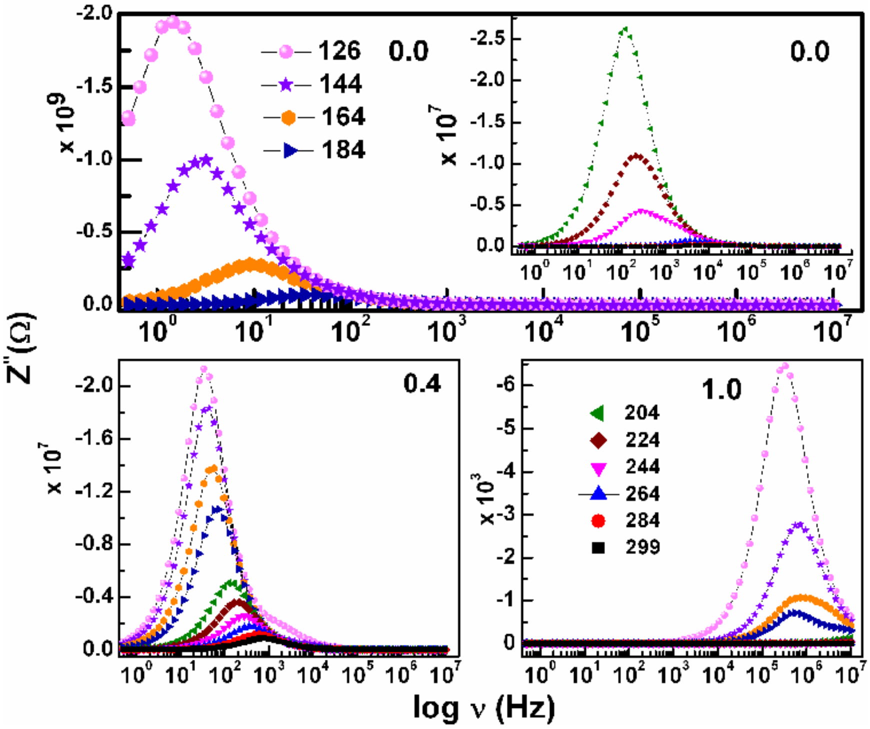

Figure 6.15. (b) Imaginary component of impedance (Z'') spectra of $Dy_{0.55}Sr_{0.45}Mn_{1-x}Fe_xO_3$ for x=0.0, 0.4 and 1.0 as mentioned in the respective panels at different temperatures.

In Fig. 6.15 (b) a single peak is observed for all the compounds and the frequency corresponding to the maximum value of Z" (ν_{peak}) is shifted towards higher frequencies with increasing temperature. Figure 6.16 (a) and (b) show log (ν_{peak}) versus $1/T^{0.25}$ plots for x=0.0 and 0.4 respectively. Activation energies for the observed hopping conduction investigated from dielectric loss, modulus and impedance spectra are calculated from the equation (3.10) and are tabulated in Table 6.3.

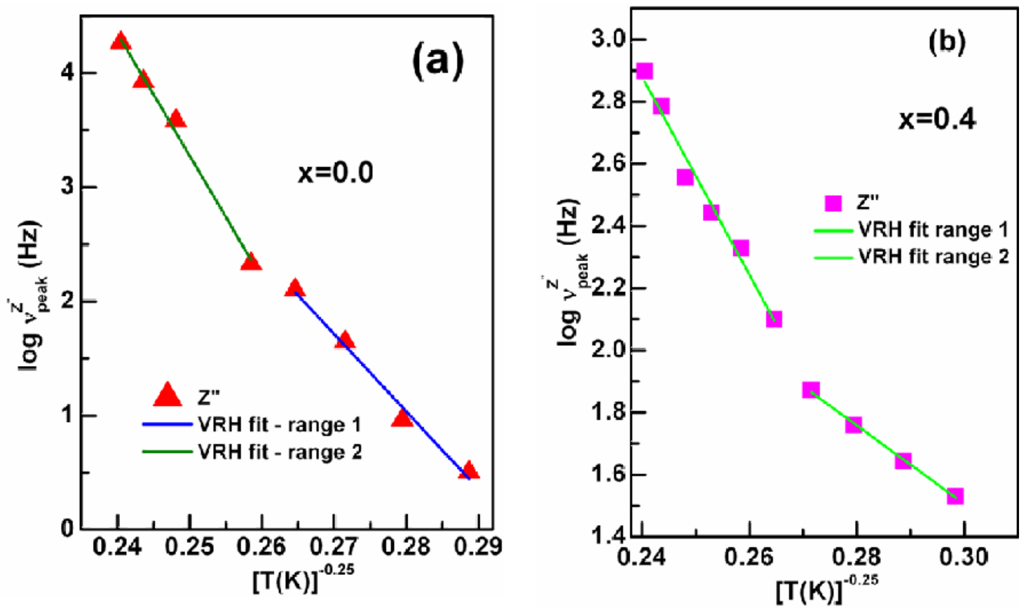

Figure 6.16. A plot of VRH fit to the peak frequency observed in the imaginary part of the impedance spectra for $Dy_{0.55}Sr_{0.45}Mn_{1-x}Fe_xO_3$ (a) x=0.0 and (b) x=0.4.

Table 6.3. Activation energies obtained from dielectric loss, modulus and impedance spectra of $Dy_{0.55}Sr_{0.45}Mn_{1-x}Fe_xO_3$. R1: Range 1 (244 K to 299 K) and R2: Range 2 (126 K to 224 K); LF: Low Frequency and HF: High Frequency

x	**Activation energy (meV)**		
	Dielectric loss	**Modulus**	**Impedance**
0.0	No peak	R1: 78 - 149 R2: 59 - 112	R1: 87 – 166 R2: 55 - 105
0.4	49 – 93 (126 K to 299 K)	LF: 24 - 46 HF: 48 - 92	R1: 10 - 20 R2: 26 - 49
1.0	No peak	38 - 50 (126 K to 184 K)	-

Figures 6.17 (a) to (c) show Cole-Cole plots for all the three compounds whose results of dielectric studies are discussed above. For the compound with x=0.0, a single semicircle was observed for temperatures above 144 K. As temperature increased the radius of the semi circle decreased indicating the reduction in the resistance of the grain boundaries. As the iron concentration (x) increases, impedance values decrease with respect to temperature and frequency indicating the increase in the ac conductivity. It may be seen from the Figs. 6.17 (a) and (c) that semicircular arcs are observed at low temperatures (126 K and 144 K) and at temperatures higher than 204 K with non-zero intercept at low and high frequencies respectively. This indicates that the compounds are electrically inhomogeneous.

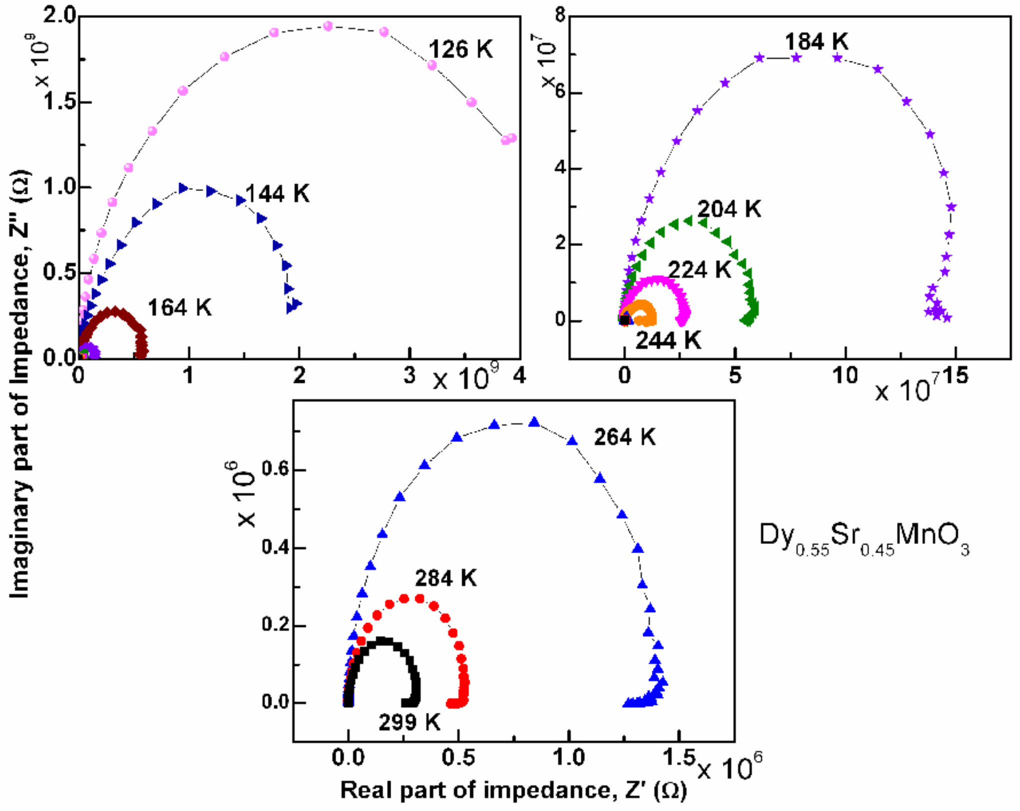

Figure 6.17. (a) Cole-Cole plots of impedance for $Dy_{0.55}Sr_{0.45}MnO_3$ at different temperatures as mention in the respective panels.

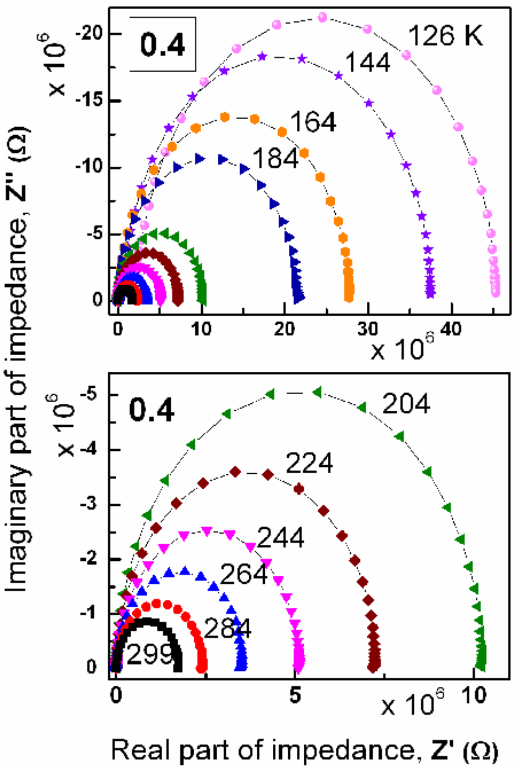

Figure 6.17. (b) Cole-Cole plots of impedance for $Dy_{0.55}Sr_{0.45}Mn_{0.6}Fe_{0.4}O_3$ at different temperatures as mentioned against the plots.

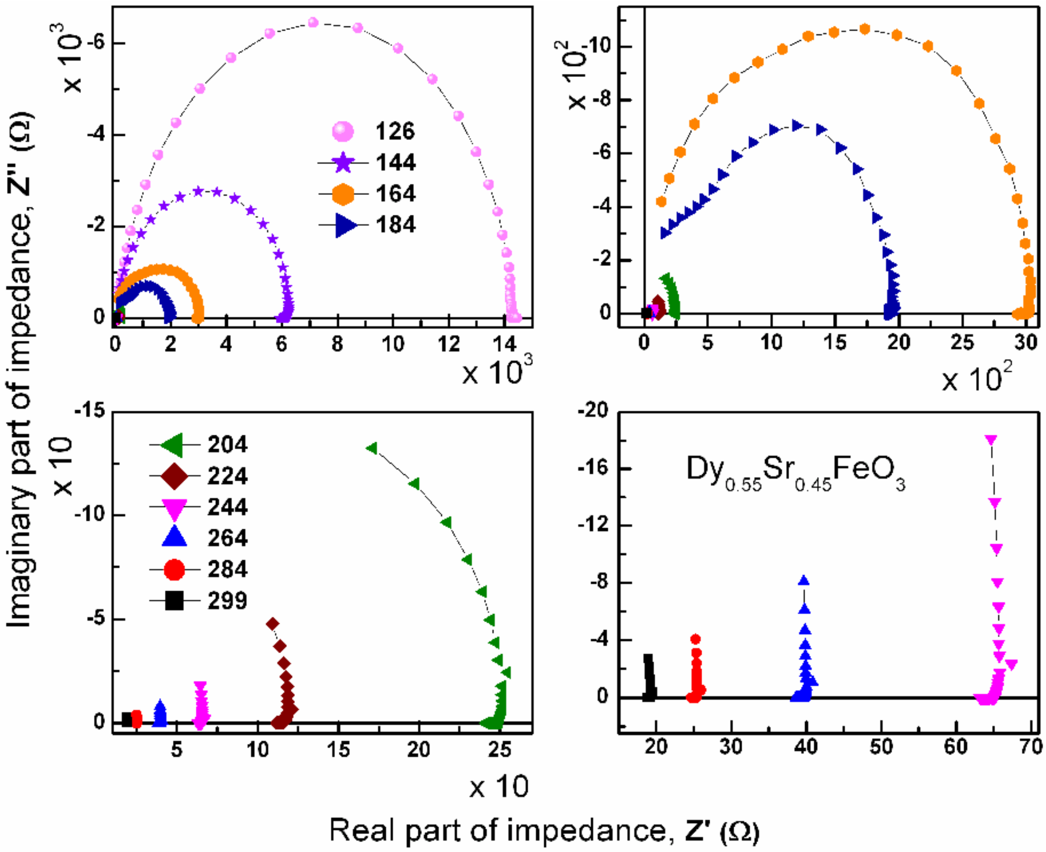

Figure 6.17. (c) Cole-Cole plots of impedance for $Dy_{0.55}Sr_{0.45}FeO_3$ at different temperatures.

Scaling behavior of DSMFO

The temperature dependence of distributions of relaxation times in x=0.0, 0.4 and 1.0 may be explained through the scaling of M" vs. ν and Z" vs. ν spectra as shown in Figs. 6.18 and 6.19 in separate panels respectively. As seen from the figures that the curves do not merge into a single curve indicating that there exists a distribution of relaxation times involved for the conduction of charge carriers over small distances. As temperature increases, peak is shifted towards high frequency side instead of peak merging on a master peak. This means that relaxation times are temperature dependent [29, 30].

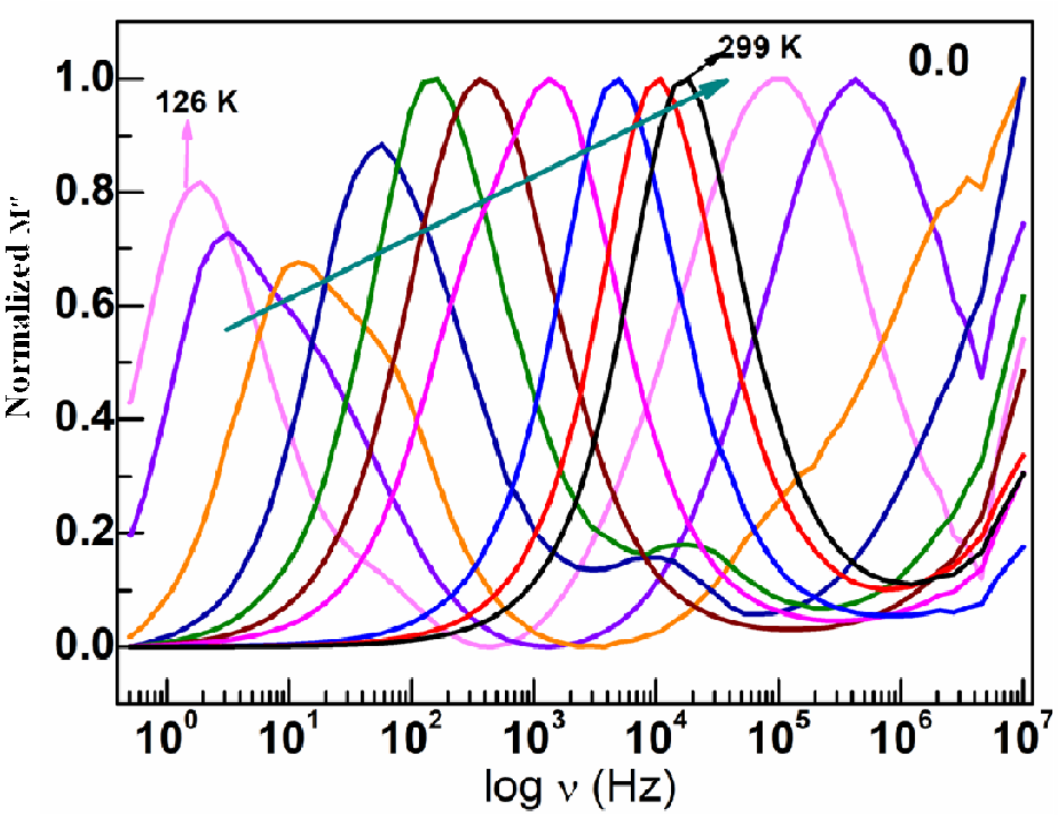

Figure 6.18. Continued.

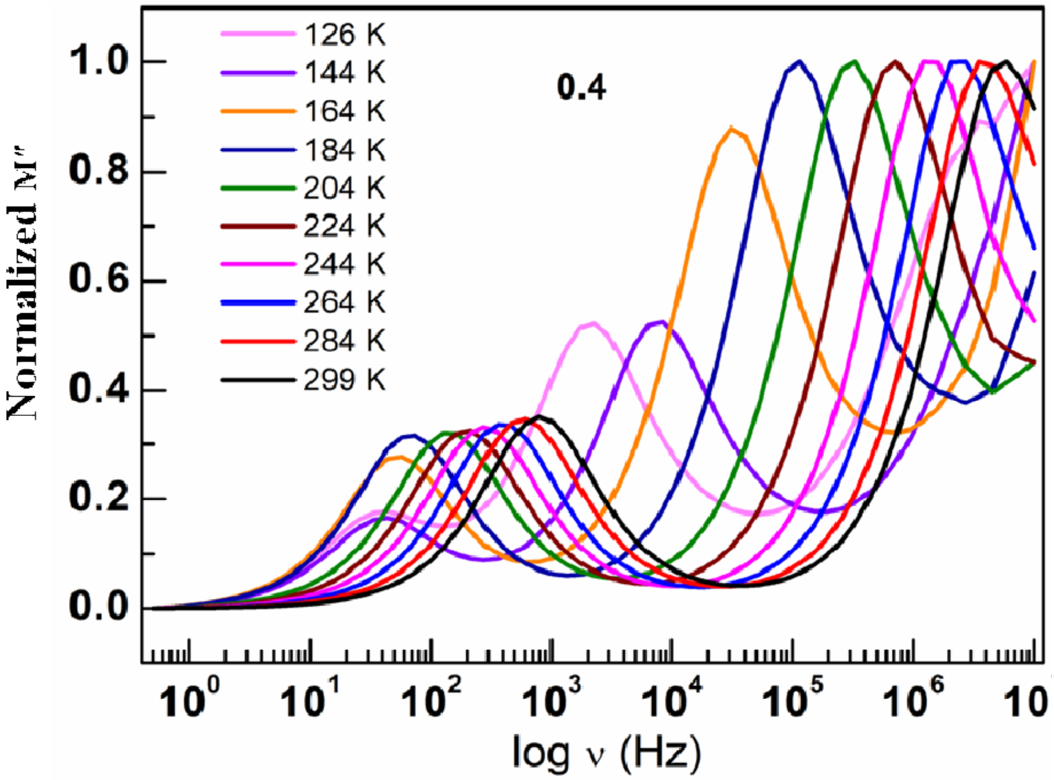

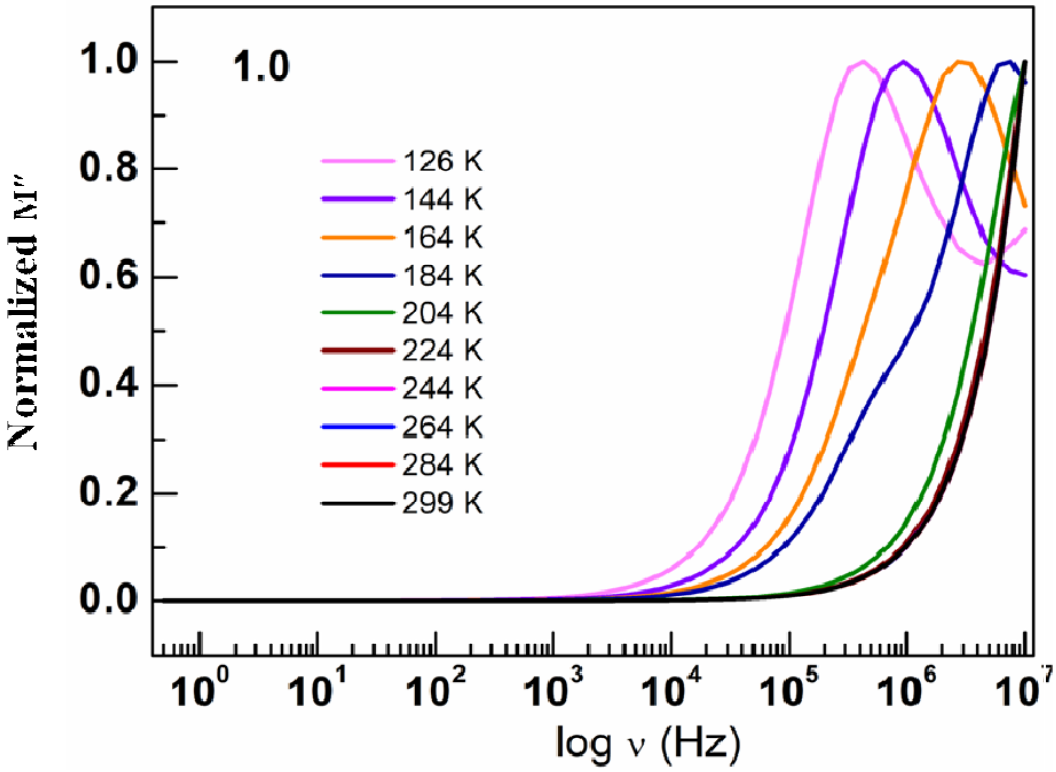

Figure 6.18. Scaling of frequency dependence of imaginary part of Modulus, M" for x=0.4 and x=1.0 in separate panels with legends corresponding to the respective temperatures.

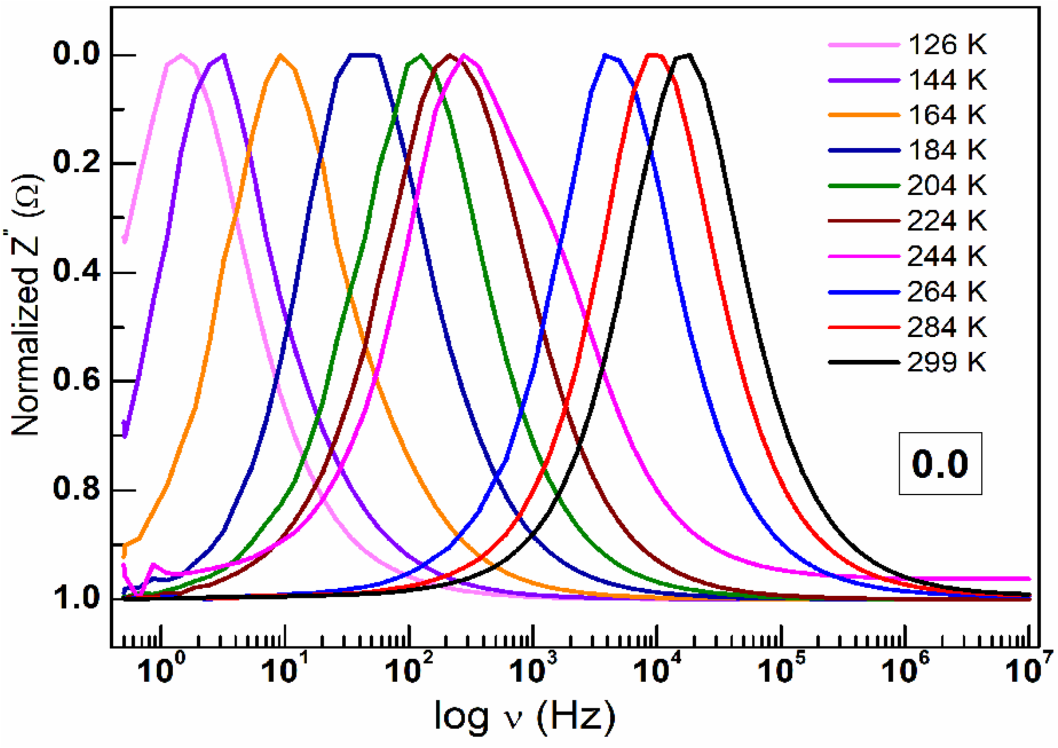

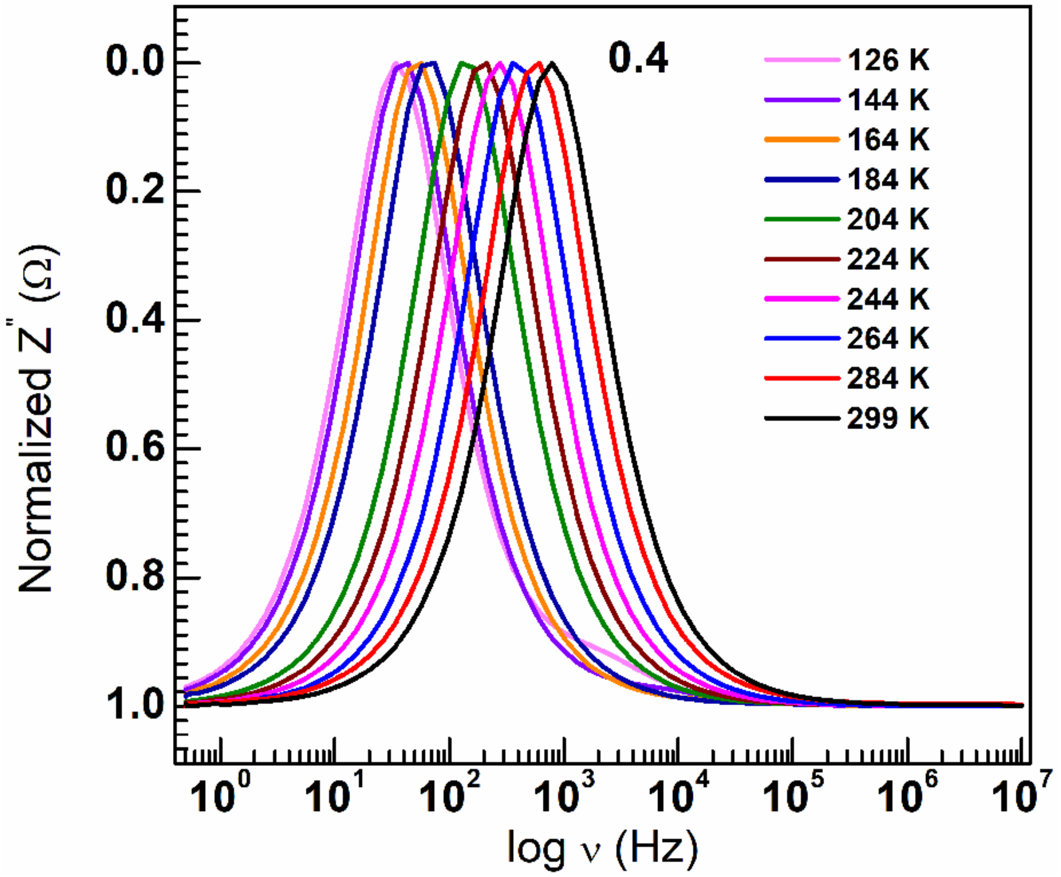

Figure 6.19. Continued.

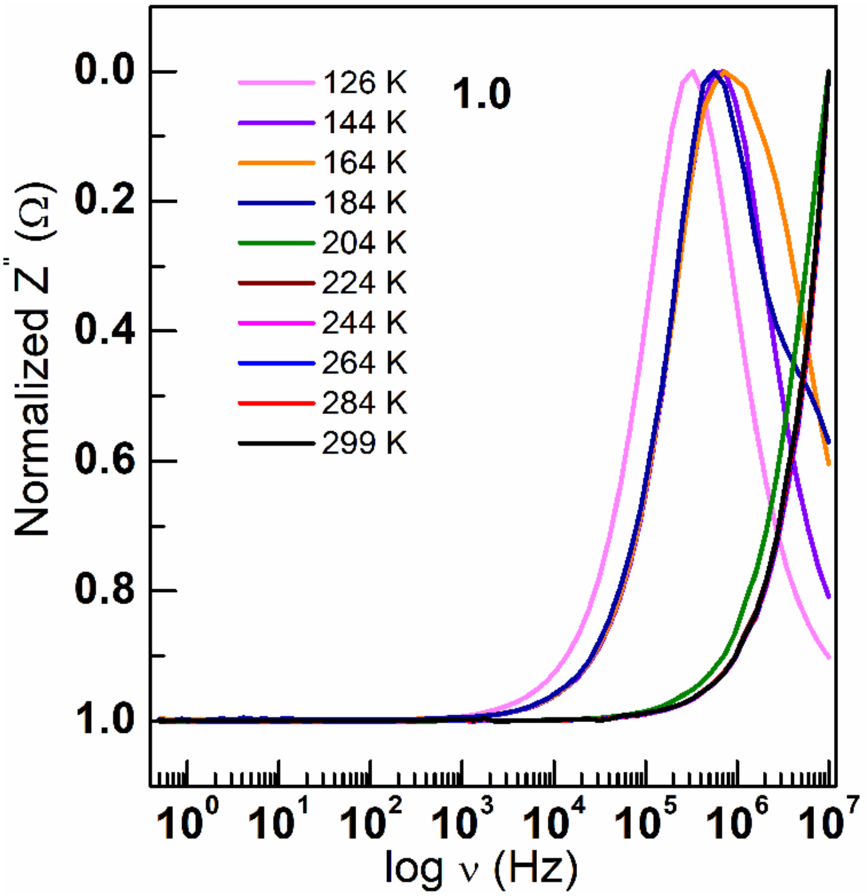

Figure 6.19. Scaling of frequency dependence of imaginary part of Impedance, Z'' for $Dy_{0.55}Sr_{0.45}Mn_{1-x}Fe_xO_3$, with x=0.0, x=0.4 and x=1.0 as mention in the respective panel.

6.4. CONCLUSIONS

The polycrystalline materials of $Dy_{0.55}Sr_{0.45}Mn_{1-x}Fe_xO_3$ (x=0.0-1.0; 0.2) (DSMFO) were synthesized by solid state reaction at high temperatures and the structure was found to be orthorhombic from X-ray diffraction method. Raman spectroscopy of these materials revealed that peak broadening decreased and modes were shifted to higher wave number side (hardening). Electrical properties of these materials revealed the semiconducting nature of the compounds and also it was observed that this insulating nature increased with Fe concentration in DSMFO. The dominant conduction mechanism in the temperature range: 300 K down to 150 K was found to be variable range hopping type.

The Mossbauer spectroscopy has been carried out on these materials at room temperature. From the values of isomer shift, Fe was found to exist in both tri and tetravalent states in the compounds with $x \geq 0.6$. Six line pattern observed for $x=0.6$, 0.8 and 1.0 indicated the presence of a magnetic phase in the compounds. Magnetization studies supported this conjecture. The ratio of the experimental effective magnetic moment to the calculated moment was found to be more than one implying cluster formation. Hysteresis loops were observed in the room temperature data for high concentrations of iron.

A.C. electrical properties, dielectric, impedance and modulus properties of these materials were investigated as a function of frequency in temperature range 126 K - 299 K. Dielectric permittivity as a function of temperature increased with increasing Fe concentration in the materials. The analysis of dielectric loss, modulus impedance spectra showed variable range hopping conduction is present in the materials. Activation energies which are temperature dependent are found to be consistent and lie in the meV range. Scaling behavior of modulus and impedance also corroborated this finding.

6.5. REFERENCES

[1] H. Kawano, R. Kajimoto, H. Yoshizawa, Y. Tomioka, H. Kuwahara and Y. Tokura, Phy. Rev. Lett., **78**, (1997), 4253.

[2] I.A. Abdel-Latif , A.S. Khramov, V.A. Trounov, A.P. Smirnov, Sh. Bashkirov, V.V. Parfenov, E.A. Tserkovnaya, G.G. Gumarov, Z. Ibragimov, Egypt. J. Solids, **29**, (2006), 341.

[3] S. Shravan Kumar Reddy, N. Raju, Ch. Gopal Reddy, P. Yadagiri Reddy, K. Rama Reddy and V. Raghavendra Reddy, J. Magn. Magn. Mater, **396**, (2015), 214.

[4] D. Kothari, V. Raghavendra Reddy, V.G. Sathe, A. Gupta, A. Banerjee and A.M. Awasthi, J. Magn. Magn. Mater., **320**, (2008), 548.

[5] F. Studer, N. Nguyen, O. Toulemonde, A. Ducouret, Int. J. Inorg. Mater., **2**, (2000), 671.

[6] K. Yadagiri and R. Nithya, J. Powder Diffr., **31**, (2016), 285.

[7] M.N. Iliev, M.V. Abrashev, V.N. Popo, and V.G. Hadjiev, Phys. Rev. B, **67**, **(**2003), 212301.

[8] M.V. Abrashev, J. Bäckström, L. Börjesson, V.N. Popov, R.A. Chakalov, N. Kolev, R.L Meng and M.N. Iliev, Phys. Rev. B, **65**, (2002), 184301.

[9] Xuan Cai, Lei Shi, Shiming Zhou, Jiyin Zhao, Yuqiao Guo and Cailin Wang, J. Appl. Phy., **116**, (2014), 103903.

[10] M.N. Iliev, M.V. Abrashev, H.-G. Lee, V.N. Popov, Y.Y. Sun, C. Thomsen, R.L. Meng and C.W. Chu, Phys. Rev. B, **57**, (1998), 2872.

[11] M. Viret, L. Ranno and J.M.D. Coey, Phys. Rev. B, **55**, (1997), 8067.

[12] J.M.D. Coey, M. Viret, L. Ranno and K. Ounadjela, Phys. Rev. Lett., **75**, (1995), 3910.

[13] N.F. Mott, J. Non-Cryst. Solids, **1**, (1968), 1.

[14] A. Banerjee, S. Pal and B.K. Chaudaruri, J. Chem. Phys., **115**, (2001), 1550.

[15] N.F. Mott and E.A. Davis, Electronic Processes in Non–Crystalline Materials, Clarendon, Oxford 1971.

[16] I.G. Austin and N.F. Mott, Adv. Phys., **18**, (1969), 41.

[17] N.N. Greenwood and T.C. Gibb, Mossbauer Spectroscopy (Chapman and Hall) London, U.K., 1971.

[18] T. Hernandez, F. Plazaola, T. Rojo and J.M. Barandiaran, J. Alloys. Compd., **323**, (2001), 440.

[19] Wei Tong, Bei Zhang, Shun Tan, and Yuheng Zhang, Phys. Rev. B, **70**, (2004), 014422.

[20] A. Simopoulos, M. Pissas, G. Kallias, E. Devlin, N. Moutis, I. Panagiotopoulos, D. Niarchos and C. Christides, Phys. Rev. B, **59**, (1999), 1263.

[21] F. Hong, Z. Cheng, H. Zhao, H. Kimura and X. Wang, Appl. Phys. Lett., **99,** (2011), 092502.

[22] P.S. Anil Kumar, P.A. Joy and S.K. Dat, J. Phys.: Condens. Matter., **10,** (1998), L269.

[23] J. Maier, S. Prill and B. Reichert, Solid State Ionics, **28**, (1988), 1465.

[24] A.K. Jonscher, J. Phys. D: Appl. Phys., **13**, (1980), L89.

[25] L. Zhang and Z-J. Tang, Phys. Rev. B, **70**, (2004), 174306.

[26] O. Bidault, M. Maglione, M. Actis, M. Kchikech and B. Salce, Phys. Rev. B, **52**, (1995), 4191.

[27] P.B. Macedo, C.T. Moynihan and R. Bose, Phys. Chem. Glasses, **13**, (1972), 171.

[28] J. Liu, Chun-Gang Duan, Wei-Guo Yin, W.N. Mei, R.W. Smith and J.R. Hardy, J. Chem. Phys., **119**, (2003), 2812.

[29] S. Saha and T.P. Sinha, Phys. Rev. B., **65**, (2002), 134103.

[30] Rujun Tang, Chen Jiang , Jie Jian, Yan Liang, Xin Zhang, Haiyan Wang and Hao Yang, Appl. Phys. Lett., **106**, (2015), 022902.

CHAPTER – 7

CONCLUSIONS AND FUTURE SCOPE OF WORK

7.1 Summary and conclusions of thesis

Perovskite oxide materials belong to an interesting class of compounds that display a wide range of unique electronic properties from insulator to metallic and magnetic properties varying from magnetic to nonmagnetic. Hole-doped mixed valent rare earth manganite perovskites have been chosen for the present work where $DyMnO_3$ is the parent compound for the synthesis of a series of substituted compounds. The effect of average ionic size at Dy site on the structural, magnetic and electrical properties of hole-doped manganites is investigated by replacing Dy by heterovalent ions, K^{1+}, Ba^{2+}, Bi^{3+} and Eu^{3+} in the parent compound, $DyMnO_3$ and Fe^{3+}/Fe^{4+} in Mn site in the parent compound, $Dy_{0.55}Sr_{0.45}MnO_3$. Dy site substitution influences the magnetic properties of the materials leading to complexities in the electronic and magnetic properties resulting in complex ground states. All the compounds were synthesized via solid state reaction route with appropriate thermal conditions depending on the compound. A number of various techniques have been used to characterize the investigated compounds. The thesis mainly contains six **Chapters**. An introduction to the research problem is given in **Chapter 1**. **Chapter 2** describes materials synthesis and experimental details of the measurements performed in the present work. In **Chapter 3**, structural, magnetic and transport properties of potassium substituted $DyMnO_3$, viz., $Dy_{1-x}K_xMnO_3$ compounds are described. Fourth **Chapter** is dedicated to divalent substituted compounds, $Dy_{1-x}Ba_xMnO_3$. Influence of the chemical substitution of Dy site by isovalent Bi and Eu ions in $Dy_{1-x}(Bi/Eu)_xMnO_3$ on their physical properties is discussed in **Chapter 5**. In the sixth and last **Chapter**, analysis of the structural, transport, magnetic and dielectric studies of the co-substituted compounds, $Dy_{0.55}Sr_{0.45}Mn_{1-x}Fe_xO_3$ has been presented.

In **Chapter 3**, effects of monovalent ion (K^{+1}) substitution at Dy site in $DyMnO_3$ ($Dy_{1-x}K_xMnO_3$ (x=0.0-0.3)) are described. The materials were synthesized by high temperature solid state reaction. All the materials showed orthorhombic structure like parent compound $DyMnO_3$. Lattice parameters and structural parameters like, bond angle and bond lengths have been obtained from the Rietveld refinement of the powder X-ray diffraction data. It was observed that the orthorhombic unit cell volume reduced for increasing K concentration due to the generation of smaller tetravalent manganese ions upon potassium substitution. XPS spectra showed evidence for tetravalent ions in the compounds. Hardening of lattice modes with increase in the potassium content was observed. The observation of the new Raman modes for 30% K may be ascribed to the local symmetry changes. Transport properties of the materials revealed semiconducting nature with hopping conduction. The compounds with x=0.0 to 0.2 showed SPH behavior, whereas, x=0.3 displayed VRH conduction due to large amount of Mn^{4+} ions as compared to Mn^{3+} ions. Both dc and ac magnetization data revealed paramagnetic behavior at high temperatures followed by the presence of magnetic transitions at low temperatures. Compounds with partial replacement of Dy^{3+} by K^{1+} ions retained the AFM transition corresponding to Mn ions although the AFM of Dy^{3+} ions reduced to lower temperatures. The magnetic transition temperatures were determined from the first derivative of molar susceptibility against temperature and effective magnetic moments were calculated by fitting the high temperature paramagnetic susceptibility to the CW law. The parasitic ferromagnetism resulting from the canting of Mn spins in addition to the exchange correlations between Dy and Mn spins may be responsible for the observation of hysteresis loops with reasonable coercive fields without saturation of magnetization.

The ac electrical properties of $Dy_{1-x}K_xMnO_3$ were studied in the temperature range: 127-299 K. As potassium increased, dielectric constant and dielectric loss also increased indicating conduction type relaxations. The frequency dependence of the real part of the complex conductivity in the low frequency range is frequency independent which is equivalent to the dc conductivity. At high frequencies, the conductivity increased with increase in the frequency following power law. The modulus spectra suggested that two types of relaxations are present in the materials. Using circuit analysis, grain and grain boundary activation energies were found by fitting the Cole-Cole plots to a circuit diagram. As temperature increased both grain and grain boundary resistance values decreased implying the semiconducting nature of the compounds.

Chapter 4 discusses various studies on the divalent substituted $DyMnO_3$ system, $Dy_{1-x}Ba_xMnO_3$. The solid solution series of $Dy_{1-x}Ba_xMnO_3$; x=0.0 to 1.0 compounds were synthesized by the conventional solid state reaction route. The compounds with x=0.0 to x=0.5 showed orthorhombic structure while compounds with x=0.8 to 1.0 exhibited the hexagonal structure. The structural phase transition from orthorhombic to hexagonal was also observed in the room temperature Raman spectra. The temperature dependence of electrical resistivity showed semiconducting nature with hopping mechanism. Hopping and polaron binding energies were calculated from Motts equations. Analysis of room temperature XPS spectra revealed the presence of both tri and tetra valent manganese ions whose ratio decreased with increase in the Ba content. The temperature dependence magnetization of $Dy_{1-x}Ba_xMnO_3$; x=0.0 to 1.0 showed paramagnetic nature in the high temperature region. The experimental effective magnetic moments determined from the CW fit parameters were compared with the theoretical effective magnetic moments calculated from the individual atomic moments as per the chemical formula of the respective compounds. Field dependence of isothermal magnetization showed the presence of multiple exchange interactions between the magnetic ions.

Systematic investigations of the solid solution series, $Dy_{1-x}Eu_xMnO_3$; x=0.0-1.0 and $Dy_{1-x}Bi_xMnO_3$; x=0.0 and 0.1 carried out by means of several characterization techniques and physical property measurements are presented in the **Chapter 5**.

Rietveld refinement of XRD analysis showed that both the systems retained the orthorhombic structure. Raman spectra exhibited broad bands in the wave number range 200cm^{-1} to 100 cm^{-1}. The Raman modes arising from the atomic vibrations of dysprosium and oxygen ions have been identified. It is seen from the temperature dependence of electrical resistivity that all the displayed semiconducting behavior. However, various conduction mechanisms were found to be operating. Bi substituted compound, showed magnetic transitions identical to the pristine compound. In contrast to the hole doped compounds studied so far, in the europium substituted compounds, only a single magnetic transition from paramagnetic state to E-type (up-up-down-down) antiferromagnetic state was observed. The M-H curves of DEMO (0.0<x<1.0) are straight lines complementing the temperature dependent magnetic data.

The **Chapter 6** discusses about the structural, Mossbauer, vibrational, electrical, magnetic and dielectric properties of solid solution series, $Dy_{0.55}Sr_{0.45}Mn_{1-x}Fe_xO_3$

0.0≤x≤1.0. All the compounds were found to have an orthorhombic structure with Pnma space group with 4 formula units per unit cell. However, for high iron content, viz., x=0.8 and 1.0 some minor impurity phases were present. Raman modes of the substituted compounds were found to shift to high wave number as compared to x=0.0. All the compounds displayed insulating property with variable range hopping type of conduction. Mossbauer spectroscopy studies performed at room temperature revealed the presence of both trivalent and tetravalent iron ions for high concentrations of iron in DSMFO. Sextet pattern observed for high concentrations of x suggested a magnetic phase. By fitting the paramagnetic susceptibility data measured in the field cooled cycle at 1 T to the CW law, effective magnetic moments, $\mu_{eff.}$ (expt.) were obtained. Effective magnetic moments, $\mu_{eff.}$ (cal.) were calculated by considering the individual atomic magnetic moments corresponding to the nominal compositions of materials. The ratio of $\mu_{eff.}$ (expt.)/$\mu_{eff.}$ (cal.) which is more than unity suggested the formation of weak ferromagnetic clusters in the compounds. Analysis of the dielectric properties of these compounds revealed that x=0.4 showed dielectric relaxations and the two compounds, x=0.0 and 1.0 showed impedance type relaxations.

7.2 Future scope of work

- So far, physical properties of polycrystalline $DyMnO_3$ and related compounds in bulk (polycrystalline) form were studied. As concluded from the dielectric studies, the properties depend to a large extent on the grain boundaries present in the polycrystalline materials. In order to probe the intrinsic properties of the materials, single crystals are required.
- Hall Effect measurements on these hole doped materials could give a direct evidence to the nature of electrical conduction.
- Thin films of these materials may be useful for spintronics applications.

- Low temperature dielectric studies will help in identifying the ferroelectric phases.
- Polarized neutron scattering is a very good technique to probe crystal and magnetic structures of magnetic materials. Hence in this direction, further experimental efforts are required to determine the exact magnetic structures of the different anti ferromagnetic phases.

INTERNATIONAL CENTRE FOR DIFFRACTION DATA
ICDD®
INTERNATIONAL CENTRE FOR DIFFRACTION DATA
12 CAMPUS BOULEVARD NEWTOWN SQUARE, PA 19073-3273 U.S.A
WWW.ICDD.COM • INFO@ICDD.COM
phone: 610.325.9814 • fax: 610.325.9823 • toll-free: 866.378.9331 (U.S. & Canada only)
ISO 9001:2008 QUALITY ASSURED COMPANY CERT.NR. 11409.1

13 June 2017

Dear Dr. Nithya:

Enclosed is a certificate which is being awarded in recognition of your contribution to the **Powder Diffraction File** in Release 2018.

Again, the ICDD appreciates your cooperation and interest in the **Powder Diffraction File**.

Yours truly,

Soorya Kabekkodu

Dr. Soorya N. Kabekkodu
Editor-in-Chief

SK:jah
Enclosure

ICDD®
INTERNATIONAL CENTRE FOR DIFFRACTION DATA

International Centre for Diffraction Data

CERTIFICATE AWARDED TO

Dr. R. Nithya

in recognition of the significant contribution of 2 patterns to the

Powder Diffraction File - Release 2018

Soorya Kabekkodu

Editor-in-Chief

INTERNATIONAL CENTRE FOR DIFFRACTION DATA

ICDD®
INTERNATIONAL CENTRE FOR DIFFRACTION DATA

12 CAMPUS BOULEVARD NEWTOWN SQUARE, PA 19073-3273 U.S.A
WWW.ICDD.COM • INFO@ICDD.COM
phone: 610.325.9814 • fax: 610.325.9823 • toll-free: 866.378.9331 (U.S. & Canada only)

ISO 9001:2008
QUALITY ASSURED COMPANY
CERT.NR. 11409.1

13 June 2017

Dear Dr. Yadagiri:

Enclosed is a certificate which is being awarded in recognition of your contribution to the **Powder Diffraction File** in Release 2018.

Again, the ICDD appreciates your cooperation and interest in the **Powder Diffraction File**.

Yours truly,

Soorya Kabekkodu

Dr. Soorya N. Kabekkodu
Editor-in-Chief

SK:jah
Enclosure

ICDD®
INTERNATIONAL CENTRE FOR DIFFRACTION DATA

International Centre for Diffraction Data

CERTIFICATE AWARDED TO

Dr. K. Yadagiri

in recognition of the significant contribution of 2 patterns to the

Powder Diffraction File - Release 2018

Soorya Kabekkodu
Editor-in-Chief